13
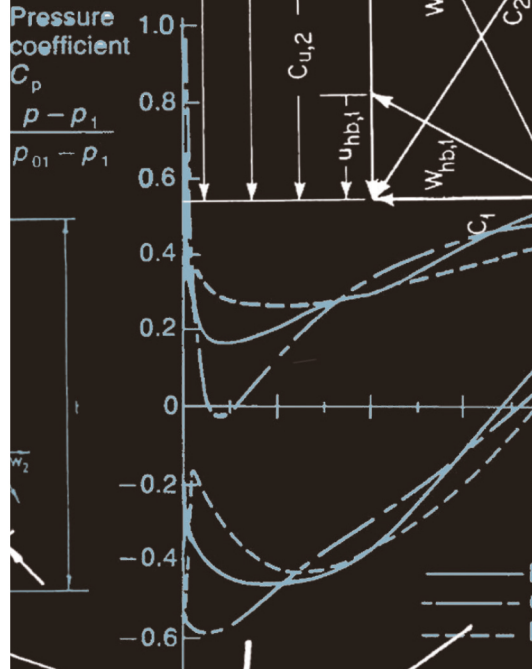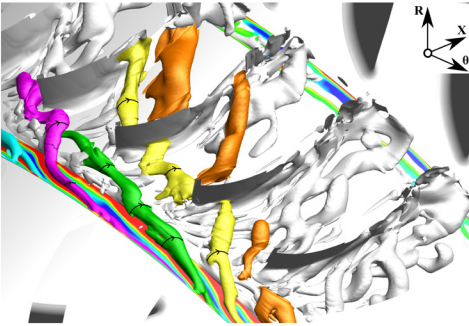
Diego R. Flores Galindo

Influence of Labyrinth Seals in Cavities on the Flow of an Axial Compressor

Institut für Turbomaschinen
und Fluid-Dynamik

Influence of Labyrinth Seals in Cavities on the Flow of an Axial Compressor

von
Diego Rodrigo Flores Galindo, M. Sc.
geboren am 4. Dezember 1982
in Mexiko Stadt, Mexiko

2018

Members of the thesis comittee:
Chairmain: Prof. Dr.-Ing. Roland Lachmeyer
1. Referent: Prof. Dr.-Ing. Jörg Seume
2. Referent: Prof. Dr. Friedrich Dinkelacker
3. Referent: Prof. PhD. Xavier Ottavy

Abstract

The vortex structure inside the upstream cavity-trench depends on the cavity outlet angle. Independently of the cavity outlet angle, the interaction of the upstream rotor wake and the leakage flow induces a wake-leakage vortex. The proximity of the cavity outlet with the rotor modifies the number of induced wake-leakage vortices. This investigation reveals that in the downstream cavity-trench a windage effect occurs similar to the upstream cavity-trench but with minor intensity. The leakage flow cannot recirculate to the upstream cavity-trench and be reheated. All investigated configurations modify the recovery factor near the hub, namely below 10% span with the inclusion of the cavity. The Kerrebrock and Mikolajczak's effect remains on the stator suction-side at the hub due to the leakage flow transported by wake-leakage vortices while at mid-span the effect appears on the stator pressure-side. The overall performance of the third compressor's stage shows that the effect of the cavity outlet angle is more influential at lower leakage rates. As the leakage rate progressively increases, the cavity outlet angle loses its influence. Independently of the cavity outlet angle, the inclusion of the cavity in the third stage reduces the total pressure level and increases the total temperature level of the stage as a consequence of the transport within the wake-leakage vortices. This combination results in a more pronounced deterioration of the isentropic stage efficiency. For every 1% of labyrinth seal clearance increase, the stage total pressure ratio decreases between 0.114 to 0.132%, and total temperature ratio increases between 0.039 to 0.051% resulting in an isentropic efficiency reduction by 0.828 to 0.944%.

Zusammenfassung

Die Wirbelstruktur innerhalb des stromaufwärts Hohlraum hängt vom kavitätsaustrittswinkel ab. Unabhängig von dem kavitätsaustrittswinkel, die interaktion zwischen Rotorsnachlauf und Leckageströmung induziert das "wake-leakage" wirbel. Die Nähe der Kavitätaustrittswinkel mit dem Rotor verändert die Anzahl der induzierten "wake-leakage" wirbeln. In der stromabwärts Hohlraum existiert ein "Windage Effekt". Alle untersuchten Konfigurationen modifizieren den "Recovery factor" nahe dem Statornabe, nämlich unter 10% von Statorhöhe mit dem betrachtung der Kavität. Die Kerrebrock- und Mikolajczak- Effekt bleibt auf der Statorsaugseite an der Statornabe aufgrund der Leckageströmung. Für jede 1% des Labyrinthdichtungsabstands steigt das Gesamtdruckverhältnis zwischen 0.114 und 0.132% ab und das Gesamttemperaturverhältnis zwischen 0.039 und 0.051%, was zu einer isentropen Wirkungsgradreduktion um 0.828 bis 0.944% führt.

Acknowledgements

This dissertation is the result from the help of many people who placed effort in different ways. It would not be possible without their contribution.

Contents

Nomenclature

Acronym	Description
ACARE	Advisory Council for Aviation Research and Innovation in Europe
ADVACT	Development of ADVanced ACTuation concepts to provide a step change in technology used in future aero-engine control systems
BPR	Bypass Ratio
CAEP	Committee on Aviation Environmental Protection
CFD	Computational Fluid Dynamics
DES	Detached Eddy Simulation
DNS	Direct Numerical Simulation
DREAM	valiDation of Radical Engine Architecture systeMs
EARSM	Explicit Algebraic Reynolds Stress Model
E-BREAK	Engine BREAKthrough Components and Subsystems
EEFAE	Efficient, Eco-Friendly Aircraft Engines
ENOVAL	ENgine MOdule VALidators
EU	European Union
GCI	Grid-Convergence Index
HPC	High-Pressure Compressor
HPT	High-Pressure Turbine
IATA	International Air Transport Association
ICAO	International Civil Aviation Organization
LE	Leading Edge
LEMCOTEC	Low EMissions COre-Engine TEChnologies
LES	Large Eddy Simulation
LUH	Leibniz Universität Hannover
MAT	Medial Axial Transformation
NACA	National Advisory Committee for Aeronautics
NEWAC	NEW Aero-Engine Core Concepts
NS	Near Stall
OPR	Overall Pressure Ratio
PE	Peak Efficiency
PS	Pressure Side
RANS	Reynolds Averaged Navier Stokes
RPM	Revolutions Per Minute
SFC	Specific Fuel Consumption
SS	Suction Side
SST	Shear Stress Transport
TE	Trailing Edge
TFD	Institut of Turbomachinery and Fluid Dynamics

TRACE	Turbomachinery Research Aerodynamic Computational Environment
UHBR	Ultra-High Bypass Ratio
UHOPR	Ultra-High Overall Pressure Ratio
URANS	Unsteady Reynolds Averaged Navier Stokes
VITAL	EnVIronmenTALly Friendly Aero Engine

Symbols

Symbol	Unit	Description	Defined by eq.
A	m^2	Clearance cross-sectional area	
c	m	Blade chord	
CO_2	%	Carbon dioxide	
C_p	J/kg K	Specific isobaric mass heat capacity (1004.71)	
d	m	Diameter	
h	m , J	Labyrinth clearance, Enthalpy	
$\dot{m}$	kg/s	Mass flow	
N, n	-	Number of fins	
NO_x	%	Nitrogen oxides	
P_T	Pa	Total pressure	
Q	-	Q-criterion	A.43
R	J/kg K	Air specific ideal gas constant (287.06)	
$\Re$	%	Recovery ratio	2.8
s	m	Labyrinth pitch, Span	
S	J/kg K, m	Entropy, Stage pitch	
t	m	Labyrinth thickness	
T_T	K	Total temperature	
U	m/s	Rotational speed	
V_{ax}	m/s	Axial flow velocity	
V_{mer}	m/s	Meridional flow velocity	A.31
V	m/s	Flow velocity magnitude	A.32
V_{rad}	m/s	Radial flow velocity	
V_{tan}	m/s	Tangential flow velocity	

Greek Symbols

Symbol	Unit	Description	Defined by eq.
α	°	Flow coefficient, Flow angle	A.33
β	°	Relative flow angle	

Δ	-	Delta	
γ	-	Specific heat ratio (Air: 1.4)	
η	-	Efficiency	
ϕ	-	Flow function	
π	-	Ratio	
ρ	kg/m^3	Density	
σ	-	Solidity	
θ_{T}	-	Normalized total temperature	A.37
θ_{P}	-	Normalized total pressure	A.36
ζ_p	-	Total pressure loss coefficient	2.15
ζ_s	-	Entropy loss coefficient	2.16

Operators

Symbol	Description
$\frac{\partial}{\partial x}$	Partial derivative
$\mathcal{O}$	Order of magnitude
δ_{ij}	Kronecker delta

Subscripts

Symbol	Description
ax	axial
cav	cavity
hub	hub
in, 1	Inlet
leak	leakage
out, 2	Outlet
is	isentropic
Mm	Multimode
max	maximal
mer	meridional
pol	polytropic
rad	radial
red	reduced
ref	reference
s	static
T,t	total
tan	tangential

| Tur | Turbulent |

Note: All reprinted figures are not intended to provide exact values of the original publications, they are reproduced in order to improve their visual quality. The nomenclature in reprinted figures is left as is found in original source in order to not alter its original significance. If the reader wants to know more accurate data and the original nomenclature please refers to the source for better explanation.

List of Figures

List of Tables

1.   Introduction

1.1   Motivation

Changes in global economic policy, population growth and growing awareness for environmental conservation have impacted the technological perspectives of civil air transport in the past decade. The report, "Vision 2020" (Argüelles et al. 2001), devised by the Advisory Council for Aviation Research and Innovation in Europe (ACARE) is the first attempt aimed at proposing a series of technological recommendations targeted at improving the aeronautical sector through research and innovation of novel concepts, materials, and shapes in order to reduce pollutant and noise emissions. More recently, the Strategic Research and Innovation Agenda (ACARE 2012) or "Flightpath 2050" identifies specific goals and fundamental challenges, including the protection of the environment. It clearly defines the time periods in which these identified goals have to be achieved. All stakeholders, namely regulatory authorities (ICAO, CAEP, IATA), airline companies, manufacturers, and suppliers are conscious of the fact that the aeronautical sector must develop more affordable, safer, cleaner, and quieter technologies. In the short- and mid-term, these technologies are mainly aimed at improving the efficiency of propulsion powerplants, it being the component that requires considerably more enhancements in order to comply with the more stringent environmental targets established by 2050: reduction of perceived noise, NO_x emissions and CO_2 emissions (per passenger kilometer) by 65%, 90%, and 75%, respectively, all relative to the year 2000.

The implementation of profound technologies in "Flightpath 2050" is not easy to accomplish. The readiness of new concepts takes time and large capital investments of both government and private initiatives, as shown in Figure 1.1a which illustrates the budget of recently launched European programs aimed at developing the aforementioned technologies. The level of sophistication of current subsystems of gas turbines made it possible to achieve high efficiencies. Due to this high-level of sophistication, the gains in efficiency have become increasingly smaller. According to ENOVAL Consortium (2014), CO_2 emissions of A320Neo engines have progressively been reduced since the launch of the program EEFAE until 2012 as shown in Figure 1.1b. The program EEFAE itself reduced CO_2 emissions by 10% in 5 years, while for an additional reduction of 10% it required 10 years more and four supplementary programs (i.e. VITAL, NEWAC, DREAM and LEMCOTEC). According to Kyprianidis (2011) for an existing axial compressor design, the effort for improving 1% in efficiency could require 10 years of development and investigation since the year of entry in service, and afterwards it would take another 10 years to achieve an extra gain of 0.5%. It would take 20 years altogether for an enhancement of 1.5%.

On one hand, the manufacturers must invest in research in the short-term, increasing cost. On the other hand, the airlines must amortize in the mid- and long-term and they must offer an attractive cost-benefit ratio to their customers. This imbalance between investment and amortization threatens the profitability of air transportation. Therefore, the technological changes must be gradually implemented in order to benefit all stakeholders in the long-term. Since the publication of the document "Vision 2020", the European Union (EU), industry partners and universities have invested in different projects such as EEFAE (European Commission 2005a), VITAL (European Commission 2010b), NEWAC (NEWAC partners 2011), DREAM (European Commission 2012b), LEMCOTEC (LEMCOTEC partners 2012) E-BREAK (E-BREAK

Partners 2014) and ENOVAL (ENOVAL Consortium 2014) which are aimed at enhancing the thermal cycle efficiency of gas turbines.

(a) Budget distribution

(b) A320Neo engine (ENOVAL Consortium 2014)
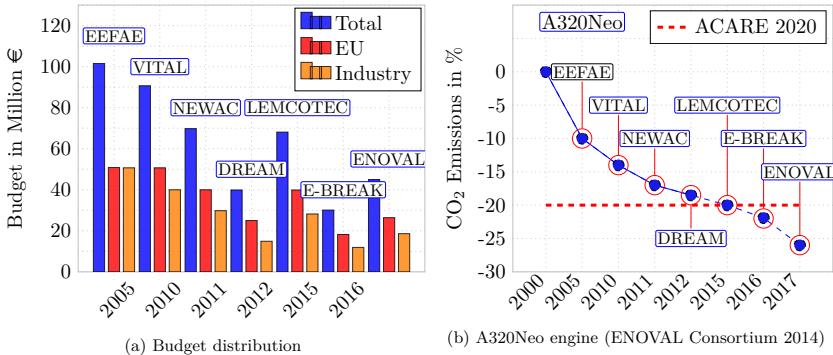
Figure 1.1: European Union's research and innovation funding programmes

These projects were substantially oriented to increase the overall pressure ratio (mainly of the core compressor) and increasing the turbine inlet temperature. The program EEFAE evaluated new technologies' benefits on overall aircraft performance with respect to a reference aircraft. All optimized aircraft showed more than 10% reduction in fuel consumption and CO_2 emissions, that in turn reduced the direct operating costs by more than 4% (European Commission 2005b). The program VITAL concentrated on new and low weight technologies for low-pressure systems in ultra-high bypass ratio (UHBR) engines. It established the foundations for turbofan engines with very high bypass ratios (BPRs) of up to 15 (Korsia 2009, European Commission 2010b, Kyprianidis 2011). The program NEWAC investigated the feasibility of implementing heat exchangers in the core of four turbofan configurations, in order to evaluate the weight-to-thermal efficiency ratio (NEWAC partners 2011). The program DREAM studied a range of completely novel designs for both contra-rotating open rotors with ultra-high BPRs of 45 to 50, and turbofans developing novel engine systems (European Commission 2010a). The program LEMCOTEC focused mainly on ultra-high pressure ratio compressors and lean combustion for ultra-high overall pressure ratio engines (LEMCOTEC partners 2012, European Commission 2012a). The program E-BREAK develops robust core sub-systems that minimize the losses in more compact engine cores. This project also expects to validate new material components, in order to endure the high turbine inlet temperature (E-BREAK Partners 2014, European Commission 2013). The program ENOVAL investigates mainly the low-pressure system of propulsion systems with UHBR from 12:1 up to 20:1, and ultra-high overall pressure ratio (UHOPR) from 50:1 up to 70:1 (ENOVAL Consortium 2014, European Commission 2013). The studies of the LEMCOTEC project (LEMCOTEC partners 2012) reported by von der Bank et al. (2015) suggested that the CO_2 emissions-to-fuel reduction objectives set for the aero engines alone in the ACARE Vision for 2020 will most likely be attained for Regional Turbofans and probably be exceeded for Mid-Size Open Rotor and Large Turbo Fan by up to 50%. Although the studies indicate positive improvement, the newly developed technologies have to be validated on corresponding test rigs. The projections of E-BREAK and ENOVAL surpass the ACARE 2020 targets and are aiming to accomplish the coming ACARE 2035 targets.

The common idea behind of the aforementioned programs is an improvement of the thermodynamic cycle of an aeroengine. The cycle can be enhanced by means of increasing the overall pressure ratio (OPR) and increasing the turbine inlet temperature. The latter involves improvements in turbine blade materials and cooling techniques to increase their endurance concerning high thermal loads, and delay the corrosion that eventually occurs through long-term operation. In addition, enhancements in the combustion sub-system with leaner injection systems are necessary. The OPR increase encompasses the need of a solution to a series of phenomena clearly identified in the compression sub-system, which eventually increase the losses and consequently decrease the compressor efficiency. These include the well-known and documented rotor tip clearance vortex, end-wall separation, and cavity clearance leakage flow illustrated in Figure 1.2a.
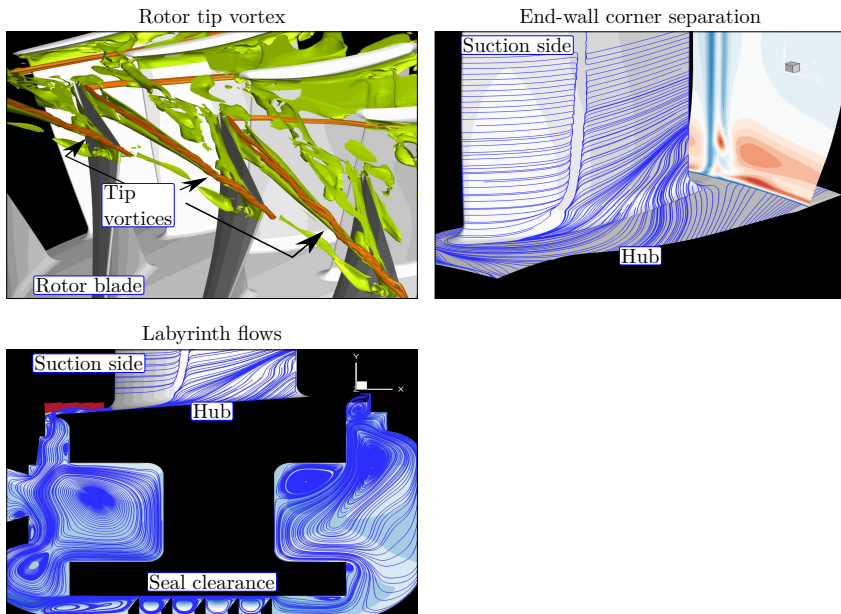
Figure 1.2: Typical flow phenomena that detriment the axial compressor efficiency

For each of these detrimental phenomena illustrated in Figure 1.2, there is a wide range of active and passive flow control techniques that promise to tackle, and thus minimize the detrimental consequences on the overall pressure ratio and efficiency of an axial compressor. In order to dissipate or at least minimize the rotor tip clearance vortex, different geometries (e.g. grooves, holes, slots) in the casing have been investigated both numerically and experimentally (see Figure 1.3). These geometries aim to modify the tip gap flow field and consequently extend the stall margin of the compressor. Even though the casing treatments have been proved to extend the stall margin, they also induce a compressor efficiency penalty, particularly at design operating conditions.

One of the active flow control (AFC) approaches more thoroughly investigated is the rotor air

flow tip injection. This AFC method delays the stall inception and extends the compressor's stable operating range. The end-wall corner separation has also been intensively investigated, because this flow phenomenon considerably increases losses and contributes to the passage block-age, which restricts the maximum loading obtainable by the compressor. In order to reduce corner separation, different slot configurations both on the stator suction-side near the trailing edge and inside the stator passage have been investigated numerically and experimentally.

As shown in Figure 1.3, Vorreiter et al. (2012) and Siemann et al. (2016) applied airflow injection and aspiration in stators, respectively, in order to reduce flow separation. In a compressor with shrouded stators, the complex structure of labyrinth leakage flow disrupts the main flow near the hub, which results in an increase in the extent of the end-wall corner separation. Increased end-wall corner separation reduces the compressor efficiency. A passive flow control counteracting the disturbed flow on the stator row is a non-axisymmetric hub design as proposed by Hergt et al. (2011) in Figure 1.3.

The leakage flow has affected the performance of turbomachinery since the manufacturing of first steam turbines due to the poor sealing (i.e. large clearances compared to current ones) between rotating and stationary parts. Great efforts have been made to understand and improve the turbomachinery sealing (Wisterfeld 1978) and new concepts and technologies are being revised continuously (Chupp et al. 2006). The evolution of materials and manufacturing processes have allowed a significant reduction of the clearance gaps. Consequently, this has minimized the leakage flow. At the same time, these advances have lead to turbomachines with higher values of pressure, temperature and mass flow. However, the current efficiency profit margin has become marginal, and therefore leakage flows have become even more important to be analyzed, understood, and then minimized in order to maximize the energy conversion capacity. Within the aeroengine components, three types of clearances have been clearly identified: blade tip, bearing, and interstage. They are distributed along the whole engine, and are associated directly with the leakage flow which potentially increases the performance loss due to the cumulative effect. An improved sealing in both high-pressure compressors (HPC) and high-pressure turbines (HPT) brings considerable enhancements in fuel savings, reduced emissions, and an extension of engine service life. Wiseman and Guo (2001) suggest as a rule-of-thumb that for 0.254 mm of clearance reduction in HPT at take-off, the exhaust gas temperature decrease by 10 K while at cruise condition, this clearance represents a reduction of 1% specific fuel consumption (SFC). Based on this latter amount, Lattime and Steinetz (2004) estimate annual projected fuel cost savings of $160 million and 0.02 billion gallons for U.S. airlines.

According to these estimates, the sealing system in an axial compressor is not a minor concern for manufacturers and airlines. The program E-BREAK (E-BREAK Partners 2014) shows the continuing interest in sealing technology improvements. This program contains a sub-project which focuses on improvements in current air and oil seals, and the development of advanced sealing technologies. This program demonstrates the strong interest in reducing the secondary flows originated by labyrinth flows. Therefore, this work investigates the interaction of labyrinth seal flows with the mainstream of an axial compressor in order to look deeper into and understand the physical mechanism behind this interaction.
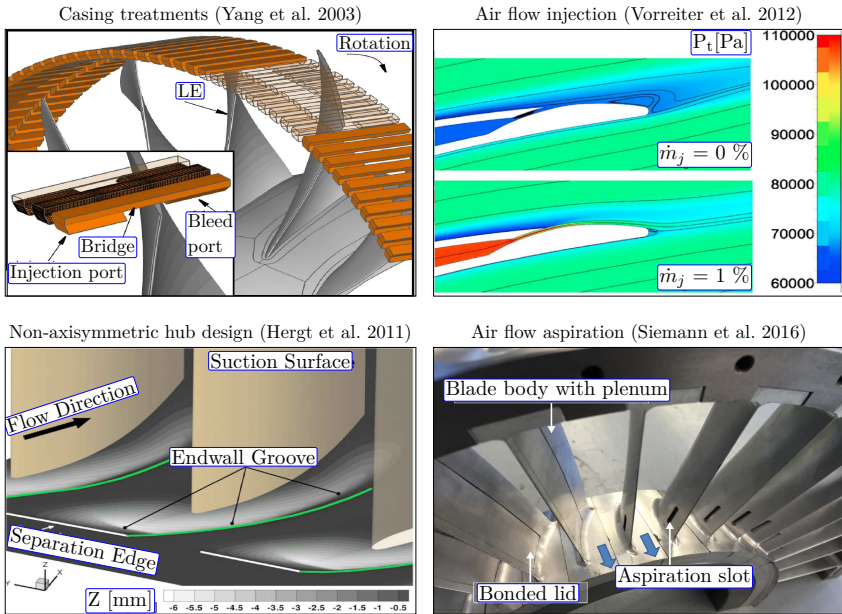
Figure 1.3: Promising solutions to typical flow phenomena in an axial compressor

1.2 Approach and objectives

Currently, numerical simulations complement analytical and experimental investigations, in order to provide further physical insight which other approaches cannot provide in detail. Additionally, numerical simulations allow the exploration of different designs with relatively fast evaluation of their performance, before launching a prototype and manufacturing a final product. The work presented here is entirely based on numerical simulations, taking advantage of the corresponding advantages of this method.

The most significant interaction between the cavity leakage flow and the main stream occurs in the discharge region between the hub and the upstream cavity-trench as shown in Figure 1.4. Based on this, the modification of the cavity outlet angle could reduce the aforementioned interaction and consequently minimize the losses. The main aim of this work is to evaluate the influence of the cavity outlet discharge angle on stage performance. To this end, three variants have been designed for the third stage of a four-stage high-speed axial compressor in order to investigate the influence and effect of the injection of leakage flow into the main flow path. The third stage was selected, because secondary flows are more pronounced and detrimental in rear stages due to the low aspect-ratio blading. In order to prove the hypothesis, different aspects of the influence of the cavity outlet angle in this work will be investigated:

- Leakage flow rate and tangential velocity at the cavity discharge are key parameters in
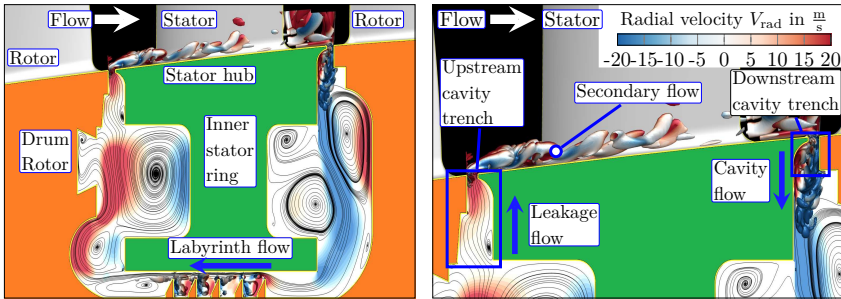
Figure 1.4: Flow through the cavity (left) and the interaction of leakage flow with the main stream flow (right)

the disruption of the main flow near the hub. The cavity leakage flow spoils the end-wall boundary layer. Due to the passage pressure gradient, the disturbed flow is more susceptible to being transported to the stator's suction-side where it interacts with the boundary layer. These three-dimensional flow interactions disrupt the main stream, increasing the losses and degrading the efficiency. Wellborn and Okiishi (1999), Demargne and Longley (2001), Sohn and Song (2006) have shown that an increase in the tangential velocity component compensates the effect of the leakage flow perturbations and thus reduces the loss in efficiency. According to this fact:

    1.- Which cavity outlet angle provides a higher tangential velocity at the upstream cavity surface?

- Wellborn and Okiishi (1996, 1999) suggest that a portion of the main flow enters into the upstream cavity slot due to the existence of a vortical structure inside the cavity-trench.

    2.- Is this existing vortical structure modified by the cavity angle outlet variation?

    3.- How does the vortex influence the ingestion of main stream flow into the cavity-trench?

    4.- Does the interaction between the leakage flow and the main stream flow cause the formation of vortex structures at the hub?

    5.- How do resulting vortices behave and how do they affect the performance?

- Bayley and Childs (1994) have shown analytically that small leakage flow rates tend to increase the windage in both downstream and upstream cavity-wells.

    6.- If the leakage flow ejection reduces, how does this affect the leakage flow windage?

- Once the heated leakage flow has been ejected from the upstream cavity slot, it interacts with the end-wall boundary layer generating secondary flow. Wellborn and Okiishi (1996) suggest that the secondary flow downstream of the stator near and close to the hub dictates which portion of the mainstream flow will be sucked into the downstream cavity-trench.

    7.- Is a portion of heated leakage flow prone to be trapped within the end-wall boundary layer?

8.- If it is, could it be sucked in again at the downstream cavity-trench and then be reheated as it will be ejected at the upstream cavity-trench?

- Unsteady numerical investigations carried out by Montomoli et al. (2009, 2013) in axial compressors with cantilevered stators have shown that a beneficial inviscid mechanism (wake recovery) occurs as the upstream wakes are transported through the next downstream stator passages. Most of these investigations have been focused on the midspan and casing region. To the author's knowledge, only Montomoli et al. (2009, 2013) have analyzed the hub region. Their investigation suggests that the interaction between the upstream wake and the penny gap flow (see Figure 1.5) leads to 15% extra recovery factor, which is completely beneficial. In the case of shrouded stators: to the author's knowledge solely Fröbel et al. (2010) have reported loss coefficient reductions near the hub due to the wake recovery. However, despite their stators being shrouded, they also have penny gaps at the hub between the mid chord and the trailing edge. They related the loss coefficient reduction to the same interaction observed by Montomoli et al. (2009, 2013).

9.- How much does the cavity leakage flow disturb the recovery effect at the hub?

10.- If the recovery effect is altered, which cavity variant minimizes this perturbation?

11.- How much span percentage of the wake recovery remains unaltered by the cavity leakage discharge?
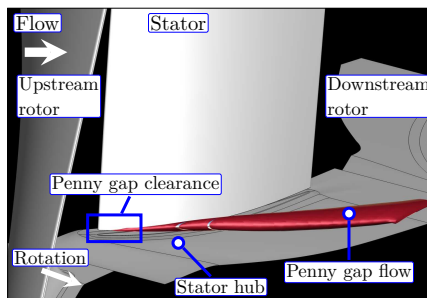
Figure 1.5: Penny gap flow in a cantilevered stator

- Typical geometrical assumptions and modeling simplifications are made when predicting labyrinth mass flow leakage by means of computational fluid dynamics (CFD) simulations. These include non-rotating walls, pre-swirl boundary conditions and small pitches.

12.- How accurate is the labyrinth mass flow leakage prediction with respect to the available analytical models taking into account more realistic cavity geometries in steady-state single-blade and unsteady multi-blade simulations?

1.3   Outline of this thesis

The remainder of this thesis is structured in the following way. Chapter 2 gives an overview of the differences between typical blading configurations in axial compressors, and their influence on the performance curve. This is followed by investigations carried out in shroud cavities in terms of both aerodynamics and thermal purposes. A subsection highlights the modeling of cavity flows. Afterwards, a summary of a few unsteady investigations including cavity geometries is given. A description of the distinct labyrinth seal configuration together with a review of the different analytical models for the leakage flow prediction is given. Furthermore, some attempts to predict labyrinth performance by means of CFD simulations are described. Ultimately, the benefits of the unsteady rotor-stator interaction are reviewed, and a brief description of the identified loss sources in axial compressors is given. Chapter 3 presents a detailed description of the numerical setup. The main features of the test rig and details of the meshing procedure are given. Preliminary studies are presented to show the grid independence and to determine the physical model error in the performance prediction. Chapter 4 is totally devoted to discussion: the leakage flow path inside the cavity and the forming recirculation structures inside the upstream and downstream cavity-wells and cavity-trenches; the sensitivity of the leakage flow to cavity outlet angle; the mechanism of the flow structures induced by leakage flow and their variation with three cavity outlet angles. Additionally, it continues with the transport of thermodynamic properties by leakage vortices in the stator passage; the unsteady effects such as the Kerrenbrock and Mikolajczak's effect and recovery effect near the stator hub and the modification of these effects under the existence of labyrinth flows; the detrimental consequences of aforementioned topics in the stage performance. Chapter 5 draws the conclusions resulting from the present investigation based on the questions posed in section 1.2 and the discussions in Chapter 4.

2. Literature survey

2.1 Blading configurations

Since the invention of turbomachinery, leakage flows have persisted due to the unavoidable clearances that exist between the rotating and non-rotating parts. In the past, leakage flows were intrinsically included in the overall losses of a turbomachine (i.e. gas turbines, axial compressors), since the loss generated by secondary leakage flow was insignificant compared to the overall output power. Over the years, turbomachinery sealing technology has improved considerably due to the advanced manufacturing techniques and the availability of new materials. Thus, current turbomachines achieve such a high level of sophistication that performance gains become marginal. Leakage flows are directly proportional to the clearance size, which is strongly dependent on the available manufacturing techniques, materials, and operating conditions of the turbomachine.

In axial compressor design, there are commonly two types of configurations of stator blading as shown in Figure 2.1: cantilevered and hub shrouded blades. Each arrangement possesses benefits and drawbacks. Cantilevered blades are connected to the outer casing, while at the hub there is a clearance between the blade and the rotor shaft. The clearance must be large enough relative to a shrouded blade in order to avoid rubbing and possible damage during transient operating conditions. A larger leakage flow results when it crosses through the larger clearance. In case of contact between the stator tip and the rotor drum, the wearing area will directly affect both the stator and the rotor, as it is wider than a shrouded configuration. Across the clearance, the flow leakage is driven by the pressure difference between pressure and suction side. Additionally, the moving rotor wall increases the shear stresses at the boundary layer that in turn increases the energy of the clearance leakage flow. These stators are easier to manufacture and consist of less parts, but they could be susceptible to vibration issues as they have a high span-to-chord ratio (e.g. in the first stages of a compressor).
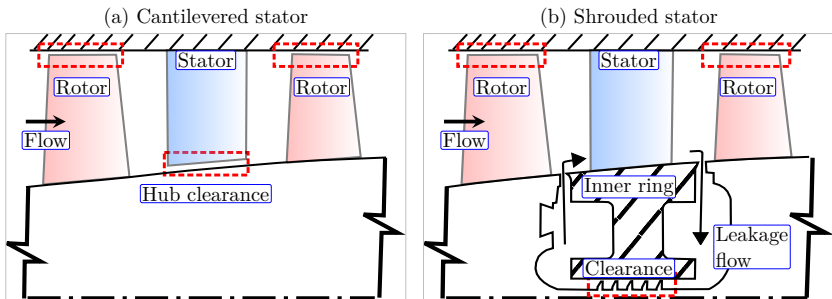
Figure 2.1: Typical configurations of axial compressor blading

The shrouded stators are held between two concentric rings, the outer and the inner ring, which are fastened to the compressor housing. The rotor blades are mounted in dove-tail grooves milled into the rotor discs as shown in Figure 2.1b. This arrangement provides increased structural

stability and allows thinner airfoils in comparison to the cantilevered stators, however it requires more mounting components which in turn increase the weight of the compressor. To accommodate the inner ring, the rotor shaft must be manufactured with a cavity in between the two rotor discs. In case of contact between the rotor seal-fins and the inner ring, the wearing will only affect the inner ring and the seal-fins. Thus, the wearing area of the rotor drum is minimized, and stator blades are protected from any contact. In order to minimize the leakage flow through this cavity, a labyrinth seal is used. Because of the existing clearance in the labyrinth seal, a flow recirculates in the direction opposite to the main flow in the cavities, passing through the clearances and gaps between the rotor seal-fins and stator inner ring. This recirculating flow is mainly driven by the static pressure rise in the main flow path. Such flows induce additional aerodynamic losses when they are re-injected and mixed with the main flow path at the stator hub.

To the best of the author's knowledge, Jefferson and Turner (1958) are the first to emphasize the importance of shroud clearances in the design and manufacture of axial compressors and the influence of such clearances on the overall performance. They experimentally investigated a series of combinations of both shrouded stators and cantilevered stators. Despite the cantilever clearance being 50% greater than the seal clearance, the cantilevered stator showed the overall better performance when the loading is increased on the compressor as shown in Figure 2.2a. However, their shrouded configuration does not have any type of labyrinth seal due to the manufacturing limitations at that time instead using a single axial seal. They also depict how the performance deteriorates when the shroud clearance increases as shown in Figure 2.2b. The isentropic efficiency reduces linearly. Approximately for each 2.7% of clearance the isentropic efficiency drops almost 1%. Below 0.5% of clearance the isentropic efficiency is almost insensitive to clearance.
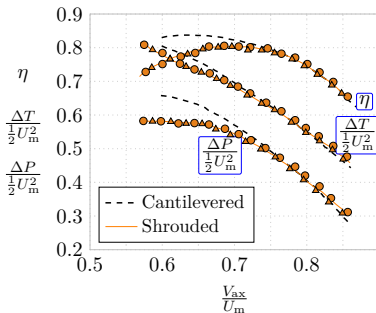
(a) Overall characteristics. Blading with shrouded stators. 0.010 inches shrouding clearance. 0.020 inches cantilevered clearance. Isentropic efficiency η. Temperature rise coefficient $\frac{\Delta T}{\frac{1}{2}U_\mathrm{m}^2}$. Pressure rise coefficient $\frac{\Delta P}{\frac{1}{2}U_\mathrm{m}^2}$.
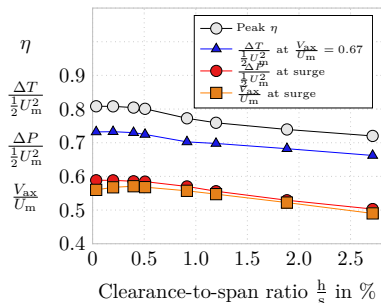
(b) Variation of overall parameters with shrouding clearance. Blading with shrouded stators. Isentropic efficiency η. Temperature rise coefficient $\frac{\Delta T}{\frac{1}{2}U_\mathrm{m}^2}$. Pressure rise coefficient $\frac{\Delta P}{\frac{1}{2}U_\mathrm{m}^2}$. Flow coefficient $\frac{V_\mathrm{ax}}{U_\mathrm{m}}$.

Figure 2.2: Performance comparison of shrouded and cantilevered stators, reprinted from Jefferson and Turner (1958)

A posteriori, Freeman (1985) compares cantilevered stators and stators with deep and shallow shrouds. He demonstrates that a shrouded stator achieved approximately 2.5% lower efficiency

than cantilevered arrangements at the peak efficiency as shown in Figure 2.3a. For this specific two-stage low-speed axial compressor, the cantilevered configuration shows the highest efficiencies up to 2.5% of clearance to flow area, whereas the shrouded stator becomes more efficient when the clearance to flow area is larger than 2.5% as shown in Figure 2.3b. The trend of shrouded stators includes both deep and shallow shrouds. Analyzing separately, deep shrouds depict a more pronounced slope, namely the efficiency drops 2% with a variation of the clearance less than 1% while shallow shrouds show a more conservative slope, the efficiency drops 2% for 3.5% of clearance increase. This suggests a higher sensitivity of deep shrouds compared to shallow shrouds when clearance increases.

(a) Efficiency characteristics of channel section shrouding

(b) Comparison of shrouded and unshrouded stators on 2nd stage of a low reaction compressor
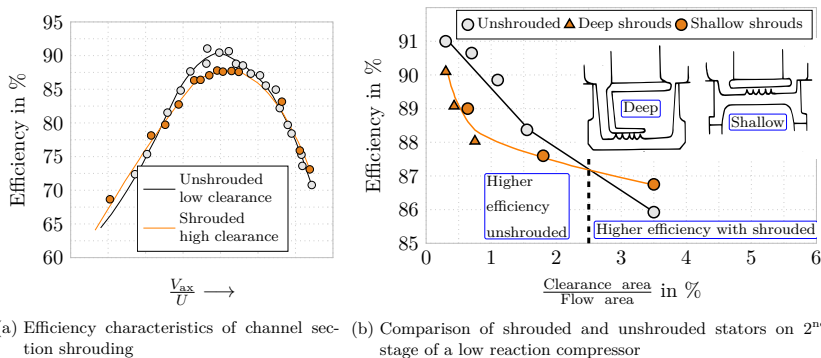
Figure 2.3: Performance comparison of shrouded and unshrouded stators, reprinted from Freeman (1985)

Recently Lange et al. (2010) experimentally investigate the influence of clearance variations in cantilevered and shrouded stators in a four-stage low-speed axial compressor. For the cantilevered configuration, four clearance ratios were tested, from 1.5% to 5% of span while for shrouded arrangement the clearance variations include 1%, 1.6% and 3.3% of span. They found that the peak efficiency approximately decreases by 1% when clearance increased by 3.5% of span over the last two stators for the cantilevered configuration. For the shrouded configuration, they estimated the same efficiency drop with an increase of the seal clearance under the third stator by 2.3% of span.Their labyrinth seal was simplified in order to measure the leakage flow through the cavity which rate is shown in Figure 2.4. Their rate of leakage flow increases linearly approximately 0.73% for each 1% of clearance increase. The increase of the leakage flow reduces linearly the corresponding isentropic efficiency in shrouded stators as shown in Figure 2.4. They also plotted the stator performance against clearance-to-span ratio for both shrouded and cantilevered configurations. For the near stall point, the cantilevered stator outperforms its counterpart while at the design point, their trend suggests that shrouded stators are more efficient for clearances smaller than 1.6% of clearance-to-span ratio. In this case, the slope of shrouded stators is more pronounced compared to cantilevered stators in both operating points. This indicates that clearance is most sensitive for shrouded stators than its counterpart.
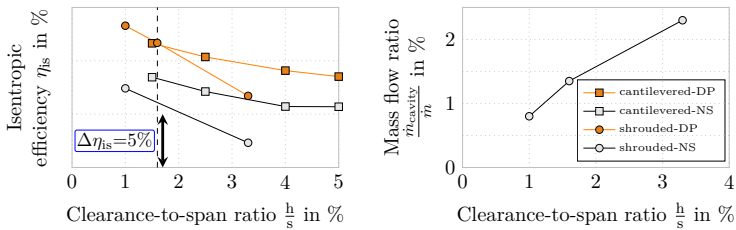
Figure 2.4: Isentropic efficiency comparison of a quasi-stage including shrouded and cantilevered stators (left) and mass flow rate through cavity at design point (right), reprinted from Lange et al. (2010)

2.2   Shrouded stator cavity flows

Cavity flows has been widely studied mostly in turbines, but in axial compressors little research has been carried out. This section is devoted to review the most relevant topics related to the interaction between leakage flow and annular flow in the open literature in which the most important findings and attempts are pointed out. This section has been divided into four main topics. The first subsection reviews the aerodynamic effects of stator cavity flows on the compressor performance. The second subsection discusses the thermal effects due to the stator cavity flows. The third subsection reviews the attempts to simulating the cavity flows with one-dimensional models. The fourth subsection reviews a few numerical unsteady simulations of axial compressors including cavities. The last part summarizes and identifies the main findings found in the above subsections and help to formulate the objectives of this work previously written in section 1.2.

2.2.1   Aerodynamic effects of stator cavity flows on the compressor performance

In the open literature, Wellborn and Okiishi (1996, 1999) were the first to conduct an experimental investigation devoted exclusively to elucidating and quantifying the influence of seal-fin leakage flows of shrouded stators on the overall performance of a multi-stage axial compressor. They split the investigation into two parts: the first one involves the variation of seal-fins leakage in all stages of the test rig, in order to quantify the cumulative deterioration in overall performance. The second part only takes the seal-fin leakage variations in the third stage into account in order to quantify the local deterioration and the effect on downstream stages. The data of the first part of the investigation shows that increasing labyrinth seal-fins leakage degrades both work input and pressure rise. This degradation leads to an expected decrease in efficiency. All reductions in work input, pressure rises, efficiency and seal-fins leakage vary almost linearly with seal-fin clearance. The variations of leakage flow and efficiency at two operating points are depicted in Figure 2.5. In their work the rate of leakage flow increases linearly approximately 0.63% for each 1% of clearance increase. This slope is lower compared to that reported by Lange et al. (2010) in Figure 2.4. A more detailed analysis of the stage degradation shows that increasing seal-fin leakage lowered the pressure rise of all stages and the deterioration is more pronounced in downstream stages. It is important to mention that the increase of seal-fin

leakage has no perceptible effect on the flow coefficient near the stall.
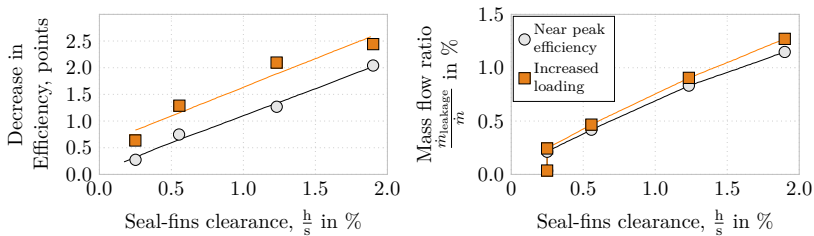
Figure 2.5: Overall performance deterioration through seal-fins clearance variation at two operating conditions, reprinted from Wellborn and Okiishi (1996)

Wellborn and Okiishi (1996, 1999) conclude that the variation of seal-fins leakage is almost imperceptible in the rotor performance of that stage. At the same time, the stator flow field near the hub is altered, resulting in modified stator exit conditions. Consequently, the next downstream rotor cannot recover the already degraded flow from the upstream stator. Circumferential distributions of the upstream cavity show that seal-fin leakage flow re-entered the main stream near the mid-pitch, while the flow appears to be sucked into the cavity-trench at the stator leading edge. In the downstream cavity-trench the flow enters over the entire pitch, but the flow near the downstream rotor leading edge enters faster into the cavity-trench than other locations.Their results indicate that for every 1% increase in the clearance-to-span ratio, the overall pressure rise drops by as much as 3% while the efficiency drops by 1 to 1.5 %.

In addition to experimental investigations, Wellborn and Okiishi (1999) simulate the isolated stator 3 with the corresponding cavity geometry, in order to demystify the mechanism of the upstream cavity tangential velocity on the near-hub flow field. The simulation results show qualitatively that leakage flow with low tangential momentum tends to be collected on the near-hub suction side, and eventually distorts the boundary layer in this location. More leakage produces lower tangential velocity leakage flow that in turn increases the passage cross-flow. As tangential velocity increases, the suction side was less prone to collect leakage flow on that side. Thus, the tangential velocity increase in a certain way compensates the leakage flow.

Heidegger et al. (1996a,b) conducted a detailed parameterized study of the shrouded stator seal cavity of a typical multi-stage axial compressor in order to numerically investigate the flow through the seal cavity. The geometric parameterization included seal-fins clearance, cavity depth, rotational speed, radial mismatch, axial trench gap, hub corner and hub edge treatments. Although the test rig was a multi-stage axial compressor, they only simulated steady-state isolated vane and unsteady rotor-stator-rotor interactions. They found that the tangential velocity increases from nearly zero to approximately 75% of the wheel speed as the leakage flow passes through the seal cavity. This in turn increases the temperature of the leakage flow due to windage. Near the stator hub, the higher tangential velocity at the cavity outlet modifies the flow incidence by up to 20° higher compared to the mid-span value. As the leakage flow through the seal cavity increases, the exit tangential velocity of the leakage flow decreases to approx. 50% of the wheel speed. Consequently, the flow incidence is reduced near the stator hub. This in turn reduces the size of the separated region on the suction-side of the stator. They identify negative radial velocities in the upstream cavity in front of the stator, because the potential flow of the stator leading edge forces a fraction of the main flow path inside the upstream cavity-

trench. A similar effect is observed in the downstream cavity-trench; the downstream rotor has a strong effect on the flow being pumped into the cavity-trench. The parameterized study reveals a linear dependence of seal-fins leakage flow on seal-fins clearance. This parameter is also the most influential in terms of leakage flow. The effects of the leakage flow are more pronounced at approximately 10% span into both up- and downstream cavity trenches.

Scott et al. (2000) performed an experimental investigation which focuses on the understanding of the flow structure in the downstream cavity through the variation of rotational speeds and main flow pressures. The measurements were made in a two-stage high-speed axial compressor and then compared with two- and three-dimensional CFD solutions. Their results of pitchwise distributions at multiple axial positions at the downstream cavity inlet show that the static pressure changes are more significant in front of the rotor wall and tend to be weaker toward the stator wall. Inside the cavity the numerical model computes a circumferentially uniform static pressure. This quasi-symmetry in static pressure supports the assumption of modeling the suck in flow at the downstream cavity as a uniform distribution.

Oeztürk et al. (2000) numerically investigates nine different stator cavity geometries, focusing on the downstream stator-well (i.e. the geometry between the cavity inlet and the first seal-fin), in order to examine the effect of the geometrical changes in the stator-well on the leakage flow passing through. Upstream distributions of radial and tangential velocity at the mid-span cavity-well exhibit little variation as a result of the geometrical variations in the downstream cavity-well. As a consequence of the seal-fins reduction, tangential velocities increased in both up- and downstream cavity-wells. Even though they found that all investigated geometries scarcely varied with respect to the leakage mass flow. The geometry with a series of fins extending over 50% of the axial width of the cavity from the downstream rotor face and circumferentially extending over one stator pitch is sketched in Figure 2.6a. This geometry showed the highest tangential velocity in the downstream cavity-well. This configuration shows a tangential velocity near the rotor velocity from the mid-span cavity to near the stator inner lip. Along the axial width of the downstream cavity well, the highest tangential velocity prevailed from 40% up to the downstream rotor face, towards the stator face the tangential velocity gradually reduced up to 60% rotor velocity as shown in Figure 2.6b. As a consequence of increasing the tangential velocity in the downstream cavity-well, the near-hub pressure increases and the inner cavity-well pressure decreases. The resultant effect is equivalent to reducing the leakage flow by 26% compared to the nominal leakage flow or reducing the clearance roughly to half.

Demargne and Longley (2000) experimentally and numerically investigated the influence of the leakage flows, focusing on the leakage tangential velocity. The test rig allowed them to control the leakage flow and the tangential velocity independently at the upstream cavity-trench while 15% chord downstream of the stator trailing edge a slot allowed them the extraction of leakage flow as shows the sketch in Figure 2.7a. As expected, as leakage flow increases, the hub corner separation expands in size and depth. In contrast, the increase in tangential velocity in both up- and downstream cavities shrinks the hub corner separation in size and shape as compared to the baseline. The total pressure loss in the flow core (e.g. at mid-span) is scarcely affected by the leakage flow. For every 10% increase in tangential velocity, the total pressure loss decreases 0.85% at the hub as shown in Figure 2.7b. This shows that the tangential velocity counteracts the detrimental effects of the leakage flow, the latter resulting in an increase of the total pressure loss at the hub. Their measurements and oil flow visualizations show that as a consequence of the tangential velocity augmentation, the flow turning at the hub also increases, leading to a redistribution of the leakage flow to the adjacent pressure-side. In this way, the leakage flow

(a) Radial fins on downstream rotor face   (b) Cavity-trench distributions
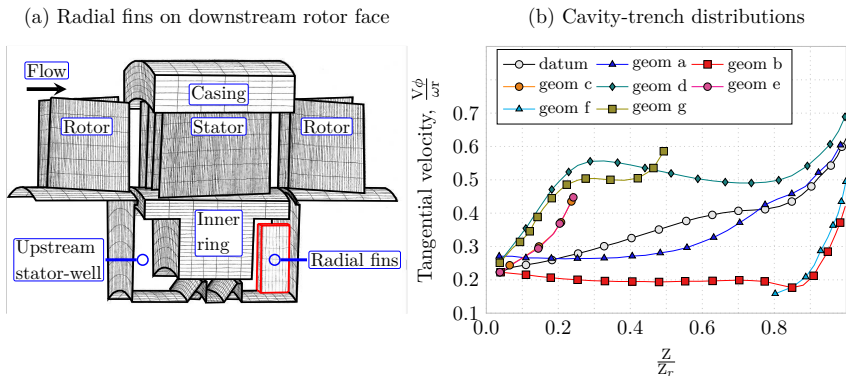
Figure 2.6: (a) Sketch of radial fins on downstream rotor face (geometry d) and (b) tangential velocity in the downstream stator well, reprinted from Oeztürk et al. (2000)

is able to overcome the passage pressure gradient and less leakage flow is prone to be collected on the suction-side, thus reducing the hub corner separation. Pitchwise distributions of the relative concentration of fluid from the cavity measured in the upstream cavity trench, confirm that in some areas of the cavity slot the mainstream flow enters into it due to the interaction with the leakage flow. Additionally, the same pitchwise distributions show that there is a relationship between the blade pressure field and the local minimum and maximum leakage corresponding to a greatest and lowest pressure field, respectively. An increase in tangential velocity in the upstream cavity tends to weaken the strength of the vortical structures in the cavity slot. Demargne and Longley (2000) moved the slot by 35% of axial chord upstream in order to investigate if the pitchwise distributions improve. The results show that for leakage fractions lower than 0.5% the stagnation pressure loss diminishes, while in the remaining leakage fractions the shifted slot depicts similar loss as the datum case. They found that leakage flow varies linearly with the difference between upstream cavity pressure and average pressure at the hub as shown in Figure 2.7c. They remark that this relationship can change depending on the cavity outlet geometry.

Wellborn (2001) focuses on the flow structure inside the cavity-trenches and its flow field near the hub. The datum cases represent typical configurations of moderately loaded subsonic rear stages of a compressor. Measurements were acquired and presented from the third stage of a multi-stage axial compressor operating near peak efficiency (Wellborn and Okiishi 1996). The first numerical model represents the isolated stator, along with the cavity geometry of the third stage of the corresponding test rig. The second case is a simplified generic cavity geometry model with one plenum in both cavity inlet and outlet. Inside the cavity-trench, the tangential velocity surpasses in magnitude the axial velocity which almost goes down to values near to zero in both up- and downstream cavities. The tangential velocity dominates in magnitude in both up- and downstream cavities, but it still remains below the tangential velocity in the main stream. In the downstream cavity the profile of tangential velocity at -10% span suggests that the rotor drum rapidly transfers energy to the incoming leakage flow. Although they do not show total temperature distributions, they report an average temperature increase of approximately 40 K as the leakage flow travels through the cavity. In both cavity-trenches, the static pressure

(a) Stagnation pressure loss coefficient

(b) Leakage fraction

(c) Skematic diagram of the cascade rig
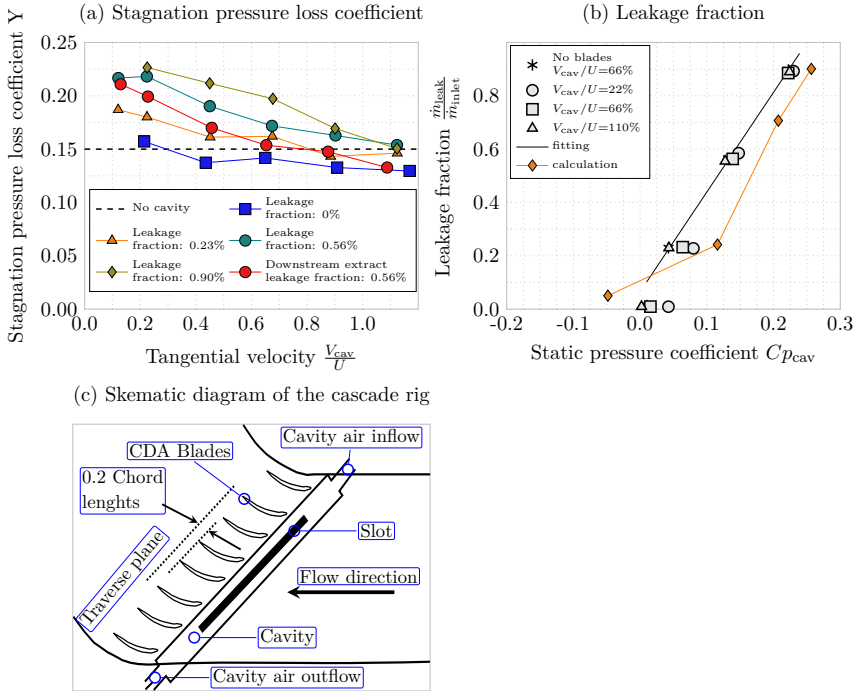
Figure 2.7: (a) Skematic diagram of the cascade rig; (b) Variation of stagnation pressure loss coefficient Y at the hub with increase of tangential velocity V_{cav} at the cavity outlet and (c) leakage flow variation $\frac{\dot{m}_{leak}}{\dot{m}_{inlet}}$ with static pressure coefficient Cp_{cav}, reprinted from Demargne and Longley (2000)

remains unaltered with respect to the main stream, however as the flow egresses and ingresses in the corresponding trenches, the total pressure drops and the upstream cavity-trench shows a more pronounced diminution. Discrepancies in tangential velocity magnitude at the upstream cavity-trench are found compared with Heidegger et al. (1996a,b). The latter reports tangential velocities up to 70% of hub speed at -5% spanwise location while Wellborn (2001) shows that the distributions reach rates of approximately 43% hub speed at the same spanwise location as illustrates Figure 2.8. They argue that the differences are due to the distinct turbulence models utilized in the corresponding investigations. Numerical and experimental data confirm that leakage flow emanates from the cavity-trench near the mid-pitch, while in front of the stator leading edge the potential field restricts the leakage flow injection into the main flow.

Sohn and Song (2006) experimentally investigated the influence of the leakage tangential velocity and the flow behavior inside the cavity geometry in order to understand the kinematics and dynamics of the leakage flow in a linear cascade. They used two different cascade rigs, the first using air with the purpose of measuring flow angles and stagnation pressure losses in the stator passage, and the second using water with the purpose of visualizing the flow inside the
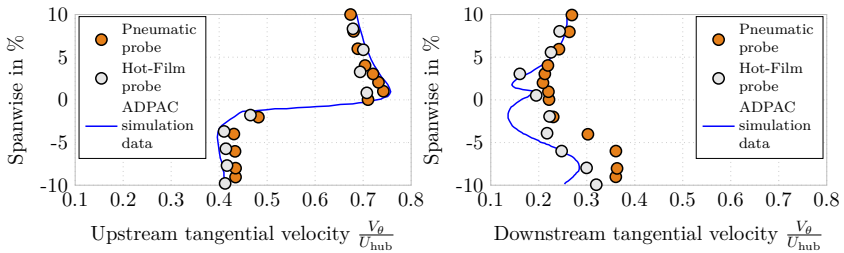
Figure 2.8: Radial distributions of tangential velocity V_θ at the mid-trench in up- and down-stream cavities, reprinted from Wellborn (2001)

cavity. Their results show that the increase in leakage tangential velocity effectively reduced the loss along the stator passage. The loss reduction is more pronounced and noticeable from 50% chordwise in the passage than downstream of the stator passage (i.e. 90% and 130% chordwise). At these latter locations, the loss core circumferentially detaches from the suction-side towards the mid-pitch, and at the same time it radially returns towards the hub casing. Visualization of the shrouded cavity confirms that, for a given stator as reference, the leakage flow sucked into the downstream cavity moves circumferentially when it crosses the labyrinth seal-fin, and is re-injected into the mainstream after it circumferentially migrates several stator passages. The circumferential migration amount depends on the leakage tangential velocity.

Becker et al. (2009) numerically investigated a 4.5 stage high-speed axial compressor in order to assess the impact of real cavity geometries on the accuracy of the performance calculation. At the stage interfaces, they employed the mixing plane technique and the non-linear harmonic approach for comparison. Additionally, they evaluated the effect of a transition model on the predictions. On the one hand, with conventional interface methods (e.g. mixing plane), they find that the coupling of three shrouded cavities with the main channel diminishes both the overall efficiency and the mass flow rate by 0.25% and 0.1%, respectively in comparison with the model without cavities. On the other hand, the application of the non-linear harmonic approach leads to a more pronounced decrease in both overall efficiency (0.65%) and mass flow rate (1%). The major penalties are observed in the first stage, the shock formation in the rotor blade passage being the dominant contributor to the corresponding reduction rather than the effect of the cavity flows. The performance trends of both interface methods, mixing plane and non-linear harmonic with the activation of the transition model results in an increase in both mass flow and overall efficiency by 0.23% and 0.65%, respectively with respect to the fully turbulent simulation.

Marty and Aupoix (2012) numerically investigated the influence of the cavity leakage flow in a three-stage high-pressure compressor with different turbulence models. Taking the cavity into account, the simulation improves the prediction of the total pressure ratio and the efficiency levels are closer to the experimental data throughout the compressor operating range. At the upstream cavity are revealed vortical structures whose location, shape, and size depend on the cavity geometry and the turbulence model used. The EARSM (i.e. Explicit Algebraic Reynolds Stress Model) turbulence model is the most accurately model to predicting the global performance.

Flores and Seume (2014) numerically investigated through steady single-pitch simulations the influence of three cavity outlet inclination angles (i.e. 45°, 90° and 135° in the counterclockwise direction with respect to the flow direction) on the third stage of a 4.5 stage high-speed axial compressor as shown in Figure 2.9, on the performance deterioration at the design operating point. In addition, the seal-fin clearance is increased to evaluate higher rates of leakage flow. In order to clarify the accuracy of physical modeling, two distinct turbulence models combined with a transition model are evaluated. The sensitivity of both turbulence models was evaluated through the comparison with experimental radial profiles which are axially distributed along the high-speed compressor. The SST turbulence model proves to be more sensitive in terms of isentropic efficiency, total pressure, and total temperature ratio to leakage flow increase in the three cavities compared to the shroudless model. Neither turbulence model correctly predicts the progressive temperature rise present in the experimental data above 55% of the blade height. The cavity with 135° (i.e. the cavity outlet pointing against the main flow) showed the lowest efficiency deterioration.
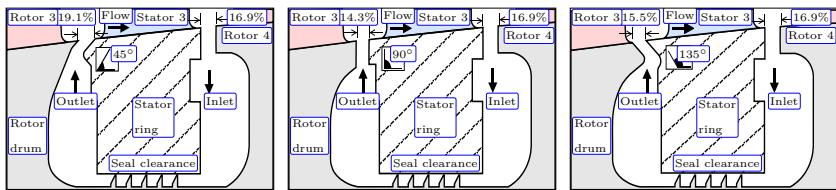
(a) Cavity outlet C_1 inclined by 45° (b) Cavity outlet C_2 inclined by 90° (c) Cavity outlet C_3 inclined by 135°

Figure 2.9: Meridional view of cavity configurations in the third stage

Flores and Seume (2015) extended the investigation in order to corroborate if the cavity with 135° could preserve the lowest efficiency deterioration over the entire speed line. At the design point, the predictions of the mass flow rate and total pressure by the shroudless model (e.g. no cavity) along with the three configurations agreed with experimental data within 0.3%. All configurations overestimated efficiency by approximately 2%. This excess is associated with the less pronounced temperature rise computed at the downstream rotor tip region by the SST turbulence model. The steady-state simulations indicate that the cavity outlet angle of 135° maintains the lowest isentropic efficiency reduction, compared to the shroudless model for a the clearance equal to 1.7% chord over the entire speed-line. The cavity of 135° opposite to the main flow allows the leakage flow to slow down the main flow near the hub. As the main flow decelerates, the axial velocity near the hub reduces, leading to an increase of the flow angle of 68° at the edge of the cavity-trench that in turn better redistributes the flow near the hub at stator inlet. Additionally, the flow deceleration near the hub allows better thermal mixing between the main flow and the leakage flow, which increases the main flow temperature near the hub.

2.2.2   Thermal effects in shrouded stator cavity

Over the years aero-engine compressor subsystems have achieved the augmentation of high pressure ratios that consequently have lead to higher gas temperatures. All compartments of the compressor subsystem such as stator shrouded cavities are exposed to such detrimental temper-

atures. As a result of this temperature increase, the components of rear stages are more prone to failure, and therefore need alloyed materials in order to endure the excessive heating. These alloyed materials are heavier and more expensive than typical titanium alloys. The windage concern is not trivial in compressor shrouded stators because if portions of heated leakage flow ejected from the upstream cavity remain attached to the stator hub end-wall boundary layer, they are prone to re-enter and recirculate through the seal-fin labyrinth seal, consequently increasing the heating and aggravating the temperature rise. The thermal management and heat generation inside of a stator-well is most critical. Scott et al. (2000) state that metal temperature measurements in the stator cavity of a HP compressor of a engine development rig have indicated up to 120 K above the mainstream annulus temperature, while Lewis (2002) observes the stator-well heating up to 130 K in previously reported tests.

The focus of the investigation of Bayley and Childs (1994) was to predict the temperature rise in stator-wells for a range of typical conditions. Their empirical model is based on the well-documented rotating disc (e.g. free disc). The model considers the annular depth of the stator-well (e.g. shallow or deep), the seal clearance and the leakage flow rate. The results show that for fixed geometrical parameters, increasing leakage flow the temperature rise decreases asymptotically. In the downstream stator-well, the highest temperature rise ($\sim$ 20 K) occurred with deep wells, tightest clearance and low leakage flow. At the same low leakage flow and tightest clearance, shallow wells attenuate the temperature rise. The lowest temperature rise is predicted with shallow wells and wider seal clearances, however high rates of leakage flow worsen the main channel performance. In all cases, the rotational speed increases linearly the temperature rise at the corresponding rate. The temperature rise in the upstream stator-well becomes more critical because it is determined by the temperature augmentation itself plus the cumulative temperature rise in the downstream stator-well. The highest temperature rise in the upstream stator-well reached approximately 90% (i.e. 18 K) with respect to the downstream stator-well temperature rise.

Oezturk et al. (1998) numerically investigate the windage effect in an isolated shrouded stator (i.e. including labyrinth seal, up- and downstream cavity-wells) by imposing a layered inlet temperature as boundary condition. They find that the maximum temperature is located at the upstream cavity-trench on the rotor face. Due to recirculation in the upstream cavity-well, the higher temperature immediately heats the flow discharged from the labyrinth. Circumferential distributions show relatively higher temperatures near the hub compared to mid-span and tip temperatures. One solution which they suggest in order to reduce the leakage flow and the corresponding windage without affecting the seal-fin clearance is a small axial protrusion (i.e. similar to that in Figure 2.6a) into the downstream cavity-well in order to restrict the flow admission to the labyrinth. Their results show a 9% reduction in both windage and mass flow through the seal-fin clearance.

Lewis (2002) presented temperature measurements in the five front stator-wells of a high-speed compressor, in order to investigate if the typical formulae for windage and leakage flow with appropriately selected factors can satisfactorily predict the measured temperatures. The investigation also intended to demonstrate that additional temperature rise is more significant at the front stage due to the forward leakage (i.e. the forward axial heated leakage flow crossing the interstices of the disc rims in the upstream direction as shown in Figure 2.10b). A new design of the cavity-wells is implemented on the engine test rig because in previous tests the reported heating in the cavity-well reached up to 130 K. The highest cavity-well heating (i.e. the temperature at downstream cavity-well minus temperature at the stator hub) was measured

in the first stage reaching 21 K, while the maximum inter-stage heating (i.e. the temperature difference between up- and downstream cavity-wells) reached 14 K in the fourth stage. The prediction of windage temperatures require seal flows, which are obtained with an in-house network flow solver. These rates represent approximately 0.3% of the annulus flow. The prediction of windage with standard formulae overestimates by about 50% and up to 97% the rates in the cavity-well heating and inter-stage seal heating, respectively. Further investigations show that heat flux absorption from the walls to the air has no influence on the estimates. However, during transients (i.e. during the engine acceleration) the heat flux from the air to walls is considerable and represents ca. 40 K inside the cavity-well. The swirl fraction influences the windage prediction because an increase in swirl fraction diminishes the windage. Thus, from this assumption he deduces the swirl velocites at the up- and downstream cavities reporting 50% and 33% V_θ (similar to those reported in Wellborn (2001) and illustrated in Figure 2.8), respectively. With these swirl fractions, he finds reduction factors related to swirl velocity which he applies to the previously overestimated rates of heating, resulting in a better correlation in all stages of less than 2 K (16.6%) in the stator-well heating and differences up to 17 K (89%) in inter-stage seal heating. The latter higher differences between measurements and typical formulae for windage are not well understood.

A second test focuses on the temperature rise from the inter-stage forward leakage as shown in Figure 2.10b, the test was carried out in a different compressor. The temperatures are solely monitored in the first, fourth, and fifth stages. The first engine test used non-extended axial roots in the rotor blades, which minimize the heated leakage between the downstream cavity-well and the adjacent cavity-well while the second engine has extended axial roots in the rotor blades as shown in Figure 2.10c,d. This latter configuration allows more heated leakage through the clearance between the outer surface of the disc rim and the inner surface of the rotor blade. Comparing the monitoring temperatures in the corresponding up- and downstream cavity-well of both engine tests, the temperature in the cavity-well in the second test at the first stage cavity-well increases by four times (88 K). The use of non-extended axial roots in the first test could explain the lowest temperatures in the front stator wells. This configuration provides an effective sealing to axial leakage. An extended revision and comparison with older engine tests with similar extended axial roots reveals that temperature in the cavity-well of the first stage depends on the number of extended axial roots downstream the first stage. According to his estimates the windage was generated approximately 50% in the downstream cavity-well, 30% in the labyrinth seal and the remaining 20% in the upstream cavity-well. The influence of the windage in all stages on the compressor efficiency reduction is about 0.1% and ca. 0.3% due to the leakage flow.

Additionally Lewis (2002) states that a portion of the annulus flow is ingested directly into the upstream cavity trenches of some of the stator wells of the test rig. This annular flow is cooler than the leakage flow that emerges from the upstream cavity trench and therefore helps to reduce the windage temperature of the leakage flow. The evidence suggests that the rate of the annular flow ingested into the upstream cavity trench varies from zero up to two times the leakage flow through the labyrinth seal.

Oezturk et al. (2002) numerically investigated the variation of tangential velocity as seal clearance increases, in order to use it as a leakage controller. Axial distributions of tangential velocity at the downstream stator-well show that by reducing seal clearance, the tangential velocity increases from the stator wall to approximately 65% of the axial distance while in the remaining axial distance the tangential velocity was scarcely affected. At the upstream stator-well, the

(a) Terminology and basic flow directions in a compressor stator well

(b) Showing the potential forward leakage path to the front stage stator well in a compressor with four stages of axial blade root

(c) Non-extended Axial Root Fixing

(d) Extended Axial Root Fixing
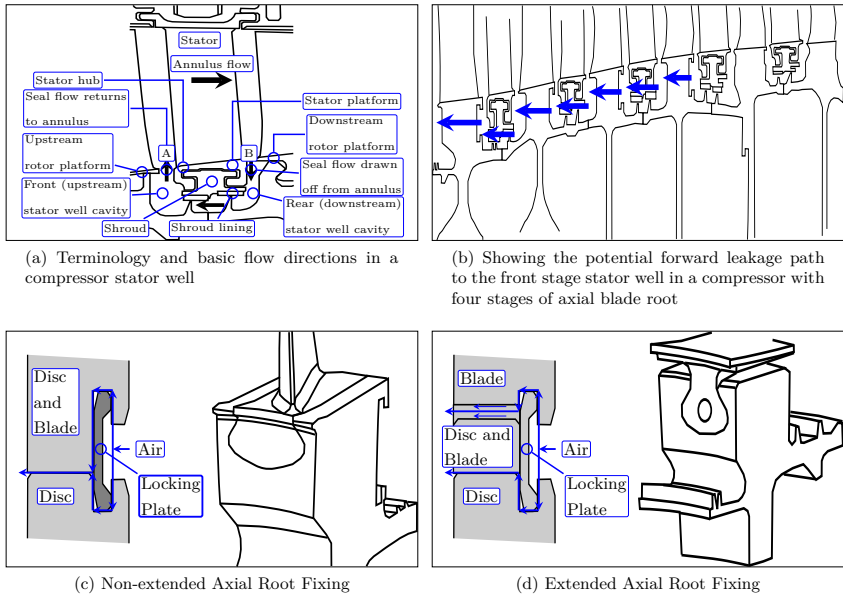
Figure 2.10: Terminology and basic flow directions in a compressor stator well, and the potential forward leakage paths through two types of axial blade root fixing, reprinted from Lewis (2002)

tangential velocity increases along the entire axial distance between the discs while distributions of radial velocity practically remained unaltered as seal clearance decreases. Radial velocity distributions become more pronounced as clearance increases, passing more leakage flow as expected. The results show that the diminution of seal-fin clearance reduces the leakage flow and slightly varies the temperature inlet at the downstream cavity-well. However, the temperature outlet at the upstream cavity-well increases. These temperature variations lead to different rates of windage heating. The two higher seal clearances (e.g. 0.5 and 1 mm) show the same temperature difference (11.4 K) between up- and downstream cavity-wells revealing that the highest clearance has the highest windage heating (e.g. 823 W) mainly due to the expected highest leakage flow. Although the tightest clearance (e.g. 0.3 mm) shows the lowest leakage flow, it also exhibits the highest temperature difference (16.5 K) leading to the second higher windage heating (646 W) being the major contributor the temperature difference. The lowest windage heating (563 W) was computed from the intermediate clearance (0.5 mm). The results show that windage heating depends on a trade-off between leakage flow rate and the temperature difference between the up- and downstream cavity-wells.

2.2.3   Use of one-dimensional models for cavity flows in 3D-flow solvers

Three-dimensional steady-state simulations give better performance agreement with test data when modeling stator cavities. However, it takes longer to achieve steady-state convergence when

stator cavities are included. In these simulations the pressure distributions converge relatively quickly compared to temperature distributions (Heidegger et al. 1996a,b). The complexity of simulating the main channel with coupled cavities arises from the interaction between high Mach number flows in the main channel, and low Mach flow regimes in the cavities. Due to the existing small temperature gradient inside the cavity, most flow codes slowly solve the energy equation which in turn considerably increases the run time. Typically, the coupled simulations require between 50 to 60% longer than a shroudless model (Flores and Seume 2015).

In this sense LeJambre et al. (1998) implemented one-dimensional single cavity and bleed models in a three-dimensional Navier-Stokes solver in order to supplant the cavity geometries, thus reducing the simulation run time. Their cavity model takes into account seal-fin clearance, rotor whirling speed and cavity depth. The cavity model is fed with a mass flow rate which is extracted downstream of the stator and re-injected upstream of the stator. The solver alters static and total pressure and total temperature until the provided mass flow is attained. Their results show that the solver with a one-dimensional cavity model is able to perceive the blockage generated by the re-entered leakage flow that in turn increases the axial velocity above 25% span, accomplishing continuity. In addition, the prediction of the radial distribution of total pressure downstream of the rotor better matches the test data as depicts Figure 2.11a. With the inclusion of the cavity model the overall pressure rise of the stage is reduced by 3%.
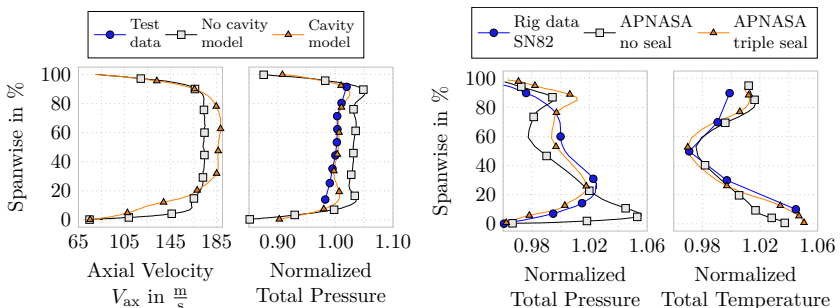
(a) Radial distributions of axial velocity V_{ax} at stator leading edge and normalized total pressure downstream of the rotor

(b) Radial distributions of rotor 11 discharge

Figure 2.11: Comparison of test data with radial distributions computed with different one-dimensional cavity leakage models coupled to distinct flow solvers; a) reprinted from LeJambre et al. (1998); b) reprinted from Wellborn et al. (2000)

Wellborn et al. (2000) developed a simplified model of cavity flows in order to corroborate that a one-dimensional cavity model coupled with a multi-stage design tool can effectively predict the change of compressor performance as the seal-fin clearance increases. Straight-trough- and stepped-tooth configurations are available in the model. They determined that leakage flow, tangential velocity, and temperature discharge of the upstream cavity are the most sensitive parameters as discussed in section 2.2. Additionally, they found that sucked leakage flow in the downstream cavity can be modeled by an elementary axi-symmetric mass extraction as Scott et al. (2000) pointed out. The results revealed that their one-dimensional cavity model was able to capture the total pressure reduction near the hub, generally matching the measurements, as

seal-fin clearance increases. In addition, the model is also able to predict the total temperature increase near the hub as depicted in Figure 2.11b. They estimate a mass flow and efficiency reduction approximately 1.6% and 0.8%, respectively, as the seal-fin leakage flows are considered.

Naylor et al. (2009) numerically investigate the fidelity, predictive accuracy, and computational effort of three different approaches to model the leakage flow and its influence on the main stream through steady three-dimensional multi-stage computations in a four-stage low-speed axial compressor. The reference configuration (0D) only takes the main flow path into account. The second (1D) and third cases (1D++) include a one-dimensional model. In the second case, the one-dimensional model is directly coupled at the annulus end-wall, while in the third case the one-dimensional model is set up at the end of the cavity-trenches. The last case (3D) includes the complete shroud cavity. The reference case predicts 1% higher efficiency than the other cases. It is found that neglecting shroud leakage results in reduced hub temperatures and reduced flow deviations. The third case (i.e. the one-dimensional model set up at the cavity trenches) shows the best trade-off in terms of accuracy and run time (60% increase being less than fully resolved cavities). Despite the good agreement with experiments, the one-dimensional model is not able to capture non-axisymmetric flow phenomena.

It is evident that one-dimensional cavity models coupled with three-dimensional flow solvers are able to elucidate the overall performance (e.g. flow, efficiency, and total pressure ratio) deterioration during the testing of axial compressors with a good trade-off between run time and accuracy. However, these one-dimensional cavity models require additional improvements, because they include several assumptions which require deep understanding and restrictions in the predictions such as circumferential variations and leakage injection angle (Naylor et al. 2009).

2.2.4   Numerical unsteady investigations including shrouded stator cavities

All the aero-thermodynamic processes in a gas turbine are highly complex. In an axial compressor the rotor blades are used to transfer work to the fluid. During the compression process the working fluid is, simultaneously redirected, compressed and heated. As a result of these thermal processes the fluid undergoes strong irregular flow interactions, fluctuations, and perturbations, also known as unsteadiness. The reduced axial distance in-between the immovable and rotating parts increases the unsteadiness of the flow in the compressor subsystem, and in the gas turbine in general. These unsteady flows perturb the core flow, inducing secondary flows which in turn generate losses. Time-resolving simulations allow to investigate the unsteadiness of small clearances (e.g. rotor tip clearance, cantilevered stator tip clearance, shrouded cavities) in more detail and to predict qualitatively the deterioration of performance in an axial compressor. In recent years, unsteady simulations of multi-stage axial compressors have become more affordable and feasible due to computational advances. However, such simulations are still prohibitive to be used in the day-to-day design due to the required resources in terms of mesh size, processing cores and iterations. Montomoli et al. (2011) numerically investigated the existing differences between RANS and URANS simulations of a multi-stage axial compressor, in order to clarify whether it would be worthwhile to invest large amounts of resources into unsteady simulations. The URANS model predicted a stall point closest to the experimental data. However, they also reported that URANS simulation increases the mesh size and pre-processing time fourfold, while the memory storage requires increases by a factor of ten and the number of cores used threefold.

The application of URANS simulations to shrouded cavity flows is scarce in open literature due to the above challenges. The numerical investigation is typically carried out with a single pitch blade and the mixing-plane technique. To the author's knowledge of the open literature, Heidegger et al. (1996a) are the pioneers of numerically investigating the rotor-stator-rotor interaction with seal cavity using unsteady multi-blade simulations in an axial compressor. They scaled the original blade count in order to achieve the minimal blade ratio 2:3:2. Due to confidentiality they revealed only general findings. The steady state simulation with mixing-plane interfaces had slightly higher mass flow, efficiency, and pressure ratio compared to an unsteady solution. The unsteady solution displays the same 1% of leakage flow as the steady case. Contours of radial velocity of the first cell at the hub shows that positive radial velocity is concentrated circumferentially along the upstream cavity at the blade passage entrance in both steady and unsteady solutions. At the downstream cavity, the mixing plane circumferentially dilutes the negative radial velocity in the steady solution, while in unsteady solutions negative radial regions are upstream of the downstream rotor's leading edge. The potential flow upstream of the downstream rotor's leading edge forces flow into the cavity trench. This supports the observations of Wellborn and Okiishi (1996) about the leakage flow suction in downstream cavity-trench.

Fröbel et al. (2010) carry out three-dimensional steady and unsteady simulations including shrouded cavities in a 1.5-stage transonic axial compressor. They present a sensitivity study of two different seal fin heights (SFH). The first represents the nominal clearance of a new compressor, and the second features the wear of an old compressor. For an increased leakage flow rate, the peak efficiency is reduced in both RANS and URANS by approx. 1% when compared to the nominal SFH. Higher flow leakage is linked to a more pronounced passage cross-flow that increases the corner separation at the suction-side, which in turn diminishes the operating range. In contrast to Montomoli et al. (2011), the numerical stall point with URANS was shifted to a higher mass flow rate than the steady solution with both SFH. The rotor loss coefficient is not influenced by the leakage flows of up- and downstream cavities, while the unsteady case shows an efficiency increase in the rotor row of approximately 0.25%. On one hand, the local loss coefficient of the first stator shows higher values both at the hub and the tip with the URANS solution compared to the RANS case. On the other hand, in the remaining downstream rows (i.e. rotor 2 and stator 2) at the same locations, the local loss coefficient is lower with URANS than in the steady solution. The wake recovery effect induced by the first stator causes the mechanism that reduces the losses at the hub and mid-span in both downstream blades. This effect leads to an efficiency increase in the rotor blade that is mainly produced by the unsteadiness effect, rather than the leakage flow.

Yamagani et al. (2011) performed unsteady three-dimensional calculations of a six-stage high-speed axial compressor, focusing on the impact of real geometry modeling on the prediction accuracy with different numerical approaches. The first and fourth cases include only the rotor tip clearances. The second case also includes the clearances of the variable stator vane (VSV). The third case adds seal cavities, and the last case was simulated with a different turbulence model. The three cases are compared against the baseline. The predicted mass flow rates of the baseline and the cases with additional geometry features (i.e. VSV and seal geometries) are about 2.5% higher than the test data. The impact of the cavities on the overall total pressure ratio yields almost no differences compared to the baseline. The case with cavity geometries predicts that the overall efficiency is reduced by 1.7% compared to the baseline. The fourth case, with a different turbulence model, predicts 0.75% lower mass flow rate than baseline.

Kato et al. (2011) numerically investigated the effects of shrouded stator seal-cavity flows on a six-stage high speed axial flow compressor through URANS simulations. Two cases are compared, one shroudless and the other with cavities. Both cases predict about 2.5% higher mass flow rate at the design point. Small differences are discernible in total pressure ratio. In terms of efficiency, the cavity-case shows 1.7% degradation compared to the baseline. In the rear stages, the temperature rise at the stator hub ahead leading edge shows increments between 1-3% of the mid-span value. The windage heating contributes approx. 0.5% point drop in overall efficiency, being more pronounced from the mid to rear stages (more than 1% in fifth and sixth stage). The interaction of unsteady wakes of the upstream rotor with the upstream leakage flow suggests that the losses increased considerably in the hub region.

Fröbel (2012) numerically investigated the interaction between shrouded cavities and the main flow in a 1.5-stage transonic axial compressor through unsteady simulations, in order to identify the unsteady nature of the interaction, and also to what extent the flow unsteadiness affects the inner cavity flow. The leakage flow rate of both steady and unsteady simulations agree very well with the Egli's labyrinth seal model (Egli 1935). The unsteadiness of the leakage flow in the cavity-trenches is minuscule compared to the dominant amplitudes of the main flow, and the corresponding interaction is confined to the discharge area between the hub and the cavity-trench. The disturbance amplitudes of the leakage flow becomes weaker inside downwards the cavity-trenches. This indicates that the main source of unsteadiness is located in the main stream. It is shown that the corresponding unsteadiness of the flow in the cavities is small compared to the amplitudes recognized in the main flow path, and is also bounded to the contact region between annulus and cavity geometry. Furthermore, the disturbance amplitudes of the cavity flow sharply reduce as the distance to the main flow path increases, indicating that the source of unsteadiness is located within the main flow. The potential field of the downstream blade rows regulates the unsteady flow structures at the cavity interface region. As the leakage flow increases, the sensitivity of the potential field becomes weaker. The shear layer identified within the contact region of the cavity can be a possible source of unsteadiness, however no unusual frequency could be observed.

2.2.5   Preliminary conclusions of the cavity flows

Based on the above survey, some particular and comprehensive observations can be drawn for the design of axial shroud compressors.

1. Aerodynamic effects of stator cavity flows on the compressor performance

    1.1 Leakage flow increases linearly as the seal clearance increases. (Wellborn and Okiishi 1996, Lange et al. 2010) They reported rates of leakage flow between 0.63% to 0.73% for 1% of clearance increase. The slope of the leakage flow depends strongly on the type of sealing for each test rig.

    1.2 As the seal clearance increases the isentropic efficiency drops linearly. (Jefferson and Turner 1958, Freeman 1985, Wellborn and Okiishi 1996, 1999, Lange et al. 2010) They have reported isentropic efficiency drops by 1% from 0.5% to 2.7% of clearance increase. Freeman (1985) shows that isentropic efficiency drop is more pronounced in deep shrouds compared to shallow shrouds.

1.3 Higher tangential velocities at the upstream cavity trench counteract the detrimental effect of the leakage flow and vice versa. (Wellborn and Okiishi 1996, 1999, Wellborn 2001, Demargne and Longley 2000, Sohn and Song 2006) An increase in tangential velocity modifies the flow turning near the hub which consequently redistributes the leakage flow to the adjacent pressure side. In this way, the leakage flow overcomes the cross-passage pressure gradient and less leakage flow is accumulated on the suction side.

1.4 Similar to the upstream cavity trench, a higher tangential velocity at the downstream cavity trench reduces the incoming leakage flow. (Oeztürk et al. 2000, Demargne and Longley 2000) The higher tangential velocity leads to increasing the near-hub pressure and thus the leakage flow is less prone to ingress inside the downstream cavity trench.

1.5 There is experimental and numerical evidence in different test rigs that a portion of the main stream flow ingresses in the upstream cavity trench but the mechanism is still not well understood. (Wellborn and Okiishi 1996, Heidegger et al. 1996a, Demargne and Longley 2000, Lewis 2002). Lewis (2002) states that the rate of ingested annular flow into the upstream cavity trench varies from zero to two times the leakage flow through the labyrinth seal.

1.6 The potential field of the corresponding downstream blade rows, in which the cavity geometry is embedded, determines the incoming flow into the cavity-trenches. (Wellborn and Okiishi 1996, Fröbel 2012) In the downstream cavity trench, the leakage flow enters faster near the downstream rotor leading edge. (Wellborn and Okiishi 1996) In front of the stator leading edge the potential field restricts the injection of the leakage flow into the main flow. The most rate of the leakage flow ingresses into the main flow near the mid-pitch. (Wellborn 2001)

1.7 A careful selection of the turbulence model when simulating compressor designs including cavities is crucial, because the accuracy and prediction of the tangential velocity at the cavity trenches is affected for the selected turbulence model. A wrong selection can lead to an overestimation of tangential velocity which is critical for both the flow angle of the leakage flow and the temperature at the cavity outlet. (Wellborn 2001, Marty and Aupoix 2012, Flores and Seume 2014)

1.8 The amplitude of the fluctuations is weaker deeper inside the cavity-trenches and cavity-well than in the interaction region of the cavity outlet. (Wellborn and Okiishi 1996, Fröbel 2012, Scott et al. 2000)

1.9 The injection of leakage flow weakens the axial momentum and the balance of tangential velocity of the main channel. The cavity leakage flow determines the tangential momentum which in turn determines whether the flow near the hub can endure the cross-passage pressure gradient. This pressure gradient can potentially decrease or increase the corresponding secondary flows. (Flores and Seume 2015)

1.10 The performance of the downstream rotor of the corresponding stage is not reduced or affected by the leakage flow emanating from the upstream cavity trench. (Wellborn and Okiishi 1996, Fröbel et al. 2010)

2. Thermal effects in shrouded stator cavity

Thermal effects are intimately joined to the leakage flow rate and the velocities into the cavity. Nevertheless the influence of the thermal effects of the leakage flow affect the main flow in the axial compressor.

2.1 Lewis (2002) estimates that windage and leakage flow reduce the efficiency by 0.1% and 0.3%, respectively. Kato et al. (2011) states that windage contributes approximately 0.5% to the efficiency drop and in the rear stages the deficit becomes more pronounced reaching more than 1%.

2.2 The depth of the cavity-well barely alters the seal leakage rate. (Freeman 1985, Heidegger et al. 1996a,b, Oeztürk et al. 2000) But the depth of the cavity-well alters the temperature rise in both up- and downstream cavity-wells. Geometries with shallow cavity-wells are less prone to high rates of windage heating. (Bayley and Childs 1994)

2.3 The highest temperature rise occurs inside the upstream cavity-well near the rotor face. This temperature rise takes into account the itself increase in the upstream cavity-well plus the cumulative temperature rise in the labyrinth seal and the downstream cavity-well. Bayley and Childs (1994), Oezturk et al. (1998), Lewis (2002)

2.4 The highest windage occurs inside the downstream cavity-well. Bayley and Childs (1994), Lewis (2002) The latter estimated that 50% is generated in the downstream cavity-well, 30% in the labyrinth seal, and 20% in the upstream cavity-well.

2.5 Small leakage flow rates tend to increase the temperature rise in both up- and downstream cavity-wells and vice versa. (Bayley and Childs 1994) Therefore, a trade-off between aerodynamic and thermal performance would be considered.

2.6 The increase of the tangential velocity linearly increases the temperature rise inside the cavity. (Bayley and Childs 1994).

3. Use of one-dimensional models for cavity flows in 3D-flow solvers

3.1 The most significant parameters identified to characterize the leakage flow passing through a cavity in a one-dimensional model for cavity flows are the seal clearance, rotor speed, cavity deep, mass flow, and temperature discharge. (LeJambre et al. 1998, Wellborn et al. 2000)

3.2 Under appropriate circumstances, the flow variations in the downstream cavity-trench are diluted in circumferential direction such that they are almost axisymmetric. Therefore, in one-dimensional models the boundary conditions at the downstream cavity trench can be modeled as axisymmetric. (Oeztürk et al. 2000, Scott et al. 2000, Wellborn et al. 2000)

3.3 The use of one-dimensional models for cavity flows accelerates the run time up to 60% compared with a simulation with fully resolved cavities. (Naylor et al. 2009)

4. Numerical unsteady investigations including shrouded stator cavities

4.1 The unsteadiness of the leakage flow inside the cavity-trenches is small compared to the dominant amplitudes of the main flow. The major flow interaction is confined to the discharge area between the hub and the cavity trench. Disturbance amplitudes of the cavity flow sharply decrease as the distance to the main flow path increases. (Fröbel 2012)

Mass flow and tangential velocity at the interface of the cavity outlet are the main parameters which control the interaction between the leakage flow with the main flow. An increase in tangential velocity could counteract the high rate of leakage flow. However, higher tangential velocity consequently involves a temperature rise at the cavity discharge which increases the

Table 2.1: Aero thermodynamic investigations related to labyrinth cavity flows in axial compressors

Author	Facility	Stages	Method	Analized stage
Wellborn and Okiishi (1996)	Low-speed axial compressor	4	Exp.	3
Heidegger et al. (1996a) Heidegger et al. (1996b)	Subsonic axial compressor	10	Num.	8
LeJambre et al. (1998)	Compressor rig	11	Num.&Exp.	-
Oezturk et al. (1998)	High-speed axial compressor	2	Num.	1
Wellborn and Okiishi (1999)	Low-speed axial compressor	4	Num.&Exp.	3
Oeztürk et al. (2000)	High-speed axial compressor	2	Num.	1
Wellborn et al. (2000)	Axial compressor	12	Num.&Exp.	7...12
Scott et al. (2000)	High-speed axial compressor rig	2	Num.&Exp.	1
Demargne and Longley (2000)	Linear cascade rig	-	Num.&Exp.	-
Demargne and Longley (2001)	Low-speed axial compressor	1	Num.&Exp.	1
Wellborn (2001)	Low-speed axial compressor	4	Num.&Exp.	3
Lewis (2002)	High-pressure axial compressor	5	Exp.	1...5
Oezturk et al. (2002)	High-speed axial compressor	2	Num.	1
Sohn and Song (2006)	Linear cascade rig	-	Exp.	-
Becker et al. (2009)	Research axial compressor	4.5	Num.&Exp.	1...4
Naylor et al. (2009)	Low-speed research compressor	4	Num.&Exp.	3
Lange et al. (2010)	Low-speed research compressor	4	Num.&Exp.	3
Fröbel et al. (2010)	Transonic axial compressor	1.5	Num.	1
Yamagani et al. (2011)	Highly-loaded axial compressor	6	Num.&Exp.	1...6
Kato et al. (2011)	Highly-loaded axial compressor	6	Num.&Exp.	1...6
Marty and Aupoix (2012)	Highly-loaded axial compressor	3	Num.&Exp.	-
Fröbel (2012)	Transonic axial compressor	1.5	Num.	1
Flores and Seume (2014)	High-speed axial compressor	4	Num.	3
Flores and Seume (2015)	High-speed axial compressor	4	Num.	3

windage which per se is detrimental to the stage efficiency, therefore an optimal balance between these three variables is necessary for an optimal design. Table 2.1 summarizes chronologically the investigations related to labyrinth cavity flows in axial compressors which were revised for this work.

2.3   Seal configurations

The labyrinth sealing aims to accomplish three purposes: to minimize the recirculation leakage flows caused by the driving pressure difference, to control the coolant and purge air flows and, thirdly, not to disturb the rotordynamic stability especially at high speeds. Their simplicity, reliability and low manufacturing cost makes labyrinth seals the most widely used sealing devices in both gas and steam turbine components. In addition, they offer benefits in terms of operating pressure and temperature. A labyrinth seal is a device manufactured with a series of fins or tips

which protrude from the rotor shaft radially outwards towards the stator inner ring. They should be as thin as possible, in order to restrict the heat transfer into the rotor and prevent a higher rotor thermal effect. The seal fins and the inner ring must not come into physical contact with each other, in order to avoid any type of wear. Consequently, a clearance exists between the rotor-side labyrinth fins and the surrounding shroud formed by the inner ring as shown in Figure 2.12a. The operating principle of the labyrinth seal is to remove the most amount of kinetic energy from the flow through a set of consecutive narrows and cavities which accelerate and decelerate the flow, respectively. Ideally, all kinetic energy would be transformed into heat because of the higher friction created at the narrows. However, in practice not all the kinetic energy is dissipated, and a high percentage is transferred through the cavities and thus will thermally perturb the main flow at the stator hub. The labyrinth seal configuration has several variants and combinations as shown in Figure 2.12. Each configuration mainly depends on the available axial and radial spacing, and on the intended specific application.

(a) Straight   (b) Straight-Inclined   (c) Staggered   (d) Stepped

(e) Interlocked   (f) Abradable   (g) Honey comb   (h) Brush
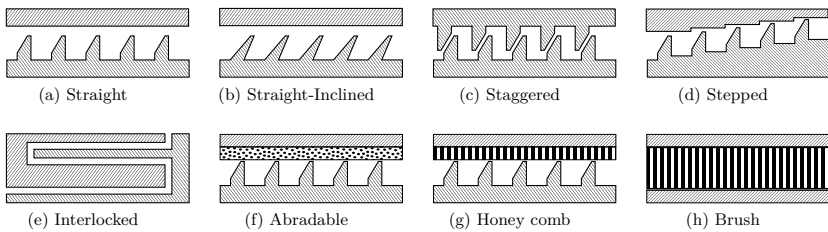
Figure 2.12: Typical labyrinth seal configurations in turbomachinery

2.3.1   Analytical models for leakage flow prediction

This subsection provides a brief review of the most known analytical models to estimate the mass flow through a labyrinth seal. For a long time, researchers have proposed analytical models in order to correctly estimate the mass flow through labyrinth seals. Since the first model specifically for labyrinth seals was proposed, it has been modified and complemented with empirical coefficients derived from experimental data in order to achieve more reliability in the mass flow prediction. However, the models have had limitations to accurately predict the mass flow rates. Some authors, Egli (1935), Hodkinson (1939), Vermes (1961), Neumann (1964), Zimmerman and Wolff (1987), only took into account the aerodynamics while more recently, Scharrer (1988), Eser and Kazakia (1995), Sriti et al. (1997), Gamal (2007), took advantage of those previous leakage models and they incorporated them into their corresponding rotordynamics analysis.

The model of Egli (1935) in Eq. (2.1) has been widely used for straight labyrinths. He introduced the concept of flow coefficient (α), which is a cross-section area ratio between the area of the clearance A with an upstream area A_1 where the pressure in the flow jet will be equal to the chamber pressure. The flow coefficient α depends on the fins-clearance-to-thickness ratio and has to be directly determined from measurements. The carry-over coefficient γ is a correction of the fin number that would be used in an ideal labyrinth, and depends on the fins-pitch-to-thickness ratio. Both coefficients, α and γ shown in Figure 2.13 determine the percentage of kinetic energy available for the expansion through the downstream throttle. The flow function

ϕ depends on the pressure ratio and the number of fins n as shown in Figure 2.13a.

$$\dot{m} = A \cdot \phi \cdot \alpha \cdot \gamma \cdot \sqrt{g \cdot \rho_U \cdot P_U} \quad \text{with} \quad \phi = \sqrt{\frac{1 - \left(\frac{p_n}{p_0}\right)^2}{n - \frac{2}{\kappa} \cdot \ln\left(\frac{p_0}{p_n}\right)}}$$

(2.1)

$$\text{and} \quad \gamma = \sqrt{\frac{n}{(1 - \beta) \cdot n + \beta}} \quad \text{and} \quad \beta = 1 - \frac{1}{\left(1 + 16.6 \cdot \frac{h}{s}\right)^2}$$

(a) Leakage function ϕ as a function of labyrinth pressure ratio $\frac{P_n}{P_0}$ for labyrinths with one to thirty six throttles

(b) Flow coefficient $\alpha = \frac{A}{A_1}$ as a function of the fins-clearance-to-thickness ratio for labyrinths with sharp-edged fins determined from tests

(c) Carry-over correction factor γ as a function of the fins-clearance-to-pitch ratio $\frac{h}{s}$ for straight-through labyrinths

Figure 2.13: Functions used in Egli labyrinth seal leakage equation, reprinted from Egli (1935)

Vermes (1961) took the well-known formula of Martin (1908) and modified the original constant in order to gain accuracy. His model Eq. (2.2) includes the clearance factor of an annular orifice K, which is dependent of the Reynolds number as shown in Figure 2.14. He incorporates the residual-energy factor ψ based on an analysis of boundary layer theory. It refers to the kinetic energy of the jet emanating from a constriction that is not converted into heat when acceleration begins into the next constriction. By comparing the models of Vermes (1961) and Egli (1935), the residual-energy factor ψ involves pitch s, thickness t and clearance h in a single factor, it replaces both the flow coefficient α and the carry-over factor γ in Egli's model.

$$\dot{m} = 5.76 \cdot A \cdot \phi \cdot K \cdot \frac{p_0}{\sqrt{R \cdot T_0}} \cdot \frac{1}{\sqrt{1 - \psi}}$$

(2.2)

$$\text{with} \quad \phi = \sqrt{\frac{1 - \left(\frac{p_n}{p_0}\right)^2}{n - \ln\left(\frac{p_n}{p_0}\right)}} \quad \text{and} \quad \psi = \frac{8.52}{\frac{s - t}{h} + 7.23}.$$
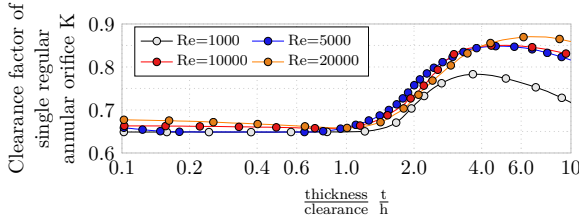
Figure 2.14: Clearance factor of annular orifices as function of teeth thickness-to-clearance ratio, reprinted from Vermes (1961)

Neumann (1964) reworked Saint-Venant's formulae and proposed an analytical model Eq. (2.3) which includes the known carry-over coefficient $\gamma = \gamma(n, \frac{s}{t})$, flow function $\phi = \phi(n, \frac{p_n}{p_0})$ and the flow coefficient $\alpha = \alpha(\frac{h}{t})$. Based on the research of Trojanovskij (1950), he highlighted the strong influence of the fins shape on the flow coefficient α as shown in Figure 2.15a. In addition, he included the inclination factor $K_N = \frac{\mu_\epsilon}{\mu_{90°}}$, which is the theoretical ratio of the jet contraction with different fin inclinations with respect to the contraction of a perpendicular fin ($\epsilon = 90°$) as illustrates Figure 2.15b.

$$\dot{m} = 3.54 \cdot A \cdot \alpha \cdot \phi \cdot \gamma \cdot k_N \cdot \sqrt{\frac{p_0}{v_0}} \qquad \text{with} \qquad \phi = \sqrt{\frac{1 - (\frac{p_n}{p_0})^2}{n}}$$

$$\text{and} \qquad \gamma = \sqrt{\frac{n}{(1 - \beta) \cdot n + \beta}}; \qquad \beta = 1 - \frac{1}{(1 + 16.6 \cdot \frac{h}{t})^2} \tag{2.3}$$

Based on the Egli (1935)'s definition to determine the leakage mass flow in a straight seal, Aungier (2000) reformulated the definition (here rewritten in Aungier's nomenclature) Eq. (2.4) where ρ and T are evaluated on the higher pressure side of the labyrinth, h is the clearance height, d is the radius of the fin's tip:

$$\dot{m} = \pi \cdot d \cdot h \cdot \alpha \cdot \phi \cdot \gamma \cdot \rho \cdot \sqrt{R \cdot T} \tag{2.4}$$

In addition he presented empirical equations to determine the flow coefficient α in function of clearance-to-thickness seal ratio $\frac{h}{t}$, flow function ϕ depending on number of fins N and seal pressure ratio P_R

$$\alpha = 1 - \frac{1}{3 + \left[\frac{54.3}{1 + 100 \cdot \frac{h}{t}}\right]^{3.45}} \qquad \text{and} \qquad \phi = \frac{2.143 \cdot [\ln(N) - 1.464]}{N - 4.322} [1 - P_R]^{(0.375 \cdot P_R)} \tag{2.5}$$

and carry-over coefficient γ being function of the number of fins N and the clearance-to-pitch seal ratio $\frac{h}{s}$

$$\gamma = 1 + \frac{X_1 \left[\frac{h}{s} - X_2 \cdot \ln\left(1 + \frac{h}{s}\right)\right]}{(1 - X_2)} \qquad \text{with a limiter} \qquad \frac{h}{s} \leq (X_2 - 1) \tag{2.6}$$

(a) Flow coefficient dependent of tip shape and clearance

(b) Contraction coefficient for a thin tip at different inclinations
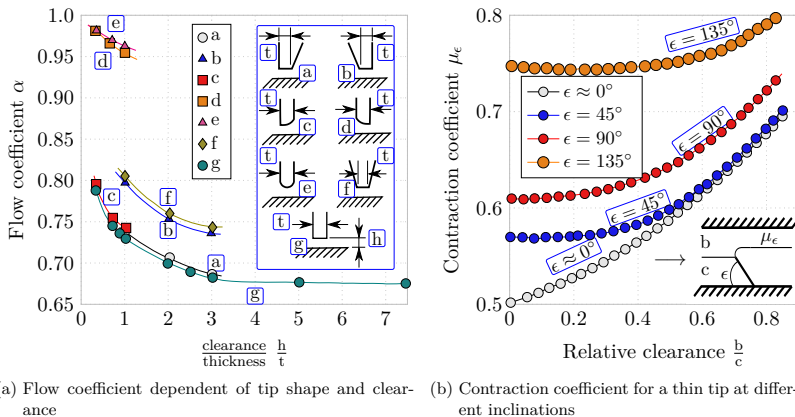
Figure 2.15: Flow coefficient α as a function of knife-edge fin shape and contraction coefficient μ_ϵ, reprinted from (Neumann 1964)

the values of X_1 and X_2 also depend on the number of fins

$$
\begin{aligned}
X_1 &= 15.1 - 0.05255 \cdot \exp[0.507 \cdot (12 - N)] && \text{for} && N \leq 12 \\
X_1 &= 13.15 + 0.1625 \cdot N && \text{for} && N > 12 \\
X_2 &= 1.058 + 0.0218 \cdot N && \text{for} && N \leq 12 \\
X_2 &= 1.32 && \text{for} && N > 12
\end{aligned}
\tag{2.7}
$$

the use of these three empirical fitting (Eq. 2.5, 2.6 and 2.7) reproduce the corresponding coefficients depicted in Figure 2.13.

2.3.2   Labyrinth performance prediction through CFD

This subsection is aimed at giving a brief insight into the potential use of numerical solvers with advanced simulation models such as Large Eddy Simulations (LES) in labyrinth seal investigations. It is not focused on an extensive literature research in the topic.

Tyacke et al. (2012) numerically investigated the flow in two labyrinth seal geometries (e.g. straight and stepped) and the accuracy of pure Large Eddy Simulation (LES), hybrid RANS-LES and pure RANS simulations. They point out that the labyrinth flow includes zones of recirculation, separation, acceleration, laminarisation, and transition which the RANS models have difficulty resolving. The accuracy of the solutions is evaluated by measuring the deviation (e.g. error) of leakage flow with respect to experimental values of the corresponding seal geometry. For the straight seal, the errors of LES simulations (including RANS-LES) are between 0.94 and 9.8% while RANS errors are between -10 and 28.56%.

Dai et al. (2016) explored the optimization of the seal geometry (i.e. a single-fin) using a

genetic algorithm and LES models. The optimization depends on geometric parameters and manufacturing constraints. The target is the minimization of the mass flow rate at a given pressure ratio. The reference case considers a rectangular straight single-fin. They find that the geometry with grooves at the tooth tip tend to decrease the leakage mass flow compared to the reference case. In fact, the more grooves the single-fin possesses, the lesser the leakage is. This is caused by the high viscous loss as the flow enters inside the grooves generating a large blockage. The seal with three grooves reduces the leakage flow by up to 16% compared to the baseline. In addition, they confirmed that inclined seal-fins reduce the leakage flow by 3.2% compared to the reference case.

2.3.3   Preliminary conclusions of the labyrinth performance

1. Fröbel (2012) shows that the leakage flow rate of both steady and unsteady simulations agree very well with Egli's labyrinth seal model Egli (1935).

2. Advanced simulation models (LES) give an error less than 10% reaching in some cases less than 1% in the prediction of leakage flows while RANS-based models give a deviation between -10% and 28%. Tyacke et al. (2012)

3. The use of grooves on the tip of the seal-fin reduces the leakage flow by 16%. The leakage flow enters inside the grooves, the flow inside the grooves generate large blockage which in turn induces a larger pressure drop. This leads a lower leakage flow rate crossing the labyrinth seal. Dai et al. (2016)

2.4   Rotor-stator interaction in axial compressors

This section reviews the main phenomena observed in a compressor stage due to the interaction of rotor and stator. Some analytical models are reviewed for further comparison with the current work.

2.4.1   Wake recovery effect in axial compressors

Since the mid-end 30s the analysis of the wake characteristics was investigated in wing airfoils (Silverstein et al. 1939). In turbomachinery applications, the rotor wake has been intensively investigated since the mid 50s in order to predict and quantify the losses. The first attempts fundamentally were analytically based and experimentally validated.

Smith (1958) described a mechanism occurring in a stage of certain axial flow compressors. As an upstream distorted flow (e.g a wake) enters into a stage, there is an effect inside the stage that compensates the distorted flow in such way that the outlet flow will have a smaller magnitude of distortion than the inlet flow. He defined as "recovery", the capacity of the stage to compensate the upstream distortions and "recovery ratio" as the measure of this ability, mathematically modeled as follows:

$$\Re = 1 - \frac{d(\Delta P)}{dP_1} \tag{2.8}$$

Physically, the differential operator (d) represents the loss that occurs in the flow that earlier did not posses any losses. If the recovery ratio ($\Re$) has a value equal to unity, this means that the downstream rotor or stator recovers the upstream loss resulting in smooth downstream total pressure distribution. By neglecting secondary flows and spanwise losses and by assuming uniform static pressure and polytropic efficiency in the wake and the main stream and the flow is incompressible, the recovery factor can be expressed in terms of relative flow angles β, absolute flow angles α, flow coefficient φ and cascade solidity σ while subscripts 1 and 2 refer to inlet and outlet of the rotor, respectively:

$$\Re = \eta \left\{ \frac{\sin\beta_2 \cos\beta_2}{\varphi_2} + \frac{\sin\alpha_1 \cos\alpha_1}{\varphi_1} - \frac{\sin\beta_2 \cos\beta_2 \sin\alpha_1 \cos\alpha_1}{\varphi_2\varphi_1} \right.$$
$$\left. - \frac{\cos^2\beta_2 \cos^2\alpha_1}{\varphi_2\varphi_1} \exp\left[-\pi\sigma\left(\cos\beta_2 + \frac{1-\cos\beta_2}{1.28}\sigma^{\sec\beta_2} \right) \right] \right\} \tag{2.9}$$

Ashby (1957), in an independent investigation, developed a theoretical model, in order to determine the optimal velocity diagram which minimizes the total pressure distortions generated as the wake passes through a blade row. In addition to the fact that his model predicts with good agreement the downstream total pressure distortions, the model can compute the loss in total pressure in Smith's recovery model, namely the right term of Eq. (2.8) for an incompressible flow. In fact with proper assumptions, the recovery factor can be deduced only in geometrical terms from Eq. (2.9), resulting as follows

$$\Re = 1 - \left[\overbrace{\cos(\beta_1 + \alpha_1)\cos(\beta_2 + \alpha_2)\frac{\cos\alpha_1 \cos\beta_2}{\cos\beta_1 \cos\alpha_2}}^{\textit{Ashby} \ (1957)} \right] \tag{2.10}$$

Smith (1966) presented evidence that the upstream waves are chopped in the next downstream row of a four-stage low-speed axial compressor. He found that the wakes behave in an unsteady but periodic fashion. The first mechanism occurs as the IGV wakes are chopped by the rotor (see Figure 2.16). The resulting segments are attenuated by dispersion because the fluid is gaining stagnation enthalpy (i.e. the opposite occurs in a turbine row, the wake is amplified because the fluid provides stagnation enthalpy to the rotor). The second mechanism is associated with the different energy exchange of the main flow and the wake mainly due to the different velocities of the corresponding streams under the nearly same static pressure field. Assuming an inviscid, incompressible, and two-dimensional flow, he suggested that knowing the wake width the whole flow field can be reconstructed with appropriate geometrical considerations.

Through an unsteady, two-dimensional, inviscid and incompressible flow model Adamczyk (1996) confirmed the existence of the recovery effect $\Re$ envisioned by Smith (1958, 1966). He showed that the recovery process is linked with the kinetic energy of the unsteady velocity field as the wake crosses the passage row. His model neglects upstream viscous effects. Therefore, the upstream wakes are modeled as a series of one-dimensional shear flows which are simulated by means of the reduced frequency parameter k_n which is an approximate of the wave length of the incoming disturbance in the stream flow direction. The results show that if the reduced frequency is sufficiently large so that the recovery process becomes a function of flow turning (i.e. the time average airfoil circulation) and independent of the reduced frequency. He pointed out that the recovery process can reduce the wake mixing loss by as much as 70%, which was
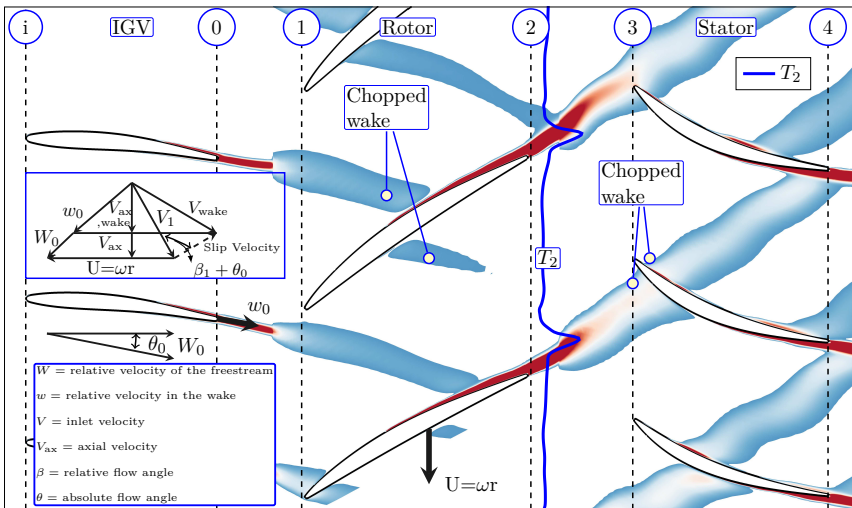
Figure 2.16: Schematic of a compressor stage depicting the chopping of the IGV wakes by the rotor action, adapted from Smith (1966), and the velocity vectors of the main stream and the IGV wake with the subscripts referred to the planes depicted over the top, adapted from Kerrebrock and Mikolajczak (1970)

nearly a point increase in the stage efficiency. Additionally, his expression in terms of relative flow angle β_r, absolute angle β and a constant C_1 results as:

$$\Re = 1 - \left(\frac{\cos\beta_1}{\cos\beta_2}\right)^2 \frac{1}{\sin^2(\beta_r - \beta_1)} \left\{ 1 + \left(\frac{\cos\beta_1}{\cos\beta_2}\right)^2 \left[\frac{\sin\beta_2}{\cos\beta_1} + \frac{\cos\beta_r}{\cos\beta_2 \sin(\beta_r - \beta_1)} - \frac{C_1}{\cos\beta_2}\right]^2 \right\}^{-1}$$

$$+ \mathcal{O}(\frac{1}{k_n}) \qquad \text{with} \quad C_1 = \frac{4\Gamma}{L}\left(1 + \frac{\cos\beta_1}{\cos\beta_2}\right)^{-2}; \quad k_n = \frac{2\pi n}{h_r}W$$

(2.11)

VanZante et al. (1997) provided an improved model (Eq. 2.12, 2.13 and 2.14) solely dependent on flow angles and a rotor wake profile (see Figure 2.17), in order to predict the wake decay due to viscosity and wake stretching. The model was evaluated by comparing the wake decay occurring in an isolated rotor and that in a stage at peak efficiency (PE) and near stall (NS) operating points. For the isolated rotor, the entire rotor wake decay is due to viscous mixing in both operating points. But in the case of the stage, the viscous effects (i.e. losses) solely represent 22% and 46% of the rotor wake decay at PE and NS, respectively. Of the remaining rotor wake decay, the inviscid stretching (i.e. no losses) comprises 68% and 52% for PE and NS, respectively. According to the above percentages, it is discernible that loss correlations based on isolated rotors may be deceptive for multistage designs. Their results show that the main mechanism on the wake decay is the wake stretching, while the viscous dissipation is less significant. They also suggest that reducing the axial spacing of blade rows would prevent the viscous dissipation of the rotor wake, and loading the stators at the front of the rotor, the wake

would be stretched earlier, thus reducing the viscous dissipation.

$$\Re = 1 - \left(\frac{L_{in}}{L_{exit}}\right)^2 \tag{2.12}$$

with

$$\frac{L_{exit}}{L_{in}} = \frac{sin(\beta_{rel} - \beta_{abs})}{cos(\beta_{abs})} \cdot \left[1 + 2 \cdot \frac{(\overline{s} - c)}{h} \cdot sin(\beta_{exit}) + \left(\frac{(\overline{s} - c)}{h}\right)^2\right]^{\frac{1}{2}} \tag{2.13}$$

being

$$\frac{(\overline{s} - c)}{h} = \frac{cos(\beta_{rel})}{sin(\beta_{rel} - \beta_{abs})} \cdot \frac{cos(\beta_{-\infty})}{cos(\beta_{\infty})} - \frac{4 \cdot \left[tan(\beta_{-\infty}) - tan(\beta_{\infty})\right]}{\left(cos(\beta_{-\infty}) + cos(\beta_{\infty})\right)^2} \cdot cos(\beta_{\infty}) \cdot cos(\beta_{-\infty})^2 \tag{2.14}$$
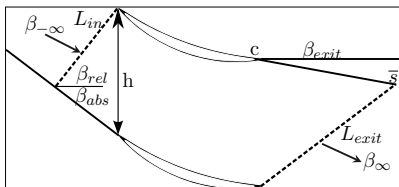
(a) Definition of angles and lengths used in the wake stretching model
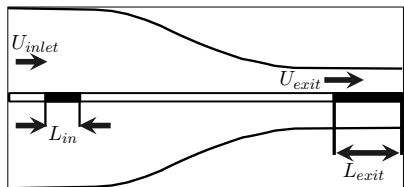
(b) Illustration of wake stretching in a 2D converging channel

Figure 2.17: Nomenclature used in the wake stretching model in Eq. 2.12, 2.13 and 2.14, adapted from VanZante et al. (1997)

Montomoli et al. (2009, 2013) numerically investigated the unsteady blade-to-blade interactions in a four-stage axial compressor with cantilevered stators and repeating stages. At midspan, they compute that more than 70% of the wake decay in the stator passage is frictionless, contributing positively in the loss reduction. They highlighted strong interactions between the wake impingement on the boundary layer like those observed by Valkov and Tan (1998a,b). As the loading increases (i.e. moving towards the stall), the contribution of the wake recovery remains as demonstrated by VanZante et al. (1997). More interesting are the results at the hub region. They highlight a strong interaction between the upstream wake and the hub stator leakage vortex. This interaction deflects the upstream wake by about 30°, making it more parallel to the stator vane. Due to the wake reorientation, the original length of the wake grows resulting in 15% more stretching that in turn gives about 15% extra recovery, according to Smith's model (Smith 1958, 1966). Additionally, as the upstream wake is transported through the passage, it interacts with the hub leakage flow. The latter partially restrains the upstream wake, and some wake flow passes under the two adjacent stators. The flow which crosses two stator blades possess lower stagnation pressure which in turn reduces the total pressure losses near the hub. Although some wake flow passes through the stator hub gap, the other small portion is not able to pass through, and it migrates radially interacting with the pressure-side boundary layer. The pressure-side boundary layer has low momentum fluid which is transported to the middle of the passage.

Fröbel et al. (2010) numerically investigated the wake recovery effect on the loss coefficient in a 1.5-stage transonic axial compressor with variable-shrouded stators (i.e. from the mid chord to the trailing edge a gap exists at the hub and at the tip). The loss coefficient reductions are more pronounced at the hub and the midspan. The benefit of the wake recovery is only perceived in downstream blades. The rotor depicts discernible high gains in loss coefficient at the hub from the upstream incoming wakes. The wake of the upstream stator 1 near the hub is influenced by leakage fluid emerged from the hub gap vortex.

2.4.2   Kerrebrock and Mikolajczak's effect

The theoretical model of Kerrebrock and Mikolajczak (1970) confirms the existence of approximately 10% higher circumferential temperature non-unifomities in the wake downstream of the rotor than the temperature rise of the stage as sketched in Figure 2.16. The non-uniformities are due to a change of the upstream wakes by the stator row, occurring as the wakes are transported relatively to the inviscid flow as they cross through the stator passage. In an inviscid context, the mechanism can be explained by the superposition of the wake and the main stream velocity triangles, as the blue box shows in Figure 2.16. The resulting deficit in relative velocities of the wake and the main flow induces a slip velocity in the IGV wake, which is oriented toward the rotor's pressure side. This effect is known as "negative jet". As the IGV wakes cross the rotor passage, they are transported towards to the rotor's pressure side and impinge on it. In this location, the IGV wakes will be collected, and the IGV wake will appear in the rotor wakes. A cascade effect is observed as the downstream stator collects the resulting rotor wakes. The model shows that the stator-rotor interaction adds more energy to the wake fluid than to the inviscid flow. During the induced wake transport within the passage, high-energy fluid is transported through the wake towards the rotor's pressure side where it accumulates, resulting in an excess of stagnation temperature in the rotor wakes.

Lurie and Breeze-Stringfellow (2015) present measurements and numerical results in an advanced transonic compressor, analogous to the observations of Kerrebrock and Mikolajczak (1970), namely that the wake possesses a higher total temperature, more pronounced on the pressure-side than the free-stream, but not necessarily higher total pressure (i.e. the wake can also have lower total pressure). The hot temperature on the blade pressure-side suggests that fluid of the rotor wake is transported due to the "negative jet". The data match suggests that the loss is created as the rotor wakes impinge on the stator pressure-side and are convected through the blade passage. Since the rotor wake accumulates on the stator pressure-side, it creates a region of high entropy rise.

Hah (2015a,b) employed Large Eddy Simulation (LES) in order to identify loss sources and to elucidate whether this approach could reveal supplementary flow physics in an advanced transonic compressor. As the rotor releases the wake, it exhibits higher negative tangential velocity that slowly decays as it enters to the stator passage. At the stator exit, numerical and experimental results show a circumferential asymmetric total temperature distribution with higher values on the blade pressure-side. Presumably, this asymmetry is due to an inviscid redistribution as the upstream wake sweeps the stator passage. Instantaneous distributions of vorticity and tangential velocity show that the negative jet velocity rapidly decays as it enters the stator passage. Thus it is not able to directly transport wake fluid towards the blade pressure-side. This disagrees with the hypothesis of Kerrebrock and Mikolajczak (1970) which attributes the transport of total temperature to the wake-induced negative jet velocity.

Hah (2015a,b) shows that the wake impinges on the suction-side boundary layer where the negative jet velocity yields counter-clockwise vortices, which are then transported within the wake towards the pressure-side. During the travel of the vortices, they push fluid outside the wake just behind the wake, resulting in a wider wake on the pressure-side. He argued that the transport of counter-rotating vortices seems to be the actual mechanism that redistributes the total temperature on the pressure-side. As none of the wake crosses the passage, the suction-side boundary layer appears thinner, cleaner, and more stable than the counterpart on the pressure-side, in which the thicker boundary layer possesses higher total temperature and lower total pressure, consequently generating large losses. He remarks that this pressure-side region of high loss is not predicted by any previous URANS approach.

2.4.3   Effects of the upstream wakes into the downstream stators

Although by moving the stator row closer to the rotor trailing edge would be beneficial in counteracting the viscous mixing, other consequences would also appear. Valkov and Tan (1998a,b) numerically investigated the unsteady interaction of upstream rotor wakes with the stator row, in order to determine the mechanisms that influence the time-averaged performance of the stator row. They reaffirmed the existence of the beneficial reversible recovery wake. As the wakes cross the passage, they are strongly attenuated in both velocity and thickness. The attenuation occurs by means of reversible recovery and irreversible mixing. They pointed out that in typical stator configurations, the wake recovery occurs over a distance between 25% and 33% of chord length. They also reaffirmed that the wake recovery benefit depends on the frequency of the fluctuations (Adamczyk 1996). During the blade rotation there are intervals during which the recovery is suppressed due to discrete wake vortices. Outside these intervals, the wake recovery occurs. In addition, the wake recovery is associated with a boundary layer distortion which is a detrimental mechanism. As the wake impinges on the suction-side of the downstream stator, it distorts the boundary layer and increases the vorticity fluctuations near the surface which in turn increase the passage losses. The "negative jet effect" of the wake transports low total pressure fluid from the boundary layer towards the pressure-side of the adjacent stator. It is noticeable that the recovery benefit increasing with decreasing axial spacing between rotor and stator, however the boundary layer's distortion effect also has to be considered in the design. The reduced axial spacing could increase the boundary layer distortion and then suppress the potential recovery benefit. Valkov and Tan (1998a,b) find that the mechanisms described above are apparently generic. In the analyzed stage under typical axial spacing, their unsteady simulation shows 0.5% due to recovery effect and minus 0.3% due to boundary layer distortions, resulting in a 0.2% higher efficiency than the steady-state approach. As they reduced the axial spacing to 0.07 of chord, the effect of the tip vortex and the wake on the efficiency become more significant. The recovery achieves 1.2% benefit, while the boundary layer distortion costs 0.6%, resulting in an overall benefit 0.6% with respect to steady-flow solution. It is evident that the wake recovery, and the boundary layer distortion depend on the axial spacing, loading and frequency of the wake fluctuations.

2.4.4   Preliminary conclusions of the rotor-stator interaction in axial compressors

1. The recovery factor ($\Re$) gives a measurement of how the downstream stator compensates and recovers the upstream loss. (Ashby 1957, Smith 1958, 1966, Adamczyk 1996, VanZante

et al. 1997).

2. Analytical models of the recovery factor $\Re$ help to estimate the recovery capacity of a stage in the preliminary design only in terms of flow angles. (Ashby 1957, Smith 1958, Adamczyk 1996, VanZante et al. 1997).

3. The wake recovery depends on the frequency of the fluctuations. (Adamczyk 1996) During the blade rotation there are intervals during which the recovery is suppressed due to discrete wake vortices. Outside these intervals, the wake recovery occurs. (Valkov and Tan 1998a,b)

4. The benefit of the wake recovery increases with the decreasing axial distance between rotor and stator. (VanZante et al. 1997, Valkov and Tan 1998a,b) The recovery effect increases the efficiency and surpasses the losses of the boundary layer distortion nearly twofold. (Valkov and Tan 1998a,b)

5. In cantilevered stators at the hub, the interaction of the upstream wake and the hub leakage vortex leads to an extra recovery benefit consequently reducing the losses at the hub region. (Montomoli et al. 2009, 2013, Fröbel et al. 2010)

6. Upstream wakes transport flow with higher temperature compared to the temperature rise of the stage. (Kerrebrock and Mikolajczak 1970, Lurie and Breeze-Stringfellow 2015, Hah 2015a,b) The deficit of velocities between the main flow and the wake induces a slip velocity which directs to the upstream direction. This effect is called "negative jet" which transports fluid through the wake to the stator's pressure side. Therefore, the higher temperature is more pronounced on the pressure-side of the wake than the main flow. (Kerrebrock and Mikolajczak 1970, Lurie and Breeze-Stringfellow 2015) In addition, as the wake impinges on the suction-side boundary layer the negative jet yields counter-clockwise vortices, which are then transported within the wake towards the pressure-side of the adjacent blade. The transport of counter-rotating vortices seems to be the actual mechanism that redistributes the total temperature on the pressure-side. Hah (2015a,b)

2.5   Losses in axial compressors

The performance of a turbomachine (e.g. compressor or turbine) is always associated with the terms of efficiency and loss. The former relates the available work compared with the work in an ideal process, and the latter can be understood as a disturbed portion of flow which does not generate work. As the first turbomachines were built (e.g. steam turbines), the learning process was predominantly based on trial and error. The development of new measurement techniques, together with the evolution and refinement of numerical methods led to better models and a better understanding of the complex flow physics through the turbomachines. Although current numerical methods are not sufficiently robust to give accurate predictions, they help to better understand the unsteadiness and three-dimensional interaction and effects, even in the turbomachine core. The progressive advances reveal that both efficiency and loss are strongly influenced by the interaction of thermodynamic and fluid variables, which makes analysis exceptionally complex. The three-dimensional flow patterns and the inner boundary-layer mixing flow make it extremely complicated to predict the quantification, and even more so to predict the isolation of loss sources. The semi-empirical method and model tuning have been used since the 1940s, but they only work for the designs on which they are based.

2.5.1   Loss sources

In the axial compressor stage several physical phenomena occur simultaneously which reduce the performance and limit the maximal capacity for energy conversion. This subsection describes briefly most of these sources of loss.

- Tip clearance: This spacing between the blade tip and the outer casing exists because of the need to prevent rubbing due to rotation of the blading. The pressure difference between the pressure and suction sides drives flow which passes through the tip clearance. As the leakage flow crosses the tip clearance gap it meets the main flow, which tends to roll up the leakage flow, forming the tip leakage vortex. The latter is mixed out with the more uniform flow, thus generating losses. The rotor tip vortex is widely studied due to its complexity because it is one of the major contributors to the loss generation and it restricts the stall margin. A similar phenomenon can be observed in cantilevered stators as the leakage flow induces a similar vortex called the penny gap vortex (see Figure 1.5), which in turn generates losses at the hub.

- Stagnation point vortex: This vortical structure is formed as a flow layer near the hub approaches the stator leading edge and the layer splits, separates, and rolls up acquiring a shape of a horse-shoe. The resulting horseshoe vortex possesses one leg close to the suction-side and the other leg on the pressure-side is forced by the pressure gradient to move in the direction of the suction-side of the adjacent blade. This vortex depends on the blade thickness and is most observed in turbine blades than in compressor blades.

- Passage vortex: As the flow crosses through a passage, comprised of the suction and pressure sides of the adjacent blade, a natural pressure gradient is established. Due to the no-slip condition, the velocity within the end-wall boundary layer is lower than the main stream velocity. The flow with low momentum within the boundary layer is then forced perpendicular to the axial flow by the pressure gradient across the blade passage in the suction side direction. This phenomenon is called passage vortex.

- Corner separation: As a result of the passage cross-flow (i.e. passage vortex), the low momentum within the boundary layer is moved and accumulated on the corner suction-side of the adjacent blade, where a separation region is located.

- Radial flow: Within the boundary layer on the stator suction-side, the flow with low momentum is transported radially by a local pressure gradient. For the rotor case, the centrifugal force contributes to displacing the flow with low momentum.

- Blade boundary layer: The no-slip condition at the blade surfaces, suction and pressure side, restrains the flow in the vicinity of the blade. These regions of low momentum are known as boundary layers. Boundary layers start from the blade leading edge covering both sides of the blade and increasing in thickness on the suction side approximately at mid-chord. The pressure side exhibits a thinner boundary layer. At the trailing edge, both boundary layers interact and mix, producing a wake as shown in Figure 2.18b.

Some of these phenomena are better illustrated in Figure 2.18a. Due to the rotor tip clearance, the tip vortex appears as the blade rotates. The region of streamlines on the first cell on the passage wall indicates how the pressure gradient dominates the low momentum flow within the

end-wall boundary layer, and how it is transported to the corner separation region located on the suction-side of the adjacent blade. This low momentum flow moves radially in the spanwise direction due to the low pressure within the boundary layer in the blade aft (see Figure 2.18b). As a consequence of the corner separation, a region of separated flow downstream of the stator is discernible. The radial flow not only appears in the corner separation region inside the separation bubble, but the flow also moves radially as shown in Figure 2.18a.
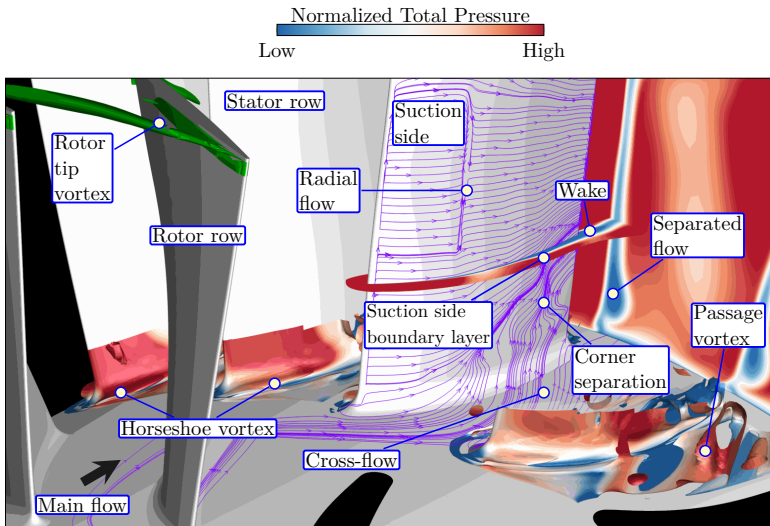
(a) Stage of an axial compressor
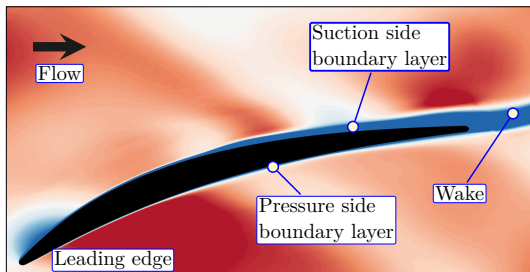
(b) Boundary layer in a blade-to-blade view at mid-span of a stator blade

Figure 2.18: Typical phenomena causing loss in a typical axial compressor stage

2.5.2   Loss quantification

Although there are various ways to quantify the losses such as drag coefficient and wake coefficient, probably the most common definition of a loss coefficient for compressor blades that has

been historically used is the stagnation pressure loss coefficient ζ Eq. (2.15). It has remained in the scientific collective, because currently the data acquisition in multi-blade cascades is relatively easy to implement compared to the early investigations developed in single row blade cascades. This definition relates the difference of stagnation pressure to the free-stream dynamic pressure at inlet. Despite the popularity of this loss coefficient definition, it can be exclusively used in cascades where the temperature gradient is negligible. In practical applications with significant temperature increase the use of this definition will underestimate the loss.

$$\zeta_{\mathrm{p}} = \frac{P_{\mathrm{t}_1} - P_{\mathrm{t}_2}}{P_{\mathrm{t}_1} - P_{\mathrm{s}_1}} = \frac{P_{\mathrm{t}_1} - P_{\mathrm{t}_2}}{\frac{1}{2}\rho_1 V_1^2} \tag{2.15}$$

Denton (1993) suggested the use of the entropy concept in the loss coefficient for compressor blades Eq. (2.16). He pointed out that entropy definition can take into account mechanisms that create losses such as viscous friction in either boundary layers and free shear layers and heat transfer across finite temperature differences. Entropy is a convenient measure because, unlike stagnation pressure, stagnation enthalpy, or kinetic energy, its value does not depend on the reference frame in which the blade is viewed.

$$\zeta_{\mathrm{S}} = \frac{T_2 \Delta S}{h_{01} - h_1} \qquad \text{with} \qquad \Delta s = C_p \ln\left(\frac{T}{T_{\mathrm{ref}}}\right) - R \ln\left(\frac{P}{P_{\mathrm{ref}}}\right) \tag{2.16}$$

Although the classification of losses is helpful, due to the three-dimensional interaction of the flow in a blade row the losses are inherently coupled and their synergy makes it extremely complicated to isolate and quantify them with enough accuracy. An attempt to categorize the losses or at least to identify the main sources has been made by Denton (1993). He classified the losses as follows: profile loss, end-wall loss, leakage loss, shock loss.

Denton (1993) gave an extended review of the above loss classification and emphasizes the lack of understanding of many loss mechanisms in both turbines and compressors. He pointed out that the typical stagnation pressure loss coefficient satisfies enough cascade test data, but it cannot be applied to real machines because of the rotation and thermodynamics effects are not taken into account in the cascade. Although the entropy cannot be measured directly, he proposes the entropy as the only rational measure of loss because of its definition involves any two thermodynamic properties (e.g. pressure, temperature or density), which can be measured.

3. Numerical discretization and flow simulation

3.1 Test rig and experimental data

The four-stage high-speed axial compressor, 4AV, is a research compressor at the Institute of Turbomachinery and Fluid-Dynamics (TFD) of the Leibniz Universität Hannover (LUH). It comprises four stages with inlet-guide vanes as shown in Figure 3.1a. The compressor blading is entirely composed of controlled diffusion airfoils (CDA). The maximal rotational speed is 18,000 RPM. The test rig has been used in distinct investigations in order to increase the aerodynamic load by optimizing geometrical features of the stator rows. Walkenhorst (2000) investigated an end-wall contour modification at the hub in a set of stator blades. Fischer and Seume (2003), Fischer et al. (2004), and Fischer (2004) implemented strongly bowed stators in the last two stages. Braun and Seume (2006) and Braun (2007) implemented forward swept blades and vanes in the first three stages. Recently Vorreiter et al. (2012) and Siemann et al. (2016) have applied airflow injection and aspiration in the first stator row, respectively. The experimental
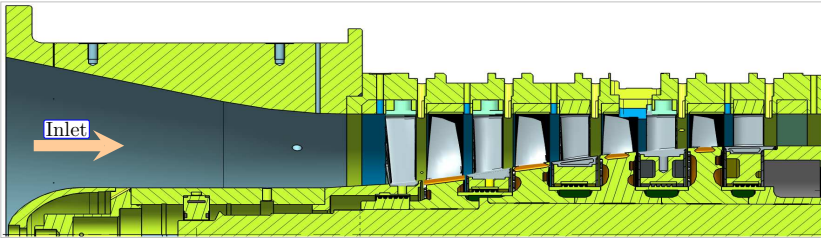
Figure 3.1: Meridional view of the test rig with corresponding reference cavities

data for the validation of the shroudless simulations are taken from the measurements carried out by Braun (2007) at a design rotational speed of 17,100 RPM, with the overall total pressure ratio of 2.712 and a maximum isentropic efficiency of 89.919% at the aerodynamic design point. Further details of the rig and the measurement techniques are given in Braun and Seume (2006), Braun (2007). More details of the axial compressor are listed in Table 3.1. The measurements were performed using the reference cavities shown in Figure 3.1a. The performance curves at design speed and radial distributions downstream each row are given in Appendix B.

3.2 Features of stator and cavity design

The stator vanes of the four-stage axial compressor are pinned between two concentric rings, the outer and the inner, which are fastened to the compressor housing while the rotor blades are mounted in dove-tail grooves milled into the rotor discs. To accommodate the inner ring, the rotor shaft is manufactured with a cavity between two rotor adjacent discs. The labyrinth

Table 3.1: Axial compressor features at design operating point

Parameter	Symbol	Value	Units
Design rotational speed	-	17,100	RPM
Mass flow	$\dot{m}$	7.825	kg/s
Inlet total pressure	P_{inlet}	60,000	Pa
Interstage axial velocity	V_{ax}	150...190	m/s
Inlet Mach number	M	0.5	-
Overall isentropic efficiency	η_{is}	89.919	%
Overall total pressure ratio	π_{P}	2.712	-
Chord based-Reynolds number of stator 3	Re_{c}	$5.6 \cdot 10^5$	-
Stator 3 chord	c_{s3}	0.0350	m
Stator 3 span	S_{s3}	0.0505	m

seal fins protrude from the rotor shaft radially outwards towards the stator inner ring. The computational domain of the main flow path of the four-stage axial compressor is confined with the casing, hub, blade pressure and suction walls of each row. The boundaries of the cavity computational domain are defined by the rotor shaft and the stator inner ring. The domain inlet is located in a distance of 2 chords (referred to stator 3) upstream of the inlet-guide-vane leading edge, while the domain outlet is 1.28 chords downstream of the stator 4 trailing edge. Figure 3.2 shows the model of the entire main flow path domain including the cavity geometry integrated into the third stage. It also shows the definition of each single stage and the axial locations of mixing-planes.
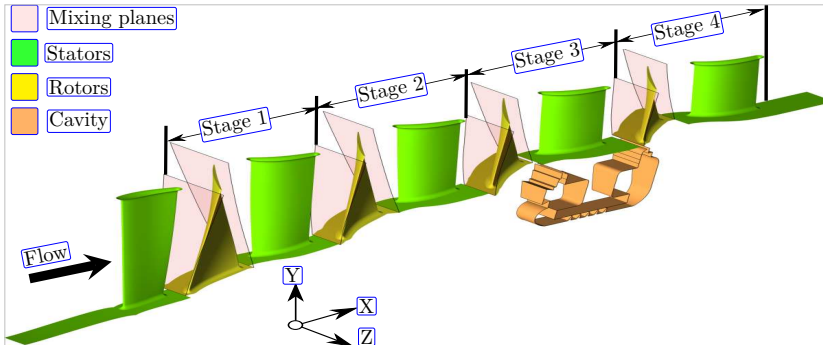
Figure 3.2: Geometry of the axial compressor used in the CFD simulations (casing wall is hidden)

The cavity leakage jet strongly influences the inlet and outlet velocity profiles of the main flow near the stator hub (see chapter 2). Consequently, the cavity leakage flow spoils the flow field at the stator hub that in turn deteriorates the performance. The deterioration becomes more pronounced in the last stages of the compressor because of the low aspect-ratio[1] blading. The low aspect-ratio allows a more pronounced interaction between the core flow and end-wall flows.

---

[1]For a constant-chord blade of chord c and span s, the aspect ratio is given by: $\text{AR} = \frac{s}{c}$

This strong flow interaction is found in the third stage of the compressor, therefore it is chosen as the geometry to be modified. In order to minimize the influence of leakage flow of the baseline cavity geometry on the main flow, the cavity outlet angle is varied. Three distinct configurations are proposed: the cavity outlet slot pointing in the main flow direction (C_1=45°), the cavity outlet slot perpendicular to the main flow path (C_2=90°) and the cavity outlet slot pointing against the main flow (C_3=135°). Figure 3.3 shows the original configuration along with the three cavity configurations. The axial gap widths in Figure 3.3 are expressed as a percentage in terms of the third stator chord. During the compressor's life the sealing clearances increase because the wear, consequently the leakage flow rises. Therefore, this work also considers three distinct seal clearances of 1.18%, 2.37% and 3.56% of blade span to better distinguish and analyze the influence of the cavity outlet angle as leakage flow varies.

(a) Baseline cavity of third stage

(b) Cavity outlet C_1 inclined by 45°

(c) Cavity outlet C_2 inclined by 90°

(d) Cavity outlet C_3 inclined by 135°
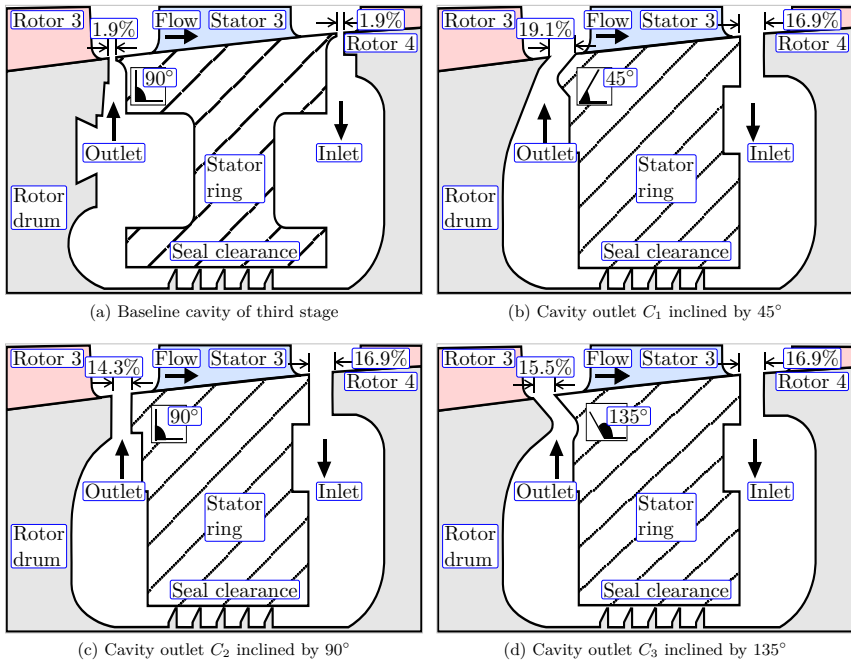
Figure 3.3: Meridional view of cavity configurations

3.3   Stator and cavity meshes

The grid was generated by considering spatial resolution, element aspect ratio, stretching, orthogonality, grid singularities, and zonal boundary interfaces. The mesh of the axial compressor blades is generated with G3DHexa, which is a parameterized meshing tool developed for turbomachinery geometries. G3DHexa requires a meridional grid of the main channel and a blade

shape formed with distinct sections as shown in Figure 3.4. The resulting interpolated mesh is shown in the right side of Figure 3.4.
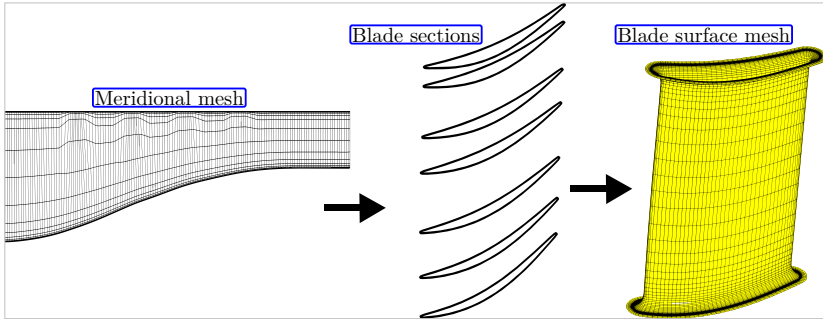
Figure 3.4: Meshing procedure of blading

Every blade and vane is meshed with an O-C-H topology, based on a structured multi-block scheme as shown by the blade-to-blade view of the third stator mesh in Figure 3.5. The spanwise discretization yields in total 147 points, with 25 points in the tip-clearance gap of every rotor row. The radial gap of each rotor row is considered as a cold tip for all configurations. The distance between rotor tip and housing remains constant, because warm clearance measurements are not available. The inclusion of fillet radii in every blade row of an axial compressor has shown better agreement with experimental data. (Kügeler et al. 2008). Thus, fillets are included in numerical simulations. The fillet radii in upstream stages hinder the coupling of the remaining cavities due to the reduced axial gap between adjacent rows. Therefore, the cavities are not simulated. In order to resolve boundary-layer flows along the blades, hub, and tip surfaces accurately, a low-Reynolds mesh is used with a non-dimensional wall distance y^+ of approximately 1 and a maximum expansion ratio of 1.2.
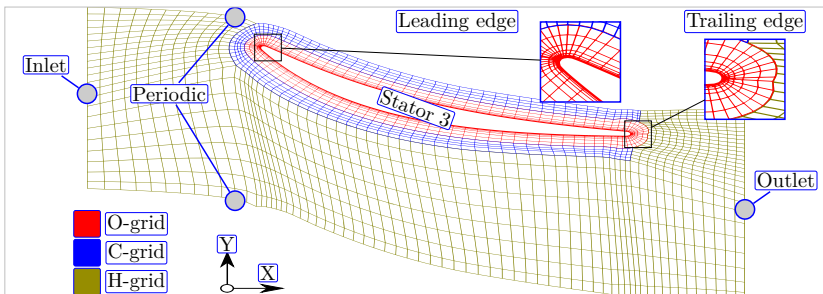
Figure 3.5: Blade-to-blade view of third stator mesh at the mid-span (every second line)

The cavity mesh must meet the high quality criteria and the same structured multi-block scheme as the blade mesh. Different approaches have been developed and implemented in order to structurally mesh the non-uniform geometry of the end-wall cavities of secondary air systems. (Malcevic 2011) The Medial Axis Transform (MAT), or skeletonization method, which is the

locus of the centers of all maximal inscribed circles in 2D and spheres in 3D. The MAT method is based on two distinct approaches: the general-field method, which typically is characterized with a differential equation, and the Voronoi-based method which is purely geometry-based. The former method can be easily extended to the three-dimensional space, and also can be coupled with a flow solver. Ali and Tucker (2014) assessed distinct meshing methods applied to end-wall cavity geometries. The results of Ali and Tucker (2014) indicate that the MAT approach provides more accurate values for the objective function than the other aforementioned methods, due to the better alignment with the flow and the more uniform cell distribution.

According to Ali and Tucker (2014) analysis, the MAT approach is more accurate. Therefore, the present work adopts the MAT approach in order to mesh the proposed cavity geometries. The vertices are obtained through the "Skeletal Element Method", proposed and programmed in a MATLAB script by Suresh (2003). Figure 3.6a shows the outline of the cavity geometry with an outlet angle of 90° with the resulting red lines of the Medial Axis Transformation. The resulting coordinates are exported into the CAD model, in order to generate the 3D cavity model. After, the 3D cavity model is meshed in ANSYS ICEM. Figure 3.6b shows the resulting cavity mesh with the cell distribution aligned with the flow direction. The cavity surfaces are meshed with a non-dimensional wall distance y^+ of approximately 1 and a maximum expansion ratio of 1.2 in order to resolve boundary layers in the seal clearances. All cavity seal-fin clearances are discretized with 50 grid points in the radial direction except for the baseline cavity where only 25 grid points are used.

(a) Cavity contour after Meridional Axial Transformation

(b) Cavity mesh
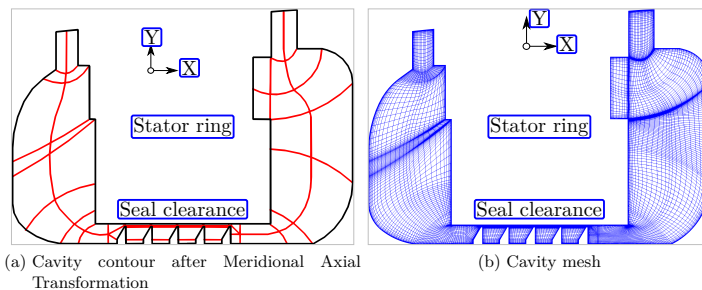
Figure 3.6: Meshing procedure of the cavity

3.4   Preliminary studies

TRACE has been widely used and validated in previous investigations (Kügeler 2004, Nürnberger 2004, Kožulović et al. 2007, Kügeler et al. 2008, Marciniak et al. 2010). Therefore in this thesis, the programming errors in the source code are assumed to be already minimized. The round-off error is diminished by using double precision numbers. In next subsections, an analysis of the discretization and physical model error is carried out for the axial compressor mesh by means of steady-state simulations.

3.4.1   Spatial discretization error analysis

The dependency of spatial discretization error is directly linked to the grid spacing. In order to quantify the spatial discretization error in the numerical methods, a grid convergence index (GCI) analysis is made in order to guarantee grid independence of the results. Roache (1994, 1997) presents the GCI analysis based on the Richardson extrapolation (RE). The extrapolation is made from the results of at least two different grid solutions. But it is highly recommended to verify the asymptotic range at least with three grid solutions. The limitations of the RE method are well known. Nonetheless, it is currently the most reliable method available for the prediction of numerical uncertainty. Another advantage is that GCI analysis is faithful not only to grid values, but also to solution functionals.

For the GCI analysis, solely the main flow path mesh of the entire axial compressor without the cavity is taken into account at the design operating point. In each spatial direction, the baseline mesh is coarsened and refined with a ratio of 1.976 and 2.180, respectively. All GCI values are calculated with a conservative p=1 and a safety factor F_s=1.25. These values are summarized in Table 3.2. Complete details of GCI analysis are given in Appendix C.

Table 3.2: Grid independence analysis of the axial compressor at design operating point

Mesh	Cells	$\dot{m}_{red}$	π_P	η_{is}	$EERE$ in %			GCI in %		
	Mio	%	%	%	$\dot{m}_{red}$	π_P	η_{is}	$\dot{m}_{red}$	π_P	η_{is}
Fine	132.35	1.300	2.706	92.136	0.183	0.026	0.149	0.229	1.054	3.895
Baseline	12.76	1.297	2.705	91.973	0.399	0.057	0.326	3.452	0.533	1.971
Coarse	1.65	1.262	2.694	90.557	3.085	0.474	1.860	6.822	0.033	0.187

Solutions of mass flow $\dot{m}_{red}$, total pressure ratio π_P and isentropic efficiency η_{is} with the corresponding extrapolated value for three meshes are shown in Figure 3.7. The solutions show an asymptotic behavior. The major deviations with respect to extrapolated values are observed for the coarse mesh. The $EERE's$ of the three variables for the baseline and fine mesh are less than 1% with respect to extrapolated reference. However, the computing resources and the computing time considerably increased for the finer mesh with respect to the baseline mesh as shown in Table 3.3. In this sense, the baseline mesh offers the best trade-off between computing time, relative error and mesh size. Therefore, the baseline mesh is selected as reference mesh, and will be used in the following simulations and analysis.

3.4.2   Validation of the reference mesh

Figure 3.8 shows the curves of total pressure ratio π_P and isentropic efficiency η_{is} against mass flow $\dot{m}_{red}$ computed for the three meshes which are compared with existing experimental data (Braun 2007). As stated previously, the $EERE$ of the baseline and the fine mesh is less than 1%. Therefore, the fine mesh only is simulated at the design operating point, due to the high computational effort required for the simulation and the minimal expected gain. The iso-speed lines of total pressure ratio of coarse and base meshes depict the trend of experimental data. However, the coarse mesh predicts lower rates of mass flow. Nevertheless, the value of π_P at
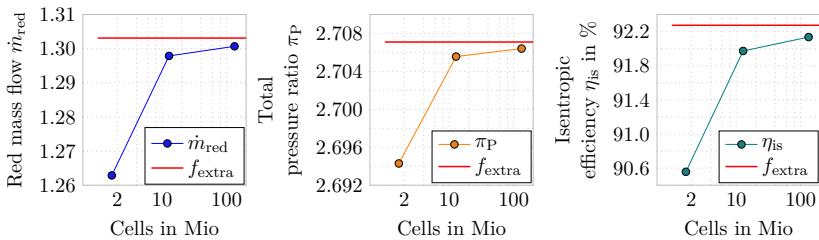
Figure 3.7: Grid independence analysis of the axial compressor at design operating point

design point (DP_C) is 0.67% near to the experimental value. The low spatial discretization also restricts the mass flow range as the compressor increases loading towards the near stall point. The base mesh follows the trend very close to experimental results in terms of total pressure ratio π_P for higher mass flow rates than the rate at the design point. After the design point (DP_E), in the direction of lower mass flow rates, the base mesh is located above the experimental line. At design point, base and fine mesh ($DP_{M,F}$) agree very well with the measurement value (DP_E). Table 3.3 contains details of total pressure ratio π_P, isentropic efficiencyη_{is}, mass flow $\dot{m}_{red}$ and the computational resources required for the three meshes at design point. All deviations are computed with respect to corresponding values at experimental design point (DP_E). The design point of the coarse mesh (DP_C) locates at -2.69% and 0.67% with respect of the experimental design point (DP_E) in mass flow and isentropic efficiency, respectively. At design point ($DP_{M,F}$), base and fine meshes vary less than 0.26% in mass flow, while for isentropic efficiency overestimate 2.28% and 2.46%, respectively as shown in the right side of the Figure 3.8.

Table 3.3: Behavior of overall compressor performance under spatial discretization variation

Mesh / Experiment	Design point			CPUs	Hours
	$\Delta\pi_P$ in %	$\Delta\dot{m}_{red}$ in %	$\Delta\eta_{is}$ in %		
Experimental (E)	0	0	0	-	-
Coarse (C)	-0.673	-2.699	+0.710	24	24
Baseline (B)	-0.257	-0.002	+2.284	24	48
Fine (F)	-0.226	+0.215	+2.466	64	720

Figure 3.9 shows computed radial distributions of normalized axial velocity V_{ax}, normalized total pressure Θ_P, and normalized total temperature Θ_T which are compared with existing experimental radial distributions (Braun 2007) downstream of the third stator. Total pressure and total temperature are normalized with respect to the corresponding values at inlet and outlet of the axial compressor while axial velocity is normalized with respect to the rotational velocity at the rotor tip. The sketch shows the axial location behind the third stator where the measurements were carried out. The profiles of axial velocity V_{ax} between the baseline and fine mesh practically coincide along the entire spanwise. The coarse mesh shows a deficit of 2% with respect to other meshes. The good agreement of the two finer meshes with the experimental profile is visible from the casing up to 44% span. Below this value, both finer meshes overestimate
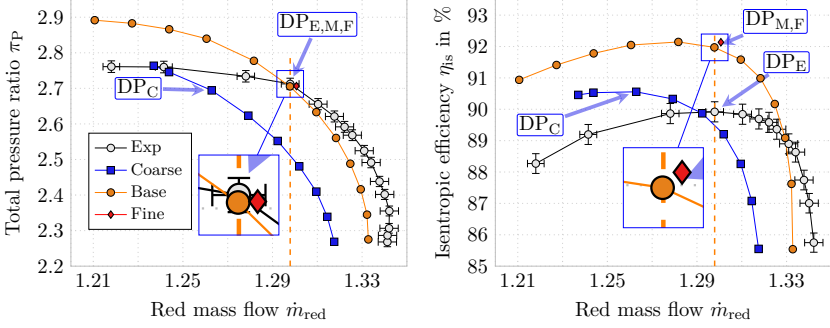
Figure 3.8: Influence of spatial discretization on overall compressor performance

the values up to 5%, with respect to experimental points. Radial distributions of total pressure Θ_P vary from each other approx. less than 0.5% over the entire span, except at 87% span where the deviations differ up to 1%. The computations underestimate with respect of experimental data up to 3% higher values of Θ_P underneath 35% span, while above this percentage there are overestimations of up to 1%. Finer meshes (i.e. baseline and fine mesh) depict normalized total temperature Θ_T distributions up to 1.8% beneath to experimental data at the midspan. The deviation is more pronounced above the midspan, specifically at 80% spanwise where the deviations reach up to 6.9%. These computed deviations of normalized total temperature Θ_T with respect to experimental data presumably cause the overestimation by more than 2% of the isentropic efficiency at the design operating point as shown in the Figure 3.8. The coarse mesh depicts 1% higher values of normalized total temperature Θ_T with respect to finer meshes as a consequence of lower axial velocity values. The analysis of the spatial discretization error shows that baseline mesh achieves the best trade-off between grid spacing and computational effort, therefore this mesh configuration will be used for later simulations.
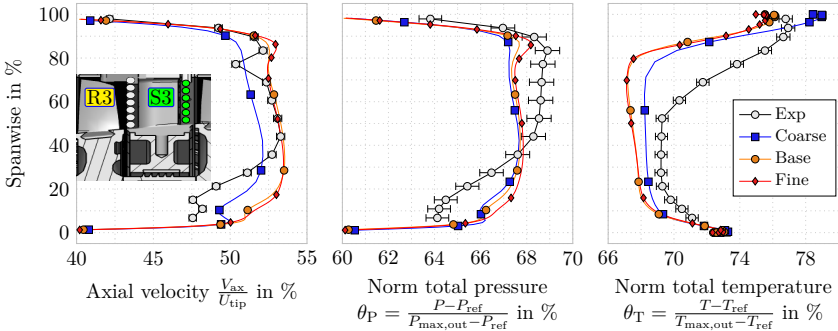
Figure 3.9: Radial distributions downstream third stator with distinct grid spacing at design point (DP)

3.4.3   Physical modeling error analysis

As already described in point 1.7 of subsection 2.2.5, the turbulence model has to be carefully selected to guarantee the accuracy in the simulations. Therefore in this work a variety of turbulence and transition models are simulated in order to determine the level of uncertainty of the models (i.e turbulence and transition models) implemented in TRACE and its effects on the overall compressor performance. All simulations use the base mesh without cavities in order to speed up the analysis. The turbulence models used in this analysis are Menter's model (k-ω SST) and Wilcox's model (k-ω). The transition models used are Multimode (Mm) and $\gamma - Re_\theta$. The combination of turbulence, transition, and fully turbulent models results in six distinct combinations which are written in table 3.4, the nomenclature obviate the content of each combination.

Table 3.4: Combinations of turbulence models with transition models

Turbulence model	Transition model	Combination
	Multimode	SST_{Mm}
SST	$\gamma - Re_\theta$	$SST_{\gamma-Re_\theta}$
	None	SST_{Turb}
	Multimode	k-ω_{Mm}
k-ω	$\gamma - Re_\theta$	k-$\omega_{\gamma-Re_\theta}$
	None	k-ω_{Turb}

Figure 3.10 shows the performance curves of total pressure ratio π_P and isentropic efficiency η_{is} against mass flow $\dot{m}_{red}$ for the six distinct combinations. The computed design point for each combination is highlighted and labeled for better identification. Despite ② $SST_{\gamma-Re_\theta}$ and ③ SST_{Tur} models achieve a deviation of less than 0.2% in mass flow with respect to experiments at the design point. At the same point, these models underestimate 5.6% and 8.6%, respectively, in terms of total pressure ratio π_P. Both models are the most restrictive to compute more points as increases the axial compressor loading. At design point, the mass flow rate of the remaining four combinations, ① SST_{Mm}, ④ k-ω_{Mm}, ⑤ k-$\omega_{\gamma-Re_\theta}$ and ⑥ k-ω_{Tur} deviate 0.009%, 0.929%, 3.587% and 2.181%, respectively with respect to experiments. These four combinations reach a deviation in total pressure ratio π_P of less than 0.75%. From these four last combinations, the most restrictive combination as loading increases is the ⑥ k-ω_{Tur} model.

The design points ② $SST_{\gamma-Re_\theta}$ and ③ SST_{Tur} achieve the largest deviations of total pressure by -5.606% and -8.660%, respectively, with respect to the experimental design point. The deficit of total pressure of these combinations suggests an isentropic efficiency overestimation as shown in the right side of Figure 3.10. The design point ⑤ of the k-$\omega_{\gamma-Re_\theta}$ combination differs 0.696% with respect to DP_E in isentropic efficiency, however this design point depicts the highest mass flow deviation by -3.587% with respect to the experimental design point DP_E. The design point ⑥ of the k-ω_{Tur} combination depicts a closer deviation of 0.231% with respect to DP_E in isentropic efficiency, but it shows the second larger mass flow deficit by -2.181%. The design point ④ of the k-ω_{Mm} combination shows a proximity less than 1% in both mass flow and isentropic efficiency, with respect to DP_E. The design point ① of the SST_{Mm} shows the largest isentropic efficiency deviation by 2.284%, and the mass flow agrees very well with DP_E. Table 3.5 summarizes the deviations of the six combinations at corresponding design point. All deviations are computed
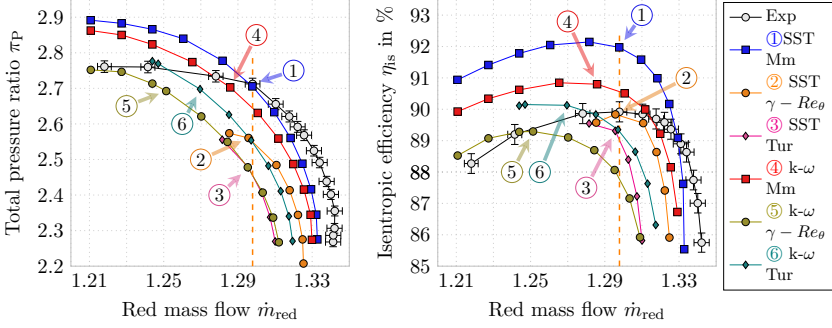
Figure 3.10: Overall performance for the base mesh and different turbulence and transition models

with respect to corresponding values at experimental design point (DP$_\mathrm{E}$).

Table 3.5: Parameters variation

Turbulence / Transition	Design Point		
	$\Delta\pi_\mathrm{P}$ in %	$\Delta\dot{m}$ in %	$\Delta\eta_\mathrm{is}$ in %
Experimental	0	0	0
① SST$_\mathrm{Mm}$	-0.257	-0.009	+2.284
② SST$_{\gamma-\mathrm{Re}_\theta}$	-5.606	-0.168	-0.091
③ SST$_\mathrm{Tur}$	-8.660	-0.175	-0.676
④ k-ω_Mm	-0.365	-0.929	+0.979
⑤ k-$\omega_{\gamma-\mathrm{Re}_\theta}$	-0.743	-3.587	-0.696
⑥ k-ω_Tur	-0.548	-2.181	+0.231

Figure 3.11 shows radial distributions of axial velocity V_ax, normalized total pressure Θ_P, and normalized total temperature Θ_T of the six combinations compared to experimental data (Braun 2007) downstream third stator. The ② SST$_{\gamma-\mathrm{Re}_\theta}$ and ③ SST$_\mathrm{Tur}$ models overestimate deviations of axial velocity V_ax by 2.2% and 1%, respectively at the midspan with respect to experiment data. The ① SST$_\mathrm{Mm}$ and ④ k-ω_Mm combinations agree very well to experimental data from casing to 44% span. Beneath this percentage, these models overestimate deviations up to 4.6% at 15% span. The remaining models ⑤ k-$\omega_{\gamma-\mathrm{Re}_\theta}$ and ⑥ k-ω_Tur predict good agreement with experimental points above 70% span, underneath this span both models underestimate up to 1.78% at 44% span. The underestimation automatically discard these combinations and agrees with the low rates of mass flow of the ⑤ k-$\omega_{\gamma-\mathrm{Re}_\theta}$ and ⑥ k-ω_Tur illustrated in Figure 3.10.

In terms of total pressure Θ_P is evident that ② SST$_{\gamma-\mathrm{Re}_\theta}$ and ③ SST$_\mathrm{Tur}$ models underestimate the deviations with respect to experimental radial profile up to 3.44 and 4.79%, respectively at the midspan. These deviations in radial profiles explain the deficit of both combinations in total pressure ratio shown in Figure 3.10. The remaining four models underestimate values of

Θ_P from casing to 44% reaching the maximal deviation up to 1.3% at 83% of the span. Below 44% span the profiles are located ahead of experimental data up to 2.08% at 10.8% span. The minor radial distribution deviations of the four combinations with respect to the experiments are in near agreement in terms of total pressure ratio illustrated in Figure 3.10.

The profiles of total temperature Θ_T of the ② $SST_{\gamma-Re_\theta}$ and ③ SST_{Tur} combinations keep higher deviations with respect of experimental measurements by 3.16% and 3.71% at 50% span, respectively. At the same span, remaining combinations ① SST_{Mm}, ④ k-ω_{Mm}, ⑥ k-ω_{Tur} and ⑤ k-$\omega_{\gamma-Re_\theta}$ compute deviations by 1.79, 0.82, 0.16 and 0.35%, respectively. At the hub, all combinations bent in the experimental trend. Above 52% span, the models can not capture the total temperature deflection of experimental data. All combinations start to deflect at 80% span while experimental distribution deflects at 52% span.
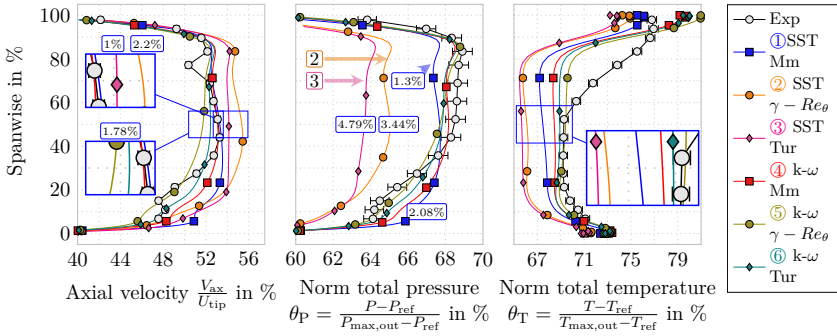
Figure 3.11: Radial distributions of different physical modeling downstream of the third stator

According to the previous comparison of computed overall performance and radial distributions with experimental data at the design point the combinations ② $SST_{\gamma-Re_\theta}$ and ⑥ SST_{Tur} are completely discarded, because the radial profiles show an overestimation in axial velocity V_{ax} and a deficit of accuracy in total pressure Θ_P and total temperature Θ_T. Low values of axial velocity V_{ax} in the radial distributions of the combinations ⑤ k-$\omega_{\gamma-Re_\theta}$ and ⑥ k-ω_{Tur} lead to the lowest rates in mass flow of the corresponding models depicted in Figure 3.10. In terms of total pressure Θ_P, the radial distributions of these combinations agree very well with experimental data. This agreement supports the small deviation in total pressure ratio illustrated in Figure 3.10. The ⑤ k-$\omega_{\gamma-Re_\theta}$ and ⑥ k-ω_{Tur} combinations depict the nearest radial distributions of total temperature Θ_T with respect of experimental data below 52% span but these combinations also are discarded because they predict a lower rate of mass flow.

The remaining combinations ① SST_{Mm} and ④ k-ω_{Mm} depict the lowest deviations in mass flow $\dot{m}_{red}$ due to the good agreement in V_{ax} above 44% span. Above this percentage these models underestimate deviations of total pressure Θ_P up to 1.29% at 83.4% of span, while at the hub zone the deviations reach overestimations up to 2% at 10% of span. In terms of total temperature Θ_T, the closest deviations with respect to experiments observe a maximum deviation by 1.85% at 52% span. Above this span, the combinations predict colder radial distributions than experimental results. Due to the good agreement in mass flow and total pressure ratio, both combinations are chosen to simulate the main flow path with the original cavity configuration in the next

subsection.

3.4.4   Physical modeling validation with cavities

It is important to know the sensitivity of the selected physical models as the cavity is added into the model. Therefore, additional simulations with the combinations SST_{Mm} and k-ω_{Mm} are implemented including the original cavity configuration sketched in Figure 3.3a. The models are simulated up to the last stable point by increasing the compressor load. Figure 3.12 illustrates overall performance curves and radial distributions of axial velocity V_{ax}, total pressure Θ_P, and total temperature Θ_T of the two combinations compared to measurement data downstream third stator.

(a) Overall performance of axial compressor

(b) Radial distributions downstream of the third stator at design point
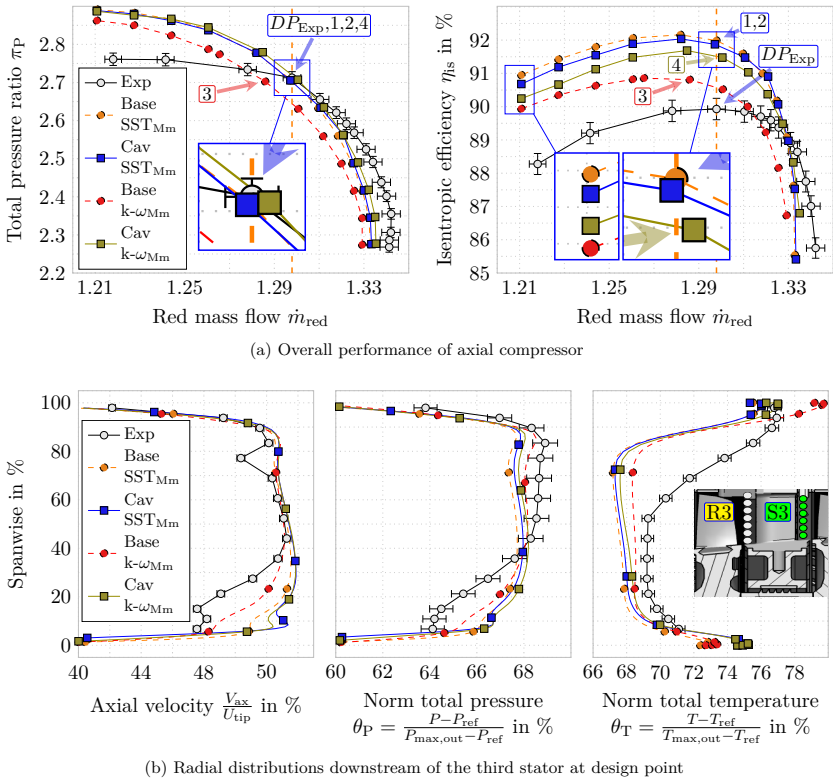
Figure 3.12: Overall performance and radial distributions with the cavity inclusion

With the k-ω_{Mm} combination, it is evident that both mass flow $\dot{m}_{red}$ and total pressure ratio π_P increase their values slightly more than 1% as the cavity is considered. This augmentation yields

a better prediction at the design point, moving from point ③ (Baseline) to point ④ (cavity). With the cavity inclusion the k-ω_{Mm} combination increases the rate of isentropic efficiency up to 0.66% at the design point with respect to the corresponding baseline. However, this increase of total pressure and isentropic efficiency phisically is not feasible as the cavity is considered and therefore the combination k-ω_{Mm} is discarded for further simulations.

In contrast, with the combination SST_{Mm} mass flow $\dot{m}_{\text{red}}$ and total pressure ratio π_{P} decrease as much as 0.2% and less than 0.1% at near stall and design point, respectively. In terms of isentropic efficiency the SST_{Mm} combination depicts a decay with respect to corresponding baseline model up to 0.29% at the near stall point. This combination SST_{Mm} reveals expected reductions in total pressure and isentropic efficiency as the cavity is considered.

As the cavity model is included, both profiles of axial velocity coincide over the entire span except from 6% to 15% span. In this range, k-ω_{Mm} combination predicts 1% slower V_{ax} than SST_{Mm}. The latter combination seems to capture the bending of experimental radial profile below 15% span. This agreement of both profiles supports the small deviations in mass flow $\dot{m}_{\text{red}}$ in Figure 3.12a. At midspan, both models predicted 0.24∼0.27% higher V_{ax} than experiments. Above midspan, the profiles of the cavity models barely vary by less than 0.5% with respect to the corresponding baseline models. Below midspan, deviations are more pronounced and the models with cavity, SST_{Mm} and k-ω_{Mm} reach deviations up to 2.42% and 3.57% respectively, at 8.5% span with respect to the corresponding base models.

With the SST_{Mm} combination, the total pressure Θ_{P} profile of the cavity model starts to increase its values at 15% span, and reaches up to 0.2% higher values than baseline from 30% to 90% span. In contrast, the k-ω_{Mm} combination with cavity starts to deviate from midspan to the casing, showing a major deficit by 0.5% at 85% span with respect to baseline. From midspan to the hub, the deviation reaches a difference up to 1.26% at 9% span with respect to the baseline. By comparing only the radial profiles as the cavity is included, the k-ω_{Mm} combination shows 0.2% higher values than SST_{Mm} from 9% to 90% span. This difference is proportional to the total pressure ratio increase depicted in Figure 3.12a at the design point. The total temperature profiles of shroudless and cavity models coincide from the casing to 80% span with the SST_{Mm} combination. Beneath this span percentage, the profiles start to diverge each other by reaching the highest deviation of 2.1% at the hub. With the k-ω_{Mm} combination, the profile of the cavity model is located behind the shroudless profile over the entire span except below 20% span, where the positions reverse and the deviations reach a difference up to 1.9% at the hub. At the tip, the difference is more pronounced reaching up to 2.7%. When comparing solely the radial profiles with the k-ω_{Mm} combination, the shroudless model depicts higher temperatures that predict lower isentropic efficiency in Figure 3.12a at the design point. As expected, both turbulence models show an increase in the radial temperature profile mainly at the hub with the cavity inclusion. However, the k-ω_{Mm} combination shows 0.2% and 1% higher values than SST_{Mm} combination at midspan and at the tip, respectively.

The k-ω_{Mm} combination shows more sensitivity as the cavity was included, specifically the total pressure Θ_{P} and mass flow $\dot{m}_{\text{red}}$ increased considerably with respect to the shroudless model. In contrast, the total temperature Θ_{T} decreases with respect to the baseline. This latter deficit combined with total pressure increase considerably affects the computed isentropic efficiency leading to higher values than baseline model which is not phisically expected. This augmentation of isentropic efficiency reveals that the k-ω_{Mm} is not able to simulate the cavities. The SST_{Mm} combination under the same cavity inclusion shows a moderately and conservative decrease of

the aforementioned variables with respect to the shroudless model. This moderate sensitivity to
the cavity inclusion resulting from combination of the SST turbulence and Multimode transition
model (SST_{Mm}) determines the selection of this combination for simulating the configurations
with the proposed cavities sketched in Figure 3.3b-d.

3.5   Approaches for unsteady simulations

Time-dependent simulations have the capacity to show unsteadiness phenomena such as ro-
tor wakes, tip and hub vortices and secondary flow that exist between the turbomachinery
stages, however they require more CPU resources and storage memory than steady-state simu-
lations.(Montomoli et al. 2009, 2013) The analysis of the resulting data becomes more complex
because all variables have to be temporally averaged. Currently, there are three distinct ap-
proaches which are implemented in CFD solvers for unsteady simulations in multi-stage axial
turbomachines. The most accurate approach but with enormous computational effort is the
simulation of the full annulus of the turbomachine. In most cases, this approach is unfeasible
for day-to-day applications. For this reason, the main concern of the remaining approaches is
to keep the computational effort low while maintaining high accuracy. The second approach is
the phase-lag which is handled by a technique that inclines the computational plane in time.
(Erdos et al. 1977, Giles 1988) The third approach is the pitch-scaling method, which is used
in this thesis for unsteady simulations. This approach is conditioned to have the same pitch in
both rotor and stator rows, but not necessarily the same number of blades on each row. The
third stage of the axial compressor under consideration in this thesis has 29 rotor blades and
34 stator vanes as shown in the counting blading in Figure 3.3b. The optimal scaling can be
found by taking advantage of spatial and temporal circumferential periodicity in terms of com-
putational resources is to have a ratio of 1 rotor blade to 1 stator vane. However, this scaling in
real applications is not always feasible, because the rotor blades frequently are an odd number,
and the stator vanes are an even number due to structural and dynamic concerns. Thus, it is
necessary to scale both numbers of blades to find the greatest common divisor (GCD) of rotor
and stator. According to this concept, the third stage is scaled in order to slightly modify the
original counting blading, resulting in 28 rotor blades and 35 stator vanes for a full annulus.
By applying a GCD of 7, an equal pitch by 51.42° in which 4 rotor blades and 5 stator vanes
for the third stage are obtained. The remaining stages also are scaled with the same GCD. It
is important to say that this approach has lower computational cost and sufficient accuracy in
comparison to full annulus simulation.

4. Peculiarities of labyrinth flows

4.1 Labyrinth performance

The variation of the cavity outlet angle should not affect the computed leakage mass flow on the first labyrinth seal-fin because the geometric modification is far sufficient from the labyrinth seal-fin. However, steady-state solutions can capture discernible variations of the labyrinth leakage flow between the cavity outlet configurations. The steady-state simulations in this work consider more detailed boundary conditions rather than the typical simplifications made as the labyrinth seal flow is isolated and simulated. Figure 4.1 shows an augmentation of leakage flow as the compressor increases the loading for all clearance heights. For the tightest clearance the configuration $C_2=90°$ shows the lowest leakage flow rate over the speed-line while the variant $C_1=45°$ depicts the highest rates followed by the $C_3=135°$. These latter configurations interchange their ranking with each other with the intermediate clearance while the case $C_2=90°$ keeps the lowest leakage flow rates. For the highest clearance, the configuration $C_3=135°$ exhibits the highest rates of leakage flow, while the remaining models show small deviations of each other. The maximum rates are found near the numerical stall region reaching approximately 0.3%, 0.7% and up to 1% for $H_1=1.18\%$, $H_2=2.37\%$ and $H_3=3.56\%$, respectively.
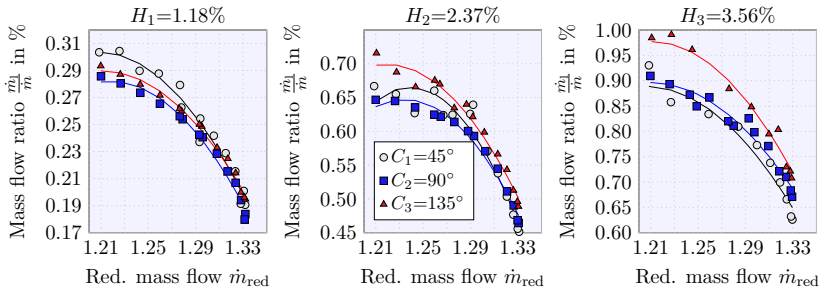
Figure 4.1: Comparison of the seal-fin labyrinth mass flow with distinct clearance heights and three angle configurations

The prediction of the leakage flow is crucial for other research topics in turbomachinery such as rotordynamics and heat transfer. The importance of validating one-dimensional models with three-dimensional flow solutions under distinct operating conditions ensures the thrust of one-dimensional modeling in the development of new labyrinth designs. Figure 4.2 shows the comparison of distinct one-dimensional models in the prediction of leakage flow against the three-dimensional CFD solutions. Egli's model predicts with sufficient accuracy the leakage flow for all configurations with the tightest clearance of $H_1=1.18\%$. For the intermediate clearance $H_2=2.37\%$, Egli's and Vermes models are more conservative to predict the case $C_1=45°$. Aungier's model fits better to CFD data in the remaining configurations. For an increased clearance of $H_3=3.56\%$, Egli's model predicts more conservative rates (i.e. below CFD rates) for three configurations. Nevertheless, for the configuration $C_3=135°$, Neumann's and Vermes

models fit very well for the CFD data. These models overestimate slightly the rates of leakage flow, but the fit still depicts good agreement for the case C_2=90°. These latter models overestimate approximately one tenth of the CFD value over the entire speed-line for the variant C_1=45°.
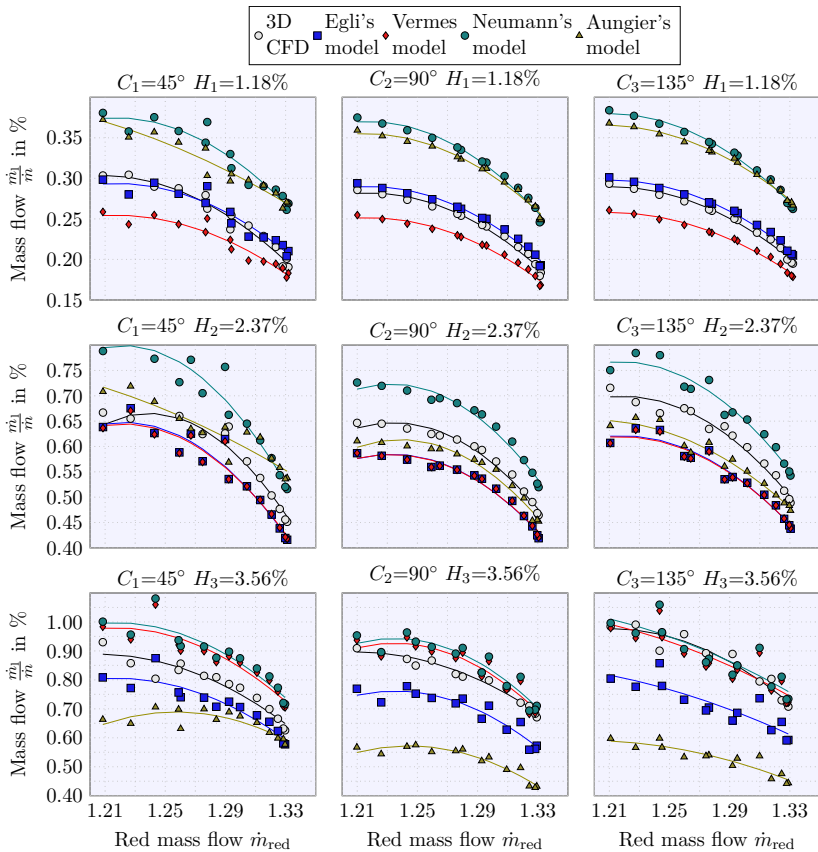
Figure 4.2: Comparison of the prediction of labyrinth mass flow rates with distinct one-dimensional models

Egli's model predicts more conservative flow rates for all configurations and all clearances. For low rates of leakage flow (H_1=1.18%), the model predicts with sufficient accuracy the three-dimensional CFD values. Aungier's model better approaches the CFD data only for the intermediate clearances. For high leakage mass flow rates, Neumann's and Vermes model fit better for the CFD rates. Egli's model shows more robustness and application range.

4.2   Performance deterioration Single-blade vs Multi-blade including cavities

Single-blade steady simulations are the most frequent method used in the turbomachinery design due to the robust and effectiveness in terms of computational resources. However, it is necessary to know if these single-blade steady simulations applied to cavity simulations deliver similar trends in terms of leakage flow rate and efficiency penalties compared to multi-blade steady simulations. Figure 4.3 provides the comparison between single- and multi-blade steady solutions in order to elucidate the differences as the clearance increases. In addition they are compared with experimental data from other axial compressors, Freeman (1985), Wellborn and Okiishi (1996) and Lange et al. (2010). The experimental data from Freeman (1985) were separated into deep and shallow shrouds because every configuration has a distinct slope of leakage flow.
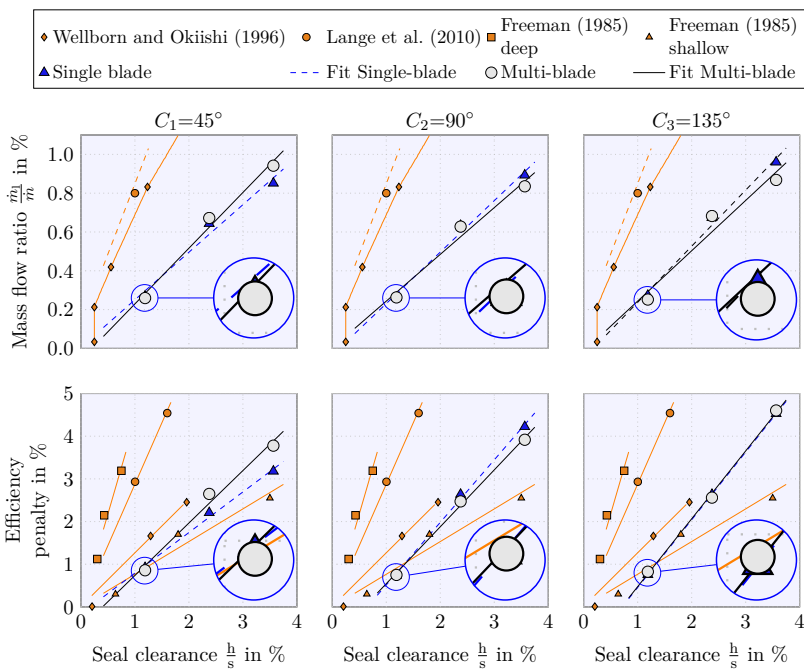
Figure 4.3:   Differences in the third stage between single-pitch and multi-blade steady simulations at near peak efficiency

Single- and multi-blade models depict a moderate slope for the leakage flow rate compared with the experimental data of Wellborn and Okiishi (1996) and Lange et al. (2010). Both experimental data show that the rate of leakage flow is more sensitive to the seal clearance increase, namely for each 1% of clearance the leakage flow increases approximately 0.7∼0.8%. The leakage flow slope is directly associated to the seal's effectiveness. The experimental data from Wellborn and Okiishi (1996) and Lange et al. (2010) are obtained with a single seal-fin

while the current investigation uses a labyrinth seal with five seal-fins. In terms of leakage flow below 1.5% of seal clearance there is not significant difference from single- and multi-blade simulations. Above 1.5% of seal clearance, single-blade simulations show slightly higher rates compared to multi-blade cases for the configurations C_2=90° and C_3=135° while the remaining case depicts the opposite. For this investigation the leakage flow increases approximately 0.25% for each 1% of clearance. The efficiency's data from Lange et al. (2010) and Freeman (1985) (i.e. deep shrouds) retains the most pronounced slope which indicates higher efficiency sensitivity to the seal's opening clearance. The data from Wellborn and Okiishi (1996) and Freeman (1985) (i.e. shallow shrouds) possess very close slope compared each other with current results. For a minor seal clearance by 1.18%, the efficiency deterioration is insensitive to single- or multi-blade modeling. Above 1.8% seal-clearance multi-blade simulations show higher efficiency penalty compared to single-blade modeling for the case C_1=45° while the model C_2=90° shows the opposite trend. The slope of efficiency with single- and multi-blade simulations coincide for the configuration C_3=135°. For all cases the efficiency penalty increases approximately 0.7∼0.9% for each 1% of clearance.

4.3   Leakage flow at cavity trenches

This section is devoted to analyze thermal properties and features of the flow inside the cavity but with more detail at cavity-trenches. Figure 4.4a shows a portion of the main flow coming inside the downstream cavity-trench entirely adhered to the rotor-wall side. Simultaneously on the stator-wall side, the leakage flow returns to the main channel. This balance of negative and positive radial velocity indicates a recirculation structure inside the downstream cavity-trench which is easily identified in Figure 4.4a. Once a portion of the leakage flow enters into the downstream cavity-well, the leakage flow immediately redirects and attaches to the stator ring wall. Inside the downstream cavity-well, the attachment is dictated by the recirculating flow structure which is generated by the energy transferred from the rotor disc to the leakage flow. The leakage flow passes through the labyrinth seal where it rotates in the seal chambers. The leakage flow discharges directly to the rotor disc wall and travels in direction to the outlet cavity-trench partially adhered to the rotor drum. The rotor disc continues providing additional energy to the leakage flow in the upstream cavity-well. This energy makes to recirculate the leakage flow inside the upstream cavity-well forming other recirculation structure that rotates in the clockwise direction. The leakage flow leaves the cavity-trench attached to the rotor disc wall while on the opposite side a portion of main flow ingresses inside the upstream cavity-trench. The outgoing and incoming flow generate a recirculation zone inside the upstream cavity-trench.

Pitchwise distributions of radial velocity V_{rad} which are normalized with the rotor speed at the hub and are distributed uniformly inside the downstream cavity trench for all configurations which are shown in Figure 4.6. The measurement points are located along the cavity inlet at 10% (i.e. near the stator ring), 50% (i.e. cavity's mid-trench) and 90% (i.e. near the rotor disc) of the cavity's axial distance and downwards at 0%, -5% and -10% of the cavity's span as shown in Figure 4.5a. Figure 4.6a shows the distributions at 0% of cavity's span, namely at the interface between the cavity inlet and the main channel. The distributions at 10% and 50% of the cavity's axial distance show peaks of negative radial velocity V_{rad} by -6∼-7% and -10%, respectively, just behind the stator trailing edge. Simultaneously, the distributions show peaks of positive radial velocity V_{rad} by 3∼4% and 10% for 0% and 50% of the cavity's axial distance, respectively, located on the stator suction side. At 90% of the cavity's axial distance, all distributions show

Radial velocity $V_{\mathrm{rad}}/U_{\mathrm{hub}}$ in %

(a) Seal clearance $H_1 = 1.18\%$

Radial velocity $V_{\mathrm{rad}}/U_{\mathrm{hub}}$ in %

(b) Seal clearance $H_2 = 2.37\%$

Figure 4.4: Streamlines and contours of time-average radial velocity for a cavity angle of 90° with seal clearance H_1=1.18% and H_2=2.37%

negative radial velocity V_{rad} of -6∼-7% with peaks of positive radial velocity V_{rad} that scarcely exceed 0% just behind the stator trailing edge. The contours show that the peaks of positive radial velocity are located mostly on the stator suction side and they encompass from 10% to 60% of the cavity's axial distance. In addition, positive radial velocity covers from 10% to 50% of the cavity's axial distance and along the entire pitch. Just behind the stator trailing edge, the contours of negative radial velocity by -10% encompass from 10% to 90% of the cavity's axial distance. At the latter cavity's axial distance, the negative radial velocity spreads along the stator pitch. Spots of radial velocity of -2% are seen below 10% of the cavity's axial distance.

Deeper in the cavity's trench at 5% and 10% of the cavity's span the distributions of radial velocity V_{rad} are shown in Figure 4.6b and 4.6c, respectively. The contours depict only positive radial velocity from 0% to 50% of the cavity's axial distance while on the remaining cavity's axial distance the contours show negative radial velocity. The distributions and contours highlight the peaks of positive radial velocity at 10% of the cavity's axial distance (i.e. near the stator ring) while at 90% of the cavity's axial distance (i.e. near the rotor disc) the peaks of negative radial velocity appear along the entire pitchwise direction. At 10% of the cavity's axial distance

the distributions of radial velocity V_{rad} depict values approximately between 10% and 20%. These distributions confirm that leakage flow goes out from the downstream cavity trench. The emanated leakage flow is attached to the stator ring. At 50% of the cavity's axial distance the distributions depict practically 0% of radial velocity V_{rad} with small variations. These distributions show that in the middle's cavity trench the leakage flow can not enter into the cavity trench. The distributions of all configurations along the span's cavity-trench at 90% axial distance show negative radial velocity V_{rad} approximately between -7% and -20%. These distributions confirm that the most part of the leakage flow comes into the downstream cavity near the downstream rotor disc. The distributions of radial velocity V_{rad} depicted in Figure 4.6 illustrate the recirculation structure inside the downstream cavity trench as depicted in Figure 4.5b and its rotation in the clockwise direction.

a) Cavity's locations   b) Cavity's recirculation   c) Leakage directions
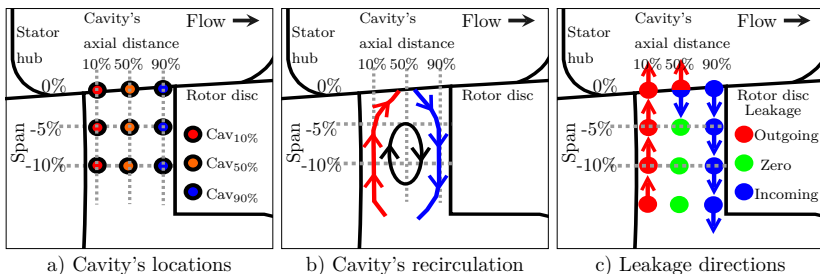
Figure 4.5: a) Sketch of the measurement points, b) recirculation and c) leakage direction into the downstream cavity. The sketch of the downstream cavity coincides for all configurations $C_1 = 45°$, $C_2 = 90°$, and $C_3 = 135°$

During the compressor's life-cycle the cavity seal clearances increase progressively due to the unavoidable wear. Because of the clearance widening, the leakage flow increases. Figure 4.4b shows streamlines and contours of time-averaged radial velocity inside the cavity geometry for the case with a cavity outlet angle of 90° with an increased clearance H_2=2.37%. The opening of the seal clearance provokes the division of the recirculation structure observed inside the downstream cavity-well with the clearance H_1=1.18%. The recirculation structure inside the cavity-trench remains and continues returning some part of the leakage flow to the main stream. The remaining leakage flow is ingested into the downstream cavity-well. Inside the downstream cavity-well, two dominant recirculation zones dictate the leakage flow path. The rotor disc wall induces the upper recirculation structure which occupies the cavity-well's width and forces the leakage flow to be attached to the stator ring wall. At approximately 50% of the cavity-well height the leakage flow is deviated by the lower recirculation structure in the direction of the rotor disc wall that deflects the leakage flow in the direction of the labyrinth seal-fins. Due to the constant rotational speed, the rotor wall disc provides energy to the fluid in both up- and downstream cavity-wells.

Pitchwise distributions of radial velocity V_{rad} for the increased clearance H_2=2.37% are shown in Figure 4.7. The measurement points are the same used for the clearance H_1=1.18% and sketched in Figure 4.5a. At 0% of the cavity's span, the contours of negative radial velocity V_{rad} increased its extension compared to those for the clearance H_1=1.18% and increase its magnitude up to -10%, namely -3% more than the clearance H_1=1.18%. Simultaneously, the contours of positive radial velocity reduce its extension compared to the tightest clearance.
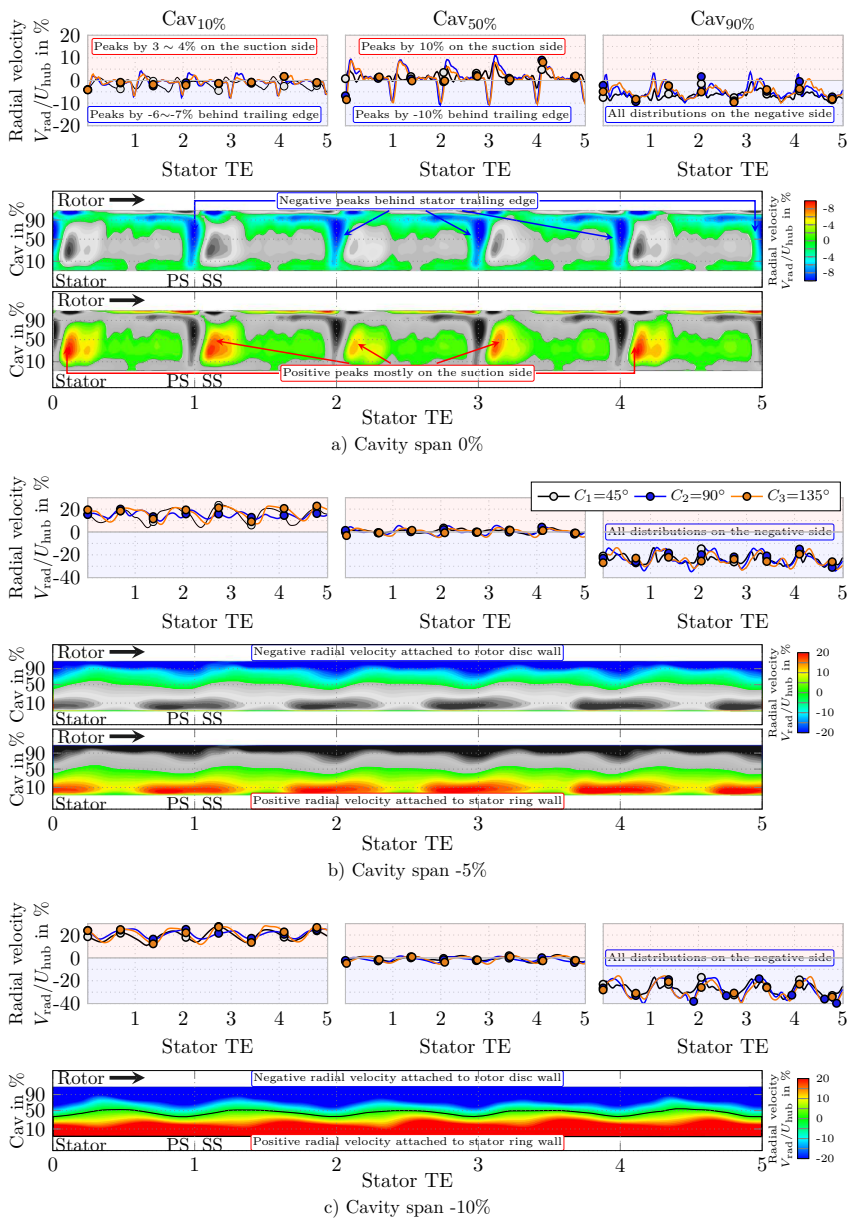
Figure 4.6: Time-average pitchwise distributions and contours of radial velocity V_{rad} at 0% (up), -5% (middle) and -10% (down) cavity's span inside the downstream cavity-trench with the clearance $H_1 = 1.18\%$

The distributions at 10% and 50% of the cavity's axial distance show the same peaks of negative radial velocity V_{rad} just behind the stator trailing edge but with an increase in magnitude by -10% and -15%, respectively. The peaks of positive radial velocity V_{rad} remain located on the stator suction side and their magnitude reaches 3∼4% and 5% for 0% and 50% of the cavity's axial distance, respectively. 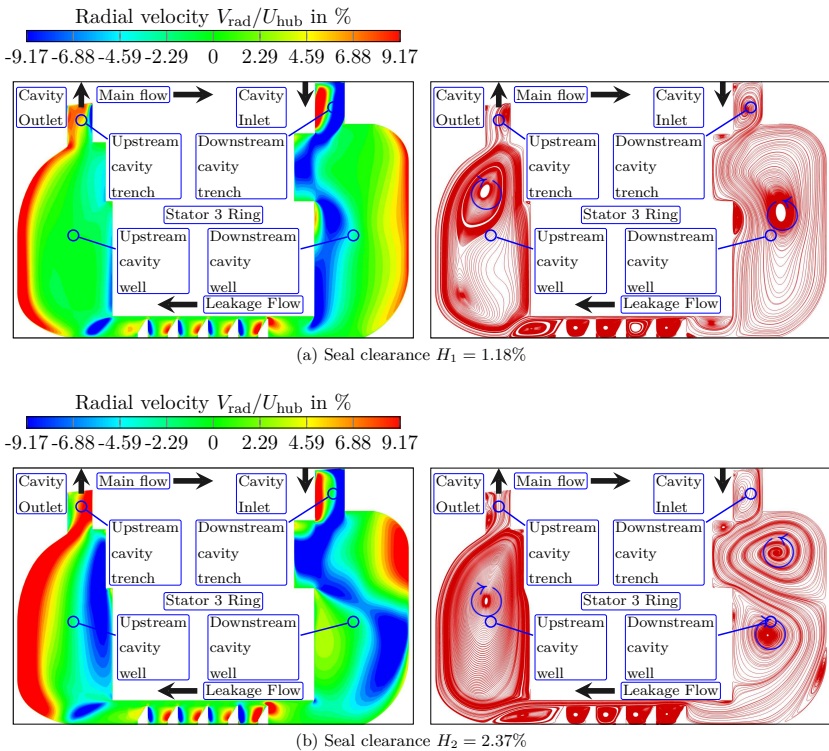At 90% of the cavity's axial distance all distributions show negative radial velocity V_{rad} by -10% with peaks of positive radial velocity V_{rad} that scarcely reach 0% just behind the stator trailing edge.

In the cavity's trench at 5% and 10% of the cavity's span, the distributions of radial velocity V_{rad} at three of the cavity's axial distances behave similar to those corresponding to the tightest clearance H_1=1.18%, but with increased magnitude and more pronounced variations. The peaks of positive radial velocity at 10% of the cavity's axial distance (i.e. near the stator ring) reach up to 15% while at 90% of the cavity's axial distance (i.e. near the rotor disc) the peaks of negative radial velocity appear along the entire pitchwise direction with an average of -30% of negative radial velocity V_{rad} with peaks reaching up to -50%. The distributions at 50% of the cavity's axial distance continue oscillate around the 0% of radial velocity V_{rad} although the variations become greater. At 10% of the cavity's axial distance the distributions of radial velocity V_{rad} oscillate approximately around the 20% with more pronounced variations. These distributions indicate that the most part of the leakage flow continue coming into the cavity-trench attached to the rotor disc wall. But in some locations of the cavity's middle trench the leakage flow comes in and comes out simultaneously. Although the incoming leakage increased, the emanated leakage flow remains practically unaltered compared to the configuration with the clearance H_1=1.18%. The distributions show that the recirculation structure inside the downstream cavity-trench remains almost unaltered except that the foci move to the stator ring wall due to the unbalance between the radial velocities as shown in Figure 4.4b.

Figures 4.5b and 4.5c show sketches of the recirculation structure and the direction of the leakage flow inside the downstream cavity trench, respectively. The sketches show the simplification of the leakage flow inside the downstream cavity trench. The leakage flow enters from 50% to 100% of the cavity's axial distance and the leakage flow remains attached to the rotor disc wall. On the other side, from 0% to 50% of the cavity's axial distance the leakage flow leaves to the main channel. At 50% of the cavity's trench, the rate of leakage flow is practically zero.

Contours of radial velocity V_{rad} at the upstream cavity trench for the clearance $H_1 = 1.18\%$ in Figure 4.4a show that leakage flow is emanated attached to the rotor disc wall while on the opposite side a portion of the main flow comes into the cavity-trench. Contours and pitchwise distributions of radial velocity V_{rad} which are distributed uniformly inside the upstream cavity trench for all configurations are shown in Figure 4.10. The measurement points are located along the cavity outlet at 10%, 50% and 90% of the cavity's axial distance and downwards at 0%, -5% and -10% of the cavity's span as shown in Figure 4.8.

In all configurations, contours of radial velocity V_{rad} at 0% of the cavity's span show similar features. In all configurations, at 10% of the cavity's axial distance (i.e. near the rotor hub) there is negative radial velocity while on the opposite side, namely at 90% of the cavity's axial distance (i.e. near the stator hub) the contours show positive radial velocity. The case $C_1 = 45°$ show the greatest regions of negative and positive radial velocity V_{rad}. For this case the region of negative radial velocity V_{rad} encompasses up near to 50% of the cavity's axial distance while for the case $C_2 = 90°$ the regions of negative radial velocity V_{rad} reach nearly up to 10% of the cavity's axial distance. The last case $C_3 = 135°$ shows the regions of negative radial velocity V_{rad}

a) Cavity span 0%

b) Cavity span -5%

c) Cavity span -10%

Figure 4.7: Time-average pitchwise distributions and contours of radial velocity V_{rad} at 0% (up), -5% (middle) and -10% (down) cavity's span inside the downstream cavity-trench with the clearance $H_2 = 2.37\%$
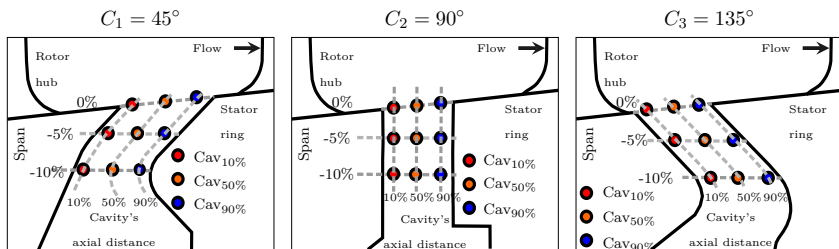
Figure 4.8: Sketch of the measurement points into the upstream cavity for all three configurations $C_1 = 45°$, $C_2 = 90°$, and $C_3 = 135°$

practically attached to the rotor disc wall with very small spots that scarcely reach 10% of the cavity's axial distance. All configurations show contours of positive radial velocity V_{rad} at 90% of the cavity's axial distance (i.e. near the stator leading edge), however the size of the spots reduce progressively when the cavity outlet increase from 45° to 135°. All pitchwise distributions show oscillations along the cavity's trench. The oscillations become more pronounced at 50% and 90% of the cavity's axial distance. The case $C_1 = 45°$ shows the highest crests in comparison to remaining cases. At 10% of the cavity's axial distance, the distributions oscillate between -5% and 5% of radial velocity V_{rad}. The pitchwise distribution of the case $C_1 = 45°$ is located mostly below 0%, namely on the negative side of radial velocity V_{rad} while the distributions of the remaining cases locate predominantly on the positive side of the radial velocity V_{rad} except on the valleys located on the stator-suction side as shown in Figure 4.9a. These distributions show that a portion of the main flow enters into the upstream cavity trench. The main flow enters into the upstream cavity-trench attached to the rotor disc wall independently of the cavity outlet angle but the case $C_1 = 45°$ shows the greatest regions of positive and negative radial velocity V_{rad} compared to the other configurations. At cavity's span of -5% and -10% the distributions of all configurations along the span's cavity-trench at 90% axial distance show negative radial velocity V_{rad} approximately by -5% with peaks reaching up to -10%. At 10% and 50% of the cavity's axial distance the distributions depict only positive values of radial velocity V_{rad} between 0∼10% with small variations. These distributions confirm that the most part of the leakage flow emanates from the middle of the cavity trench to the rotor disc wall. In these cavity's spanwise locations the emanating leakage flow encompasses the entire cavity's axial distance except the region near the stator ring where the contours show leakage flow incoming into the cavity trench as shown in Figure 4.9b,c. At cavity's span of -10% the distributions of all configurations are practically constant along the cavity trench.

When the clearance increases by $H_2 = 2.37\%$ the emanated leakage flow increases and consequently the radial velocity increases as shown the contours and pitchwise distributions in Figure 4.11. At 0% of the cavity's span the contours of all configurations show similar regions to those for the clearance $H_1 = 1.18\%$. However, the contours of negative radial velocity V_{rad} near the rotor hub reduce in size with respect to those for the clearance $H_1 = 1.18\%$ while on the opposite side, namely at 90% of the cavity's axial distance (i.e. near the stator hub) the contours of positive radial velocity increase in size and magnitude. The contours and pitchwise distributions of radial velocity show that despite the increase in leakage flow there are regions near the rotor hub in which the flow from main channel enters into the upstream cavity trench. At -5% of the cavity's span the pitchwise distributions show positive radial velocity V_{rad} practically

along the entire cavity's trench except in isolated spots of negative radial velocity $V_{\rm rad}$ near the rotor disc wall. This indicates that leakage flow emanates from the upstream cavity completely attached to the stator ring in all configurations except for the case $C_3 = 135°$. In this latter configuration the leakage flow emanates mainly at the mid-trench, namely at 50% of the cavity's axial distance. At -10% of the cavity's span (i.e. exactly where the configurations with the corresponding cavity outlet bends) the configurations $C_1=45°$ and $C_3=135°$ show the same trend of such pitchwise distributions with the clearance $H_1 = 1.18\%$. The case $C_2=90°$ shows opposite distributions to the counterpart cases. Namely, at 50% and 90% of the cavity's axial distance the distributions depict positive values reaching approximately 10% while at 10% of the cavity's axial distance the radial velocity $V_{\rm rad}$ achieves practically 0% at -10% of the cavity's span. The latter radial velocity $V_{\rm rad}$ distribution by 0% is attributed to the blockage caused by the recirculation structure completely attached to the rotor disc wall as shown in Figure 4.4b. A thermal mixing occurs inside the up- and downstream cavity-trenches due to the leakage flow

(a) Seal clearance $H_1 = 1.18\%$ (b) Seal clearance $H_2 = 3.37\%$
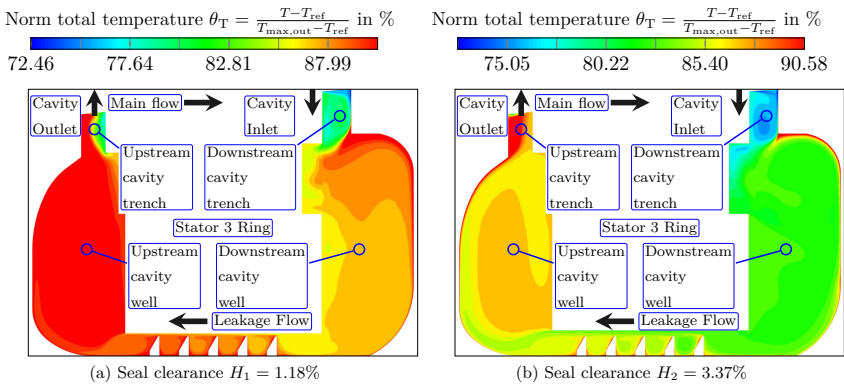
Figure 4.9: Contours of time-average total temperature for a cavity outlet angle of 90° with seal clearance $H_1 = 1.18\%$ and $H_2 = 2.37\%$

recirculation. For all configurations as the seal has the tightest clearance $H_1 = 1.18\%$ the cold main flow ingresses inside the downstream cavity-trench and the normalized total temperature θ_T rapidly increases approximately by ~7.77% because the rotor disc wall exerts work into the leakage flow as depicted in Figure 4.9a. A portion of the heated leakage flow returns to the main flow as proven by the radial velocity $V_{\rm rad}$ distributions in Figure 4.6, while the remaining leakage flow attaches to the stator ring where it slowly increases the total temperature downwards the cavity-well as shown in Figure 4.9a. Inside the downstream cavity-well, the higher total temperature is depicted on the rotor disc wall near the cavity-trench neck. As the leakage flow crosses the labyrinth seal the total pressure falls because the kinetic energy diminishes through the seal chambers while the total temperature progressively increases because the rotor drum transfers progressively energy to the leakage flow. When the leakage flow is low the total temperature covers the whole upstream cavity-well and depicts the highest values within the upstream cavity trench as shown in Figure 4.9a. Inside the upstream cavity-trench the incoming flow promotes a colder zone attached to the stator ring wall. However, the heated leakage flow dominates at the upstream cavity-trench. Inside the upstream cavity-well the rate of incoming cold leakage flow cools down only a portion of the upstream cavity-trench near the stator ring wall and thus

the recirculation distributes the higher total temperature over the entire upstream cavity-well.

When the seal clearance is opened the leakage flow increases and it allows to cool down the flow inside the cavity-wells by reducing the normalized total temperature approximately ∼5% compared with the values of the tightest clearance. The total temperature reduction is carried out by means of the recirculation structures shown in Figure 4.4. Inside the downstream cavity-trench the leakage flow reduces the total temperature up to 5.18% compared to the tightest clearance. However, inside the upstream cavity trench the higher total temperature remains despite the increase of leakage flow as shown in Figure 4.9b.

Pitchwise distributions and contours of the upstream cavity-trench for all configurations depicting normalized total temperature θ_T which are normalized with respect to inlet and outlet conditions of the axial compressor for the tightest H_1=1.18% and increased clearance H_2=2.37% are shown in Figure 4.12 and Figure 4.13, respectively. The measurement points along the corresponding cavity's axial distance and downwards the cavity's span correspond to each configuration sketched in Figure 4.8. At 0% of the cavity's span, in Figure 4.12a, the contours of total temperature θ_T for the case C_1=45° show a more uniform distribution compared to remaining cases throughout the cavity outlet. The cases C_2=90° and C_3=135° concentrate the contours of highest total temperature approx. by 90% while the case C_1=45° reaches approx. 80% near the rotor hub at 10% of the cavity's axial distance. At 50% of the cavity's axial distance, the cases C_2=90° and C_3=135° oscillate around 85% while the case C_1=45° oscillates around 80%. The peaks of all configurations exceed 85%. At 90% of the cavity's axial distance, the distributions continue decreasing by 82.5% for the cases C_2=90° and C_3=135° while for the case C_1=45° oscillates around 77%.

At -5% of the cavity's span, in Figure 4.12b, the distributions of all configurations practically coincide at 10% and 90% of the cavity's axial distance oscillating around 97% and 80%, respectively. While at 50% of the cavity's axial distance the distributions show a difference $\Delta\theta_T$ approx. by 5% between each configuration. The case C_1=45° reaches the highest value by approx. 95%, followed successively by the cases C_2=90° and C_3=135°. At -10% of the cavity's span the distributions of total temperature of the cases C_2=90° and C_3=135° practically coincide each other in all cavity's axial distances of 10%, 50%, and 90% by 97%, 87% and 81%, respectively. The case C_1=45° surpasses the other cases by 94% and 90% at 50% and 90% of the cavity's axial distance, respectively.

The contours of total temperature at cavity's span of -5% and -10%, in Figure 4.12b and 4.12c, respectively, depict similar dissemination of total temperature, namely the highest rates of total temperature locate near the rotor disc wall and progressively the leakage flow cools down in the direction of the stator ring side, there is a deviation of $\Delta\theta_T$ from 0% to 100% of the cavity's axial distance by approx. 20%. At cavity's span of -5% and -10% the distributions of all configurations for the tightest clearance H_1=1.18% along the span's cavity-trench at 90% of the axial distance show values of total temperature Θ_T which oscillate below 85% except for the case C_1=45° that reaches an average by 90%. These values are the lowest compared to other two cavity axial locations. These distributions confirm that the coming main flow comes into the upstream cavity near the stator ring wall with a colder temperature with respect to the highest total temperature inside the cavity. At 50% of the cavity-trench the distributions of all configurations increase approximately between 85% and 95%. These distributions show that in the middle's cavity trench the energy transferred from the rotor disc to the leakage flow rises the total temperature. At 10% of the cavity's axial distance the highest rates of total temperature
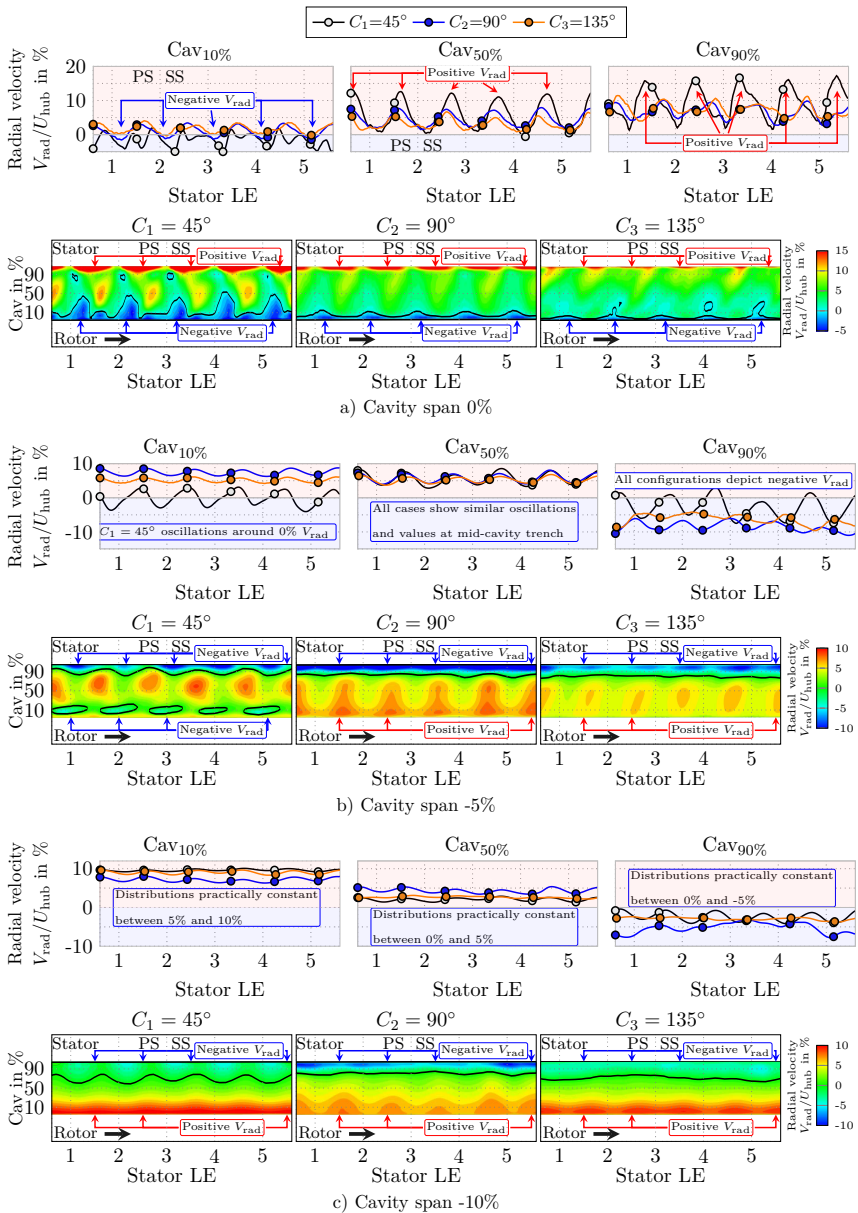
Figure 4.10: Time-average pitchwise distributions and contours of radial velocity V_{rad} at 0% (a), -5% (b) and -10% (c) cavity's span inside the upstream cavity-trench with the clearance $H_1 = 1.18\%$
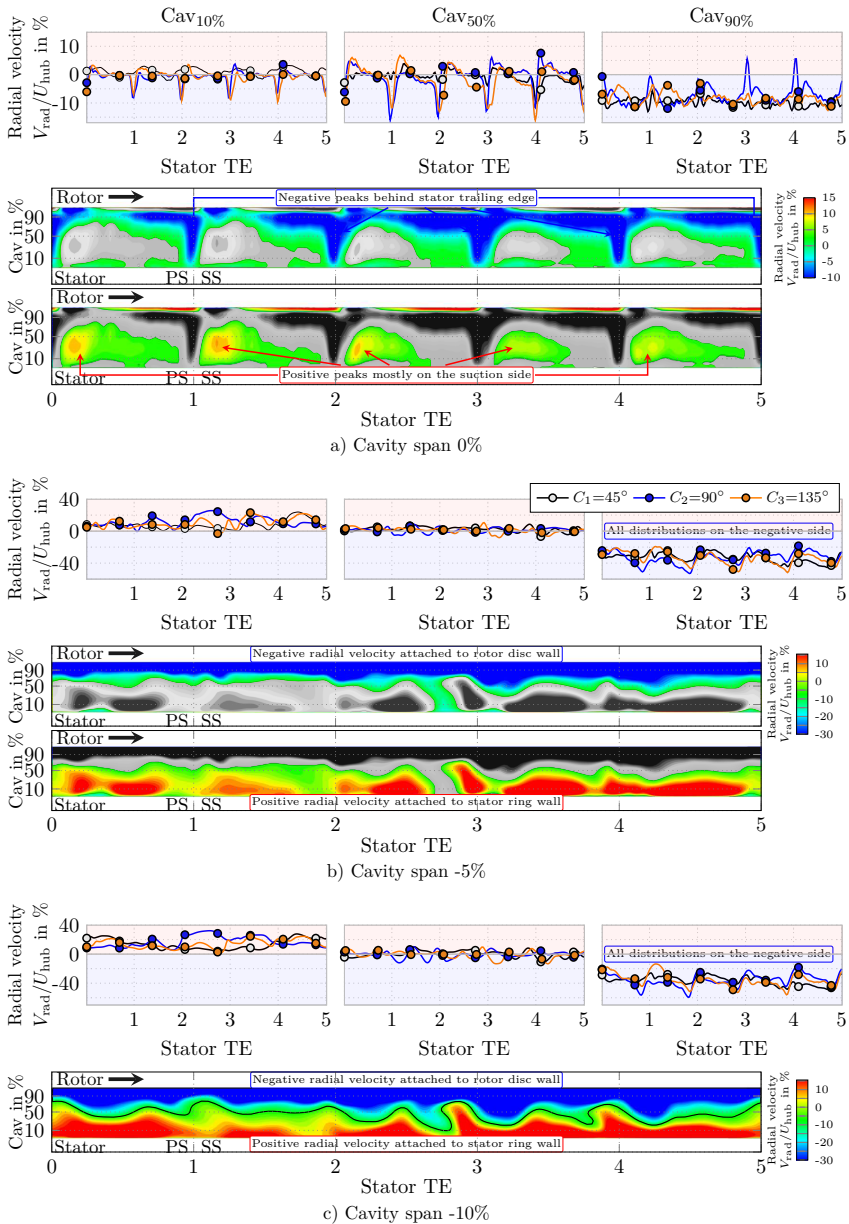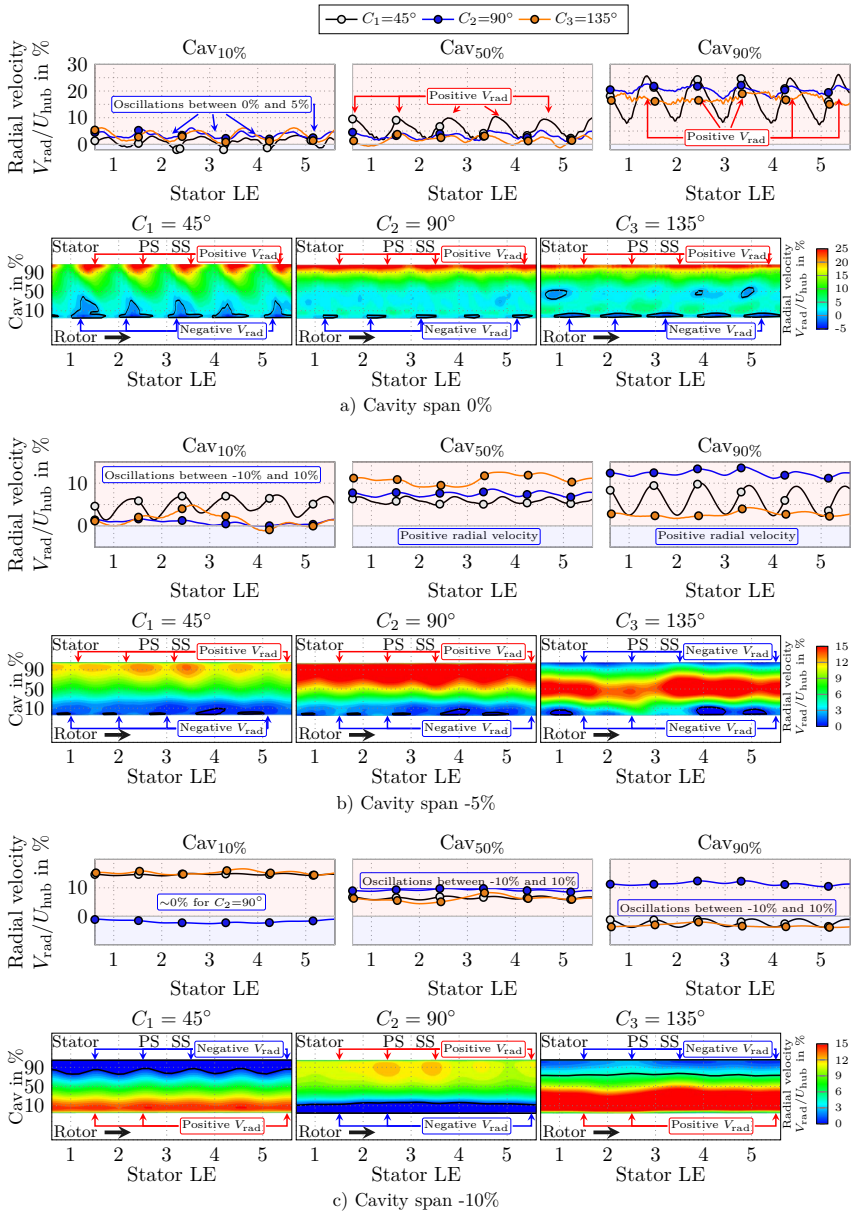
Figure 4.11: Time-average pitchwise distributions and contours of radial velocity V_{rad} at 0% (up), -5% (middle) and -10% (down) cavity's span inside the upstream cavity-trench with the clearance $H_2 = 2.37\%$

reach values by 100% and peaks exceeding such value. These distributions show that leakage flow is emanated from the upstream cavity trench with total temperature approx. ∼18% higher with respect to the total temperature at the cavity-trench inlet.

For the increased clearance H_2=2.37%, in Figure 4.13a, the distributions of normalized total temperature Θ_T at 0% of the cavity's span show smaller values compared to those for the tightest clearance due to the increase of leakage flow. The contours show that the regions of higher total temperature concentrate near the stator and rotor hub for the cases C_2=90° and C_3=135° while for the case C_1=45° the higher total temperature appears at 50% of the cavity's axial distance and the total temperature is distributed uniformly throughout all the cavity outlet as shown in Figure 4.13a. At -5% of the cavity's span, in Figure 4.13b, all distributions show similar values of θ_T by approx. 83% at 90% of the cavity's axial distance. At mid-trench, namely 50% of the cavity's axial distance, the total temperature distributions of all cases oscillate around 85% except the configuration C_2=90° which distribution locates above 87.5%. Deeper at -10% of the cavity's span, in Figure 4.13c, the distribution of the case C_2=90° at 10% of the cavity's axial distance reaches approx. 93% while the other configurations do not surpass 90%. In this axial position, the case C_1=90° depicts higher values $\Delta\theta_T$ by 3% than the other cases. This corresponds to distributions of radial velocity V_{rad} whose value was near 0% and the recirculation structure located in this region (see Figure 4.4b) provokes blockage that in turn increases the temperature. The case C_2=90° at 50% of the cavity's axial distance remains above the other cases in total temperature, keeping the difference of $\Delta\theta_T$ by 3%. At 90% of the cavity's axial distance the distributions of all configurations coincide each other at approx. 83% (Figure 4.13b and c).

For tighter clearances, the increase of total temperature is more critical than for widening clearances due to the reduction of leakage flow. As the clearance increases the labyrinth seal-fins weaken its sealing capacity. Therefore, the rate of leakage flow increases transporting more colder flow from the main flow inside the downstream cavity-well. This cold leakage flow mixes inside the up- and downstream cavity-wells and consequently it reduces the temperature in both cavity-wells. Despite the leakage flow increases and cools down both up- and downstream cavity wells the total temperature inside the cavity-trench near the rotor disc wall remains high and the emanated leakage flow is injected with higher total temperature into he main flow. Inside the downstream cavity-trench the flow enters completely attached to the upstream rotor disc wall which energizes the near incoming flow. Simultaneously on the opposite side leakage flow is emanated to the main flow. This balance of emanating and incoming flow provokes a recirculation structure inside the cavity trench which is insensitive to the increase of the incoming leakage flow. The increase of leakage flow only moves the foci of such structure in the direction of the stator ring wall.

4.4   Sensitivity of leakage flow to cavity outlet angle

Figure 4.14 sketches the configurations of the cavity outlet C_1=45°, C_2=90°, C_3=135°, and the downstream cavity inlet, which is coincident for three configurations. Three variants are designed to not alter the original blading axial position. The sketch clearly shows the configuration C_1=45° pointing out in the direction of the main flow path followed by the case C_2=90° that discharges the leakage flow perpendicular to the mainstream and finally the shape C_3=135° pointing out against the main flow. In addition the sketch shows the vector decomposition of
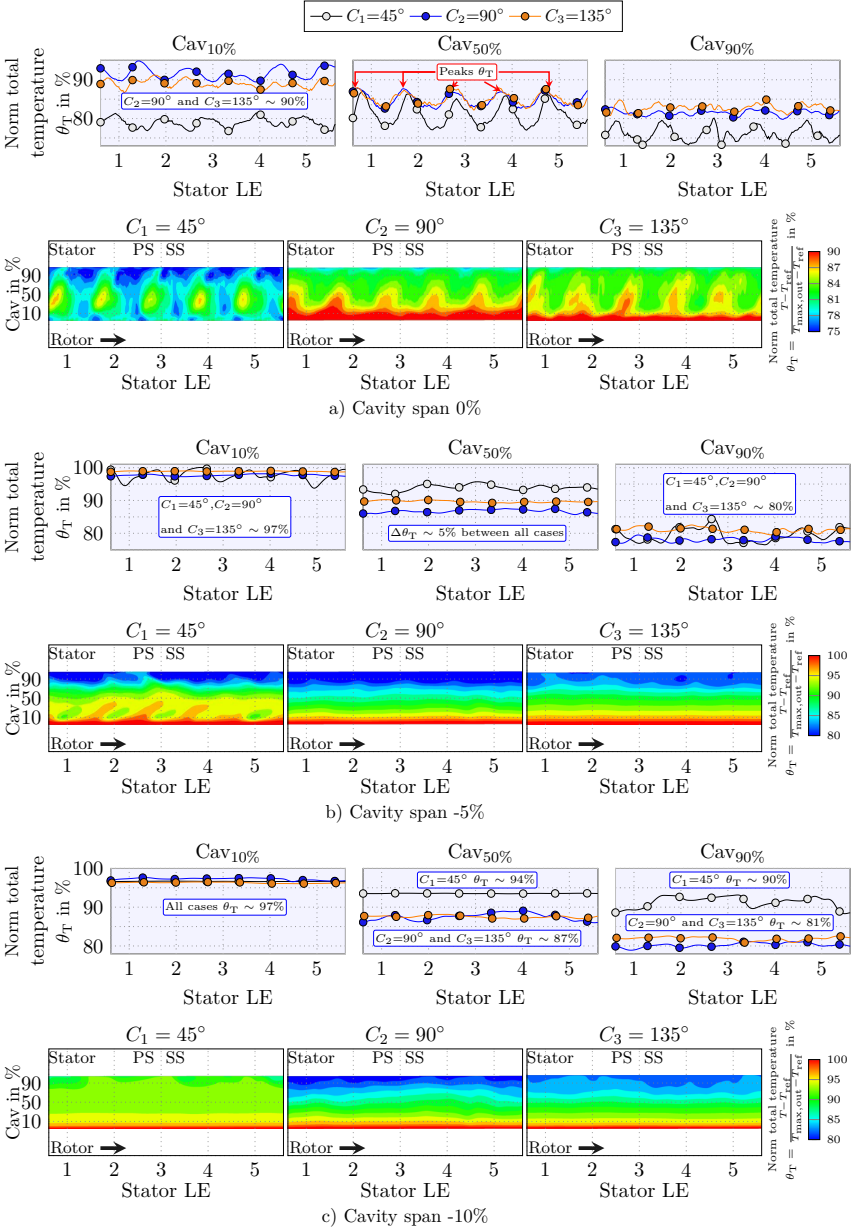
Figure 4.12: Time-average pitchwise distributions and contours of normalized total temperature $\theta_T = \frac{T - T_{ref}}{T_{max,out} - T_{ref}}$ at 0% (a), -5% (b) and -10% (c) cavity's span inside the upstream cavity-trench with the clearance $H_1 = 1.18\%$
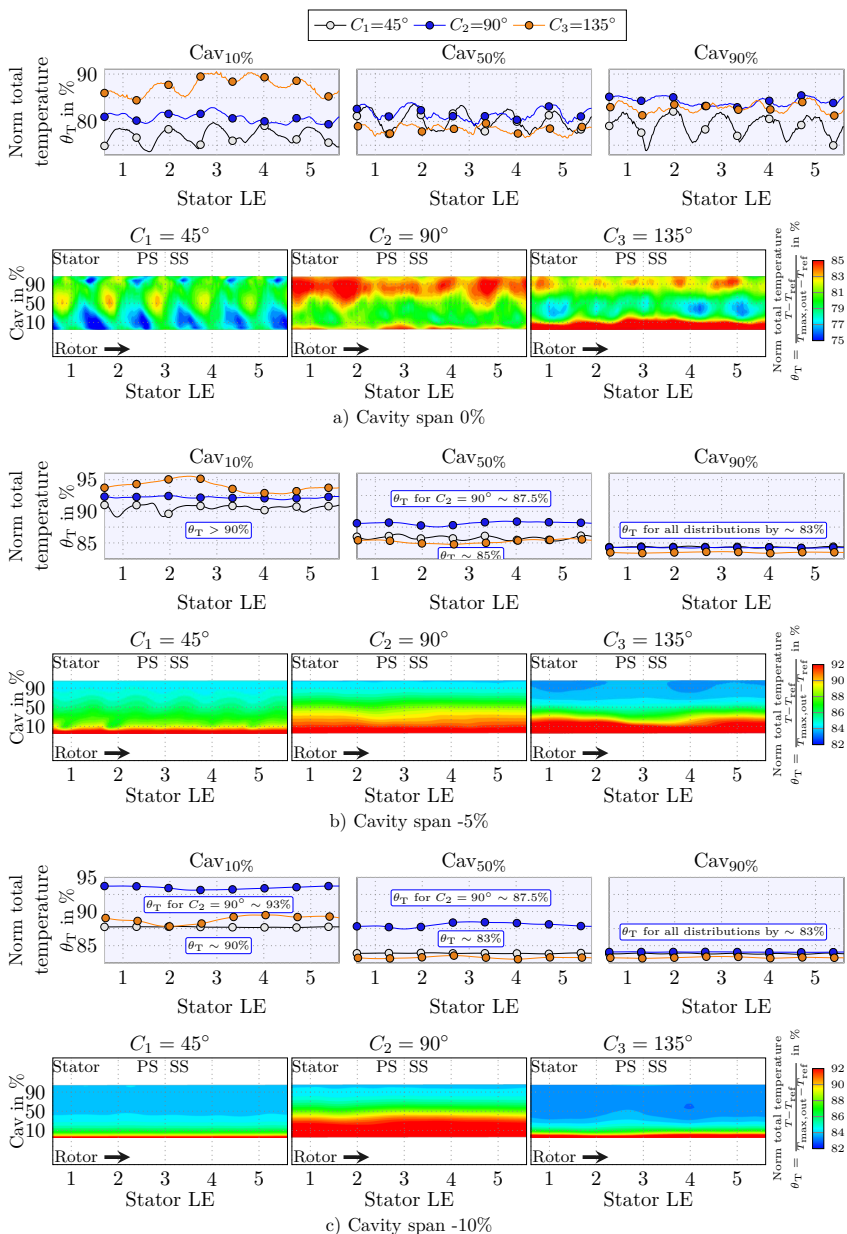
Figure 4.13: Time-average pitchwise distributions and contours of normalized total temperature $\theta_T = \frac{T - T_{ref}}{T_{max,out} - T_{ref}}$ at 0% (a), -5% (b) and -10% (c) cavity's span inside the upstream cavity-trench with the clearance $H_2 = 2.37\%$

the leakage flow into three velocity components which correspond to the X-axis parallel to main flow, r-axis perpendicular to main flow, and the θ-axis perpendicular to the reader's view. It is expected that case $C_1=45°$ offers less deceleration of the mean flow due to the cavity flow to be injected into the main flow. The deceleration of the mean flow due to the cavity flow intensifies according to the cavity angle increase, namely the configuration $C_3=135°$ will show the highest deceleration because of its shape.
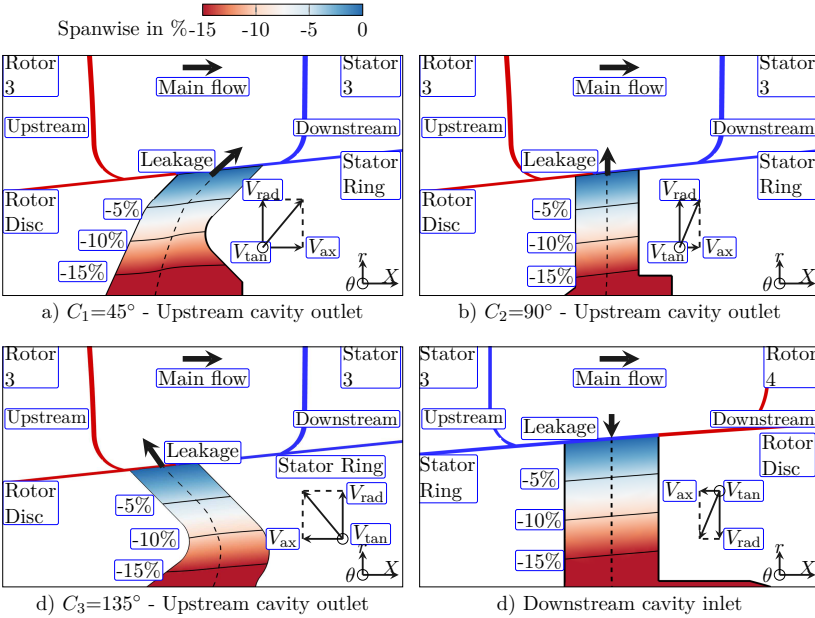
Figure 4.14: Sketch of the three upstream cavity outlet configurations and the downstream cavity inlet which has the same geometry for all configurations

4.4.1   Velocity variations at upstream cavity trench

Figure 4.15 shows the time-pitch-averaged radial distributions of the velocity components inside the upstream cavities and the corresponding thermodynamic properties at the mid-trench. Experimental data of axial V_{ax} and tangential velocity V_{tan} of Wellborn (2001) are included to compare the trends of the current investigation. Upstream cavity depth is normalized being 0% spanwise at the border of the hub wall. Numerical radial profiles are obtained at the mid-trench as it shows the dashed line in Figure 4.14.

Figure 4.15a depicts the three velocity components for all cavity outlet configurations. At the top, the illustrations correspond to tightest clearance $H_1=1.18\%$ while at the bottom correspond to an increased clearance $H_2=2.37\%$. For the tightest clearance, all profiles of axial velocity V_{ax}
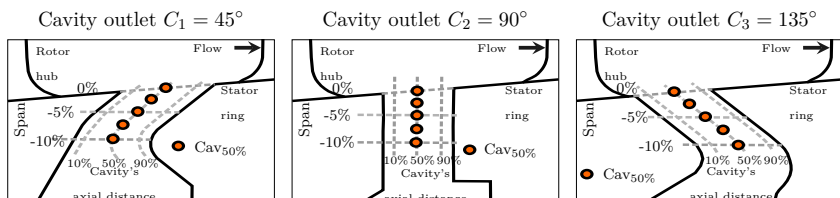
(a) Sketch of the measurement line into the upstream cavity at the mid-trench for all three configurations $C_1 = 45°$, $C_2 = 90°$, and $C_3 = 135°$.
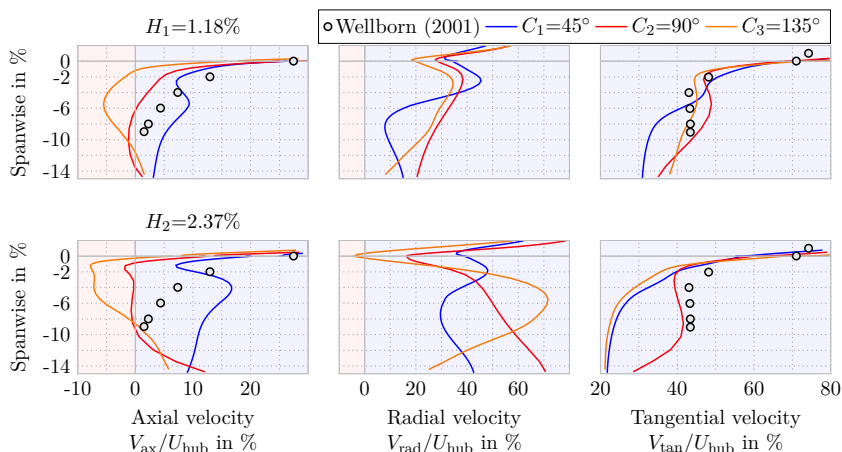
(b) Variation of velocities due to clearance increase
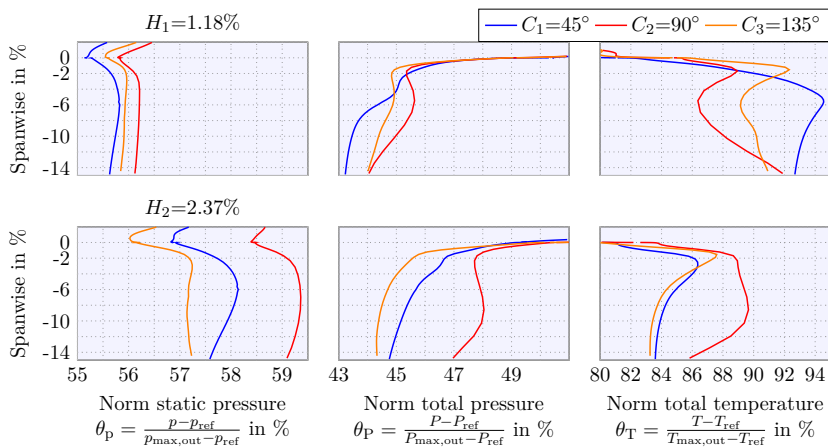
(c) Variation of thermodynamic properties due to clearance increase

Figure 4.15: Comparison of time-averaged spanwise distributions inside upstream cavity-trench with three distinct cavity outlets

scarcely vary between 1∼3% V_{ax} at -15% spanwise. The profile of axial velocity V_{ax} of the case C_1=45° depicts positive values from the cavity-trench depth up to the hub surface at 0% spanwise while the case C_3=135° shows the opposite values except above -1% spanwise the axial velocity V_{ax} increases to reach the value at the hub. The case C_2=90° follows the trend of Wellborn's data. As the leakage flow increases (H_2=2.37%), axial velocity V_{ax} profiles do not alter the order with respect to those depicted with the tightest clearance, namely positive, zero, and negative V_{ax} correspond to C_1=45°, C_2=90°, and C_3=135°, respectively. None of the configurations follow the trend of Wellborn's data. At -15% spanwise the case C_2=90° decelerates V_{ax} to reach a value of 0% at -10% spanwise. Above this span the profile keeps 0% up to -3% spanwise. Remaining configurations increase their magnitude in the corresponding direction. Inside the cavity-trench at -5% spanwise, the cases C_1=45° and C_3=135° increment 6% V_{ax} and diminish 2% V_{ax}, respectively with respect to profiles with the tightest clearance. For both clearances, the cavity outlet angle modifies the profiles of axial velocity V_{ax} along the cavity-trench depth.

For the tightest clearance, all configurations show profiles of radial velocity V_{rad} between 10% to 20% at -14% spanwise. All configurations increase gradually the radial velocity V_{rad} up to -4% spanwise. At this cavity spanwise all configurations bend and decrease the radial velocity V_{rad} up to 0% spanwise. In this range the case C_3=135°, which has the cavity outlet pointing against the main flow direction, achieves the lowest radial velocity V_{rad} compared to the remaining configurations, and it is followed for the cases C_2=90° and C_1=45°. When the seal clearance increases, the profiles of radial velocity V_{rad} depict increments and variations more pronounced below -2% spanwise with respect to those profiles with narrow clearance. All cases decelerate rapidly from -2% to 0% spanwise following the same order to that for tightest clearance. The effect of the cavity outlet angle with both clearances is most noticeable in the range from -4% to 0% spanwise. The increase of the cavity outlet angle decelerate the profile of radial velocity for both clearances.

For tightest clearance, all configurations follow the trend of tangential velocity V_{tan} of Wellborn's data (43% tangential velocity). The values oscillate near experimental data inside the cavity-trench. From -14% spanwise all profiles of tangential velocity V_{tan} accelerate progressively to reach higher tangential velocity in the main channel. The configuration C_1=45° depicts the maximum tangential velocity V_{tan} inside the cavity-trench at -2% spanwise. When clearance increases, the case C_2=90° is the only profile that approaches the trend of Wellborn's data and keeps 40% V_{tan} up to -2% spanwise where it bends to equalize the rate of remaining configurations. Other remaining cases depict lower values along the cavity spanwise. At -15% spanwise, the cases C_1=45° and C_3=135° depict the lowest tangential velocity V_{tan} by 22%. Both profiles accelerate very close to each other, asymptotically up to reach 60% V_{tan} at 0% spanwise and continue increasing inside the main flow. The cavity outlet angle has little influence in the profiles of tangential velocity V_{tan} for the clearance H_1=1.18%. However, the cavity outlet inclination reduces the rates of tangential velocity V_{tan} when clearance increases H_2=2.37%.

The effect of the cavity angle is superiorly evident in the velocity profiles of the three velocity components between 0 to -2% spanwise. In this spanwise range the case C_1=45°, which points in the flow direction shows the highest velocities because the leakage flow has less resistance to be injected inside the main flow. As the cavity angle is parallel (C_2=90°) and opposite (C_3=135°) to the main flow the velocities progressively slow down with the cavity angle variation. Inside the cavity-trench the profiles of axial and tangential velocity suggest that they have a strong relationship with each other. By looking at the graphics of axial and tangential velocity with

increased clearance H_2=2.37%, the case C_2=90° shows zero axial velocity that consequently allows to keep the 40% tangential velocity. The other cases have positive (C_3=45°) or negative (C_3=135°) axial velocity that reduces the tangential velocity. The dependency of radial velocity profiles has less influence on other components. Tangential velocity is the dominant component that provides circumferential movement to the leakage flow while radial component dictates how fast or slow the leakage flow abandons the cavity-trench to be discharged in the main flow.

4.4.2   Thermodynamic variations at upstream cavity trench

Figure 4.15b shows time-pitch-averaged profiles of normalized static pressure θ_p, normalized total pressure θ_P, and normalized total temperature θ_T inside the cavity-trench at mid-trench, all of them normalized to inlet and outlet conditions. Small variations are shown in terms of static pressure and total pressure inside the cavity-trench for the tightest clearance H_1=1.18%. Profiles of static pressure of all configurations cover from 55% to 56.5%. They depict the same trend and they are almost uniform along the entire cavity-trench. The cavity outlet angle does not modify the shape of the pressure profiles and it only modifies the magnitude. Total pressure and static pressure profiles of all configurations vary less than 1% each other. Total pressure profiles preserve similar shape to those depicted for tangential velocity which suggests that tangential velocity V_{tan} drives total pressure inside the upstream cavity-trench. All configurations show an increase of total temperature from 4% to 12% with respect to the total temperature at the hub inside the cavity-trench. This increase of total temperature relates to the tangential velocity V_{tan} that oscillates between 30% to 50%. The behavior of total temperature profiles depends strongly on the radial and tangential velocity components. In cavity-trench depth at -15% spanwise the total temperature profiles vary less than 2% of each other. Configuration C_1=45° shows the highest total temperature by 94% below -2% spanwise because the leakage flow moves radially slower and the tangential velocity V_{tan} warms sufficiently the leakage flow. Near the surface (0 to -2% spanwise) the case C_3=135° depicts the highest total temperature by 92% because the cavity outlet angle restrains radial velocity V_{rad} by 20% and slows down the ejection of the leakage flow, thus the windage effect is more pronounced.

As the clearance increases, H_2=2.37%, the magnitude of static pressure and total pressure profiles increase with respect to those profiles with clearance H_1=1.18% inside the cavity-trench because the leakage flow transports more flow with higher static and total pressure. Total pressure and pressure profiles vary 4% and 2.5% each other, respectively. The profiles remain almost uniform along the entire cavity-trench. For both clearances, the cavity outlet angle of the configurations C_1=45° and C_3=135° reduce static and total pressure inside the cavity trench compared to the case C_2=90°. The cavity outlet angle does not modify the shape of the static pressure and total pressure profiles and it only modifies the magnitude in comparison to the clearance H_1=1.18%. Total pressure profiles continue being mostly driven by tangential velocity V_{tan} inside the cavity-trench. As expected the total temperature values inside the cavity-trench diminish with respect to those with the tightest clearance because the leakage flow rate increases and the cavity outlet angle modifies the profiles of tangential velocity V_{tan}. Below -4% spanwise the configurations C_1=45° and C_3=135° show reductions by 2∼6% of total temperature compared to the remaining case because these profiles have also reductions of tangential velocity V_{tan}. Both cases depict very near values of total temperature despite that both configurations have distinct radial velocity V_{rad}. The remaining case C_2=90° has the highest tangential velocity V_{rad} resulting in a total temperature increase up to 5% inside the cavity-trench. Between 0 to -2% spanwise the effects of the radial velocity V_{rad} take more importance and dominance over

other velocities. In this span range the case C_3=135° increases the total temperature because it has the most severe restrain in radial velocity V_{rad}. These observations show that windage effect is strongly dependent of the tangential V_{tan} and radial V_{rad} components. The former provides the energy to the leakage flow and the latter determines the rate in which the leakage flow is heated.

4.4.3   Variations at downstream cavity trench

The analysis of the cavity flow involves not only the upstream cavity-trench, but also the downstream cavity-trench in order to show how the main features of the leakage flow when is sucked inside the cavity-trench and to elucidate which features are important to the stage performance deterioration. Velocity components and thermodynamic properties of the downstream cavity-trench are shown in Figure 4.16. The radial distributions are time-pitch-averaged at the mid-trench. Downstream cavity depth is normalized being 0% spanwise on the border of the hub wall and numerical radial profiles are obtained at the mid-trench as it shows the dashed line in Figure 4.14d. Experimental data of Wellborn (2001) is included to compare the trends of the current investigation.

Downstream axial velocity V_{ax} profiles decelerate from 30% at the hub to 0% at -15% spanwise. All configurations depict barely any variations with each other. At the cavity-trench depth all configurations trend to the zero axial velocity V_{ax}. All profiles follow the trend of Wellborn's data and the axial velocity approaches to zero downwards the cavity-trench. As clearance increases, the descending slope of the axial velocity profiles is more pronounced, but they are practically insensitive to clearance increase. Negative radial velocities are expected due to the existing leakage flow suction in downstream cavity-trench. For tight clearance H_1=1.18%, at the surface (i.e. 0% spanwise), values fall between 20~40% V_{rad}. Inside the cavity at -1% spanwise, the profiles slightly accelerate and immediately bend to decelerate progressively in the remaining cavity-trench depth. At -6% spanwise, the profiles reach zero radial velocity V_{rad} and continue with the pronounced slope to reach a negative radial velocity V_{rad} which indicates that leakage flow directs inside the cavity-well. As the clearance increases H_2=2.37%, the profiles immediately depict negative radial velocity V_{rad} at 0% spanwise. As the leakage flow comes inside the cavity-trench it accelerates up to 40% radial velocity V_{rad} at -3% spanwise. Below this span, leakage flow gradually decelerates to reach negative radial velocity V_{rad} for all cases except for the case C_1=45° whose profile depicts only positive radial velocity V_{rad}.

Tangential velocity profiles V_{tan} show 10% and 0% at the surface (i.e. 0% spanwise), for the clearances H_1=1.18% and H_2=2.37%, respectively. But inside the cavity-trench the profiles increase up to 45% tangential velocity V_{tan} and remain almost constant between -6 to -15% spanwise for the clearance H_1=1.18%. Although numerical data does not match with experiments the trend is similar for the clearance H_1=1.18%. The rotor disc wall provides the velocity tangential rise. As clearance increases tangential velocity V_{tan} becomes weaker inside the cavity-trench and the cases C_1=45° and C_3=135° barely reach between 0~10% V_{tan} at -1% spanwise while the values of all configurations do not exceed more than 7% V_{tan} between -4 to -15% spanwise. The case C_2=90° depicts a deceleration reaching approx. 2% at -1% spanwise and then the profile accelerates up to 5% and it remains practically uniform downwards the cavity. The diminution of tangential velocity V_{tan} is caused by the radial velocity V_{rad} dominance as the leakage flow increases.
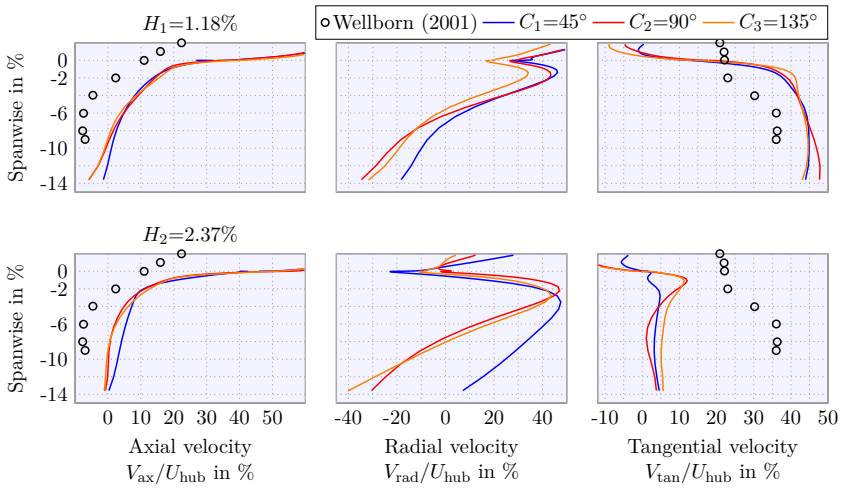
(a) Variation of velocities due to clearance increase
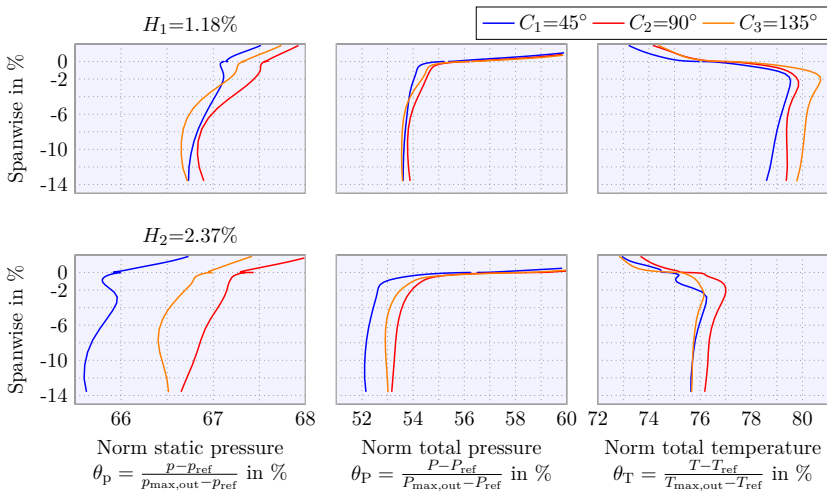
(b) Variation of thermodynamic properties due to clearance increase

Figure 4.16: Comparison of time-averaged spanwise distributions at downstream cavity trench with three distinct cavity outlets

For tightest clearance H_1=1.18% at 0% spanwise, static pressure and total pressure profiles differ as much as 1% each other; the variations become smaller downwards the cavity-trench. It is expected that both pressures diminish their values inside the cavity-trench with respect to the main channel values. The most significant variations are seen in total temperature profiles. These profiles increase approx. 3∼4% inside the cavity-trench with respect to the main flow. The total temperature augmentation originates by the 45% increase in tangential velocity V_{tan}. The main differences between the profiles inside the cavity-trench are due to the rate of radial velocity V_{rad}, namely how fast or slow the leakage flow is sucked into the cavity-trench. The case C_3=135° sucks the leakage flow slowly compared to the configuration C_1=45°, and the rotor disc wall can rise a higher total temperature. The opposite occurs with the case C_1=45°. The phenomenon is similar to that in upstream cavity-trench but the total temperature rise is minor compared to the upstream cavity outlet.

As the clearance increases, H_2=2.37%, all static and total pressure profiles slightly reduce the magnitude (e.g. less than 1%) compared to those with the tightest clearance inside the cavity-trench except the case C_1=45° that diminishes approximately by 1% in both static and total pressure. The decrease in radial V_{rad} and tangential V_{tan} velocity results in a gradual reduction by at least 3∼4% of total temperature compared to the tightest clearance inside the cavity-trench. The cases C_2=90° depicts the highest values because the leakage flow ingresses and travels slowly along the cavity-trench. Current investigation confirms that velocity components and thermodynamic profiles become more uniform and axisymmetric downwards the downstream cavity-trench. This uniformity allows to simplify the modeling of leakage flow extraction in one-dimensional models at downstream cavity interfaces as suggests Wellborn et al. (2000). The profiles of tangential velocity and total temperature show that rotor disc wall provides energy to the leakage flow and consequently the total temperature increases inside the downstream cavity-trench.

4.5   Analysis of the upstream cavity outlet interface
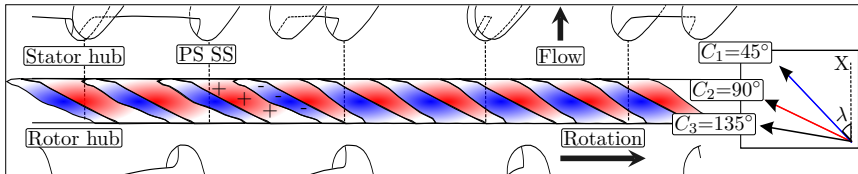
Figure 4.17: Sketch of the definition of ejection angle at the upstream cavity interface with three distinct cavity angles 45°, 90° and 135°

The analysis of the cavity interfaces allows to figure out how the leakage flow ejects from the cavity-trench and how thermodynamic properties evolve. The most interesting part of the cavity leakage flow is that all configurations are featured by outgoing and incoming leakage flow. Each spot of outgoing leakage flow is followed by a counterpart of incoming leakage flow. The spots are interleaved with each other as shown in the sketch of the Figure 4.17.

Another interesting feature is the proximity of the cavity outlet with the rotor trailing edge, namely the case C_3=135° is the nearest while the case C_2=45° is the most distant with respect

to the rotor trailing edge (see this proximity in Figure 4.14a,b,c). The proximity influences how the leakage flow will be spread over the cavity outlet surface and consequently how the leakage flow enters to the stator row. The leakage flow emanates from the cavity outlet at certain angle which is called "ejection angle" λ which is defined as the angle between the axial axis and the direction of the leakage flow ejection as shown the arrows on the right side of the Figure 4.17. As the cavity outlet is closer to the rotor (C_3=135°), the leakage flow is ejected with higher "ejection angle" $\lambda \sim 23.51°$. The remaining configurations C_2=90° and C_1=45° which are farther from the rotor depict lower ejection angle by $\lambda \sim 15.49°$ and $\lambda \sim 10.72°$, respectively.

Figure 4.18 shows the top view of three cavity outlets that are illustrated with contours of positive and negative leakage mass flow $\dot{m}_l$. In this figure the main flow path goes from bottom to top and the rotor wheels from left to right as indicates the coordinate system at the top right. Rotor hub is located at the bottom border and the stator locates at the top border of the corresponding illustration. In addition, the contours include a black line that delineates the regions with zero leakage mass flow and at the same time it depicts the frontiers of positive and negative leakage mass flow. The domain encompasses five passages (e.g. five stators) and each of them indicated in front of the stator leading edge. The aforementioned features apply for the next figures depicting contours.
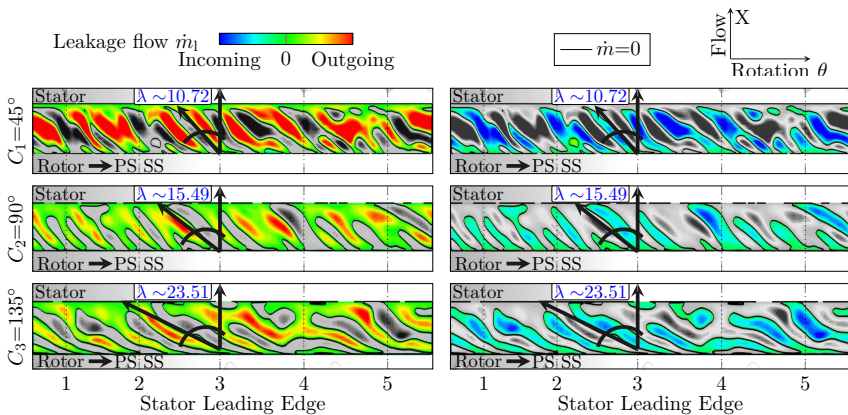
Figure 4.18: Instantaneous contours of positive and negative leakage flow $\dot{m}_l$ at the upstream cavity interface with three distinct cavity angles 45°, 90° and 135°

At first glance it is evident that the case C_1=45° shows contours with highest rate of incoming and outgoing leakage flow compared to remaining configurations. All configurations in Figure 4.18 show that leakage flow emerges on the border of the rotor hub with a low rate and it is spread opposite to the rotation, but the discharged leakage flow concentrates mainly between 10 and 90% of the cavity's axial distance. The spread leakage flow then enters to the stator row in a distinct location of which it emerges. Contours of leakage flow for the case C_1=45° show the leakage flow emerging approximately at 3rd stator leading edge and after the spreading it enters to the stator at the mid-passage (i.e. between 2nd and 3rd stator) depicting an ejection angle *lambda* by 10.72°. The case C_2=90° depicts how the leakage flow emerges also at 3rd stator leading edge and it enters the stator near the suction-side of the 2nd stator depicting an

ejection angle *lambda* by 15.49°. The last configuration $C_3=135°$ illustrates that leakage flow emerges at 3th stator leading edge and it travels one and a half passages to enter between 2nd and 1st stator passages depicting an ejection angle *lambda* by 23.51°. This configuration depicts the largest travel of the leakage flow across the cavity outlet and therefore the greatest ejection angle. The comparison shows evidently that the cavity outlet angle infers the spreading angle or the ejection angle λ of the leakage flow. As the cavity outlet angle increases, the ejection angle λ proportionally rises. The ejection angle λ dictates the direction of the leakage flow impingement on the nearest stator suction-side or on the successive stator suction-side.

Figure 4.20 shows contours and pitchwise distributions of axial velocity V_{ax} and radial velocity V_{rad} taken from time-average flow solutions. In terms of the axial velocity, at 10% of the cavity's axial distance, the distributions of all configurations mostly depict negative axial velocity except the case $C_1=45°$ that shows positive axial velocity V_{ax} by 12% exactly in front of the stator leading edge. The other cases depict distributions closer each other with almost identical oscillations between 0 and -25% V_{ax}, the maximal peaks by 0% V_{ax} locate near the stator leading edge and the minimal peaks by -25% V_{ax} locate near the mid-pitch in all passages. At 50% of the cavity's axial distance, the case $C_2=90°$ oscillates between 15 and 25% V_{ax} and the case $C_3=135°$ oscillates between 10 and 15% V_{ax} while the remaining case oscillates between 10 and 49% V_{ax}. The maximal peaks by 49% V_{ax} of the latter case are located exactly at the mid-pitch in all passages. At 90% of the cavity's axial distance, the cases $C_2=90°$ and $C_3=135°$ oscillate between 25 and 50% V_{ax} with peaks slightly above 50% V_{ax} near the mid-pith in all passages, while the case $C_1=45°$ oscillates between 25 and 110% with maximal peaks exceeding up to 100% V_{ax}. At 90% of the cavity's axial distance, the minimal peaks by 25% V_{ax} of all configurations are located exactly at the stator leading edge. The case $C_1=45°$ depicts the greatest oscillations along the pitchwise distributions together with maximal peaks of axial velocity V_{ax} compared to other configurations in all cavity's axial distances.

At 10% of the cavity's axial distance, the pitchwise distributions of axial velocity indicate that the potential flow of the stator leading edge restrains the axial component of the leakage flow in front of it and forces the flow to the mid-passage where the flow has to accelerate to accomplish with continuity. A similar effect occurs on the opposite side of the cavity, namely at 10% of the cavity's axial distance, the negative peaks are located at the mid-passage. The negative values of axial velocity for all configurations at 10% of the cavity's axial distance indicate that a vortical structure forms just attached to the top corner of the rotor disc wall. This vortical structure rotates in the counterclockwise direction. A similar vortex structure forms on the upper corner of the stator ring wall as shown in the left side of Figure 4.19. Due to the positive values of axial velocity this vortex rotates in clockwise direction. The contours and peaks of axial velocity indicate that the cavity outlet angle affects the formation of both vortical structures. The cavity outlet of the case $C_2=90°$ and $C_3=135°$ are more distant with respect to the stator leading edge and they depict a more uniform pitchwise distribution of axial velocity at 50% of the cavity's axial distance while the nearest cavity outlet with $C_1=45°$ intensify the oscillations and the peaks. The distributions of axial velocity of all configurations at 10% of the cavity's axial distance suggest a small non-uniform vortical structure attached to the rotor disc wall. The peaks of the axial velocity suggest that the diameter and strength of the non-uniform vortex structure intensifies in the mid-passage regions and the diameter and intensity decrease in front of the stator leading edge. This vortical structure could appear not as a continuous vortical structure but a small vortical structures confined in front of the mid-passage as shown in the right side of Figure 4.19. At 90% of the cavity's axial distance the axial distributions suggest that the effect of the potential flow of the stator leading edge becomes stronger and achieves

to disrupt the continuous vortical structure and divide it into small vortical structures mainly rotating in front of the mid-passage.
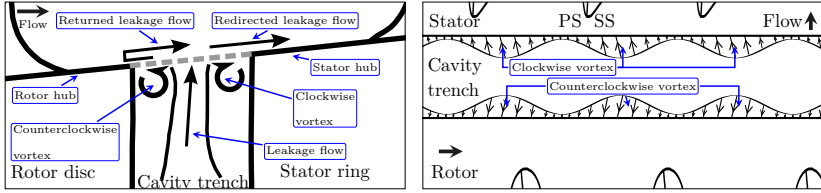
Figure 4.19: Sketch of the vortical structures into the upstream cavity trench; lateral view on the left and top view at the right

Radial velocity contours show that all configurations simultaneously have positive and negative values of V_{rad} near the stator hub and rotor hub, respectively, namely the cavity outlet ejects leakage flow and ingests flow from the main flow. The case C_1=45° shows the greatest regions compared to the other remaining cases for both positive and negative V_{rad}. The pitchwise distributions confirm that the magnitude of V_{rad} for the case C_1=45° surpasses the other cases in all cavity's axial locations except at 10%. In this axial location the distribution of the case C_1=45° appears with negative values of radial velocity V_{rad} up to -5% except the peaks of positive V_{rad} by 2% exactly at the mid-pitch of the passage. The distribution of the cases C_2=90° and C_3=135° meet practically each other with small variations along the domain. Both distributions have peaks of positive V_{rad} by 3% and valleys of negative V_{rad} between 0∼-1%. The valleys of negative velocity locate on the stator suction side between the stator leading edge and the mid-pitch.

At 50% of the cavity's axial distance, pitchwise distributions show that potential flow of the stator leading edge has a strong effect in the radial velocity distributions. In this axial distance, the peaks and valleys of all configurations coincide practically at the same circumferential location. The peaks locate just at the right of the mid-pitch in the direction of the stator pressure side between the mid-pitch and stator leading edge while the valleys locate at the right of the stator leading edge in the stator suction side. The magnitudes of the valleys practically coincide at 2.5% V_{rad} while the peaks show 12.5%, 7.5% and 5% for the cases C_1=45°, C_2=90° and C_3=135°, respectively. The distributions show that the magnitude of the peaks of radial velocity V_{rad} increases when the cavity outlet points closer to the downstream stator row, namely the case C_1=45° has 12.5% while the case C_3=135° has 5%. The potential flow of the stator leading edge contribute to accelerate the flow in the mid-passage regions together with the proximity with the stator leading edge. The acceleration occurs simultaneously at distinct mid-pitch in all passages, namely the emanated leakage flow emanates in any passage.

At 90% of the cavity's axial distance, (i.e. near the stator hub) all distributions increase their magnitude with respect to the other previous axial distances. The peaks of the case C_1=45° reach up to 16% and they remain in the mid-pitch of all passages. The peaks of the cases C_2=90° and C_3=135° coincide between the mid-pitch and the stator leading edge and they reach 10% of V_{rad}. The valleys of such cases locate exactly next to the stator leading edge on the stator suction side and reach 2.5%∼5%. The potential flow of the stator leading edge is more evident in this cavity's axial distance due to the increase of the magnitude of radial velocity of the distributions mainly at the mid-pitch and the corresponding deceleration in front of the stator leading edge. The distributions and contours of radial velocity V_{rad} show that the outgoing

leakage flow dominates over the incoming flow.

Figure 4.21 depicts contours and pitchwise distributions of tangential velocity V_{tan}, and normalized total temperature θ_{T}. The distributions of tangential velocity V_{tan} for all configurations at 10% cavity's axial distance depict the highest rates between 60∼80% over the five passages compared to remaining axial locations. At 10% of the cavity's axial distance, it is noticeable that the case C_2=90° remain almost constant around 65% and the maximal peaks of the distributions reach 81% for the cases C_1=45° and C_3=135°, and the peaks locate exactly in front of the stator leading edge. This means that the potential flow of the stator leading edge does not affect the distributions in this cavity axial location. The distribution of the case C_3=135° exceeds the other remaining cases.

At 50% of the cavity's axial distance the effect of the potential flow from the stator leading edge becomes noticeable because the peaks of the distributions move at the mid-passage. The peaks of the cases C_2=90° and C_3=135° reach near 60% V_{tan} and their valleys are around 50% V_{tan}. The proximity of the cavity outlet C_1=45° reduces the values of tangential velocity V_{tan} by 40% V_{tan} exactly in front of the stator leading edge and conversely at the mid-pitch the maximal peaks reach 81% V_{tan}.

At 90% of the cavity's axial distance the effect of the potential flow in the case C_1=45° nearest to the stator leading edge is more evident. The peaks of maximal tangential velocity V_{tan} are located in the mid-passage reaching near 80% V_{tan} while the valleys locate in front of stator leading edge reaching 5% V_{tan}. The peaks and valleys of the cases C_2=90° and C_3=135° coincide at the same circumferential location to the case C_1=45° but with lower magnitude compared to the aforementioned case, the peaks reach near 60% V_{tan} while the valleys reach approx. 45% V_{tan}.

Contours and distributions of total temperature θ_{T} for the cases C_2=90° and C_3=135° show that the maximal temperatures by approximately 92% and 90%, respectively emanate at 10% of the cavity's axial distance because the tangential velocity V_{tan} at this location is higher and almost constant than other axial locations. The rotor disc wall energizes the near leakage flow and rises the total temperature. In addition, both cases show positive radial velocity in this axial location (see Figure 4.20b, x=10%) that indicates emanated leakage flow from the cavity outlet in this axial location. In contrast, the case C_1=45° shows a lower total temperature distribution with respect to other cases approximately by 80%. This case shows similar tangential velocity in the magnitude to other cases between 60∼70% but negative radial velocity along the pitchwise distribution (see Figure 4.20b, x=10%) where the incoming flow from the main path enters into the cavity-trench with cold total temperature and then mixes with the emanated leakage flow and results in a reduced total temperature.

At 50% and 90% of the cavity's axial distance, the distributions decrease with respect to those distributions at 10% of the cavity's axial distance approximately 5% and 10%, respectively for the cases C_2=90° and C_3=135°. For the case C_1=45° the total temperature increases at 50% of the cavity's axial distance to 82% while at 90% of the cavity's axial distance the total temperature reduces to 75%. The decrease of total temperature occurs because tangential velocity decays in these cavity's axial distances and the energy transfer from the rotor disc to the leakage flow reduces. By looking the distributions of radial velocity V_{rad} and total temperatureθ_{T} seems to have a correlation between them, namely when a peak of negative radial velocity appears also a peak of lower temperature appears and vice versa. The distributions suggest that a combination
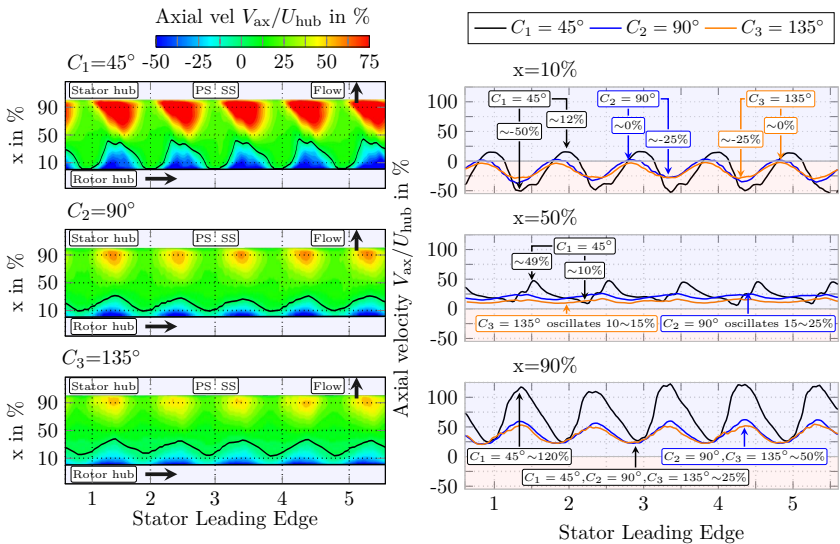
(a) Axial velocity V_{ax}/U_{hub}
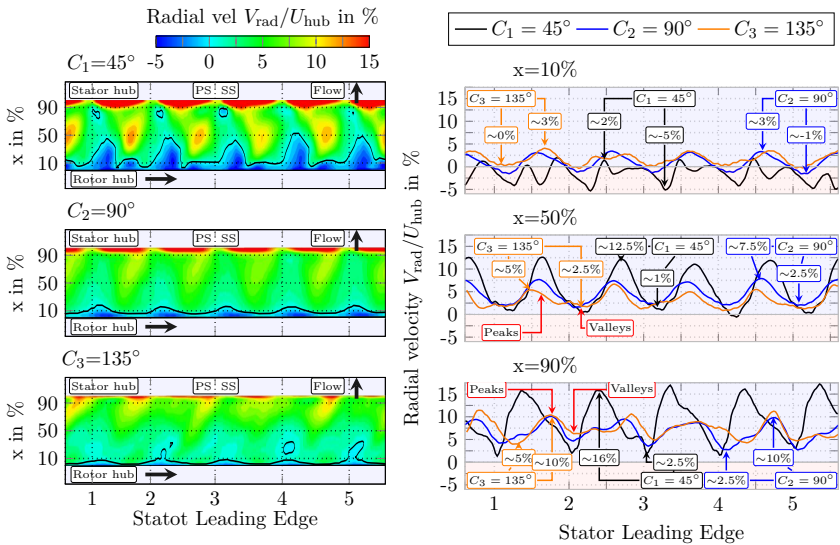
(b) Radial velocity V_{rad}/U_{hub}

Figure 4.20: Time-average contours and pitchwise distributions of axial velocity V_{ax} and radial velocity V_{rad} at the upstream cavity interface with three distinct cavity angles 45°, 90° and 135° and clerance H_1=1.18%

(a) Tangential velocity $V_{\mathrm{tan}}/U_{\mathrm{hub}}$

(b) Normalized total temperature $\theta_{\mathrm{T}} = \frac{T-T_{\mathrm{ref}}}{T_{\mathrm{max,out}}-T_{\mathrm{ref}}}$

Figure 4.21: Time-average contours and pitchwise distributions of tangential velocity V_{tan} and total temperature θ_T at the upstream cavity interface with three distinct cavity angles $45°$, $90°$ and $135°$ and clearance $H_1=1.18\%$.

of radial velocity V_{rad} and tangential velocity V_{tan} rules the total temperature distributions.

Table 4.1: Percentages of net flow $\dot{m}_{\text{net}}$, incoming flow $\dot{m}_{\text{in}}$, and outgoing flow $\dot{m}_{\text{out}}$ at upstream cavity outlet and the seal leakage flow at the first labyrinth tip $\dot{m}_{\text{seal}}$

Configuration	$\dot{m}_{\text{net}}$ in %	$\dot{m}_{\text{in}}$ in %	$\dot{m}_{\text{out}}$ in %	$\dot{m}_{\text{seal}}$ in %
$C_1{=}45°$	0.647	-0.374	1.021	0.270
$C_2{=}90°$	0.439	-0.265	0.704	0.264
$C_3{=}135°$	0.399	-0.363	0.762	0.266
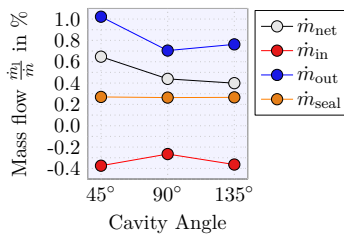
Figure 4.22: Audit of the averaged outgoing leakage $\dot{m}_{\text{out}}$, incoming $\dot{m}_{\text{in}}$ and net $\dot{m}_{\text{net}}$ flow across the upstream cavity

Figure 4.22 shows the audit of the averaged outgoing leakage $\dot{m}_{\text{out}}$, incoming $\dot{m}_{\text{in}}$ and net $\dot{m}_{\text{net}}$ flow for each cavity outlet angle and the clearance $H_1{=}1.18\%$. The case with the cavity pointing in the flow direction ($C_1{=}45°$) depicts the highest rates of leakage and incoming flow by 1% and -0.37%, respectively. Thus the net flow results to also be the dominant rate over the remaining two configurations. The angle of this cavity outlet allows less resistivity to outgoing and incoming flow. The case with a perpendicular cavity to the flow direction ($C_2{=}90°$) achieves the lowest rates of outgoing and incoming flow by 0.7% and -0.26%, respectively. However, the net flow results to be the subsequent case with higher leakage flow. The cavity pointing against the flow direction ($C_3{=}135°$) achieves the lowest net leakage flow by 0.399%. This case certainly achieves higher outgoing flow by 0.76% with respect to the case $C_2{=}90°$, but the incoming flow reaches a nearly rate to the case $C_1{=}45°$ by -0.363%. This rate compensates the outgoing leakage flow and the net leakage flow results the minor rate of all configurations. The ratio of the incoming $\dot{m}_{\text{in}}$ compared to the leakage flow in the seal $\dot{m}_{\text{seal}}$ results to be betwen 1 to 1.38. This supports the statements of Lewis (2002). The results are summarized in the Table 4.1.

4.6   Analysis of the downstream cavity inlet interface

Independently of the cavity outlet angle at the upstream cavity; inside the downstream cavity-trench exists a recirculation region as discusses the section 4.3. Due to this recirculation structure leakage flow is ejected and incoming flow ingested simultaneously. Figure 4.23 shows the top view of the three cavity inlets that are illustrated with contours of emanated leakage flow and incoming leakage flow $\dot{m}_l$. In all figures of this section the main flow path goes from bottom

to top and the rotor wheels from left to right as it indicates the coordinate system at the top right. Rotor hub locates at the top and the stator border locates at the bottom of the corresponding illustration. In addition, the contours include a black line that delineates the regions with zero leakage mass flow and at the same time it depicts the frontiers of positive and negative leakage mass flow. The domain encompasses five passages (e.g. five stators), each of them illustrated with a dashed line behind the stator trailing edge. Similar to the upstream cavity outlet interface, leakage flow contours of the downstream cavity inlet interface reveal that all configurations ingest and eject leakage mass flow simultaneously along the domain. But the contours differ to those of the cavity outlet in shape and the distributions reduce the intensity.
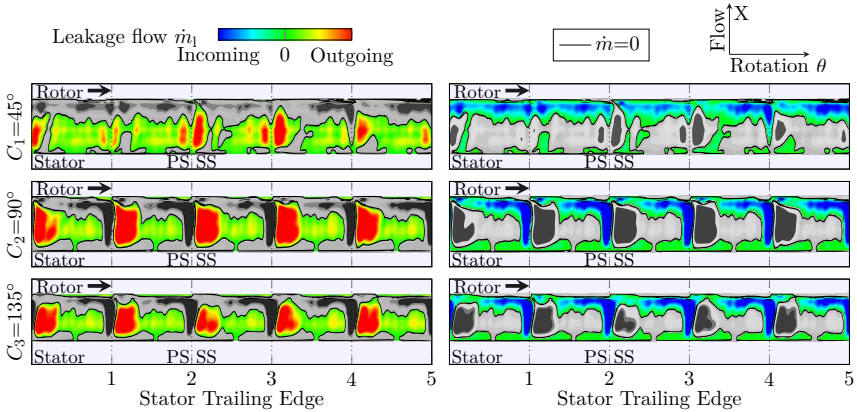
Figure 4.23: Time-average contours of positive and negative leakage flow $\dot{m}_l$ at the downstream cavity interface with three distinct cavity angles 45°, 90° and 135°

All configurations except the case $C_1=45°$ show that incoming flow from the main path enters the downstream cavity-trench behind the trailing edge of each stator and the region of the incoming flow covers the entire cavity inlet width, namely from stator hub border to rotor hub border. The region of incoming leakage flow is mostly concentrated behind the stator trailing edge and slightly on the pressure-side of each stator. Together to this incoming flow region exists the counterpart region of outgoing leakage flow located mostly concentrated on the suction-side of each stator. In addition, in the mid-passage exist spots of outgoing flow, these regions covers approximately all the pitch and are surrounded by incoming leakage flow. At the rotor hub border both regions of incoming and outgoing leakage flow spread in the direction of the rotor's whirling (i.e. at the right of the page). Due to the spreading both flows interact with the corresponding regions of the adjacent stator. Although the spreading occurs for all configurations, the case $C_3=135°$ better illustrates how the spreading is carried out.

Figure 4.24 illustrates time-average contours and distributions of axial velocity V_{ax} and radial velocity V_{rad}. Similarly to the upstream cavity trench the contours and pitchwise distributions of axial velocity V_{ax} reveal rotating vortices attached to the upper border of the stator wall ring and to the rotor disc wall. According to negative velocities at 10% of the cavity's axial distance the vortex rotates in counterclockwise direction while the analogous vortex on the opposite side rotates in the clockwise direction. These distributions are driven for the potential flow of the downstream rotor. Therefore the valleys of the distributions do not coincide with the stator

trailing edge. At the mid-trench of cavity and 90% of the cavity's axial distance the distributions depict only positive axial velocity and the oscillations depict clearly the four valleys originated by the potential flow of the four downstream rotors.

At 10% of the cavity's axial distance the leakage flow emanate and simultaneously incoming main flow enters behind the stator trailing edge on the pressure side. A portion of leakage flow emanates from the cavity behind the stator trailing edge on the suction side. In the mid-passage the variations are smaller compared to pressure side peaks. At mid-trench the incoming and emanated leakage flow increase their magnitude behind the trailing edge and the suction side, respectively. At 90% of cavity's axial trench the main flow enters into the cavity trench practically along the entire cavity except behind the stator trailing edge where appear peaks of positive radial velocity. The distributions of radial velocity indicate that they are driven for the stator's wake rather than the potential flow of the downstream rotor. The rotor disc wall is responsible of disseminate the incoming main flow downwards the cavity trench.

Figure 4.25 illustrates time-average contours and pitchwise distributions of tangential velocity V_{tan} and total temperature ratio θ_{T}. Pitchwise distributions of tangential velocity V_{tan} show the major oscillations at the mid-trench. At 90% of the cavity's axial distance, the distributions and contours show an uniform tangential velocity along the cavity inlet. Pitchwise distributions of normalized total temperature θ_{T} depict peaks of high temperature exactly in the locations where the leakage flow emanates to the main flow. These peaks are located exactly behind the stator trailing edge on the suction side. The peaks of high total temperature coincide with the peaks of positive radial velocity. This means that heated leakage flow emanates behind the stator trailing edge on the suction side. In contrast, the valleys of lower total temperature coincide with the locations of incoming main flow just behind the trailing edge. The potential flow effect of the downstream rotor seems not to affect the distributions of total temperature θ_{T} and velocity radial V_{rad}.

Similar to the analysis of the upstream cavity outlet, the mass flow across the cavity inlet is decomposed in incoming and outgoing leakage flow. Figure 4.26 shows the audit of the averaged outgoing $\dot{m}_{\text{out}}$ and incoming $\dot{m}_{\text{in}}$ leakage flow. All configurations exceed the outgoing flow by 0.3%. The case with the cavity pointing in the flow direction (C_1=45°) reaches the highest rate by 0.34%. The incoming flow is symmetrically opposite to outgoing leakage flow, but with rates exceeding -0.35% and reaching the highest rate by -0.43% (C_1=45°). As expected, the imbalance of incoming and outgoing leakage flow results in negative net leakage flow by -0.09%, -0.06% and -0.04% for C_1=45°, C_2=90°, and C_3=135°, respectively. The audit reveals that outgoing leakage flow is ejected from the downstream cavity-trench with approximately 1.5% higher total temperature with respect to the incoming flow. In this sense in the downstream cavity-trench exists the windage effect, but with a smaller magnitude compared to the upstream cavity-trench.

4.7   Flow structures induced by leakage flow

To understand the deterioration of the stage performance it is necessary to identify the flow structures near the hub and its interaction with the main flow. Figure 4.27 emphasizes the main flow structures as the upstream cavity outlet ejects the leakage flow and interacts with the main flow near the hub. Figure 4.27a shows the stator top view in which the main flow goes from
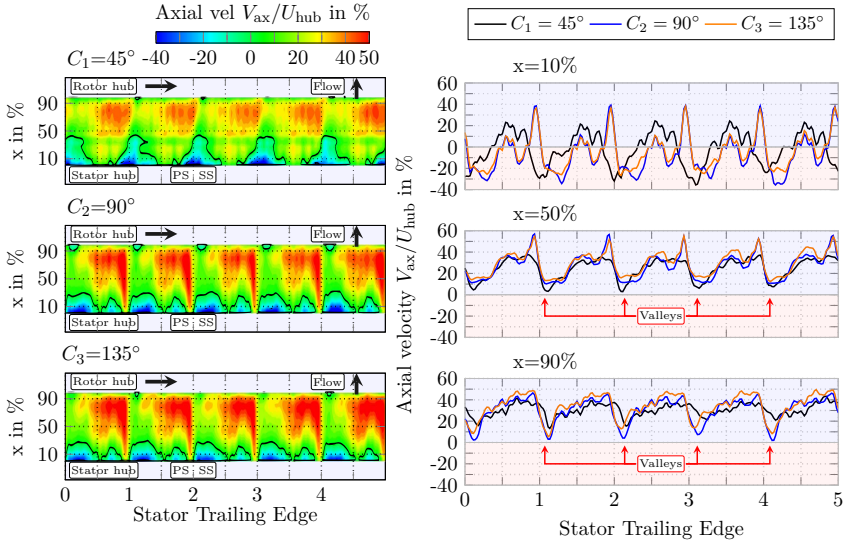
(a) Axial velocity V_{ax}/U_{hub}
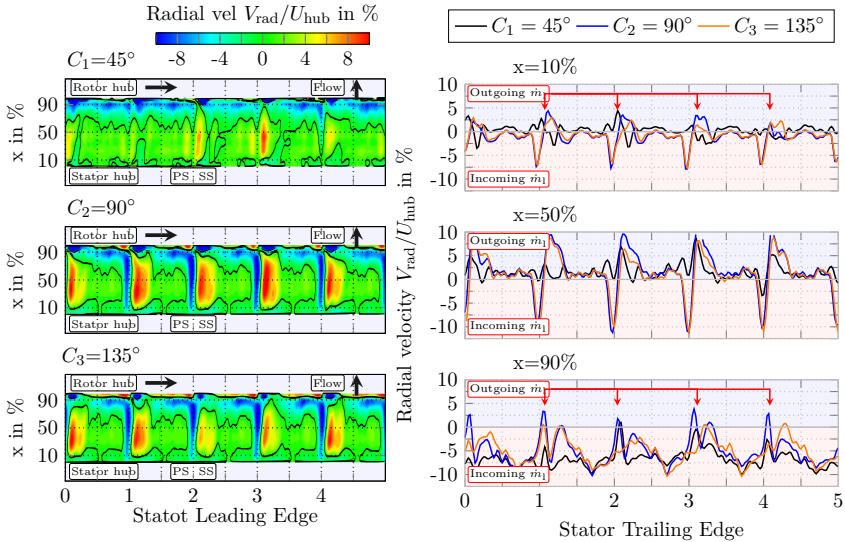
(b) Radial velocity V_{rad}/U_{hub}

Figure 4.24: Time-average contours and pitchwsise distributions of axial velocity V_{ax} and radial velocity V_{rad} at the downstream cavity interface with three distinct cavity angles 45°, 90° and 135° and clerance H_1=1.18%
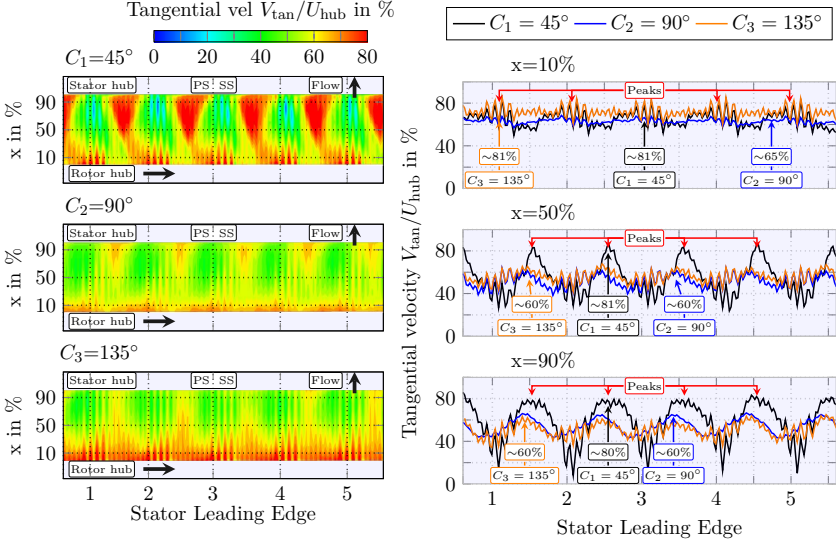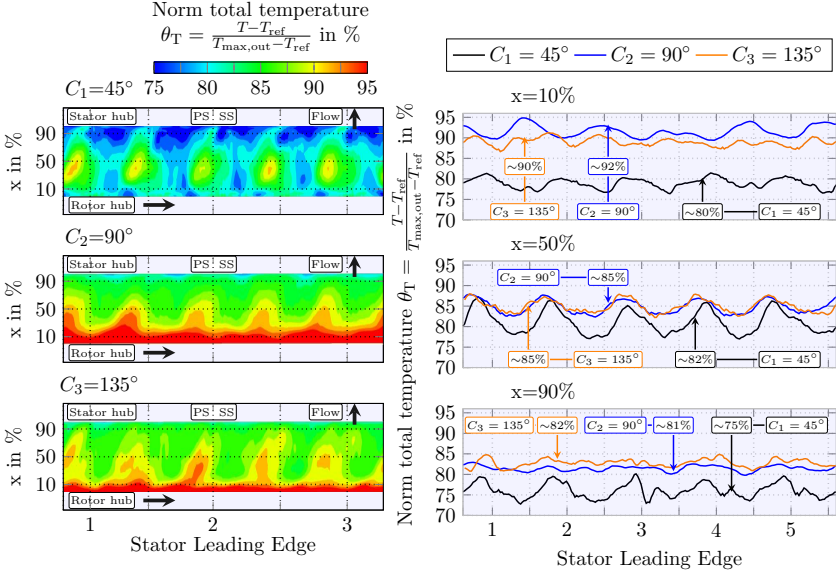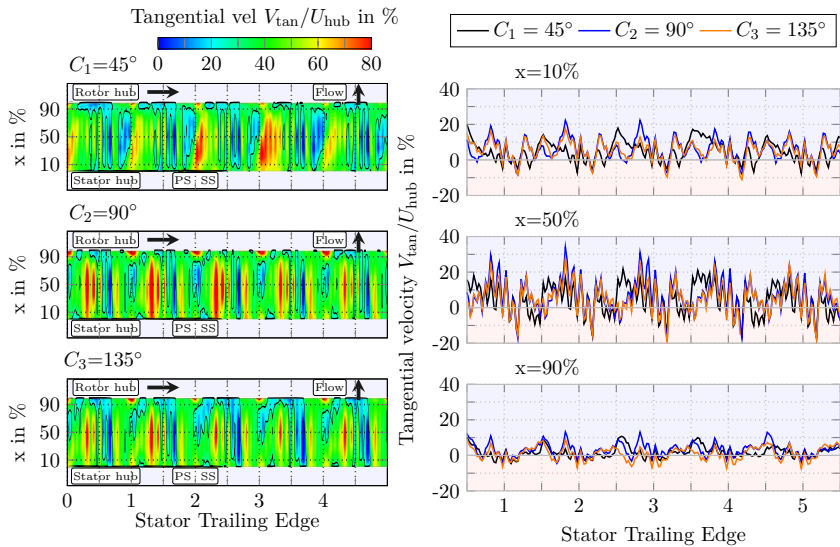
(a) Tangential velocity $V_{\text{tan}}/U_{\text{hub}}$
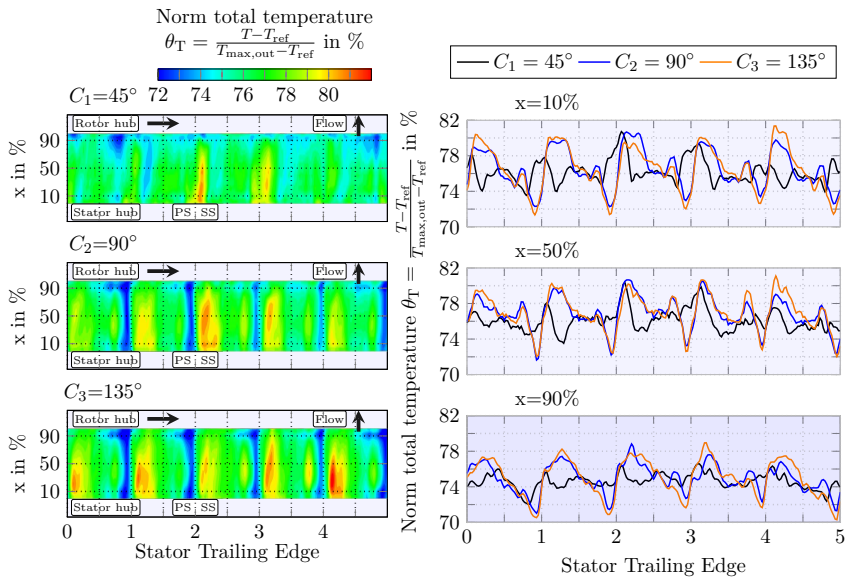
(b) Normalized total temperature $\theta_T = \frac{T-T_{\text{ref}}}{T_{\text{max,out}}-T_{\text{ref}}}$

Figure 4.25: Time-average contours and pitchwise distributions of tangential velocity V_{tan} and total temperature θ_T at the downstream cavity interface with three distinct cavity angles 45°, 90° and 135° and clearance H_1=1.18%.
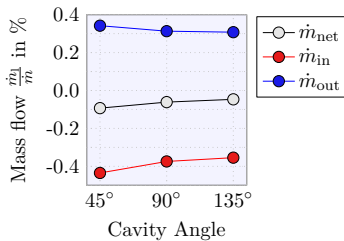
Figure 4.26: Audit of the averaged outgoing leakage $\dot{m}_{\text{out}}$, incoming $\dot{m}_{\text{in}}$ and net $\dot{m}_{\text{net}}$ flow across the downstream cavity

the bottom border to the top border. At the bottom the upstream rotor trailing edge appears. Just behind the trailing edge the rotor disc border delineates the upstream cavity outlet that is followed by the stator row that ends on the border with the downstream cavity inlet. After the cavity trench the downstream rotor leading edge is evident.

The rotor whirls from left to the right side. Upstream cavity ejects leakage flow. The origin of the ejection locates on the rotor disc hub border as shown in Figure 4.18. The rotation of the rotor disc induces a deflection of the leakage flow and consequently the leakage flow smears inclined with respect to the main flow axis over the cavity-trench spacing. The inclination of the leakage flow ejection is defined as "ejection angle". This angle depends on the proximity of the cavity outlet with the rotor blading as it explains in section 4.5. As the rotor whirls a wake is produced behind the rotor trailing edge. The rotor wake continues its natural path in downstream direction crossing the leakage flow ejected from the upstream cavity-trench. As the rotor wake enters in the stator row (e.g in the absolute system) the wake immediately deflects opposite to the rotor whirling. As the rotor wake crosses the cavity-trench it partially blocks the leakage flow on that region. The blockage of the rotor wake allows that main flow near the hub come inside the upstream cavity-trench which is called incoming flow. Additionally, the incoming flow has higher static pressure compared to the leakage flow inside the cavity outlet, therefore the existing static pressure gradient between the cavity outlet and the main flow facilitates the incoming flow going into the cavity outlet. The alternating interaction of the wake-incoming flow with cavity-outgoing flow produces the "wake-leakage vortex" clearly identified in Figure 4.27a. The wake-leakage vortex moves inclined with respect to the main flow axis along the cavity-trench.

The wake-leakage vortex moves attached to the cavity-trench surface inducing blockage around it. The main flow near the hub cannot circumvent the wake-leakage vortex blockage and consequently deviates inside the cavity-trench. A new induced alternating interaction of the incoming flow and the outgoing leakage flow produces an induced vortex located adjacent behind the wake-leakage vortex. The induced vortex blocks part of the outgoing leakage flow and additionally the hub flow incomes again into the cavity-trench. The wake-leakage vortex produces a cascade effect of induced vortices along the cavity-trench as shown in the labeled vortex structures in front of the stator leading edge located between the 2nd and 3rd passages in Figure 4.27a. Each wake-leakage vortex behind the rotor trailing edge promotes several induced vortices depending on the cavity outlet configuration and it is mainly located in the mid-passage of the upstream rotor. The strongest vortex is the wake-leakage vortex while the induced vortices decay as they
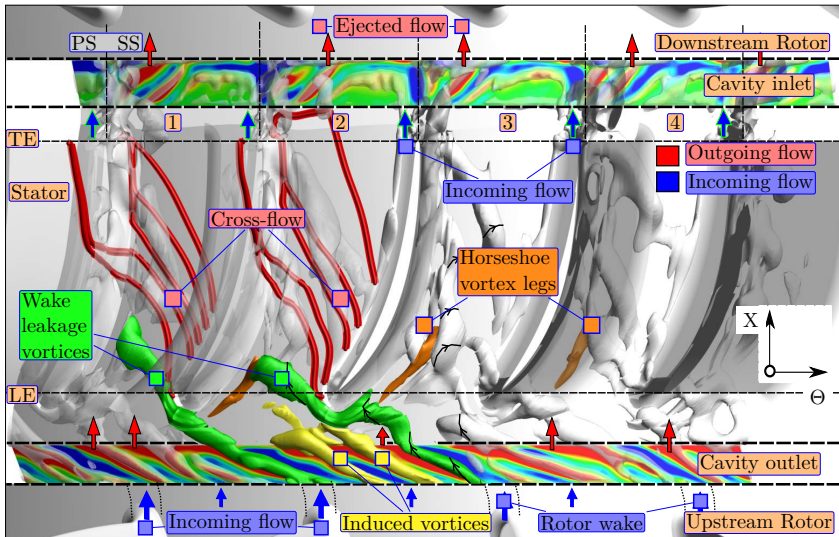
(a) Top view (Stator blading removed for visualization purposes)
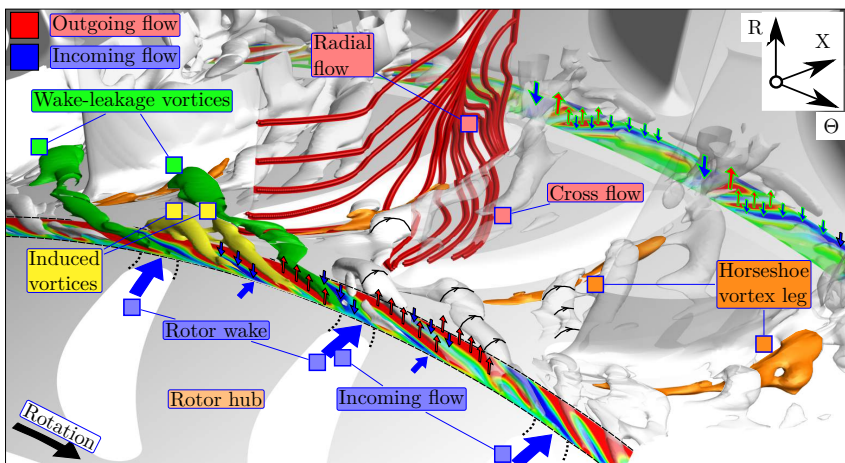
(b) Isometric view (Rotor blading removed for visualization purposes)

Figure 4.27: Flow structures induced by the interaction between main flow and cavity leakage flow

are close to the next wake-leakage vortex. Induced vortices are not enough long to disturb the wake-leakage vortex in the mid-passage, however as induced vortices coincide in front of stator leading edge the potential flow of the stator leading edge facilitates the interaction with the wake-leakage vortex. As the induced vortices and the wake-leakage vortex interact with each other they form bigger vortical structures. Both wake-leakage and induced vortices rotate in clockwise direction.

Once the wake-leakage vortex of each rotor has induced more adjacent induced vortices all of them ingress in the stator row with certain "ejection angle". This angle causes the wake-leakage vortex to impinge directly on the stator suction-side as the horseshoe vortex does not hinder its trajectory as shown the wake-leakage vortex in the 1st passage in Figure 4.27. In other flow circumstances the wake-leakage vortex meets the horseshoe vortex, as shown in the 2nd passage in Figure 4.27a and the wake-leakage vortex circumvent the horseshoe vortex and impinges in a upward radial location on the stator suction-side. As the wake-leakage vortex does not circumvent the horseshoe vortex they interact with each other and the wake-leakage vortex deflects in axial direction. The deflection avoids the impingement of the wake-leakage vortex on the stator suction-side as shown in the 3rd passage in Figure 4.27a. In certain instants, the wake-leakage vortex finds the leg of the horseshoe vortex near the stator leading edge and they interact with each other causing the leakage vortex to not contact the suction-side boundary-layer. However, the synergy of such vortices does not suppress the posterior downstream interaction with the suction-side boundary-layer.

As the wake-leakage vortices enter in the stator row they are split by the stator leading edge in distinct pieces. The piece in front of the stator leading edge reinforces the horseshoe vortex while the remaining flow structures move both axially and circumferentially inside the stator passage. The flow in the suction-side boundary-layer moves faster due to the high velocity on the surface while on the pressure side occurs the opposite. This velocity difference produces a velocity imbalance inside the stator passage. As the wake-leakage vortex impinges on the stator suction-side the momentum of the boundary-layer accelerates the wake-leakage vortices on the stator suction-side while on the stator pressure-side the corresponding boundary-layer decelerates the wake-leakage vortex on that stator side. Because of the existing velocity imbalance inside the stator passage the flow structures modify the original ejection angle as they travel inside the stator passage. In addition, as upstream cavity-trench ejects the leakage vortices (i.e. wake-leakage and induced vortices) they impinge directly to the stator suction-side disturbing the boundary-layer on such side. Inside the passage the main flow causes the axial movement of the leakage vortex structures while the passage pressure gradient moves the flow structures in the direction of the adjacent stator suction-side. Downstream the passage-pressure-gradient eventually forces the vortical structures to the stator suction-side and the deleterious interaction with the boundary-layer is unavoidable.

Not all the leakage flow is sufficiently energized to be ejected inside the wake-leakage vortices and then a portion of such leakage flow emerges directly on the border between the cavity-trench and the stator hub. This leakage flow stays trapped within the hub flow which moves mostly axially up to approximately the mid-chord of the stator where the hub flow, that contains leakage flow, deflects to the stator suction-side direction. The deflected flow is known as the cross-flow and is provoked by the passage-pressure-gradient on the stator passage. The cross-flow occurs mostly on the flow near the hub underneath the leakage vortices as shown in the top and isometric views in Figure 4.27. Eventually the cross-flow ingresses inside the suction-side boundary-layer and travels radially on the stator suction-side as shows Figure 4.27b. The passage-pressure-gradient

becomes more pronounced on the stator rear and consequently forces all flow structures to move circumferentially on the stator suction-side direction. As all flow structures converge in the well-known stator end-wall corner (i.e. at the stator rear) all of them interact with each other and they distort the pure axial flow.

Behind the stator trailing edge a stator wake is induced by the main flow and it has a fixed position. The stator wake moves axially and crosses the downstream cavity-trench. At the hub the stator wake facilitates the ingress of main flow inside the downstream cavity-trench as it shows the arrows on the pressure-side in Figure 4.27. As the incoming flow is near the rotor disc, it smears the incoming flow in the rotation direction up to interact with the adjacent stator wake. Similar to the upstream cavity-trench, the downstream cavity-trench interleaves incoming flow and outgoing flow regions along the cavity-trench surface (see Figure 4.17 for more clear visualization). Flow structures form above the outgoing leakage flow regions. As the outgoing leakage flow emerges from the downstream cavity-trench it continues moving axially.

In order to better understand the repercussion of the wake-leakage vortex on the stator performance, the evolution of the wake-leakage vortex is shown in Figure 4.28. Vortex 5 shows the interaction with the horseshoe vortex leg and the posterior impingement of the wake-leakage vortex on the stator suction-side. Vortex 4 depicts the wake-leakage vortex breaking at the stator leading edge. The vortex breaks in three pieces. The vortex tail will continue traveling inside the 1st passage. Another piece stays in front of the stator leading edge. This piece reinforces the horseshoe vortex. The remaining part continues moving both circumferentially and axially until it breaks in the next adjacent stator leading edge. Vortex 3 illustrates that in some instants the vortex length encompasses up to three passages before the wake-leakage vortex will be broken by the corresponding stator leading edges and the vortex pieces enter to the corresponding stator passages. The half of the wake-leakage vortex moves circumferentially above the upstream cavity-trench. Vortex 2 shows the resulting pieces of the wake-leakage breaking and evidences that the wake-leakage vortex effectively encompasses up to three pitches. The vortex piece in the 4th passage shows an immediate axial acceleration on the vortex structure near the stator suction-side. The vortex piece in the 3rd passage enters uniform into the stator passage except on the part near the stator suction-side where the vortex structure immediately deflects due to the axial acceleration of the boundary-layer. The vortex piece in the 2nd passage appears evidently inclined due to the axial acceleration in the suction-side boundary-layer. Vortex 1 shows the final state of the broken wake-leakage vortex. The vortex piece in the 2nd passage mixes with previous remaining vortex structures and it moves circumferentially to the stator suction-side. The vortex piece in the 3rd passage shows the more pronounced deflection due to the suction-side boundary-layer acceleration. The remaining vortex piece in the 4th passage moves axially slowly because it's far to the stator suction-side. Non colored structures in the 3rd and 4th passages show the major flow concentrations on the end-wall corner region. It is evident that the evolution of the wake-leakage vortex contributes to increase the end-wall losses.

Figure 4.29 shows a reverse view of the upstream cavity trench and the upstream rotor. The sketch shows the mechanism of incoming main flow into the upstream cavity-trench. When the rotor whirls from the right to the left, the rotor blade generates the wake along the entire rotor spanwise. At the hub the rotor wake crosses the upstream cavity trench from which emanates leakage flow. When the rotor wake enters into the stator row the wake deflects opposite to the rotor whirling. The interaction between the wake and the leakage flow induce the wake-leakage vortices as shown in Figure 4.28. The most part of the wake leakage vortex travels in the direction to the stator passage. Nevertheless a small portion of that vortical structure is
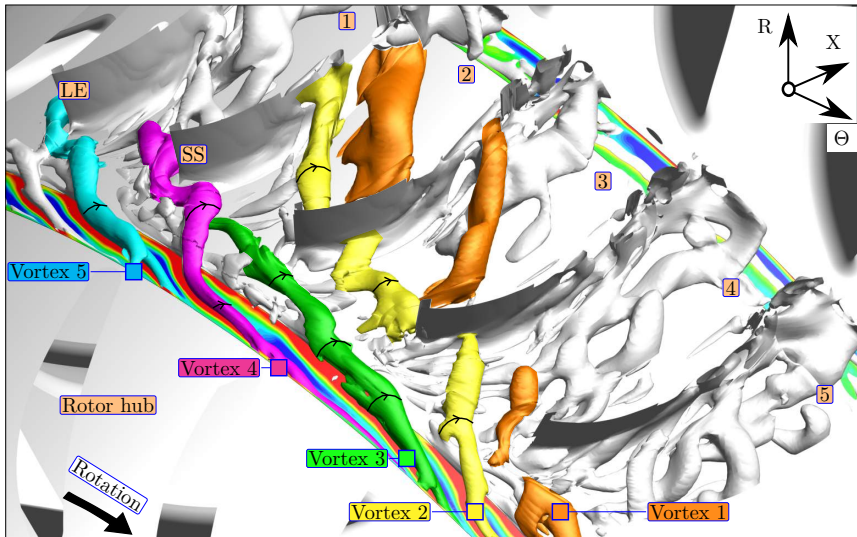
Figure 4.28: Evolution of wake-leakage vortex on the stator row with the case $C_3=135°$ and clearance $H_2=2.37\%$

not able to overcome the cavity-trench and remains trapped inside the upstream cavity-trench. When the wake-leakage vortex finds the stator ring wall it travels downwards the cavity-trench. Some portion of the induced vortices ingress in the same way as the wake-leakage vortex. Once the wake-leakage vortices and induced vortices remain inside the cavity-trench they interact with each other. Simultaneously the leakage flow continues emanating in the regions where the wake-leakage and induced vortices cannot cross. A similar effect occurs in the downstream cavity trench when the leakage flow comes into the cavity.

4.8   Effects of the cavity outlet angle on the wake-leakage vortices

As previously discussed in section 4.5 the leakage flow of each cavity outlet configuration emerges with determined angle depending on the proximity with the rotor trailing edge, such angle is called "ejection angle". Because of the distinct ejection angles between three configurations the wake-leakage vortex depicts different trajectories. Figure 4.30 illustrates the main features of the wake-leakage and induced vortices between the three cavity outlet cases. At the top it shows the case $C_1=45°$, in the middle the configuration is $C_2=90°$, and at the bottom the case is $C_3=135°$. The main flow goes from the bottom to the top in all illustrations.

As the wake-leakage vortex emerges it has positive radial velocity on the frontal face (i.e. the normal face to the main flow direction) and the opposite on the back face. This indicates that wake-leakage vortex starts to rotate faster in clockwise direction as it locates just above the upstream cavity-trench. All configurations show that vortex structures inside the 3rd passage
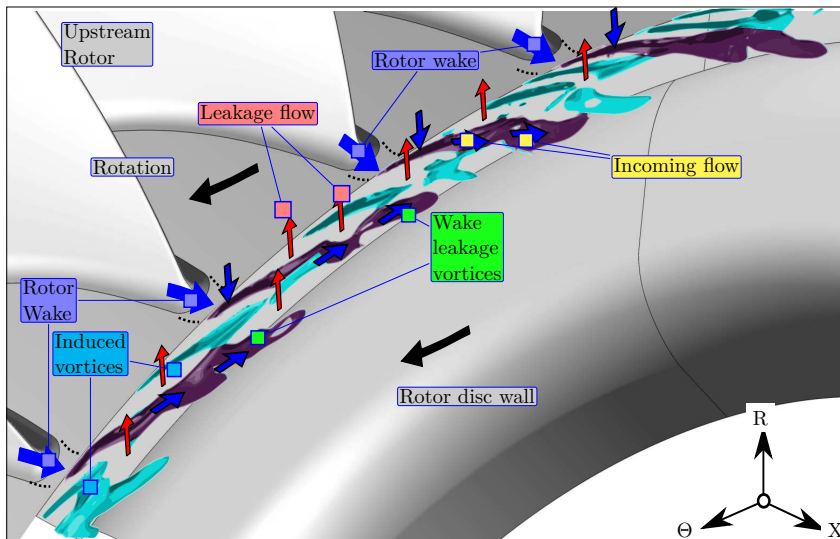
Figure 4.29: Mechanism of the incoming flow into the upstream cavity trench

remain colored with positive radial velocity on the frontal face and negative radial velocity on the back face. This indicates that vortex structures continue rotating inside the stator passage despite the main flow moves them axially. It is evident in all configurations that passage-pressure-gradient forces vortices structures near the pressure-side to move in the suction-side direction.

A couple of wake-leakage vortices emerge in front of the 2nd and 4th stator leading edges for the cases $C_1=45°$ and $C_2=90°$. For the configuration $C_3=135°$ the wake-leakage vortices emerge even more to the right in front of the 3rd and 4th passages. The comparison of all configurations shows that the proximity of the cavity outlet with the rotor evidently modifies the ejection angle. While closer to the rotor, the ejection angle is higher. The ejection angle influences the length of the wake-leakage structures. The vortex length is considered from the vortex tip to the moment as the wake-leakage vortex impinges on the stator suction-side. For the case $C_1=45°$, the wake-leakage vortex tip locates in front of the 4th stator leading edge and immediately impinges on the 3rd stator suction-side and thus depicts the shortest wake-leakage vortex length. For the case $C_2=90°$ the wake-leakage vortex emerges in the 2nd mid-passage and impinges on the 1st stator suction-side. The vortex length is considerably longer because the ejection angle also increases. Configuration $C_3=135°$ shows the longest wake-leakage vortex as it emerges in front of the 3rd mid-passage and it extends to 1st stator suction-side. While higher the ejection angle, the longer the wake-leakage vortex is.

Figure 4.30 reveals that in the middle of a couple of wake-leakage vortices exist induced vortices. For the case $C_1=45°$ there are up to three isolated induced vortices. These induced vortices do not interact with each other due to its shortest length except as one of them impinges on the stator leading edge and disrupts the coming induced vortex. The case $C_2=90°$ depicts only
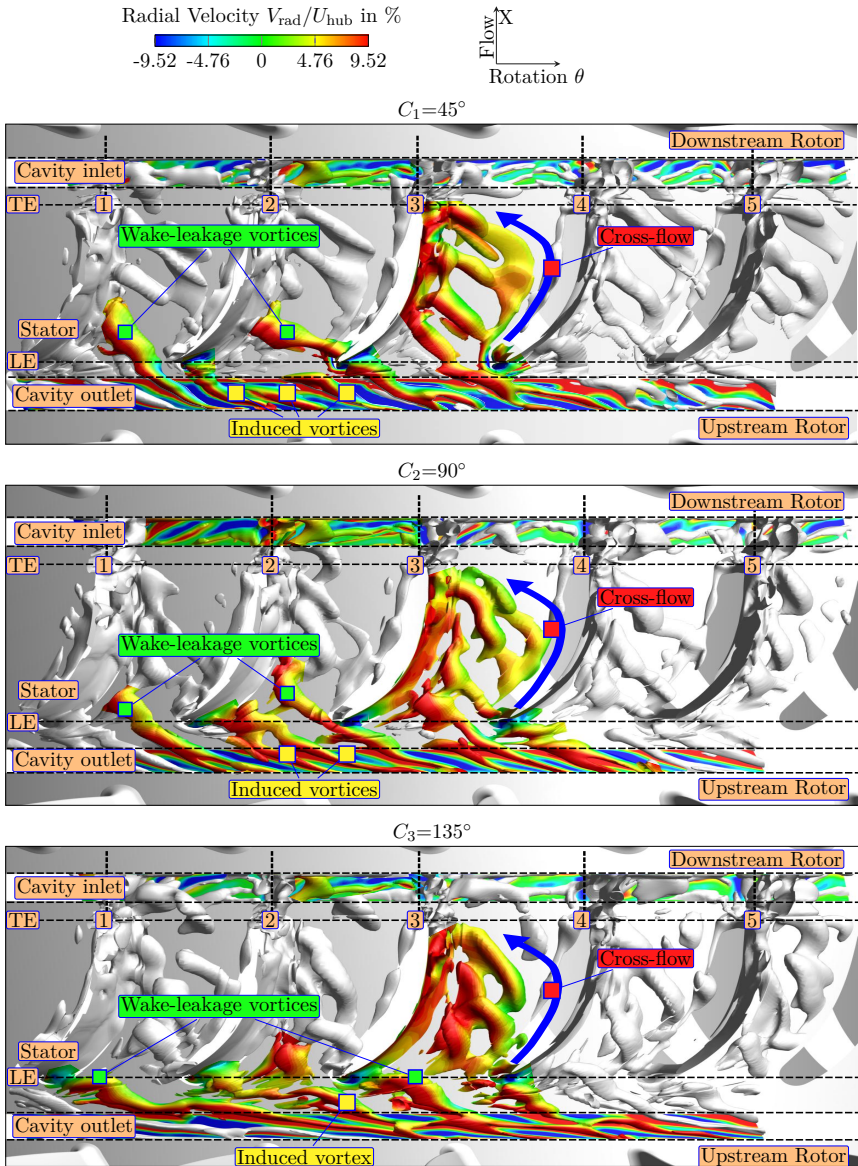
Figure 4.30: Q-criterion isosurfaces, Q=1E+08, colored with contours of radial velocity at the stator row with three distinct cavity angles 45°, 90°, 135° and tightest clearance H_1=1.18%

Radial Velocity V_{rad}/U_{hub} in %

-9.52 -4.76   0   4.76 9.52

Flow X

Rotation θ

$C_1 = 45°$

$C_2 = 90°$

$C_3 = 135°$
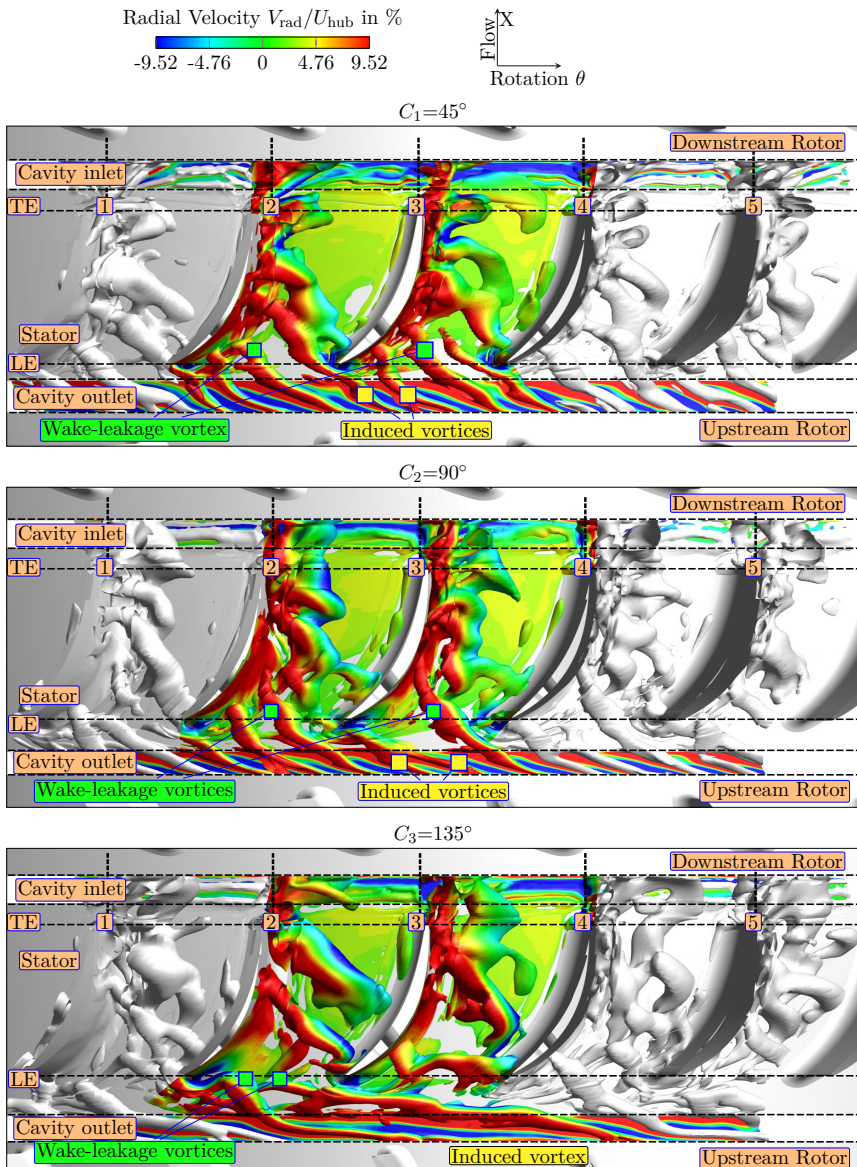
Figure 4.31: Q-criterion isosurface, Q=1E+08, colored with contours of radial velocity at the stator row with three distinct cavity angles $45°, 90°, 135°$ and increased clearance $H_2 = 2.37\%$

two induced vortices between the wake-leakage vortices. Finally, the case $C_3=135°$ shows only one induced vortex between the wake-leakage vortices. While higher the ejection angle, lesser the induced vortices. The augmentation of the ejection angle increases the length of the wake-leakage vortex that in turn reduces the number of induced vortices between the wake-leakage vortices. All configurations depict practically the same flow structure in downstream cavity-trench in the middle of the 2nd and 3rd stator trailing edges. The flow structure is sucked into the cavity-trench and the rotor disc spreads it in the whirling direction. Main flow comes into the cavity-trench as indicates the negative radial velocity.

As leakage flow rises the wake-leakage vortices also modify their structure and features. Figure 4.31 illustrates the main features of the wake-leakage vortex and the induced vortex between the three cavity outlet cases as clearance increases $H_2=2.37\%$. The wake-leakage vortex does not change its origin, namely on the rotor disc border, however as the vortex crosses the cavity trench and it approaches to stator row border it deflects and modifies its ejection angle.

All configurations depict this slight change on the ejection angle as the wake-clearance vortex is near the stator hub border as shown in the shaded vortices in front of the stator leading edge in the middle of the 4th and 5th passages. The case $C_1=45°$ depicts the most noticeable deflection of the ejection angle while the case $C_3=135°$ shows that the deflection is almost imperceptible. It is evident the increase of positive radial velocity in frontal face of the wake-leakage vortices in all configurations compared with those vortices with tightest clearance. In addition, the vortex surface colored with positive radial velocity extends on the full vortex length. The increase of positive radial velocity results in an increase of the wake-leakage diameter. Another feature is that induced vortices between wake-leakage vortices become stronger, namely their length increases. For the case $C_1=45°$ the induced vortices do not interact with each other as they emerge from the cavity-trench. The interaction appears as they break in the stator leading edge and they enter in the stator passage. In some instants, the broken vortex structure stagnates in the passage and the incoming vortex stacks on it by forming a bigger flow structure as it illustrates in 2nd passage in Figure 4.31. The broken vortex structure blocks the incoming vortex and leaves the passage clean at the rear. In other circumstances the broken vortex structures move separately from each other as shown in the 3rd passage. The stacking of the broken flow is a consequence of the vortex diameter increase and the obtuse ejection angle that the case $C_1=45°$ depicts.

Although the ejection angle increases for the case $C_2=90°$ the induced vortices do not interact with each other as they emerge from the cavity-trench. The impingement of one induced vortex on the stator leading edge provokes the interaction with the next induced vortex as it shows the labeled induced vortices in Figure 4.31. In the 2nd and 3rd passages the vortex structures stack and interact more pronounced on the stator suction-side. The stator pressure-side is practically clean from the mid-chord to stator trailing edge.

The case $C_3=135°$ shows an almost flat ejection angle that consequently deflect the wake-leakage vortex almost perpendicular to the main flow direction. The pronounced inclination of the wake-leakage vortex suppresses the formation of induced vortices in between of two wake-leakage vortices. As one induced vortex forms the wake-leakage vortex forces it to the rotor hub border as it shows the small induced vortex fully adhered to the rotor hub disc in front of the 3rd passage in Figure 4.31.

In other circumstances the induced vortex reach to form, but the wake-leakage vortex immedi-

ately forces it to merge with the next incoming wake-leakage vortex and consequently disappears the induced vortex. Due to the pronounced ejection angle the vortex structures enter more perpendicular to the main flow as it shows the broken vortex at stator leading edge in the 3rd passage. This perpendicularity helps vortex structures to travel separately from each other and delays the interaction downstream.

The generation of wake-leakage and induced vortices disturb the main flow with pure axial velocity which is responsible of generate total pressure. The vortices decelerate axial velocity and thus total pressure reduces. As the leakage flow rises the wake-leakage and induced vortices increase their diameter and length. This vortex dimensional increase promotes the axial velocity deceleration and the total pressure reduces even more.

4.9   Transport of thermodynamic properties by leakage vortices

Inner variations of thermodynamic properties in subsection 4.4.1 show that total temperature increases and total pressure decreases inside the upstream cavity-trench and thus the leakage flow emerges with higher total temperature and lower total pressure with respect of the midspan flow. Moreover, previous section shows that the interaction of rotor wake with the leakage flow produces the wake-leakage vortex and a series of induced vortices. Figure 4.32 illustrates an isometric view of the stator row with isosurfaces of the Q-criterion and planes axially distributed along the stator row. The planes are colored with total temperature and total pressure at the middle and at the bottom, respectively. The previous section shows that wake-leakage vortices and resulting induced vortices rotate in clockwise direction. This means that frontal face of the vortex has positive radial velocity while the back face has the opposite. This velocity disparity keeps rotating the vortex in clockwise direction during its travel across the passage.

Immediately after the wake-leakage and induced vortices are generated, they simultaneously collect the leakage flow with higher total temperature that emerges from the cavity-trench. Additionally the wake-leakage vortices drag more heated leakage flow in front of them due to their rotation as depict the vortex 1 and vortex 4 in the cavity outlet region sketched in Figure 4.32. These vortices point to the stator rear on the stator suction-side thus as they impinge on the stator surface and the flow with high total temperature mixes with suction-side boundary-layer. In some circumstances of the flow, the wake-leakage vortex 1 impinges direct to the stator suction-side and the heated leakage flow is discharged on it. In addition the adjacent vortex 2 blocks such heated leakage flow to escape from the stator suction-side. In other circumstances of the flow, the wake-vortex transports heated leakage flow only in front of it as shown the vortex 2 and 6. In their interior the contours of total temperature are lower than those depicted in front of it. There are wake-leakage vortices that do not impinge direct on the stator suction-side and they travel almost in the mid-pitch of the stator-passage. In these vortices the heated leakage flow remains encapsulated inside the vortices and it is transported within the vortices downstream to the stator rear as shown in the vortices 3, 5, and 7.

Figure 4.32 shows the regions of low total pressure near the hub which are concentrated between the stator leading edge and the upstream rotor. Above the upstream cavity outlet surface the vortices emerge and they transport in the core leakage flow with low total pressure. As the vortices enter in the stator passage, the part of the flow with the lowest total pressure locates just in front of the vortex and a small remaining portion stays in the vortex core as show the

vortices 1, 2, 4 and 6. The rotation of the vortex drags the flow with low total pressure located in front of it as the vortex travels inside the stator passage. Vortices 3 and 5 located downstream continue dragging the flow with low total pressure located in front of the vortex. These vortices point to the stator suction-side and consequently the flow with low total pressure will discharge on that stator side. Downstream vortices 3 and 5 block the flow with low total pressure to cross the mid-passage and therefore at the end of the passage the flow with low total pressure delineates only inside the hub boundary-layer. On the pressure side a few vortex structures are shown and the flow with low total pressure is only seen in the suction-side boundary-layer. The vortices 3, 5, and 7 show that vortices can transport heated leakage flow but not neccesarily with low total pressure.

As the leakage flow increases the wake-leakage and induced vortices increase its diameter and length. Because of the increase in the dimensions of the wake-leakage vortex it transports more flow with a higher total temperature and lower total pressure within the vortex core as shown all vortices marked in Figure 4.33. The leakage flow increase results in a higher positive radial velocity in frontal face of the vortices. The higher positive radial velocity makes the vortex drag more flow in front of it with high total temperature or lower total pressure depending on the flow conditions. Vortex 3 transports a higher total temperature and lower total pressure in the vortex core and at the same time drags flow in front of it with a higher total temperature and lower total pressure. The proximity of the wake-leakage vortices provokes that leakage flow with low total pressure accumulates on the stator suction-side. Additionally the stator pressure-gradient forces the wake-leakage vortices to the stator suction-side and practically the stator pressure-side appears clean of leakage flow with low total pressure.

4.10   Evolution of total pressure and total temperature in stator passage

This section depicts the effect of the leakage flow on the total pressure and total temperature near the stator hub in the main channel. The evolution of the total pressure and total temperature will be traced at distinct axial locations uniformly distributed along the stator passage in the streamwise direction as shown in Figure 4.34. Additionally the sketch includes the corresponding cavity outlet angle of each configuration. All total pressure and total temperature distributions are normalized with respect to the stage inlet conditions, namely with rotor inlet conditions.

For the clearance H_1=1.18%, Figure 4.35 shows that total pressure distribution of the shroudless model (i.e. the model without cavity) surpasses by 3∼7% the distributions of the models with cavity below 5% spanwise in all axial locations. This is expected due to the shroudless model has no leakage flow prior to the stator leading edge. In rear axial locations (i.e. from 80% to 120%) the dominance of the total pressure distribution of the shroudless model becomes more visible below 35% spanwise. From leading edge to 40% LE, all profiles exceed the baseline and depict a bump at 10% spanwise where the case C_3=135° has a maximum by 0.5% in total pressure.

At 80%LE and below 5% spanwise all profiles bend depicting peaks of low total pressure by 25.5∼27.5%. The peak's deviation between the configurations depict approximately less than 2% of each other and is mainly caused by the cavity outlet angle. The case pointing in the flow direction (C_1=45°) shows the a peak of low total pressure by 27.5% while other remaining configurations reach 26.7% and 25.6% for C_2=90° and C_3=135°, respectively. This arises because the cavity outlet angle facilitates the injection of the leakage flow with higher axial velocity and
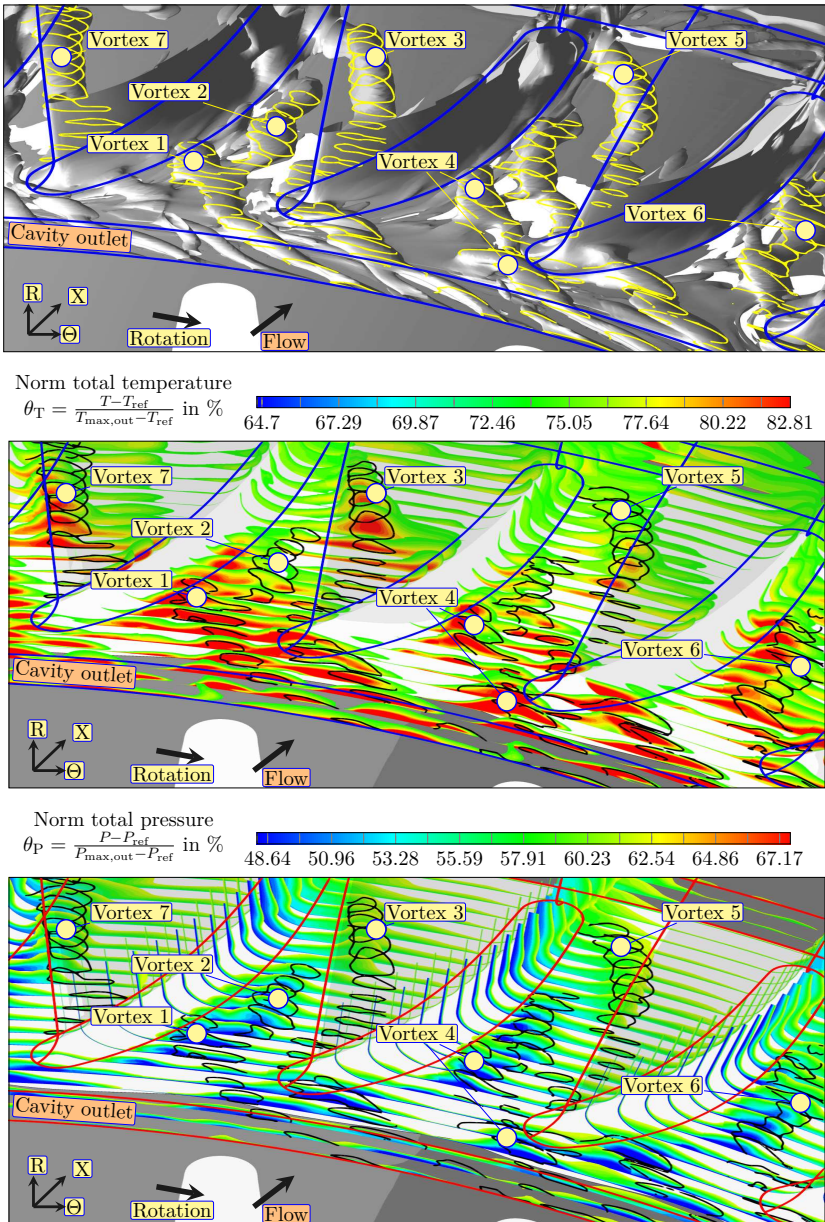
Figure 4.32: Q-criterion isosurfaces and axially distributed planes colored with contours of total temperature and total pressure at the stator row with the case 90° and tightest clearance H_1=1.18%

Norm total temperature
$\theta_{\mathrm{T}} = \frac{T - T_{\mathrm{ref}}}{T_{\mathrm{max,out}} - T_{\mathrm{ref}}}$ in %

| 64.7 | 67.29 | 69.87 | 72.46 | 75.05 | 77.64 | 80.22 | 82.81 |

Norm total pressure
$\theta_{\mathrm{P}} = \frac{P - P_{\mathrm{ref}}}{P_{\mathrm{max,out}} - P_{\mathrm{ref}}}$ in %

| 48.64 | 50.96 | 53.28 | 55.59 | 57.91 | 60.23 | 62.54 | 64.86 | 67.17 |
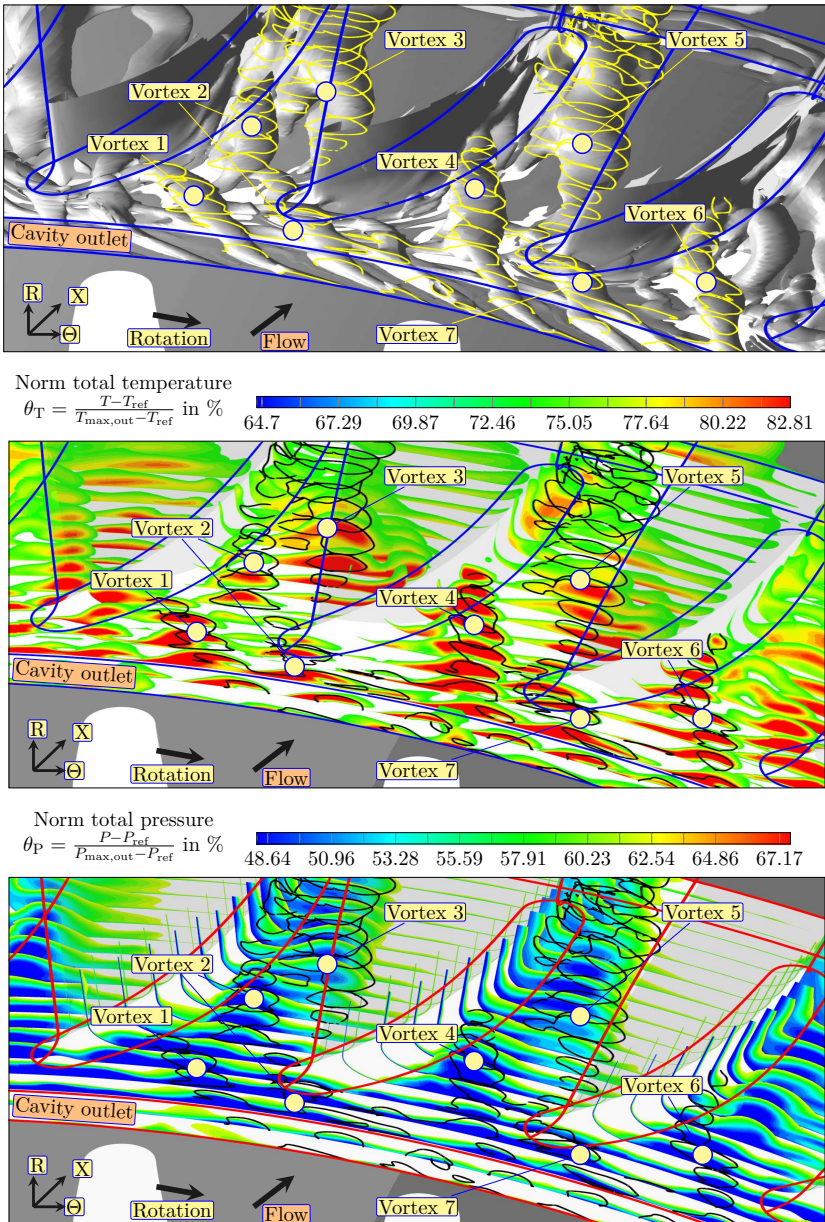
Figure 4.33: Q-criterion isosurfaces and axially distributed planes colored with contours of total temperature and total pressure at the stator row with the case 90° and tightest clearance H_2=2.37%
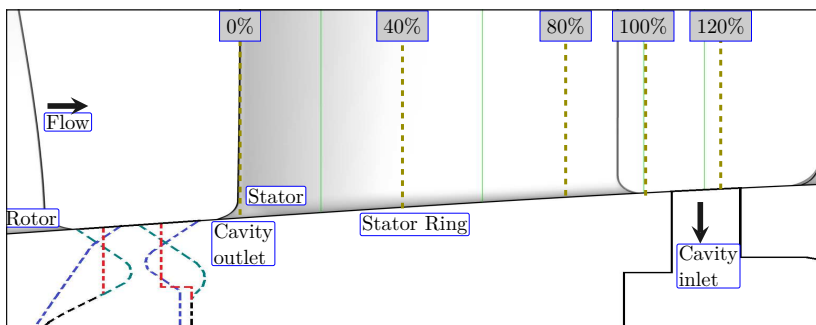
Figure 4.34: Sketch of the axial locations through the third stator

higher total pressure. Remaining configurations restrain axial velocity and total pressure of the leakage flow and therefore the peak appears behind the case C_1=45°.

For the next axial locations (i.e. 100% and 120%), the peak of low total pressure of all configurations reduces less than 0.5% but the deviations between the configurations become smaller with each other. The peak of low total pressure remains below 5% spanwise at the stage outlet for all the configurations. The case pointing against the flow direction (C_3=135°) depicts the lowest peak of total pressure by 26% and 26.5% at 100% and 120% axial locations, respectively with respect to other configurations.

Near the hub wall the axial velocity decelerates due to the wall slip condition (i.e. at the wall V_{ax}=0). The axial velocity deceleration induces two consequences: the blockage effect and the total pressure diminution. As the cavity is included, the leakage flow increases the blockage near the hub then reduces the total pressure below 5% spanwise. As a consequence of the blockage augmentation the aerodynamic loading redistributes above 6% spanwise. The most noticeable redistribution locates at 10% spanwise where the bump's peak appears. At this spanwise the case C_3=135° depicts the highest bump in all axial locations.

At the stator outlet (i.e. 120% LE) all configurations depict deviations less than 1% of each other over the whole spanwise. Total pressure evolution shows that all configurations increase the blockage effect near the hub compared to the shroudless case. Due to this blockage the aerodynamic loading increases above 6% spanwise and it redistributes from 7.5% to 40% spanwise. Despite total pressure increases above 6% spanwise, this increase is not sufficient to reach the total pressure depicted by the shroudless model except at 10% spanwise where the case C_3=135° slightly surpasses the shroudless model.

As the leakage flow increases (i.e. the labyrinth clearance increases H_2=2.37%) the blockage increases near the hub and the total pressure drop becomes more pronounced below 5% spanwise at leading edge (i.e. 0% LE). At this axial location above 10% spanwise all configurations slightly surpass the shroudless model due to the redistribution of aerodynamic loading induced by the near-hub blockage. The peaks of low total pressure are depicted completely attached to the hub. At 40% LE the peaks of low total pressure remain below 5% spanwise while the downstream remaining axial locations the peaks positioning exactly at 5% spanwise. At 80% LE the case C_3=135° practically equals the total pressure of the shroudless model except below 13% spanwise
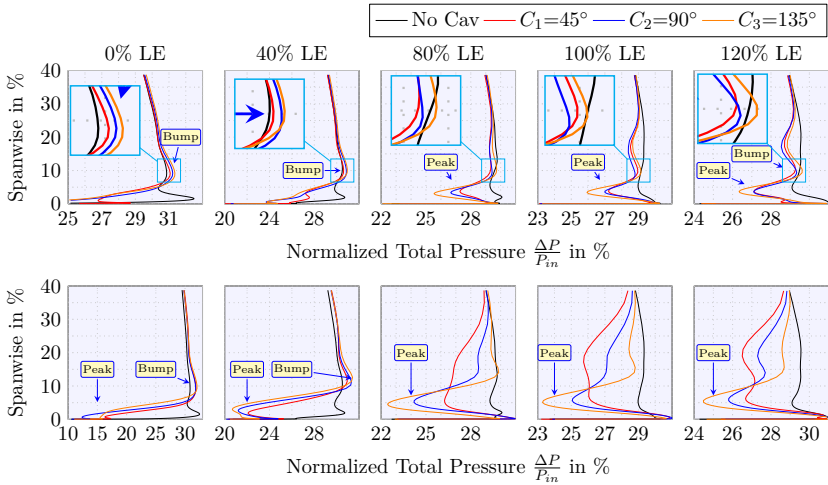
(a) Variation of total pressure near the hub along the stator 3 with clearance H_1=1.18% (upper) and H_2=2.37% (bottom)
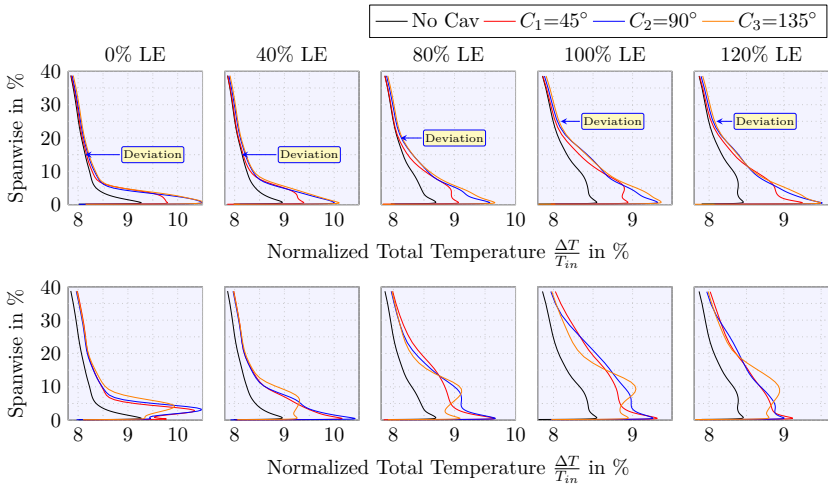
(b) Variation of total temperature near the hub along the stator 3 with clearance H_1=1.18% (upper) and H_2=2.37% (bottom)

Figure 4.35: Comparison of time-averaged spanwise distributions of total pressure and total temperature along the stator row with model without cavity and the three distinct cavity outlets

where it depicts the lowest total pressure of all configurations. The peaks of low total pressure increase 1∼2% with respect to those for the tightest clearance for locations 100% LE and 120% LE. In these axial locations the case $C_3=135°$ surpasses the other cavity angles in total pressure and shows the nearest values to the shroudless model except below 10% spanwise. In all axial locations the case $C_1=45°$ dominates total pressure over the remaining configurations below 10% spanwise. In the rear axial locations from 80% to 120% LE all configurations depict positive gains with respect to the shroudless model in the near-hub flow.

With the tightest clearance $H_1=1.18\%$ the blockage remains confined below 5∼6% spanwise while for the opened clearance $H_2=2.37\%$ the blockage increases but remains confined below 10% spanwise. The case $C_3=135°$ shows the total pressure distributions closest to the shroudless case above 5 and 10% spanwise for clearances $H_1=1.18\%$ and $H_2=2.37\%$, respectively. However, the same configuration depicts the lowest peaks of total pressure below 5 and 10% spanwise for clearances $H_1=1.18\%$ and $H_2=2.37\%$, respectively.

Each cavity outlet angle ejects the wake-leakage with distinct ejection angle as shows the sketch of the Figure 4.12. While closest the cavity outlet with the rotor is, greatest the ejection angle is. In consequence the case $C_3=135°$ induces the wake-leakage vortices with the greatest ejection angle and they are almost perpendicular to the main flow axis as shows Figure 4.30. Due to this quasi-perpendicular ejection of the wake-leakage vortices the case $C_3=135°$ induces more blockage near the hub compared to the other configurations with minor ejection angle of the wake-leakage vortices. Therefore the case $C_3=135°$ depicts the lowest peak of total pressure. The opposite occurs with the case $C_1=45°$. The blockage occurring near the hub forces the main axial flow to accelerate upwards in order to accomplish continuity, therefore appears the bump in a upward location where the blockage occurs.

In the rear section of the stator which is identified as the end-corner wall separation (i.e. 80% LE) the flow with radial velocity distorts the pure axial flow and contributes to reduce the distributions of total pressure compared to the shroudless case which does not have any leakage flow with radial velocity. When the clearance increases the leakage flow strengths the wake-leakage vortices and the blockage increases leading to more pronounced peaks of lowest total pressure below 10% spanwise. The increase of the leakage flow increases proportionally the radial velocity and the end-wall corner separation region increases and the total pressure distributions reduced compared to the tightest clearance.

Section 4.4 shows that leakage flow inside the upstream cavity-trench possess higher total temperature with respect to the main flow. As the heated leakage flow is ejected from the cavity-trench, exists the possibility that some portion of this heated leakage flow could be trapped inside the stator hub boundary-layer and could be transported to the downstream cavity-trench and consequently it could be sucked again to be reheated.

All distributions of total temperature increase progressively downwards in the hub direction and they reach their maximal values in the flow near the hub. For the clearance $H_1=1.18\%$ in the front axial locations (i.e. 0% and 40%) the cases with cavity deviate from the shroudless case at 15% spanwise while in rear axial locations (i.e. 100% and 120%) the deviation occurs at 25% spanwise. The distribution of total temperature of the shroudless model reaches a its maximum by 9.25% at 0%LE and diminishes gradually by 8.5% at 120% LE. The cases $C_2=90°$ and $C_3=135°$ exceed the values of the shroudless case by 1.5% and 1% at 0% LE and 120%, respectively. The case 45° depicts lower values by 0.5% than the cavity counterparts.

As the leakage flow increases, consequently the radial velocity component also intensifies. This intensification allows more leakage flow to be directed in the casing direction. Although the radial velocity component increases inside the cavity, total temperature remains higher compared to midspan flow. Once the leakage flow with higher total temperature is ejected from the cavity outlet it has sufficient radial velocity to spread a portion of the heated leakage flow in the casing direction. Thus all distributions of the configurations with cavity appear slightly 0.1% in front of the distribution for the shroudless case with more pronounced deviations below the 25% spanwise. At the leading edge the peaks of total temperature exceed the shroudless case by 1.5% and locate at 4% spanwise. At 40% LE the peaks practically vanish and the high values keep the deviation by 1.5% and they are located at the hub. In the last axial position, 120% LE, total temperature values exceed the shroudless case by 0.5% at the hub.

Spanwise distributions from 0% to 100% LE show that total temperature progressively cools down near the hub. The total temperature reduces from 1.5% at the leading edge to 1% behind the trailing edge for tightest clearance and 0.5% for higher clearance. Despite that the total temperature reduces at the hub, the flow still has 1% higher total temperature before (i.e. at 100% LE) it enters inside the downstream cavity-trench. Although the incoming flow does not mainly concentrate on the stator hub border as shown in Figure 4.17, a portion of the heated flow near the hub is more prone to be ingested into the downstream cavity-trench. Once that flow near the hub enters inside the downstream cavity-trench the rotor disc wall provides energy to the flow and consequently increases the total temperature of the leakage flow. The incoming flow is reheated and the recirculation structure inside the downstream cavity-trench (see Figure 4.4) is responsible to eject the reheated leakage flow as confirm the profiles near the hub at 120% LE.

For tightest clearance, the heated leakage flow influences the main flow up to 25% spanwise as shown in the profiles at stator outlet (i.e. 120% LE), but the major rates are depicted below 10% spanwise. In the case of higher clearance it is evident that heated leakage flow influences beyond 40% spanwise and the profiles exceed 0.1% the shroudless case along the spanwise at stator outlet. The major deviations of the heated leakage flow are noticeable below 15% spanwise. The profiles of 120%LE show that heated leakage flow from the downstream cavity inlet contributes to increase the total temperature near the hub. Another interesting fact is that profiles with higher clearance depict similar or lower total temperature rates near the hub compared to those with the tightest clearance at corresponding axial position from leading edge to 120% LE.

The evidence shows that heated leakage flow ejected from the upstream cavity-trench effectively remains trapped near the hub along the stator passage. As the heated flow incomes inside the downstream cavity-trench the flow is reheated. The recirculation structure inside the downstream cavity-trench ejects and returns reheated flow to the main flow. In downstream cavity-trench the incoming flow has lower total temperature compared to the outgoing flow by 1.5%. There is no evidence that heated leakage flow ingested inside the downstream cavity-trench crosses the cavity geometry and it will be reheated in the upstream cavity-trench. Additionally, temporal monitors of total temperature of the up- and downstream cavity do not show any slope that would suggest the reheating of leakage flow.

To support the aforementioned observations, distinct instantaneous total temperature contours on the stator suction-side are illustrated in Figure 4.36. On the left side appears three configurations (i.e. at the top $C_1=45°$, in the middle $C_2=90°$ and at the bottom $C_3=135°$) with the tightest clearance while on the right side the configurations are shown as clearance increases.

For the tightest clearance all configurations show that the leakage jet impinges below 5% span-wise near the stator leading edge. The location of the leakage flow impingement on the leading edge deviates approximately 2.5% spanwise between the configurations. In an instantaneous time-step it is possible to have up three spots on the stator suction-side. The path of the jet with high total temperature on the stator suction-side can be traced by means of the spots. All configurations show that spots do not exceed 15% spanwise, they move axially inside this range. From leading edge to 20% axial chord high total temperature is confined below 5% spanwise except as the incoming rotor wake impinges the entire stator spanwise as shown in the leading edge border of the graph at the top left. From 20% to 50% axial chord high total temperature is radially spread up to 15% spanwise. From 50% to trailing edge (i.e. 100% axial chord) the high total temperature continues radially spreading to reach 25% spanwise. The spanwise per-centages of the total temperature spreading coincide very well with total temperature profiles shown in Figure 4.35b. Radial velocity inside the boundary-layer is responsible for spreading high total temperature on the aft of the stator suction-side. The spots suggest that the leakage flow with high total temperature travels encapsulated along the stator passage.

As the clearance increases, namely contours on the right side, all configurations show that leakage flow impinges between 0 to 6% spanwise. All configurations depict that the spot of the jet with heated flow moves both radially and axially at the same time. It encapsulates the high total temperature flow as it shows the second spot. This spot slightly exceeds 10% spanwise as it moves axially as shown in the third spot in configuration $C_3 = 135°$. This configuration shows that heated flow remains encapsulated thus this case depicts the lowest total temperature below 5% spanwise. At 80% axial chord remaining configurations depict a considerable increase in total temperature near the hub. This augmentation comes from the cross-flow with high total temperature. As the clearance increases the heated leakage flow remains trapped in the flow near the hub. This flow travels axially in the stator passage, but the passage-pressure-gradient induces the cross-flow which transports the heated leakage flow from the hub to the stator suction-side. Cross-flow with high total temperature enters in the stator suction-side between 60 to 80% axial chord as it shows the configurations $C_1 = 45°$ and $C_2 = 90°$. As the heated flow locates on the stator suction-side it is radially spread up to 40 to 50% spanwise. Because of the spreading on the aft of the stator suction-side the total temperature distributions increase considerably below 50% spanwise as the profiles confirm in Figure 4.35b.

For the tightest clearances, the heated flow is 7% warmer with respect to the midspan flow and remains encapsulated inside the jet while it increases the temperature of the surrounding flow as much as 4% below 15% spanwise. As the clearance increases the heated flow remains encapsulated in the jet. The cross-flow contributes to transport warmer flow (i.e. 7% warmer with respect of the midspan flow) that comes from the upstream cavity outlet and increases the total temperature by 4% the inner flow on the stator suction-side at the rear up to 40 to 50% spanwise.

4.11   Unsteady effects

Section 2.3.2 reports some unsteady effects that have been experimentally and numerically ob-served in axial compressors. Most of them are unsteady effects that detriment the performance of the axial compressor (e.g. Kerrebrock and Mikolajczak's effect) and others benefit the per-formance (e.g. Recovery effect). These effects have been reported mostly at the midspan blade
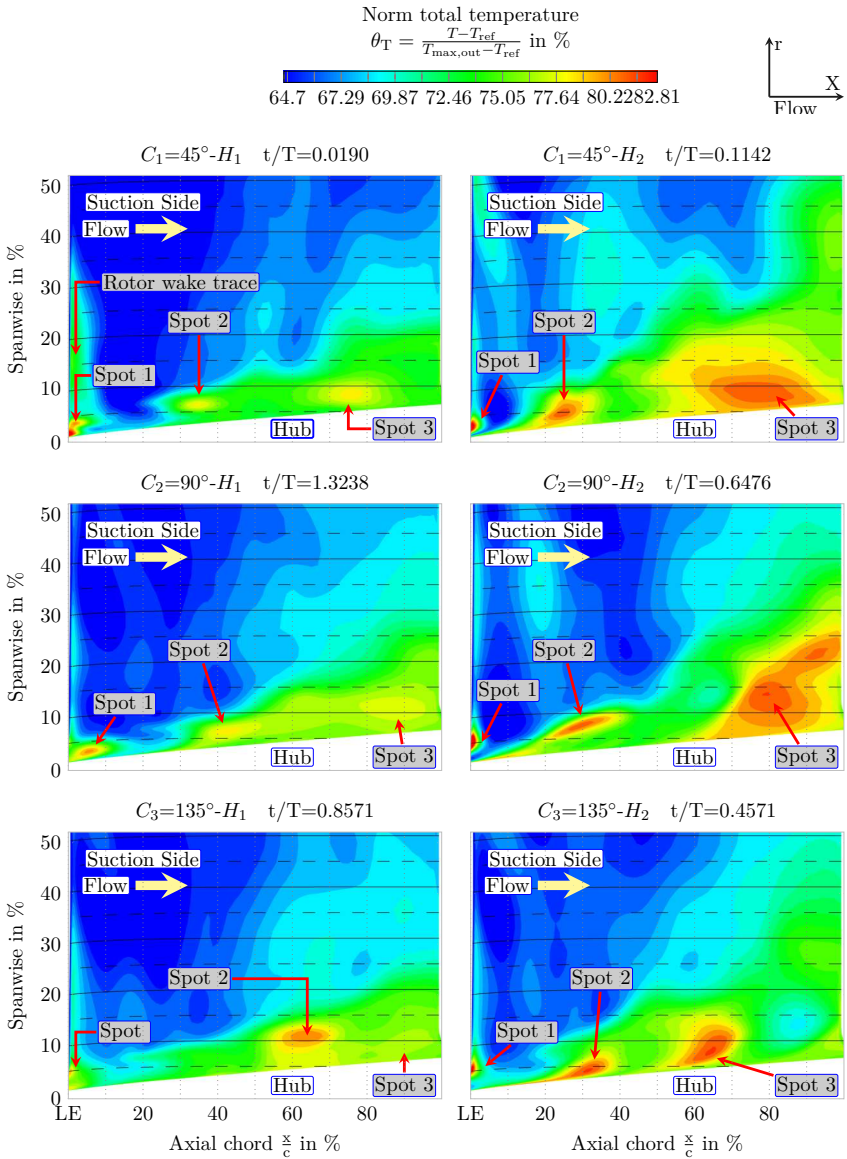
Figure 4.36: Contours of instantaneous total temperature on the third-stage stator suction side with the three variants

height. This section gives insight if these both effects remain at the midspan under the consideration of cavity leakage flow and if they alter its mechanism under the influence of cavity leakage flow near the hub.

4.11.1   Kerrebrock and Mikolajczak's effect

Kerrebrock and Mikolajczak (1970) reported a detrimental effect that occurs when the upstream wake transports high total temperature within its core to the stator pressure-side and the higher total temperature remains trapped inside the pressure-side boundary-layer. More recently Hah (2015a,b) by means of LES in a half stage of a transonic compressor gives evidence of the high total temperature accumulation on the stator pressure-side at the midspan.

Figure 4.37 shows the top view of the stator passage in which appears on the left side instantaneous velocity perturbation field while on the right side instantaneous total temperature perturbation field at 52% blade height. It is important to mention that pictures only show contours of total temperature with positive values while the black line delineates the zero value. Pictures show a sequence of three consecutive time-steps from the top to bottom. The main flow runs from left to the right in all the pictures.

As the rotor wake emerges from the trailing edge the wake gets minor relative velocity and axial velocity compared to the free-stream. The difference of relative velocities between the wake and the free stream results in a negative velocity just behind the wake which is known as "slip velocity" (see Figure 2.16). The superposition of the velocity triangle of the wake and the free-stream explains the "slip velocity". The borders of the wake, which are delineated in white, have zero perturbation velocity. The imbalance of negative velocity within the wake and positive velocity of the free stream induces perturbation vortices in the wake borders.

As the wake comes inside stator passage the adjacent stator pressure-side disrupts the wake and then the slip velocity is deviated to the free stream. Free stream returns the flow in the direction of the stator suction-side 1 and the free stream is deviated to the wake. The interaction of the wake with negative velocity and the free stream with positive velocity produces a recirculation path inside the passage as shows the three instantaneous pictures on left side of the Figures 4.37.

Time-step $\frac{t}{T}$=0.02857 shows three wakes highlighted with contours appearing in the stator passage 1 (i.e. it comprised between stator suction-side 1 and stator pressure-side 2), wake 1 locates near the trailing edge of stator 2 on the pressure-side leaving the passage. Wake 2 appears in two regions because of the chopping, the major region appears from the mid-chord of stator 2 to the stator trailing edge 1 and the remaining chopped wake locates attached on the stator suction-side 2. Wake 3 starts at rotor trailing edge in front of the stator leading edge 2, and impinges on the mid-chord of stator suction-side 1. Three wakes depict negative velocity during its axial traveling in the passage in all time lapses.

Total temperature perturbation field at time-step $\frac{t}{T}$=0.02857 clearly shows the wakes traveling through the passage. The wakes transport in the core flow with total temperature higher than the free-stream. Wake 3 shows higher total temperature uniformly distributed along the wake's trace. On the upper border appears an induced perturbation vortex, labeled as vortex 1. Once the wake has been chopped by stator 2 the portion of the wake 2 inside the passage 1 deflects due

Figure 4.37: Instantaneous velocity and total temperature perturbation field at 52% spanwise with cavity angle 135° and tight clearance H_1=1.18%

to higher velocity near the stator suction-side 1 while on the stator pressure-side 2 the velocity is considerable lower with respect to the suction-side. The remaining portion of wake 2 attached to stator suction-side 2 accelerates due to the higher velocity on that stator side.

On the tail of stator 1, the delay of the wake on the stator pressure-side is noticeable with respect to the stator suction-side. As wake 2 sweeps stator pressure-side wall 2 the wake induces two vortices in front (vortex 5) and behind (vortex 2) the wake due to the interaction of the slip velocity and the free-stream with the corresponding stator pressure-side. These vortices start at the trailing edge and they travel attached to the wake until they dissipate as the wake leaves from the passage. Inside wake 2 the spot 1 in the mid-passage reveals that warmer flow directs to the stator pressure-side wall 2. Wake 1 shows the corresponding induced vortex 3 behind of it. On the stator pressure-side 2 near the trailing edge appears a spot with higher total temperature inside the wake 1.

Next time-step $\frac{t}{T}$=0.03809 shows that the wake 3 locates in front of stator leading edge 2 just before it will be chopped. Vortex 1 moves downwards and it reduces its size. Vortices 4 and 6 are induced along the wake's borders in passages 1 and 2, respectively. The intensity of total temperature between the stator leading edge 2 and vortex 1 decreases and warmer flow remains in two regions, one just behind the rotor wake and the other attached to the stator suction-side 1. Wake 2 moves in downstream direction and continues inducing vortex 2 and 3. Spot 1 locates nearest to the stator pressure-side 2. Wake 1 continues dragging vortex 3. Spot 2 shows higher accumulated total temperature on the stator pressure-side 2 at the stator trailing edge.

Last time-step $\frac{t}{T}$=0.04761 shows that stator 2 chops wake 3 in which vortex 6 locates downwards in stator passage 2 (e.g. not shown in the illustration). Vortex 1 considerably reduces its size and locates on the stator suction-side 2 at the leading edge while vortices 2 and 4 dissipate due to the interaction with wake 2. In front of wake 3, vortex 7 appears attached to stator pressure-side 2. Spot 1 appears inside wake 2 just behind the induced vortex 5 completely attached to the stator pressure-side 2. The trail of wake 1 appears on the right lower corner with the spot 2 within. On the upper left corner appears wake 4 which induces vortex 8 on the border. With the incoming of wake 4 the mechanism periodically repeats.

Figure 4.38 shows the top view of the stator passage illustrated with instantaneous velocity perturbation field at 5% blade height. In the background vortices structures appear identified with Q-criterion isosurfaces in a sequence of six consecutive time-steps. The main flow runs from left to the right and rotation goes from top to the bottom in all the pictures.

In the first time-step $\frac{t}{T}$=0.00952, on the left side the trail of the rotor wake is clearly visible with negative velocity perturbation. Passage flow with positive velocity perturbation travels attached to the rotor wake trail. As the rotor wake trail enters to the stator row, the wake immediately is chopped up by the wake-leakage vortex or any induced vortex generated by the interaction between the leakage flow and main flow. Once the wake is chopped up then it is separated, one section remains attached behind the rotor wake trail, and the other section locates on the right side the wake-leakage vortex. At the same time the wake-leakage vortex trail losses adherence to the main vortex structure and becomes weak to continue traveling with the vortex structure and then the vortex trail separates in a small section that directs to the stator passage 1. Downstream in the stator passage 1, regions with negative velocity perturbation appear that come from the preceding wake. The mechanism that feeds these downstream regions will be explained as follows.
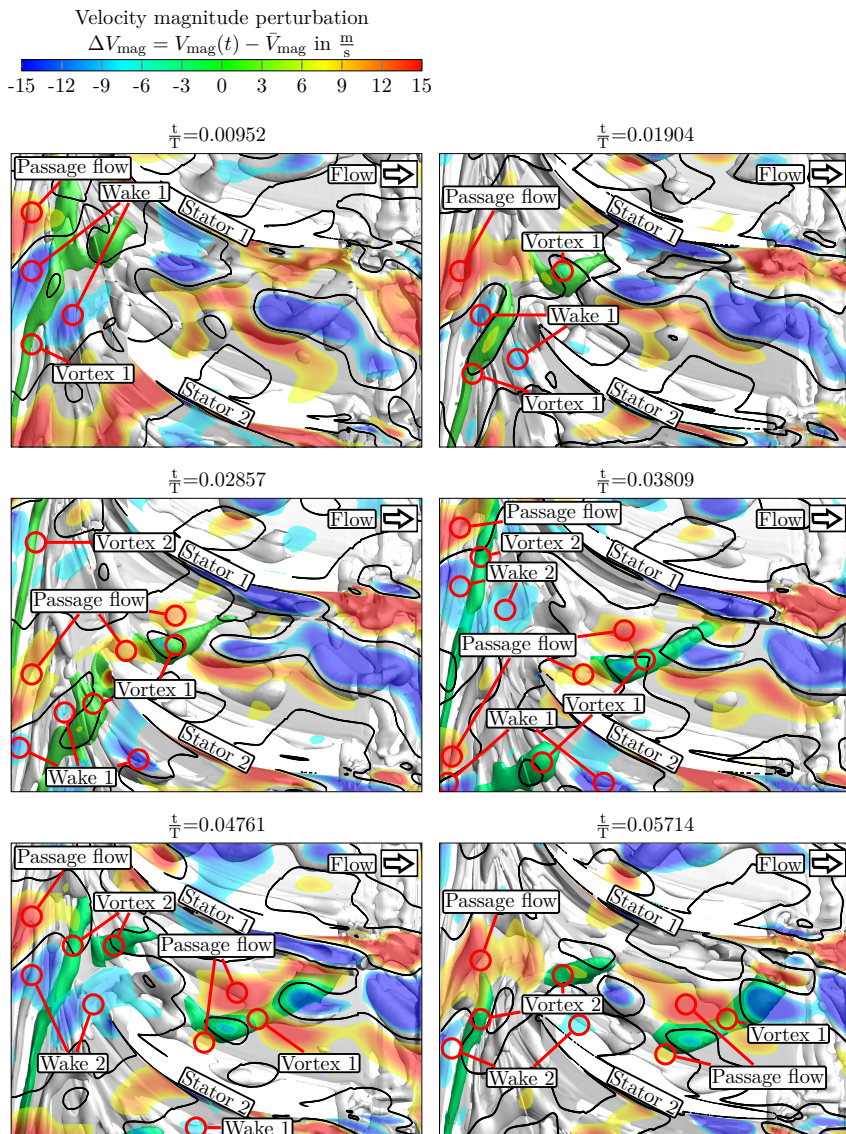
Figure 4.38: Instantaneous velocity perturbation field at 5% spanwise with cavity angle 135° and tight clearance H_1=1.18%
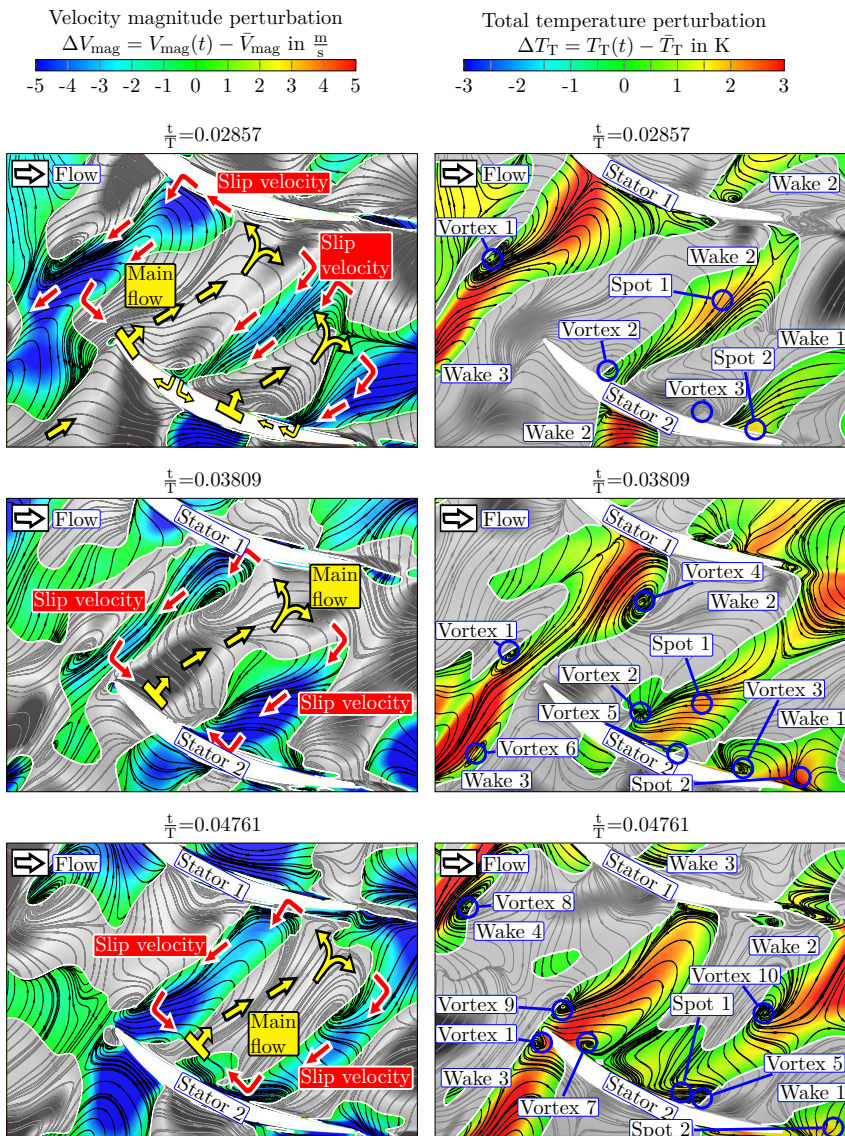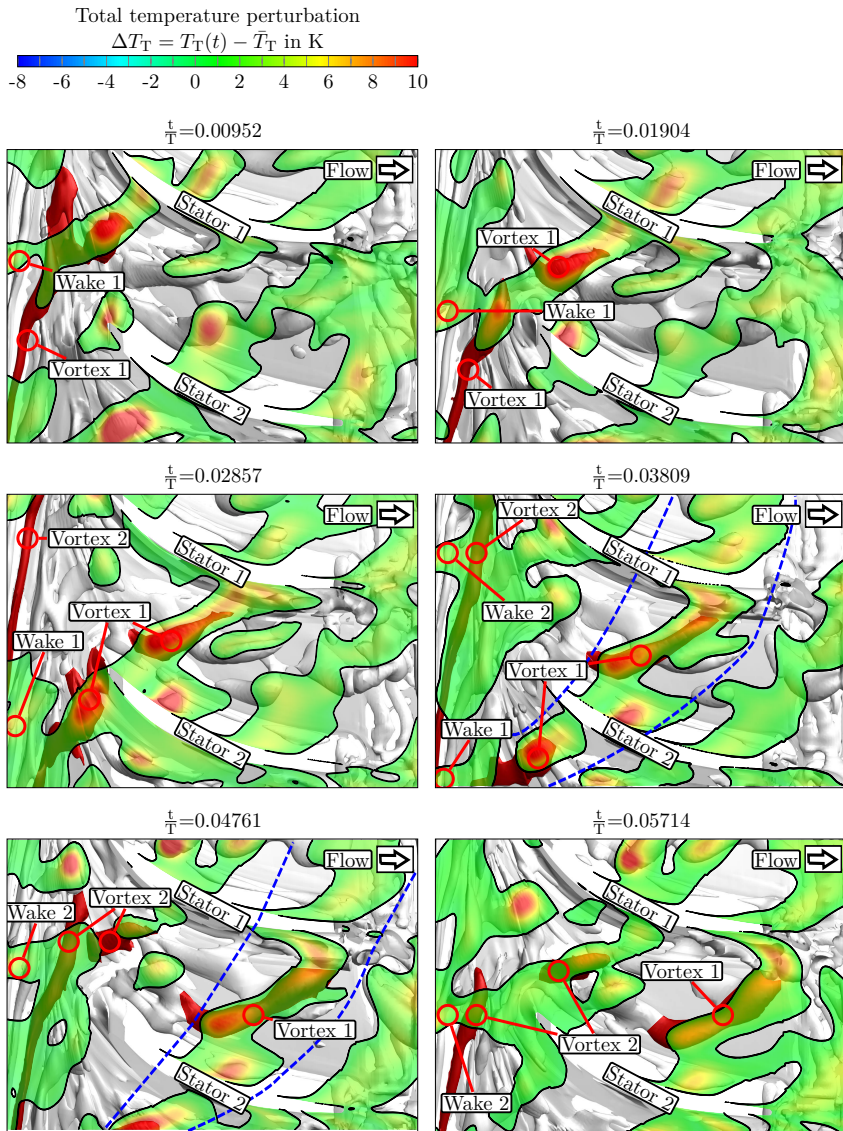
Figure 4.39: Instantaneous total temperature perturbation field at 5% spanwise with cavity angle 135° and tight clearance H_1=1.18%

In the next time-step $\frac{t}{T}$=0.01904 the rotor wake trail and the vortex move downwards due to the rotor whirling. As the vortex moves it pushes the wake section located on the right of stator passage 2. The remaining wake section stays adhered to the wake-leakage vortex. Passage flow enters in the stator row with major intensity. The leakage vortex trail separates completely from the vortex body and continues traveling in the stator passage 1. This separated vortex section pushes the regions with positive and negative velocity in front of it. In a later time-step $\frac{t}{T}$=0.02857 two sections of the passage flow enter in the stator passage 1 just behind the vortex trail. This vortex structure continues pushing the regions with negative and positive velocity in the stator passage 1. The wake-leakage vortex continues pushing the section of the wake 1 inside the stator passage 2. A new coming vortex appears on the upper left corner.

Next time-step $\frac{t}{T}$=0.03809 shows that vortex 1 continues pushing the section of the wake 1 inside the stator passage 2. Although the stator passage 2 is shown only partially, the dragged wake section should appear similar to that in the mid-passage in the first time-step $\frac{t}{T}$=0.00952. In that time-step the region with negative velocity at the mid-passage appears closer to the suction side because that region comes from a preceding wake. Vortex trail 1 continues pushing the region with negative velocity of the preceding wake. The region of positive velocity that comes from the passage flow remains behind the vortex trail 1. In addition, in this time-step vortex 2 starts chopping up the wake 2 and the wake-chopping mechanism continues.

In penultimate time-step $\frac{t}{T}$=0.04761, vortex 2 fully chops the wake 2. Aside that wake-leakage vortex 2 splits wake 2, it also pushes the wake section to the stator passage. Vortex trail 2 appears fully separated from the vortex body and is disposed to enter the stator passage 1. Vortex trail 1 has interacted with other flow structures and it appears larger. This vortex structure continues pushing the region with negative velocity. Behind the vortex trail remains the region with positive velocity.

The last time-step $\frac{t}{T}$=0.05714 shows the vortex trail 2 pushing a region with positive velocity of the passage flow and a region with negative velocity of the wake 2. Vortex 1 continues pushing the regions with negative velocity of the wake to the stator passage outlet. Six consecutive time-steps in Figure 4.38 evidently show that both wake-leakage vortex or induced vortex interrupts the wake immediately it emerges from the rotor trailing edge. Wake-leakage vortex chops the wake in two sections, one remains behind the rotor trailing edge and the other is pushed by the wake-leakage vortex to the adjacent stator passage. In this way the wake-leakage vortex distorts the wake path and the recirculation path observed at the midspan does not occur anymore. The wake-leakage vortex deviates from the trajectory of the wake. The wake-leakage vortex allows a partial impingement of the wake in the stator suction-side. The major regions with negative velocity travel almost parallel to the free stream and they are pushed by the wake-leakage vortex.

Figure 4.39 shows the top view of the stator passage illustrated with instantaneous total temperature perturbation field at 5% stator height. In the background vortices structures appear identified with Q-criterion isosurfaces in a sequence of six consecutive time steps. The first time-step $\frac{t}{T}$=0.00952 shows vortex 1 emerging from the cavity-trench as the vortex starts to rotate the leakage flow with high total temperature locates beneath the leakage vortex. Therefore the vortex does not show contours with positive total temperature above vortex 1 from the origin to the mid-body. Once the vortex has rotated the contours with higher total temperature appears from the mid-body to the vortex trail that already has been detached from the main vortex body. The contours of the wake trail mix with those of the leaking vortex due to the proximity between each other. Downstream the spots of high total temperature locate exactly above of

vortex structures.

Next time-step $\frac{t}{T}$=0.01904 shows the regions with highest total temperature just above the vortex trail and the detached vortex trail entering the stator passage. The chopped vortex structures located near stator pressure-side 1 and inside stator mid-passage 1 that belong to vortex 1 appear under the spots with high total temperature. The region with high total temperature attached to the stator pressure-side 2 corresponds to preceding detached vortex trail.

In a later time-step $\frac{t}{T}$=0.02857 the vortex trail 1 locates slightly below stator leading edge 2 and the vortex trail starts to separate from the main vortex body again to form a new detached vortex trail that will travel inside the adjacent stator passage 2. In stator passage 1 the detached vortex trail 1 starts to elongate at the front of the vortex. The elongation results in a vortex thinning. The elongation directs to the stator suction-side 1. Because of the vortex elongation the region with high total temperature spreads in the same direction. On the upper left corner appears vortex 2 from the origin to the mid-body. Beneath vortex 2, leakage flow has high total temperature that will be transported above the vortex 2 in the next time-step. The region with high total temperature continues moving along the stator passage attached to the stator pressure-side 2.

Fourth time-step $\frac{t}{T}$=0.03809 shows the detached vortex trail 1 significantly elongated in the stator mid-passage 1. The vortex elongation pushes the frontal region with high total temperature to the stator suction-side 1. The region stacks on the stator suction-side wall and the region starts to move downstream completely attached to such stator side. In the same stator passage 1 on the stator pressure-side 2 the region with high total temperature by 10 K continues moving downstream attached to it. At the bottom left the vortex trail 1 continues pushing flow with high total temperature inside the stator passage 2. In this time-step vortex 2 already rotated and warmer flow locates above vortex 2 depicting the region of moderate total temperature by 2 K along vortex 2. The same mechanism occurs in the adjacent vortex therefore the region of moderate total temperature extends above it. In this time-step is possible to identify the chopped vortex trails originally separated from vortex 1 by means of the high total temperature regions delineated between the blue dashed lines.

Penultimate time-step $\frac{t}{T}$=0.04761 shows the region with moderate total temperature by 2 K moving in circumferential direction above vortex body 2. The wake region 2 joins to the moving region. Vortex trail 2 already separates from the main body and directs to stator passage 1. Above the vortex trail 2 travels a small region with high total temperature by 8 K. In the current time-step the chopped vortex trails that separate from the vortex 1 can be better depicted in between the dashed blue lines. The spots of high total temperature show evidence of the trace of the vortex in the corresponding stator passage. Inside the stator passage 1 regions with high total temperature by 10 K are located at the stator suction-side 1, at the mid-passage, and at the stator pressure-side 2. Vortex trail 1 interacts with other flow structures and it reaches the longest length. Above the vortex trail 1 regions with high total temperature locate at the front and at the vortex tail. The frontal region continues moving attached to the stator suction-side.

Last time-step $\frac{t}{T}$=0.05714 shows the detached vortex trail 2 with a region of high total temperature by 10 K above of it entering inside the stator passage 2. Vortex 2 continues moving circumferentially dragging warmer flow above it. Above vortex trail 1 between the stator suction-side 1 and in the mid-passage, and at the stator pressure-side 2 regions with high total temperature

by 10 K continue moving downstream to the stator passage outlet. The region attached to the stator suction-side depicts the highest total temperature by 10 K compared to the two identified regions. By comparing the last time-step with second time-step is evident the periodicity of this mechanism.

Time-steps in Figure 4.39 evidently show that the major contribution of total temperature comes from the leakage flow. Contours of total temperature at 5% span reveal that the surface of the wake-leakage vortex transports flow with higher total temperature as the wake-leakage vortex rotates. As the vortex trail separates from the main vortex body the trail enters to the stator passage. Above the vortex trail always appears a region with higher total temperature with respect to the free stream. Inside the stator passage the vortex trail elongates in the direction of the stator suction-side and consequently the region with high total temperature distributes in such direction. As the flow with high total temperature reaches the stator suction-side wall the flow stacks and continues moving downstream attached to the stator suction-side. In the mid-passage other region with high total temperature does not move sufficiently faster with respect to the stator suction-side and thus this region continues moving downstream in the mid-passage sector. As the stator leading edge chops the vortex a small region with high total temperature is trapped inside the stator pressure-side boundary-layer thus this region moves axially attached to such stator side. Regions with high total temperature egress from the stator passage covering the entire passage, however the region with highest total temperature locates attached to the stator suction-side. The warmer leakage flow is the main contributor of the highest temperature depicted on the stator suction-side in the near-hub spanwise.

Figure 4.37 shows that URANS simulations can capture the higher total temperature accumulation on the pressure-side at trailing edge at the midspan which is known as Kerrebrock and Mikolajczak's effect Kerrebrock and Mikolajczak (1970). However, near the hub at 5% span the highest total temperature inside the passage locates on the stator suction-side due to the wake-leakage vortex transports flow with high total temperature to the stator suction-side as shown in Figure 4.39.

To verify if the Kerrebrock and Mikolajczak's effect occurs simultaneously in all passages at the midspan, Figure 4.40 shows time-averaged circumferential distributions of normalized total pressure, normalized total temperature, and entropy located 6.4% chords downstream of the stator trailing edge at 52 and 5% stator span, respectively.

At midspan (i.e. 52% spanwise) in passages 1 and 2 the distributions are quasi-symmetric and the peak of total pressure appears in the mid-passage and progressively diminishes in direction of pressure and suction sides. The distributions in these two passages show the highest total pressure compared to the remaining passages. Passage 4 depicts the lowest values of all passages. The lowest total pressure appears exactly behind each corresponding trailing edge (i.e. graphic does not show the lowest value). All configurations with cavity show higher total pressure with respect to the baseline model (i.e. the model without cavities) being the case $C_3 = 135°$ that reaches up to 1% higher total pressure at the peak in all passages. The distribution of total pressure of the case $C_3 = 135°$ dominates over the remaining cases in the entire passage except in specific regions where other configurations equalize the high total pressure. Values for the case $C_2 = 90°$ locate scarcely below to the case $C_3 = 135°$ while for the case $C_1 = 45°$ depict up to 0.5% lesser total pressure at the peak in some regions of all passages.

In passages 1 and 2 distributions of total temperature appear asymmetrically inclined to the

stator pressure-side depicting the peak of such distributions and confirming the Kerrebrock and Mikolajczak's effect previously shown in Figure 4.37. The peak of the distribution in passage 3 appears near the stator suction-side while the peak in passage 4 appears at the left just before the mid-passage and finally the peak in passage 5 appears at the right after the mid-passage. Kerrebrock and Mikolajczak's effect does not appear simultaneously in all passages, and the peak of each corresponding passage moves circumferentially in the direction of the rotation. As the peak approaches to the stator pressure-side the Kerrebrock and Mikolajczak's effect appears, however there is one peak in each passage at distinct pitch location. At the peak the case C_3=135° shows higher total temperature up to 0.5% with respect to the baseline model. At the midspan all configurations with cavity depict higher distributions compared to the baseline model.

The resulting entropy distributions depict the same shape to those with total temperature showing that losses in the midspan are more sensitive to total temperature changes rather than total pressure variations. As the peak of total temperature coincide near the stator pressure-side the stator wake on the pressure-side will transport additional losses downstream.

At 5% spanwise the peaks of total pressure hardly reach the value 69% and they reduce 1.25% with respect to the peaks at the midspan. The baseline model which does not include cavity depicts similar high total pressure in pressure and suction side. In passage 2 and 3 total pressure on the suction-side results higher than the pressure-side. All configurations with cavity geometry reveal that the high value of total pressure on the suction-side is overestimated up to 6%. From the mid-passage to the pressure-side the distributions only reduce by 2%. From the mid-passage to the stator-side the distributions progressively reduce to reach the lowest value by 55% at the trailing edge location. Near the pressure-side, the case C_3=135° depicts the highest total pressure, however at the mid-passage it depicts, at the same time, the lowest total pressure.

The peak of total temperature distributions appears on the suction-side for all configurations with cavity while the peak for the baseline appears exactly at the trailing edge. The deviation between the peak of the baseline and cases C_1=45° and C_2=90° surpasses 3%. The case C_3=135° depicts the highest peaks in all passages except in passages 4 and 5 where the case C_2=90° dominates the peaks. At the mid-passage the case C_3=135° continues depicting higher total temperature with respect to other configurations. It is evident that all passages depict the highest total temperature simultaneously on the suction-side. Total temperature progressively diminishes in direction to the stator pressure-side. The deviation of total temperature distributions between pressure-side and suction-side is approximately 6%.

The case C_3=135° shows the highest losses near the stator suction-side and at the mid-passage, but it shows the lowest losses near the pressure-side compared to the remaining cases with cavity. It is evident that baseline underestimates losses from the mid-passage to the stator suction-side. Distributions of total pressure show how the wake-leakage vortex mostly disturbs the flow near the hub from the mid-passage to the stator suction-side therefore the distributions of total pressure in such side reveal considerable reductions. Distributions of total temperature confirm that wake-leakage vortex transports warmer flow as shown in Figure 4.39 and it stacks on the stator suction-side resulting in highest values of total temperature in such side. Because of the low total pressure values and high total temperature values near the stator suction-side the peaks of the entropy distributions result in such location.

The blockage induced by the wake-leakage vortex near the stator hub provokes that axial ve-

locity decelerates and then the total pressure drops. At the same time the blockage provokes a redistribution of the main flow above the blockage. This redistribution accelerates the axial velocity and then the total pressure increases above where the blockage occurs. Due to the axial velocity deceleration near the hub the total temperature remains higher with respect to the main flow. The case $C_3=135°$ induces more blockage near the hub than the other configurations because the wake-leakage vortices are generated almost perpendicular to the main flow. Due to the blockage near the hub, the total pressure drop and the total temperature rise are higher than the other configurations. Nevertheless, the $C_3=135°$ shows a higher total pressure at the midspan compared to the other configurations.

4.11.2   Recovery effect

Recovery is an advantageous unsteady effect that occurs in the stator passage as a distorted upstream chopped wake enters in the next stator row and the recovery effect compensates the distortion. Ashby (1957) and Smith (1958) reported the first observations of the recovery effect and they develop separately a model to estimate the recovery effect based on the wake length. Adamczyk (1996) and VanZante et al. (1997) deepen more in the existence of the recovery factor and they develop corresponding models to quantify its benefits. Unfortunately, all existing models are based on the midspan flow because the wake is fully extended inside the stator passage as shown in Figure 4.38 and it can be measured as input for the models. In addition, the models consider assumptions such as neglecting secondary flows and uniform static pressure in the wake and the main flow. As shown in Figure 4.39 and Figure4.40 in previous section the wake is fully distorted by the wake-leakage vortex that in turn promotes secondary flows near the hub. Therefore, current models for quantify the recovery factor cannot be used near the hub. One method to highlight the unsteady effects including negative and positive phenomena is to show the difference between the URANS-averaged with the RANS solution. Montomoli et al. (2013) and Fröbel et al. (2010) have shown that this aforementioned method highlights the recovery effect.

Figure 4.41 shows the difference of the baseline model (i.e. without cavity) between the URANS-averaged and RANS solution. Total pressure distribution shows the unsteady benefit which includes the recovery factor in all spanwise. At 90% spanwise the unsteady benefit is practically zero because the tip vortex limits the total pressure ratio.

In the casing region, there is a benefit by 0.5% while at the hub region the benefit exceeds 1% being the maximum value over the stator span. At 12% spanwise there is a local minimum by 0.25% and this reduction is originated by the vortex passage. Between 20 and 50% spanwise the total pressure benefit exceeds 0.5%, above 50% spanwise the total pressure diminishes progressively up to reach the minimal at 90% spanwise. The overall unsteady benefit in total pressure reaches 0.453%. Within the unsteady effects the total temperature undergoes changes over the spanwise. At the casing, total temperature increases by a maximum 0.5% while 30% spanwise a local maximum depicts 0.2%. Near the hub URANS solution computes 0.3% less total temperature than RANS solution while at 75% spanwise appears other local minimum showing a deviation by 0.07%. The overall unsteady augmentation in total temperature results by 0.088%. Entropy is used to quantify the unsteady benefits and drawbacks from total pressure and total temperature, respectively.

At the casing region, the benefit of total pressure is minimal compared to the midspan region
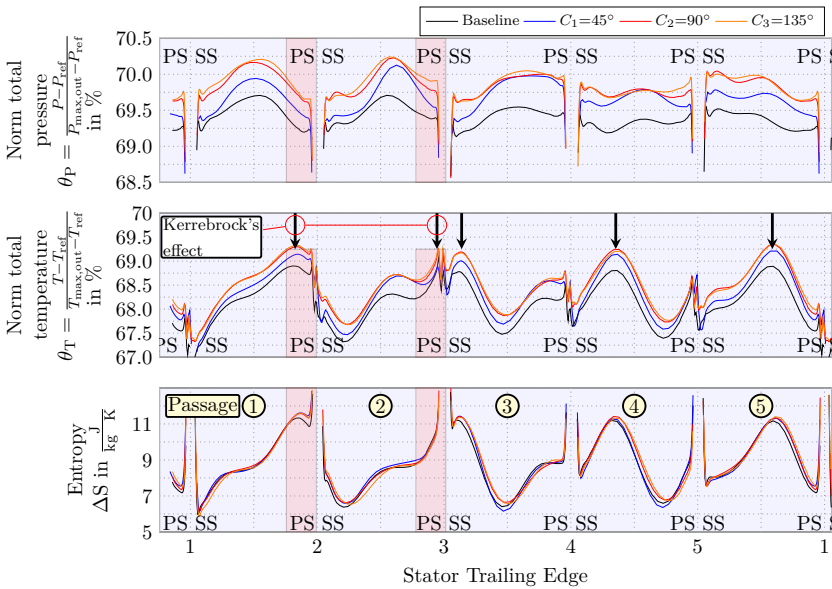
(a) 52% spanwise
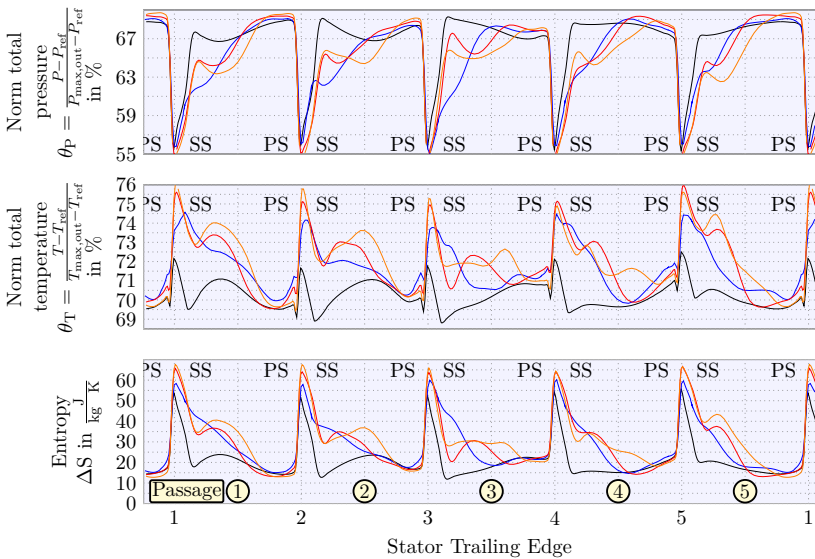
(b) 5% spanwise

Figure 4.40: Time-averaged circumferential distributions of total temperature, total pressure and entropy 6.4% chords downstream stator trailing edge with clearance H_1=1.18%

and total temperature shows the maximum, consequently the highest entropy appears from 80% to 100% spanwise. From 40 to 80% spanwise the entropy reduces because in that range total pressure increases and total temperature diminishes. From 10 to 40% spanwise there is an increase in both total pressure and total temperature, however despite the total pressure benefit is greater than total temperature augmentation the entropy increases in that spanwise segment. This shows the high sensitivity of the entropy to small total temperature changes. In the hub region, from 0 to 10% spanwise entropy shows the major reductions due to the major total pressure benefit and colder total temperature. Despite the overall total pressure benefit by 0.453% and colder regions of total temperature near the hub and at 70% spanwise, the overall entropy for URANS solution results 0.119 higher than RANS solution.

The inclusion of cavity strongly modifies the unsteady effects near the hub due to the leakage vortex and consequently the recovery factor is modified. Figure 4.42 illustrates the difference of the models with cavity between the corresponding URANS-averaged and RANS solution to show which configuration achieves the major benefit and its consequence in the entropy generation. Graphics depict the case $C_1=45°$ at the top, the case $C_2=90°$ in the middle, and the case $C_3=135°$ at the bottom. The case without cavity (i.e. baseline) is plotted as reference.
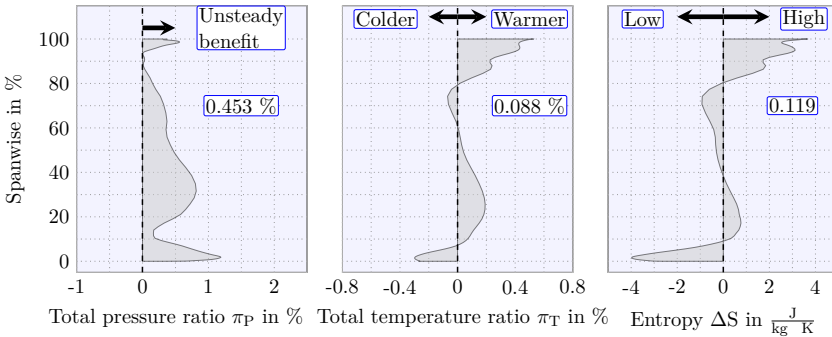
Figure 4.41: URANS-RANS spanwise distributions of total pressure, total temperature and entropy 6.4% chords downstream stator trailing edge

For case $C_1=45°$ the total pressure benefit diminishes with respect of the baseline above 20% spanwise. At 10% spanwise the maximum benefit reaches 1%. Below 10% spanwise there are two negative fluctuations while the positive peak reduces compared to the baseline. Below 60% spanwise total temperature appears colder than baseline reaching at the hub the lowest total temperature by 0.6%. Entropy augmentation appears from 80 to 100% spanwise and at specific locations at 30 and 5% spanwise. The remaining spanwise locations show beneficial reductions of entropy.

For case $C_2=90°$, the total pressure benefit is practically the same compared to the baseline above 55% spanwise. From 5 to 55% spanwise total pressure considerably diminishes and no benefit is depicted at 15% spanwise. Near the hub, below 5% spanwise total pressure reaches 2.5% depicting the greatest benefit. Although total temperature practically coincides with baseline along the stator spanwise. Remarkable differences appear at the casing and at the hub depicting warmer and colder temperature, respectively with respect to baseline. Reductions in entropy

appear between 40 to 80% spanwise and below 10% spanwise while the remaining spanwise sections entropy increases.

For case $C_3=135°$, the total pressure matches above 30% spanwise with the baseline. From 5 to 30% spanwise the total pressure shows an augmentation compared to the baseline even at 10% spanwise and reaches the maximal total pressure benefit reaching 1%. Near the hub, below 5% spanwise total pressure diminishes 0.5% compared to baseline. Total temperature distribution matches with baseline along the stator spanwise except below 25%. From 5 to 25% spanwise total temperature is colder than baseline while near the hub the opposite occurs. Beneficial reductions in entropy appear from 40 to 80% spanwise and below 20% spanwise while remaining locations the entropy depicts augmentation.

The case $C_3=135°$ depicts the highest overall unsteady benefit by 0.46% in terms of total pressure, this value includes the recovery factor. For total temperature, the case $C_1=45°$ reaches the lowest overall value by 0.034%. Consequently, the case $C_1=45°$ shows a beneficial entropy diminution by -0.039 generated mainly for the total temperature decrease.

The major effect of the blockage generated by the wake-leakage vortices in the upstream cavity outlet is depicted in the distributions of total pressure. For the cases $C_1=45°$ and $C_3=135°$ the blockage decreases the total pressure below 10% but at the same time modifies the distribution in the remaining span reaching the major benefit at 10% span. The blockage of the case $C_2=90°$ modifies the total pressure distribution in such a way to the shroudless case, namely there is a reduction at 15% span and the benefit occurs at 5% span. By comparing the distributions of total temperature for all configurations, the distributions depict practically the same shape from 20% to 100% span. Below 20% span the case $C_3=135°$ depicts a warmer flow compared to the other cases due to the bigger blockage in the upstream cavity outlet generated by the wake-leakage vortices that restrain the axial velocity and allow a temperature rise in the main flow near the hub. Although the remaining configurations generate a blockage in the upstream cavity outlet, the distributions of total temperature show a minor temperature rise in the near-hub flow. The effect of total pressure and total temperature changes affect the distributions of entropy from 0% to 40% span. In the remaining spanwise the distributions of all configurations are practically the same.

4.12   Third stage overall performance

The cavity inclusion not only affects the region near the stator hub, but it alters the core flow. Figure 4.43 illustrates spanwise distributions of total pressure, total temperature, and entropy at the stator outlet. The distributions show the difference between the baseline without cavity and the corresponding model with cavity.

Below 5% span three configurations depict reductions of total pressure below -3% but the case $C_3=135°$ reaches the lowest value by -4.5% which indicates a bigger blockage at the hub. These reductions are associated with the distortion of the main flow at the hub by wake-leakage vortices. They restrain the pure axial flow, and a blockage forms which reduce total pressure. Above 10% span, the case $C_3=135°$ shows dominance over the other cases. The blockage generated near the hub by the wake-leakage vortices modifies the total pressure distribution above 10% span. The blockage near the hub reduces the effective area of the channel and the main flow which
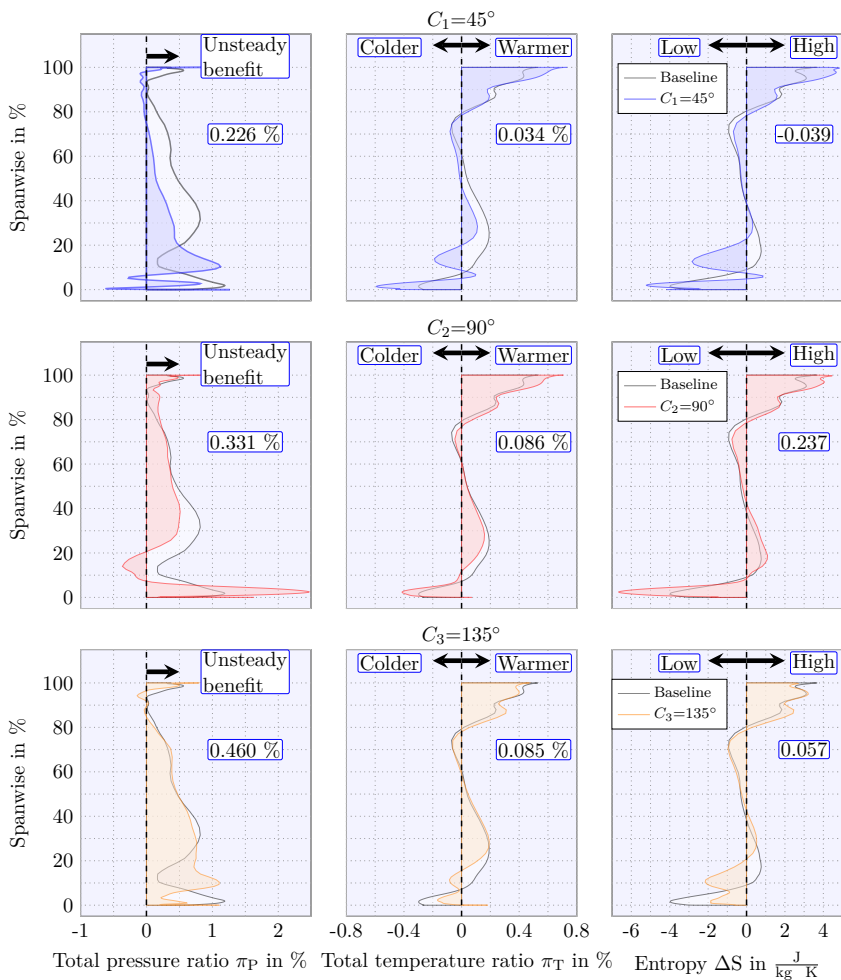
Figure 4.42: URANS-RANS spanwise distributions of total pressure, total temperature and entropy 6.4% chords downstream stator trailing edge with clearance H_1=1.18%

does not interact at the hub it is pushed upwards and accelerates modifying the total pressure distribution.

The deviations do not exceed more than 1% each other from the hub to 70% spanwise. All configurations depict total pressure increase from 30 to 70% spanwise. Below 30% spanwise all configurations show a deficit in total pressure except the case C_3=135° that shows gains by approximately 0.5% at 10% spanwise. The case C_3=135° shows the highest total temperature

distribution along the entire spanwise except at 15% spanwise where it equals with the case C_2=90° by 0.3%. Below 70% spanwise the deviations do not exceed more than 0.2% between each other. From 30 to 70% spanwise the values remain constant while below 30% spanwise the distributions bend and progressively increase to reach at the hub 1.8%, 1.9% and 2% for the case C_1=45°, C_2=90° and C_3=135°, respectively.
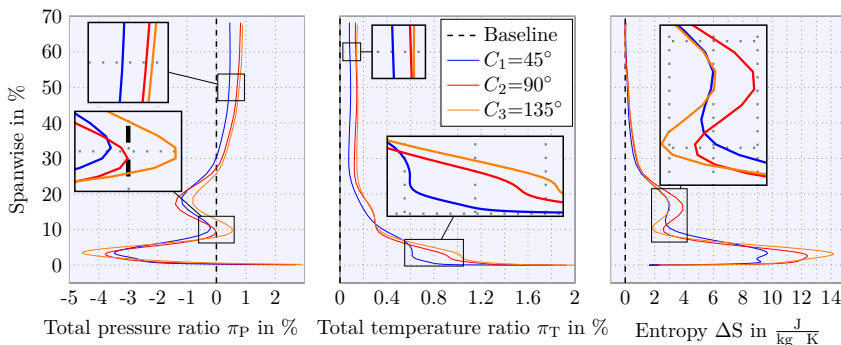
Figure 4.43: Stage performance of time-averaged spanwise distributions at stator 3 outlet

Entropy distributions of all the configurations practically coincide each other from 22 to 70% spanwise, even between 60 to 70% spanwise all cases with cavity generate same entropy as shroudless case. From 9 to 15% spanwise the case C_3=135° produce less entropy by 2 compared to the counterparts. This entropy reduction is due to the gain in total pressure at the same spanwise. However near the hub at 2.5% spanwise the same case produce the highest entropy peak by 14.

The inclusion of cavity shows that leakage flow interacts with the rotor wake and both generate the wake-leakage vortex that in turn produces more induced vortices. These vortices disturb the main flow restraining axial velocity near the hub and consequently the total pressure decreases. In addition, inside the upstream cavity-trench the total temperature of the leakage flow rises due to the energy transfer from the rotor disc to the fluid. The vortices can transport leakage flow with high total temperature and low total pressure in the core and they impinge in the stator suction-side. Wake-leakage vortices modify the recovery factor benefit along the stator height. All these effects will modify the overall performance of the third stage.

Figure 4.44 shows the performance of time-averaged solutions in the third stage as the labyrinth seal clearance varies. The curve fitting includes the shroudless case for 0% clearance. The seal clearance varies at H_1=1.18%, H_2=2.37% and H_3=3.57%. The shroudless case achieves the highest total pressure π_P by 1.285. For all configurations with cavity, the total pressure π_P diminishes as seal clearance increases. At first seal clearance H_1=1.18%, the cavity angle makes the deviation more noticeable between three clearances. The case C_3=135° depicts the lowest deviation of total pressure π_P by 0.043% compared to shroudless model while the cases C_2=90° and C_1=45° deviate by 0.133% and 0.196%, respectively. For the next seal clearance H_2=2.37%, the case C_3=135° continues showing the lowest deviation of total pressure π_P by 0.211% compared to shroudless model. The remaining deviations practically coincide achieving 0.311% and 0.307% for the cases C_1=45° and C_2=90°, respectively. The cases reduce their

deviations near to 0.1% each other with respect to the case $C_3=135°$ in next seal clearance $H_2=2.37\%$. The case $C_3=135°$ continue showing the minor deterioration with the inclusion of the cavity geometry. All configurations continue reducing their deviations less than 0.1% each other for the last seal clearance $H_3=3.56\%$. The case $C_3=135°$ depicts the lowest total pressure deterioration by 0.394% while the cases $C_1=45°$ and $C_2=90°$ the deviations increase by 0.486% and 0.445%, respectively. The linear curve fitting suggests that case $C_3=135°$ depicts the lowest deterioration compared to remaining counterparts. For every 1% in seal clearance total pressure reduces by 0.132%, 0.127% and 0.114% for cases $C_1=45°$, $C_2=90°$ and $C_3=135°$, respectively.

All configurations show that total temperature rises as seal clearance increases. The cases show variations less than 0.05% each other with the first seal clearance $H_1=1.18\%$ in which the case $C_3=135°$ achieves the largest deviation by 0.065% with respect to the shroudless case. As the leakage flow is minimal (i.e. seal clearance $H_1=1.18\%$) the diameter of the leakage vortices result relatively smaller and consequently the leakage flow with higher total temperature travels encapsulated inside the vortex as shown in Figure 4.32. As the leakage vortex impinges on the stator suction-side, the warmer leakage flow scarcely exceed 15% spanwise and continue axially traveling to the next row. As leakage flow increases, namely for the seal clearance $H_2=2.37\%$ and $H_3=3.56\%$, the case $C_3=135°$ achieves the largest deviations with respect to the shroudless case by 0.121% and 0.182%, respectively. As leakage flow increases, the diameter of leakage vortices increase and they can transport more leakage flow with higher total temperature in the core. In addition the velocity radial component increases and as the leakage vortices impinge on the stator suction-side the radial component spreads leakage flow with higher total temperature up to mid-span. This transport process is better illustrated in Figure 4.36. A similar transport of low total pressure occurs in the core of leakage vortices. For every 1% in seal clearance total temperature increases with respect to the shroudless case by 0.048%, 0.039% and 0.051% for cases $C_1=45°$, $C_2=90°$ and $C_3=135°$, respectively.

For every 1% increase in seal clearance the percentages of total pressure (0.114 to 0.132%) and total temperature (0.039 to 0.051%) seem to be negligible. However, the efficiency deterioration in the stage with respect to the shroudless case results 0.944, 0.828, and 0.924% for the cases $C_1=45°$, $C_2=90°$ and $C_3=135°$, respectively. This reveals that leakage flows are equally important as rotor tip flows.
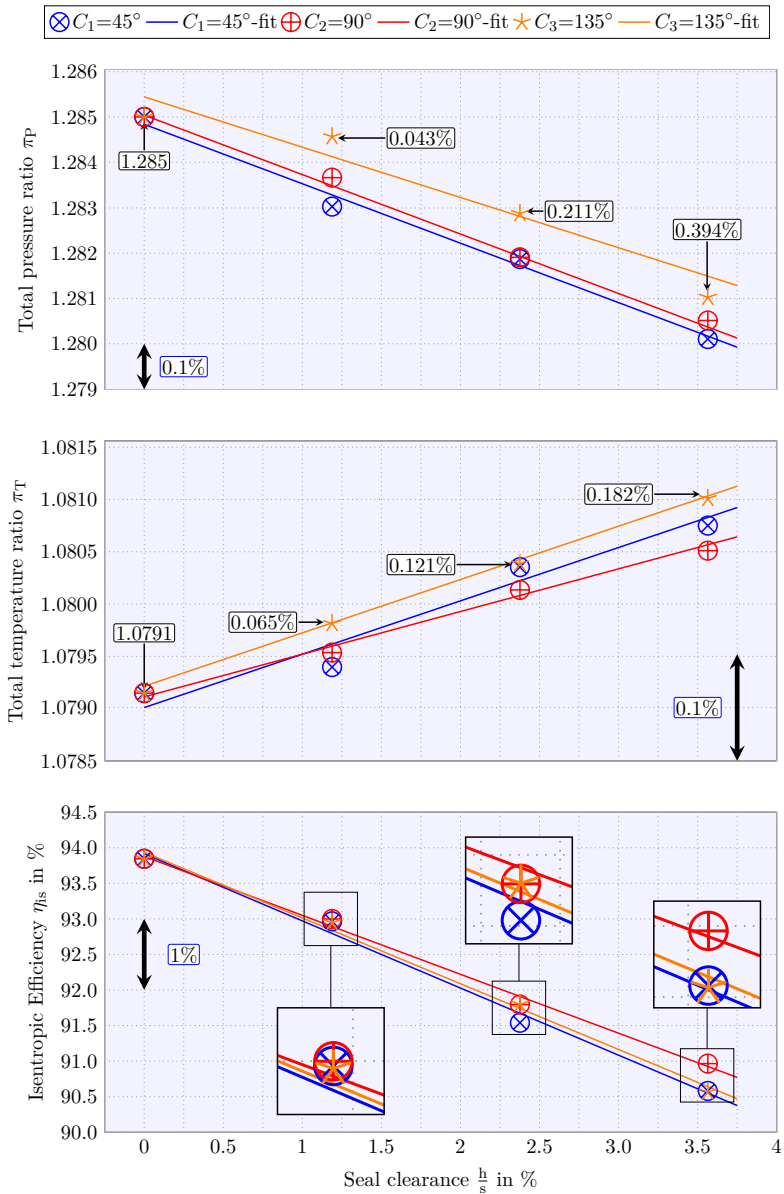
Figure 4.44: Third stage performance at design operating point

5. Conclusions

5.1 Aerodynamic effects

In terms of the labyrinth mass flow prediction, Egli's model (Egli 1935) predicts the labyrinth mass flow with very high accuracy for all configurations with mass flow rates below 0.3 %. For higher clerances this model estimates more conservative rates of leakage flow.

The configuration pointing in the main flow direction (C_1=45°) depicts the highest tangential velocity of 83.49%. Despite this case achieving the highest tangential velocity, it not necessarily compensates the highest rate of leakage flow.

Independently of the cavity outlet angle, the interaction of the upstream rotor wake and the leakage flow induces a wake-leakage vortex which provokes the formation of an adjacent induced-leakage vortex. This mechanism repeats until the next adjacent rotor wake induces a new wake-leakage vortex. The cavity outlet angle modifies the number of induced-leakage vortices.

The overall performance of the third compressor's stage shows that the effect of the cavity outlet angle is more sensitive with respect to lower leakage rates. As the leakage rate progressively increases, the cavity outlet angle reduces its sensitivity. For every 1% of labyrinth seal clearance increase, the stage total pressure ratio decreases between 0.114 to 0.132%, and total temperature ratio increases between 0.039 to 0.051% resulting in an isentropic efficiency reduction by 0.828 to 0.924% (i.e. almost 1%).

The case pointing against the main flow direction (C_3=135°) achieves the lowest total pressure ratio reduction but the highest total temperature ratio compared to remaining cases.

5.2 Thermal effects

The windage effect does not depend only on the tangential velocity component, but also on the radial velocity which dictates the leakage flow rate. The radial velocity component determines how fast the leakage flow is heated inside the cavity-trench. The case pointing against the main flow direction (C_3=135°) depicts the highest total temperature at the upstream cavity outlet surface. The case pointing in the main flow direction (C_1=45°) depicts the opposite effect, namely the windage effect is the minimal. The case pointing perpendicular to the main flow direction (C_2=90°) offers a trade-off between leakage flow rate and the windage effect. This investigation reveals that in the downstream cavity-trench a windage effect occurs similar to the upstream cavity-trench but with reduced intensity. Therefore, the downstream cavity-trench contributes a reduced windage effect. Downstream of the stator trailing edge, the flow of the main stream enters in the downstream cavity-trench. This incoming flow is re-energized and reheated as a consequence of the energy transfer that the rotor disc wall provides to the fluid. As a consequence the outgoing cavity flow is ejected with higher total temperature.

As the upstream cavity outlet ejects heated leakage flow into the main flow, a portion of the

warmer leakage mass flow remains trapped within the end-wall boundary layer region. The flow within the end-wall boundary layer reduces its temperature fast enough during its travel through the stator passage. This flow directs to the stator suction-side due to the cross-flow induced by the circumferential passage pressure gradient. As the leakage flow rate is low, the main part of the warmer leakage flow travels inside the wake-leakage vortices and a smaller portion remains within the end-wall boundary layer. As the leakage flow rate increases, the wake-leakage vortices do not transport all of the warmer leakage flow and a portion of this warmer leakage flow remains trapped within the end-wall boundary layer and the cross-flow is responsible of disseminating it on the stator suction-side. The recirculating flow structure inside the downstream cavity-trench prevents that warmer leakage flow re-enters in the downstream cavity-well and recirculates into the upstream cavity-trench. At the same time, the recirculation structure expels the re-energized leakage flow from the downstream cavity-trench. In this way, the leakage flow cannot recirculate to the upstream cavity-trench and be reheated.

Downstream of the stator trailing edge near the hub (approx. 5% span), circumferential flow distributions show that the highest total temperature locates on the stator suction-side. The origin of this highest total temperature comes from the warmer leakage flow transported by the wake-leakage vortices. Thus, the effect reported by Kerrebrock and Mikolajczak remains on the stator suction-side at the hub while at mid-span the effect appears on the stator pressure-side.

5.3   Unsteady effects

All investigated configurations modify the recovery effect near the hub, namely below 10% span with the inclusion of the cavity. The case pointing against the main flow direction (C_3=135°) reaches the highest overall recovery factor. The leakage flow affects the recovery effect mainly below 50% span.

5.4   Future work

This work shows the existence of the wake-leakage vortices due to the interaction of the leakage flow and the rotor wake. These wake-leakage vortices transport warmer leakage flow with low total pressure to the stator rear. As a consequence of this transport the stage performance severely diminishes. Considering that the rotor disc wall provides the most part of the energy to the leakage flow inside the cavity, however, the energy transfer has no benefit to the leakage flow. In contrast this energy transfer is wasted by heating the leakage flow. This energy could be better applied to the leakage flow. By means of a series of fins, protrusions or in the best case blades (i.e. as those used in a centrifugal impeller) manufactured on the rotor disc wall inside the cavity-trenches, the tangential impulse of the leakage flow could increase and consequently the effect on the main flow would be minimized. With these blades in the cavity, the energy transfer to the leakage flow would benefit the main flow by reducing the secondary flow near the hub. The windage effect probably diminishes because the blades accelerate tangentially the leakage flow and the energy would be better used.

A. Numerical discretization and flow simulation

All numerical simulations in this present investigation are conducted with the flow solver TRACE (Turbomachinery Research Aerodynamics Computational Environment) developed by the Institute of Propulsion Technology of the German Aerospace Center (DLR). This chapter depicts the fundamental equations of the fluid dynamics, turbulence and transition models, as well as boundary conditions.

A.1 Governing equations

The modelling of any phenomenon of the nature requires mathematical statements in order to be analyzed rationally and understood. In fluid mechanics, the governing equations allow fluid flows to be described mathematically. Computational fluid dynamics (CFD) is an approach that allows the governing equations to be solved numerically in order to predict with enough accuracy the behavior of fluid flows. The majority of CFD methods are based on continuity, impulse and energy equations. The physics of distinct types of flows included internal flows as turbomachinery flows can be studied and analyzed through fundamental equations.

Conservation of mass (continuity equation)

$$\frac{\partial \rho}{\partial t} + \frac{\partial (\rho u_i)}{\partial x_i} = 0,$$ (A.1)

Conservation of impulse (Newton's 2nd law)

$$\rho\Big(\frac{\partial u_i}{\partial t} + u_i \frac{\partial (u_j)}{\partial x_i}\Big) = \rho g_i + \frac{\partial \tau_{ij}}{\partial x_j}$$ (A.2)

Conservation of energy (1st law of thermodynamics)

$$\rho\Big(\frac{\partial e}{\partial t} + \frac{\partial (e u_i)}{\partial x_i}\Big) = \tau_{ji}\frac{\partial u_i}{\partial x_j} - \frac{\partial q_i}{\partial x_i}$$ (A.3)

As this equation system is posed in a three-dimensional spatial coordinate system, it becomes an undetermined consistent equations system, because it has less equations than unknown variables. More specifically, this system of equations contains five differential equations and 17 unknowns that are the density ρ, velocity components u_i, the stress tensor τ_{ij}, the specific internal energy per unit mass e and the heat flux vector q_k. The stress tensor is symmetric, leading to 14 unknowns. In order to achieve a determined equation system, additional equations have to complement the original system. Under the consideration of an isotropic[1] Newtonian[2] fluid and under consideration of the Stoke's hypothesis, the stress tensor results as folllows.

$$\tau_{ij} = -p\delta_{ij} + \mu\left(\frac{\partial u_i}{\partial x_j} + \frac{\partial u_j}{\partial x_i} - \frac{2}{3}\delta_{ij}\frac{\partial u_k}{\partial x_k}\right).$$ (A.4)

---

[1]A property is uniformly distributed in all directions

[2]This implies that the stress tensor and the symmetric part of the deformation tensor have a linear relation

After substitution of the stress tensor in equations A.1 to A.3, with the expression given in eq. A.4 the system results on the well known Navier-Stokes equations.

Even with the aforementioned assumptions the system is still not closed. Assuming that the fluid is a calorically perfect gas, the ideal gas equation can be used to relate pressure p, density ρ and temperature T by the specific gas constant for air R_a

$$p = \rho R_a T \quad \text{with} \quad R_a = 287.06 \;\; \frac{\text{J}}{\text{kg K}} \tag{A.5}$$

In order to compute the dynamic viscosity, the Sutherland's law is considered

$$\mu = \mu_0 \Big(\frac{T_0 + T_S}{T + T_S} \Big) \Big(\frac{T}{T_0} \Big)^{\frac{3}{2}} \quad \text{with} \quad \mu_0 = 1.7198 x 10^{-5} \text{Pa s,} \tag{A.6}$$

$$T_0 = 273 \text{ K,} \quad \text{and} \quad T_S = 110 \text{ K}$$

The specific internal energy e is computed by means

$$e = \frac{p}{(1 - \gamma)\rho} \tag{A.7}$$

with a heat capacity ratio γ of 1.4 for the air. The heat flux vector is computed using the Fourier's law by considering isotropy in the fluid and a heat conduction which relates linearly the temperature gradient

$$q_i = -k_l \frac{\partial T}{\partial x_i} \tag{A.8}$$

A.2   Turbulence models

The numerical solution of the Navier-Stokes equations for turbulent flows in all spatial and temporal scales of the flow is currently impractical and prohibitive. This type of simulation is called Direct Numerical Simulation (DNS), and is limited to low Reynolds numbers and elementary geometries. According to Riéra (2014) these simulations require extremely fine meshes in the order $\text{Re}^{\frac{9}{4}}$ with extremely tiny time-steps in the order $\text{Re}^{\frac{11}{4}}$ in order to capture the smallest scales. In order to employ the Navier-Stokes equations to practical engineering applications, the variables are decomposed into a time-averaged mean flow component ϕ_i and the corresponding fluctuating component ϕ_i'

$$\phi_i(t) = \bar{\phi}_i + \phi_i' \tag{A.9}$$

with the time-averaged definition

$$\bar{\phi} = \frac{1}{T} \int_0^T \phi dt \tag{A.10}$$

By averaging the impulse equation (A.2) and neglecting the fluctuating part, the averaged stress tensor results

$$\tau_{ij} = -\bar{p}\delta_{ij} + \eta \left(\frac{\partial \bar{u}_i}{\partial x_j} + \frac{\partial \bar{u}_j}{\partial x_i} \right) - \rho \overline{u_i' u_j'} \tag{A.11}$$

By substituting the averaged-stress tensor in equations A.1 to A.3, the Reynolds Averaged Navier Stokes (RANS) equations are obtained. The resulting term $\rho \overline{u_i' u_j'}$ in eq. A.11 is known as the Reynolds stresses. This term is unknown, thus it has to be modeled with supplementary differential equations. There is a huge variety of models for closing the system of equations. The complexity of the closing depends on the number of partial differential equations to close the problem, they can have zero- (algebraic models), one- (Spallarat-Allmaras), two- (k-ω, SST), three- (k-ϵ-A), four- (v^2-f) or seven (Reynolds stress) equations. The computational cost is directly linked to the number of additional equations to close the problem, however the closing does not guarantee that the physical phenomenon will be modeled succssfully.

One other important consideration used is the Boussinesq hypothesis, which relates the Reynolds stresses to the mean velocity gradients

$$\tau_{ij} = -\rho \overline{u_i' u_j'} = 2\mu_\text{T} s_{ij} - \frac{2}{3}\rho k \delta_{ij} \tag{A.12}$$

For this work, the k-ω by Wilcox (1988) and k-ω SST by Menter et al. (2003) are evaluated. A brief introduction of both turbulence models will be given in subsections A.2.1 and A.2.2.

A.2.1   Wilcox's k-ω model

This two-equation turbulence model has its origin in late 80s, and came about due to the lack of "complete" models of turbulence for closing the RANS equations. Wilcox (1988) defines the term "complete" as a set of equations that can be used to predict a given turbulent flow with no advance information other than boundary conditions required in order to achieve the solution. The model has been used worldwide in academy and industry, as well as turbomachinery applications such as TRACE.

The eddy viscosity is modeled as

$$\mu_\text{T} = \gamma^* \frac{\rho k}{\omega}. \tag{A.13}$$

The turbulent mixing energy is modeled with

$$\frac{\partial(\rho k)}{\partial t} + \frac{\partial(\rho u_j k)}{\partial x_j} = \tau_{ij}\frac{\partial u_i}{\partial x_j} - \beta^* \rho \omega k + \frac{\partial}{\partial x_j}\left[(\mu + \sigma^* \mu_T)\frac{\partial k}{\partial x_j}\right]. \tag{A.14}$$

while the specific dissipation term is

$$\frac{\partial(\rho\omega)}{\partial t} + \frac{\partial(\rho u_j \omega)}{\partial x_j} = (\frac{\gamma\omega}{k})\tau_{ij}\frac{\partial u_i}{\partial x_j} - \beta\rho\omega^2 + \frac{\partial}{\partial x_j}\left[(\mu + \sigma\mu_T)\frac{\partial\omega}{\partial x_j}\right]. \tag{A.15}$$

The coefficients of the model are:

$$\beta = \frac{3}{40}, \quad \beta^* = \frac{9}{100}, \quad \gamma = \frac{5}{9}, \quad \gamma^* = 1, \quad \sigma = \frac{1}{2}, \quad \sigma^* = \frac{1}{2}.$$

The turbulence model's production terms have been modified in order to avoid high rates of turbulent kinetic energy at the stagnation point by using the Kato and Launder (1993) correction

$$\tau_{ij}\frac{\partial u_i}{\partial x_j} = \mu_T |S_{ij}|^2 \approx \mu_T |S_{ij}| |\Omega_{ij}| \quad \text{with} \quad \Omega_{ij} = \frac{1}{2}\left(\frac{\partial u_i}{\partial x_j} - \frac{\partial u_j}{\partial x_i}\right). \tag{A.16}$$

A.2.2   Menter's k-ω SST model

The SST turbulence model from (Menter 1993) originated as a variant of the Wilcox's model (e.g. k-ω) because the previous turbulence models (e.g. k-ϵ) had a lack of sensitivity to adverse pressure-gradients, that in turn overestimate shear-stresses and thus delay the separation. The idea behind this model is to use the k-ω model near the wall, and the k-ϵ model far away from the boundary layer. The SST model has the particularity of modifying the definition of the eddy-viscosity for adverse pressure-gradient boundary-layer flows. In this work, the version of Menter et al. (2003) is used.

The turbulent energy k is modeled by SST model

$$\frac{\partial(\rho k)}{\partial t} + \frac{\partial(\rho u_j k)}{\partial x_j} = \tilde{P}_k - \beta^* \rho \omega k + \frac{\partial}{\partial x_j}\left[(\mu + \sigma_k \mu_t)\frac{\partial k}{\partial x_j}\right]. \tag{A.17}$$

In order to prevent the build-up of turbulence in stagnation regions, a production limiter is introduced in the turbulent energy equation:

$$\tilde{P}_k = \min(P_k, 10 \cdot \beta^* \rho \omega k) \quad \text{with} \quad P_k = \mu_t \frac{\partial u_i}{\partial x_j}\left(\frac{\partial u_i}{\partial x_j} + \frac{\partial u_j}{\partial x_i}\right). \tag{A.18}$$

While the dissipation term is computed as

$$\frac{\partial(\rho \omega)}{\partial t} + \frac{\partial(\rho u_j \omega)}{\partial x_j} = \alpha \rho S^2 - \beta \rho \omega^2 + \frac{\partial}{\partial x_j}\left[(\mu + \sigma_\omega \mu_t)\frac{\partial \omega}{\partial x_j}\right] + 2(1 - F_1)\rho \sigma_{\omega 2}\frac{1}{\omega}\frac{\partial k}{\partial x_j}\frac{\partial \omega}{\partial x_j} \tag{A.19}$$

where the blending function F_1 is defined by

$$F_1 = \tanh\left\{\left\{\min\left[\max\left(\frac{\sqrt{k}}{\beta^* \omega y}, \frac{500\nu}{y^2\omega}\right), \frac{4\rho \sigma_{\omega 2}k}{CD_{k\omega}y^2}\right]\right\}^4\right\} \tag{A.20}$$

with the cross-diffusion term as

$$CD_{k\omega} = \max\left(2\rho \sigma_{\omega 2}\frac{1}{\omega}\frac{\partial k}{\partial x_j}\frac{\partial \omega}{\partial x_j}, 10^{-10}\right). \tag{A.21}$$

The SST model defines the turbulent eddy viscosity for regions with adverse pressure gradients as

$$\nu_t = \frac{a_1 k}{\max\left(a_1\omega, SF_2\right)} \tag{A.22}$$

with F_2 the second blending function and S the invariant measure of the strain

$$F_2 = \tanh\left\{\left[\max\left(\frac{2\sqrt{k}}{\beta^* \omega y}, \frac{500\nu}{y^2\omega}\right)\right]^2\right\}. \tag{A.23}$$

The constants of this model are:

$$\beta = \frac{3}{40}, \quad \beta^* = \frac{9}{100}, \quad \alpha_1 = \frac{5}{9}, \quad \sigma_{k1} = \frac{17}{20}, \quad \sigma_{\omega 1} = \frac{1}{2},$$

$$\alpha_2 = \frac{11}{25}, \quad \beta_2 = \frac{207}{2500}, \quad \sigma_{k2} = 1, \quad \sigma_{\omega 2} = \frac{107}{1250}.$$

The high turbulent kinetic energy at the stagnation point bases on the Cauchy-Schwarz inequality

$$\left(\overline{u'_i u'_j}\right)\left(\overline{u'_i u'_j}\right) \leq \overline{u'^2_i u'^2_j} \tag{A.24}$$

and corrected by means of the lower bound

$$\omega = \max\left(\omega, \frac{1}{2}\sqrt{3}\cdot\sqrt{2S_{ij}S_{ij}}\right). \tag{A.25}$$

A.3   Transition models

Besides turbulence models, TRACE contains two transition models based on experimental correlations, which can be independently added to the turbulence model. Marciniak et al. (2010) implemented the multimode and the $\gamma - Re_\theta$ transition model in TRACE.

A.3.1 $\gamma - Re_\theta$ model

The $\gamma - Re_\theta$ transition model originally was developed by Langtry et al. (2006), Langtry (2006) and Menter et al. (2006) for turbomachinery flows. Over the years it has been modified with numerous enhancements and generalizations to be applied in other flows (Langtry and Menter 2009). The model is based in experimental correlations that are based on freestream values.

The model is based on two equations, one for the intermittency which is used to trigger the transition process

$$\frac{\partial(\rho\gamma)}{\partial t} + \frac{\partial(\rho u_i \gamma)}{\partial x_i} = P_\gamma - E_\gamma + \frac{\partial}{\partial x_i}\left[\left(\mu + \frac{\mu_t}{\sigma_\gamma}\right)\frac{\partial\gamma}{\partial x_i}\right] \tag{A.26}$$

and one for the transition onset criterion Re_θ.

$$\frac{\partial(\rho\tilde{R}e_{\theta t})}{\partial t} + \frac{\partial(\rho u_i \tilde{R}e_{\theta t})}{\partial x_i} = P_{\theta t} + \frac{\partial}{\partial x_i}\left[\sigma_{\theta t}(\mu + \mu_t)\frac{\partial\tilde{R}e_{\theta t}}{\partial x_i}\right] \tag{A.27}$$

with the transition sources defined as

$$P_\gamma = f(F_{\text{length}}, F_{\text{onset}}) \quad \text{and} \quad E_\gamma = f(F_{\text{length}}, F_{\text{onset}}) \quad \text{and} \quad P_{\theta t} = f(Re_{\theta t})$$

where F_{length} and F_{onset} are empirical correlations that control the length and the beginning of the transition region, respectively. $Re_{\theta t}$ is the transition momentum-thickness Reynolds number. Because the model is based on experimental correlations, over the years several correlations have been published. All closure correlations that were implemented in TRACE are taken from Malan et al. (2009).

A.3.2   Multi-mode model

This transition model developed by Kožulović (2007), Kožulović et al. (2007) is based on the integration of momentum thickness δ_2 of the boundary layer normal to the wall. The transition onset of three different modes of transition can be modeled: natural and bypass, separation-induced, and wake-induced transition. Corresponding correlations are calibrated against experimental data. The correlation for the natural and bypass transition is based on the AGS-criterion. Separation-induced transition occurs when negative wall shear stresses are encountered. Both the natural and bypass as well as separation-induced transition are influenced by the same parameters, the turbulent intensity and the pressure gradient. The wake-induced mode can be directly coupled to a turbulence model in unsteady simulations, while for the steady state simulation a "quasi-unsteady" approach that models the unsteady wakes of the upstream blades has been implemented. The coupling of this transition model is directly applied to k-ω turbulence model by multiplying the source terms with the intermittency γ. More details about this transition model are found in Kožulović (2007). The resulting equations of the k-ω turbulence model already multiplied with intermittency are:

$$\frac{\partial(\rho k)}{\partial t} + \frac{\partial(\rho u_i k)}{\partial x_i} = \gamma \left(\tau_{ij} \frac{\partial u_i}{\partial x_i} - \beta^* \rho k \omega \right) + \frac{\partial}{\partial x_i} \left[(\mu + \sigma_k \mu_t) \frac{\partial k}{\partial x_i} \right] \tag{A.28}$$

$$\frac{\partial(\rho \omega)}{\partial t} + \frac{\partial(\rho u_i \omega)}{\partial x_i} = \max(\gamma, 0.02) \left(\alpha \frac{\omega}{k} \tau_{ij} \frac{\partial u_i}{\partial x_i} - \beta \rho \omega^2 \right) + \frac{\partial}{\partial x_i} \left[(\mu + \sigma_\omega \mu_t) \frac{\partial \omega}{\partial x_i} \right]. \tag{A.29}$$

The evaluation of both transition models on turbomachinery flows was carried out by Marciniak et al. (2010). They compare the transition models with experimental data and fully turbulent simulations for three test cases, in order to evaluate the model capability to accurately predict transitional flows. The first case is the T106A turbine cascade, with a Reynolds number from $1.5 \cdot 10^5$ to $1.1 \cdot 10^6$. For low Reynolds numbers, a separation bubble can be observed in the pressure coefficient experimental data. In contrast to a fully turbulent model, both transition models accurately predict the separation bubble length. However, the γ-Re_θ model depicts slightly higher values of pressure coefficient than the multi-mode model in the bubble-separation zone. For the remaining high Reynolds number cases, a turbulent layer is expected and all numerical predictions show good agreement with experimental data. The second case is the high-loaded T106C turbine cascade, in which the experimental Reynolds number is from $1.2 \cdot 10^5$ to $2.5 \cdot 10^5$. Both transition models follow the trend of the measurements, however the multi-mode model depicts values closer to experiment than the γ-Re_θ. The third test case is a multistage low-pressure turbine, and the experimental data are presented in terms of isentropic efficiency. Both transition models achieve good consistency with experimental data. The γ-Re_θ model seems to predict the efficiency deterioration more accurately for smaller Reynolds numbers.

A.4   Numerical methods

The simulations for this thesis are performed with the Turbomachinery Research Aerodynamics Computational Environment (TRACE) solver developed at the Institute of Propulsion Technology of the German Aerospace Center (DLR). TRACE is a multi-purpose, three-dimensional,

steady and unsteady, parallelized multi-stage Reynolds-Averaged Navier-Stokes flow solver for structured and unstructured meshes. TRACE is used at many German universities and institutes to simulate turbomachinery flows. For flux computations, TRACE uses a total variation diminishing-upwind-scheme (TVD) by Roe, with a second-order MUSCL-scheme (Monotonic Upstream-Centered Scheme for Conservation laws). Spatial discretization of steady- and unsteady simulations is solved with a second-order Fromm scheme, along with the VanAlbada-flux limiter in order to avoid numerical oscillations, while the temporal discretization uses a Predictor-Corrector method. The temporal discretization of unsteady simulations also includes the Euler backward scheme. Turbulence and transition equations are solved by means of an ILU (Incomplete LU-factorization) method. Detailed information about the numerical implementation can be found in Kügeler (2004) and Nürnberger (2004).

A.4.1   Boundary conditions

The fluid is air, modeled as an ideal gas, and viscosity is computed using Sutherland's law. All surfaces inside the computational domain are considered as adiabatic walls, which means no heat transfer through the walls and a no-slip condition (e.g. zero velocity at face) is set. The boundary conditions are taken directly from experimental data at the design operating point (Braun 2007). At the inlet, radial profiles of total pressure, total temperature, flow angles, turbulence intensity, turbulent length, and Mach number are specified. The outflow boundary condition is prescribed with radial distributions of static pressure or with the mass flow, depending on the operating point. A mass flow condition is imposed at the operating points at which there is increased loading because of convergence stability. The rotor-stator interface uses the mixing-plane approach for steady-state simulations, while a zonal interface is set up for unsteady simulations. The cavity coupling is achieved by means of a zonal interface, which is a conservative mixed-cell approach of second-order accuracy described by Yang et al. (2003). A Fourier non-reflecting approach at inlet and outlet is applied in order to vanish spurious nonphysical mass and energy exchange through the domain. Periodic boundaries are applied for both single- and multi-blade passages. All blocks are complemented with two external ghost cells at each boundary including periodic and symmetry boundaries, in order to improve the accuracy at boundary cells. Every single block of the grid is extended by ghost-cell layers at each boundary in order to get 2nd order accuracy even at the boundary cells. Depending on the boundary type, the ghost-cell values are set by values according to the special boundary condition or by values of the neighboring blocks. Steady simulations use a ramping CFL setup. Within the first 100 iterations, the CFL number is set to 1. After 100 iterations it is increased to 50 and after 1000 iterations is left constant at 400. For steady simulations, the flow field of the four-stage high-speed axial compressor is simulated by considering one pitch of every blade row, because the flow is assumed to be axi-symmetric.

For unsteady computations, a fully converged stationary simulation is set as initial solution in order to guarantee a numerically stable solution. In addition, all rotor-stator interfaces have to be changed from mixing-planes to zonal interfaces in order to allow the wake transport from upstream rows. The Fourier method also has to be changed to Giles method (Giles 1990, 1991) at interfaces, inflow and outflow. For unsteady simulations the CFL is fixed to 400 and 150 time-steps per period along with 10 sub-iterations per time-step.

A.5   Data Reduction

This section provides a brief description and definition of the techniques and performance variables utilized for the analysis and evaluation of the (U)RANS solutions within this work. The variables apply for the overall and stage performance, which is evaluated and analyzed by means of the next definitions: The mass flow is computed as the reduced mass flow $\dot{m}_{\text{red}}$ referred to inlet conditions, and can be expressed as

$$\dot{m}_{\text{red}} = \frac{\dot{m}\sqrt{RT_1}}{D^2 P_1} \tag{A.30}$$

The meridional velocity V_{mer}, the resulting velocity V and the flow angle α are defined as

$$V_{mer} = \sqrt{V_{ax}^2 + V_{rad}^2} \tag{A.31}$$

$$V = \sqrt{V_{\text{ax}}^2 + V_{\text{rad}}^2 + V_{\text{tan}}^2} = \sqrt{V_{\text{mer}}^2 + V_{\text{tan}}^2} \tag{A.32}$$

$$\alpha = tan^{-1}\left(\frac{V_{\text{tan}}}{V_{\text{mer}}}\right) \tag{A.33}$$

In the definition of any ratio it is important to compare the outlet conditions with respect to inlet or initial conditions. Herein pressure and temperature ratios are defined, the use of these ratios can be applied to total-to-total or static-to-static variables in both cases pressure

$$\pi_{\text{P}} = \frac{P_2}{P_1} \tag{A.34}$$

and temperature

$$\pi_{\text{T}} = \frac{T_2}{T_1}. \tag{A.35}$$

Additionally to total pressure and total temperature ratios, the normalized total pressure is defined as follows:

$$\theta_{\text{P}} = \frac{P - P_{\text{ref}}}{P_{\text{max,out}} - P_{\text{ref}}}. \tag{A.36}$$

and normalized total temperature

$$\theta_{\text{T}} = \frac{T - T_{\text{ref}}}{T_{\text{max,out}} - T_{\text{ref}}}. \tag{A.37}$$

both definitions are referred to inlet and outlet conditions of the axial compressor.

The use of total pressure and total temperature ratios can be used in the computation of both isentropic and polytropic efficiencies as

$$\eta_{\text{is}} = \frac{\left(\frac{P_2}{P_1}\right)^{\frac{\gamma-1}{\gamma}} - 1}{\frac{T_2}{T_1} - 1} = \frac{\left(\pi_{\text{P}}\right)^{\frac{\gamma-1}{\gamma}} - 1}{\pi_{\text{T}} - 1} \tag{A.38}$$

$$\eta_{pol} = \frac{\gamma-1}{\gamma}\frac{\ln\left(\frac{P_2}{P_1}\right)}{\ln\left(\frac{T_2}{T_1}\right)} = \frac{\gamma-1}{\gamma}\frac{\ln\left(\pi_{\text{P}}\right)}{\ln\left(\pi_{\text{T}}\right)}. \tag{A.39}$$

The use of two-dimensional loss correlations are assumed, as the radial variations of fluid are minimal, e.g. at the midspan. Due to the highly three-dimensional interaction of the upstream cavity leakage flow with the end-wall boundary layer and a posteriori with the suction side boundary layer, these two-dimensional correlations are not used. In the rear stages of an axial compressor the temperature rise plays an important role (Scott et al. 2000, Lewis 2002), which contributes to the loss generation. Therefore, entropy will be used to quantify the losses because the frame of reference is independent, and it involves both pressure and temperature.

$$\Delta S = C_p \ln\left(\frac{T}{T_{\text{ref}}}\right) - R \ln\left(\frac{P}{P_{\text{ref}}}\right). \tag{A.40}$$

In open literature there are excellent examples of the vortex detection (Roth 2000, Fuchs 2008, Holmén 2012, Kolář 2007). There are distinct methods to perceive the rotating flow structures, this section is not intended to explain or give an opinion of which is better. In this thesis the Q-criterion (Hunt et al. 1988) is used, which is a term of the characteristic equation of the velocity gradient tensor ∇u given by

$$\lambda^3 + P\lambda^2 + Q\lambda + R = 0 \tag{A.41}$$

where the coefficients or invariants P, Q and R are defined as follows

$$P = -\nabla \cdot u \tag{A.42}$$

$$Q = \frac{1}{2}(||\Omega||^2 - ||S||^2) \tag{A.43}$$

$$R = -\det \nabla u. \tag{A.44}$$

The terms involved in the Q-criterion are the rate-of-strain tensor S,

$$S = \frac{1}{2}[\nabla u + (\nabla u)^T] \tag{A.45}$$

and the rate-of-rotation tensor Ω

$$\Omega = \frac{1}{2}[\nabla u - (\nabla u)^T] \tag{A.46}$$

Physically, the Q-criterion highlights the zones where the vorticity magnitude surpasses over the strain-rate magnitude, therefore $Q > 0$.

A.5.1   Errors

This section is devoted to ponder the sensitivity of the model through the analysis of distinct modeling, numerical and systematic errors.

The confidence in CFD-solvers strongly depends on the minimization of errors during the pre-processing and simulation. A precise distinction of errors helps to diminish them, and in some cases to avoid them. It is important to distinguish between the definition of error and uncertainty. According to the ASME V & V 20 Committee (2009) Standard, Error is defined as the result of a measurement minus a true value of the measurand. The above definition is given in terms of experiments. For computational simulations, an appropriate interpretation would be that the error means the difference between the simulation result and an experiment or an analytical

solution being the reference value to be compared. This deficit contains a series of errors that can be distinguished and classified into two main categories: acknowledged errors which are recognizable and procedures exist to minimize them, while the unacknowledged errors are the opposite.

Physical modeling error is mainly due to the lack of knowledge of physical phenomena, and resulting simplifications in the formulation of the model that have to be made. Turbulence, transition and combustion modeling are good examples for this type of error. Currently, there are hundreds of turbulence models, and each contains its own constants and constraints. This is mainly due to the fact that the turbulence phenomenon is not deeply understood, and the constants strongly depend on the turbulence model application. Physical model errors are examined and potentially diminished through validation cases that are focused in specific and complex modeling (e.g. turbulence and transition in boundary layers on a flat plate). Sometimes the modeling is limited because the experimental validation is not feasible, or the information is insufficient.

Round-off error refers to the capacity of the device (i.e. computer or supercomputer) to compute a accurate realistic value. The accuracy strongly depends on the computational resources. Typically the calculations can be computed with single precision numbers, but if the round-error is intended to be minimized then double precision numbers have to be used.

Discretization error arises due to the mapping of governing equations into algebraic expressions in spatial and temporal domains, which are represented by the mesh and time-step, respectively. The discretization error can be categorized in local error, which is located at the level of the element size and global error which is the accumulation of local errors. Theoretically, the discretization error tends to zero as the grid spacing also tends to zero. However as the mesh is refined enough the solution becomes less sensitive to the spatial discretization. Although the spatial domain would be meshed with grid spacing equal to zero, the discretization error still would contain the truncation error that is caused by the use of Taylor series expansion for linear PDEs, and the high terms of discretization are neglected.

The pollution error refers to the error that is transported, advected and diffused from other regions. The level of the discretization heavily depends on the mesh density, and for the case of time-dependent solutions on the selected time-step.

Other types of errors are: Iterative convergence error, which is attributed to the difference between a converged and an exact solution. Programming error refers to bugs in the code. These errors are found consistently by debbuging the code in subparts. Usage error is due to the improper use of the code. This error is eventually diminished by training and accumulated experience.

B. Performance curves at design speed and radial distributions

This appendix gives the performance curves of the 4AV at design speed of 17,100 RPM and radial distribution downstream of each row. Braun (2007) provides more information about the setup of the test rig.

Table B.1: Overall performance of the four-stage axial compressor

Mass flow in kg/s	Static pressure ratio π_s	Static-to-total pressure ratio $\pi_{s\text{-}t}$	Total pressure ratio π_T	Isentropic efficiency η_{is}	Reduced mass flow
8.086744324	2.401987703	2.26807	2.79016661	0.83125	1.341282541
8.087206318	2.41788959	2.2865	2.80253044	0.83516	1.341359168
8.091310958	2.45581523	2.30651	2.834725693	0.84385	1.342039971
8.092051333	2.521803053	2.35518	2.890583587	0.8575	1.342162771
8.079541955	2.59951019	2.40174	2.953602707	0.87006	1.340087942
8.065640671	2.65116246	2.4382	2.99316096	0.87745	1.337782249
8.043002962	2.739401257	2.49142	3.066162977	0.88634	1.334027517
8.024422507	2.78783591	2.52462	3.10165659	0.88899	1.330945728
7.992390918	2.84703437	2.5683	3.145293073	0.89364	1.325632908
7.971559724	2.88163375	2.59173	3.17229795	0.89583	1.322177807
7.944248766	2.925536867	2.62096	3.2031722	0.89692	1.317647961
7.900306022	2.96619637	2.6556	3.23236417	0.89842	1.310359535
7.825172754	3.007643853	2.71254	3.256554123	0.89919	1.297897791
7.705747285	3.034289117	2.73396	3.263306373	0.89863	1.278089659
7.485032577	3.018821157	2.75997	3.245477117	0.89197	1.241481505
7.343774926	3.015914437	2.76102	3.23311845	0.8827	1.218052247
7.224574531	3.01119931	2.76629	3.222745097	0.87337	1.198281446
7.075095755	3.003171833	2.76641	3.208458737	0.86117	1.173488617
6.929384008	2.98587449	2.76712	3.18418391	0.85003	1.149320594
6.801358342	2.977199393	2.772	3.175100003	0.83756	1.128086017
6.742175716	2.968841227	2.76566	3.166099863	0.83207	1.118269876
6.684319842	2.923582073	2.76445	3.125134703	0.82619	1.108673793
6.627127345	2.91027776	2.75969	3.11060603	0.81931	1.099187738
6.528515301	2.900962427	2.75434	3.099386687	0.81228	1.08283176

Table B.2: Radial distributions downstream of the blades

Inlet guide vane		
Span-wise in %	Total pressure ratio	Total temper-ature ratio
5.763269	0.989365	0.996958
8.751524	0.998684	0.996805
12.486841	0.996837	0.996277
16.755776	0.997768	0.996089
23.159178	0.999724	0.995963
28.495346	0.996246	0.995421
39.167682	0.998966	0.995856
51.227423	0.997047	0.996198
65.955247	0.986755	0.996216
80.576348	0.987774	1.000447
89.327664	0.978412	1.002515
94.130215	0.965804	1.004626
95.731065	0.959914	1.006064
96.798299	0.955578	1.006878
97.865533	0.950571	1.007081

Stator 1		
Span-wise in %	Total pressure ratio	Total temper-ature ratio
6.626854	1.252858	1.076926
9.937958	1.252955	1.075632
15.235725	1.260949	1.075251
21.857934	1.273270	1.076222
28.480143	1.282523	1.076493
35.102352	1.288764	1.077024
41.724561	1.294680	1.077706
48.346770	1.297791	1.077855
54.968979	1.298523	1.077998
61.591188	1.298146	1.078178
68.213397	1.298877	1.079066
74.835606	1.299618	1.081340
81.457815	1.301872	1.084617
89.404466	1.304163	1.090842
97.351116	1.279999	1.099147

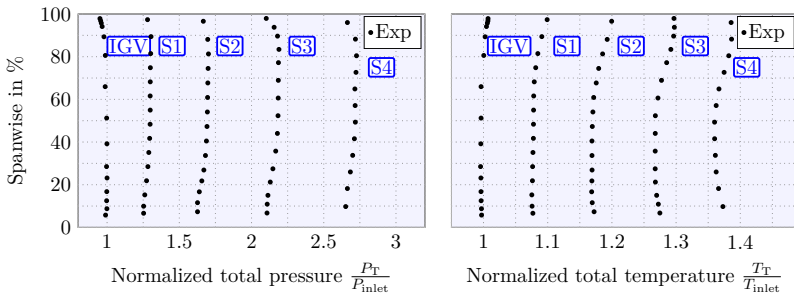| Stator 2		
Span-wise in %	Total pressure ratio	Total temper-ature ratio
7.326368	1.626063	1.172257
11.577452	1.626065	1.169349
16.678753	1.638582	1.168482
21.780054	1.655861	1.168837
26.881355	1.670005	1.169109
33.683089	1.681180	1.168975
40.484824	1.687868	1.168935
47.286558	1.691780	1.169471
54.088293	1.694413	1.170399
60.890027	1.695782	1.171647
67.691761	1.697506	1.175617
74.493496	1.699373	1.179421
81.295230	1.701844	1.185524
88.096965	1.696844	1.192670
96.599133	1.666167	1.199609

Table B.3: Radial distributions downstream of the blades

Stator 3		
Span-wise in %	Total pressure ratio	Total temper-ature ratio
6.736644	2.107299	1.274736
10.881682	2.108577	1.272348
15.026720	2.113587	1.269705
21.244277	2.129742	1.267761
27.461834	2.147871	1.267436
35.751911	2.167496	1.267457
44.041987	2.179247	1.267549
52.332063	2.183482	1.267698
60.622139	2.184697	1.271763
68.912215	2.185406	1.277262
77.202291	2.186362	1.285289
83.419848	2.189814	1.291845
89.637405	2.179895	1.296163
93.782443	2.156394	1.297289
97.927481	2.102032	1.296711

Stator 4		
Span-wise in %	Total pressure ratio	Total temper-ature ratio
9.755974	2.651859	1.372932
18.202459	2.663742	1.366133
25.982117	2.684203	1.362427
33.761774	2.700356	1.361168
41.541431	2.712107	1.360037
49.321089	2.718781	1.359948
57.100746	2.717413	1.362422
64.880404	2.715737	1.366760
72.660061	2.723363	1.374794
80.439719	2.726840	1.382060
88.219376	2.719305	1.386415
95.999033	2.663838	1.385710

Rotor 1		
Span-wise in %	Total pressure ratio	Total temper-ature ratio
5.894630	1.271615	1.073503
7.894369	1.270803	1.074093
11.188057	1.259757	1.073399
12.834901	1.266074	1.074093
18.363591	1.286200	1.075933
26.009652	1.302805	1.080167
38.831509	1.307546	1.080548
52.829683	1.307989	1.081451
66.710225	1.306093	1.083151
80.708399	1.305206	1.088600
88.236829	1.316240	1.098178
92.353939	1.301057	1.104390
95.294731	1.274372	1.106507
96.471049	1.264203	1.106403
97.647366	1.235008	1.104425
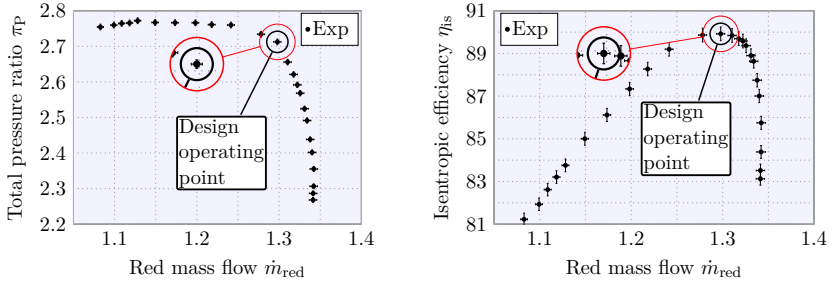
(a) Overall performance of the four-stage axial compressor

(b) Radial distributions downstream of the stators at design operating point

(c) Radial distributions downstream of the rotors at design operating point

Figure B.1: Overall performance curves and thermodynamic radial distributions

Table B.4: Radial distributions downstream of the blades

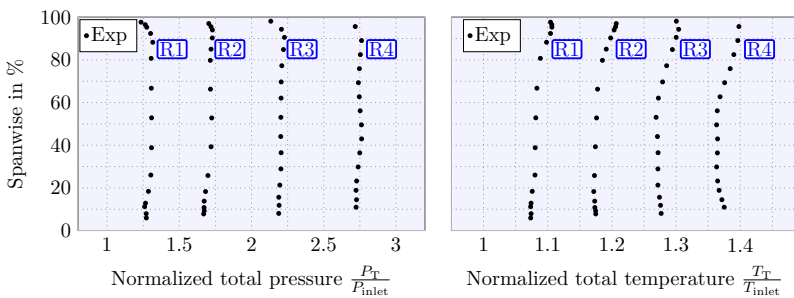| Rotor 2			Rotor 3			Rotor 4		
Span-wise in %	Total pressure ratio	Total temper-ature ratio	Span-wise in %	Total pressure ratio	Total temper-ature ratio	Span-wise in %	Total pressure ratio	Total temper-ature ratio
7.784970	1.668774	1.174839	8.022704	2.188296	1.276766	10.939702	2.723849	1.374978
9.284401	1.672839	1.174562	11.815582	2.191150	1.275724	14.449467	2.726967	1.371334
10.783832	1.671434	1.173451	15.608460	2.188747	1.274128	18.836674	2.723443	1.366996
13.782695	1.672265	1.173208	21.297777	2.195982	1.271664	23.223881	2.727572	1.364706
18.280989	1.681518	1.171751	28.883534	2.203405	1.271664	29.804691	2.738092	1.363109
25.778146	1.698451	1.172861	36.469290	2.204957	1.271907	36.385501	2.749280	1.364359
39.273029	1.719871	1.174284	44.055047	2.202401	1.270935	42.966312	2.762148	1.364602
52.767911	1.724413	1.176089	53.063132	2.203206	1.268853	49.547122	2.761342	1.363075
66.262794	1.715718	1.177651	62.071218	2.204367	1.272393	56.127932	2.752018	1.364151
79.757676	1.714495	1.185251	69.656974	2.205339	1.278952	62.708742	2.745980	1.368454
85.005686	1.719763	1.191185	77.242731	2.209571	1.285268	69.289552	2.739814	1.375603
90.253696	1.728601	1.198022	84.828487	2.221097	1.294222	75.870363	2.746891	1.384279
94.002274	1.729006	1.203505	90.517805	2.227827	1.300191	82.451173	2.753480	1.389936
95.501706	1.719395	1.205761	94.310683	2.207087	1.304008	89.031983	2.761573	1.396113
97.001137	1.704230	1.206767	98.103561	2.133388	1.300434	95.612793	2.717915	1.397848

C. GCI Analysis

Table C.1: Details of the grid convergence analysis

	Isentropic efficiency η_{is}			Total pressure ratio π_P			Reduced Mass Flow $\dot{m}_{red}$		
	N_1	N_2	N_3	N_1	N_2	N_3	N_1	N_2	N_3
Mesh in Mio	132.35	12.76	1.65	132.35	12.76	1.65	132.35	12.76	1.65
f_1, f_2, f_3	92.136	91.973	90.557	2.7064	2.7055	2.6942	1.3006	1.2978	1.2628
r_{21}	2.1808								
r_{32}	1.9764								
p		3.2224			3.839			3.735	
f_{extra}		92.1504			2.7065			1.3009	
GCI (%)	0.0195	0.2411	2.1656	0.0021	0.0411	0.5619	0.0156	0.2872	3.6578
EERE	0.0156	0.1925	1.7291	0.0016	0.0016	0.4494	0.0125	0.2292	2.9195
A_{flag}		1.0018			1.0003			1.0022	
$p_{conservative}$	1								
$f_{extrap1}$		92.274			2.7071			1.3031	
GCI_{p1} (%)	0.1873	1.971	3.8955	0.0331	0.5334	1.0543	0.2295	3.4522	6.8228
$EERE_{p1}$	0.1496	0.3262	1.8608	0.0264	0.0576	0.4741	0.1832	0.3996	3.0853

D. Convergence Criteria

D.1 Convergence criteria

In this work the quality of the solutions of all steady-state simulations of the four-stage axial compressor is evaluated by means of the global parameter convergence in the main flow path for all stages, namely mass flow $\dot{m}_{\text{red}}$, total pressure ratio π_{P} and isentropic efficiency η_{is}. All simulations use identical boundary conditions (see Appendix A.4.1), aside from the outlet conditions which are adopted to specific operating point. For convenience, Figure D.1a shows solely the convergence monitors of the third stage at 90° with the tightest clearance and the shroudless model for the purpose of comparing the computational time required in both simulations at the design operating point. For the shroudless model, the constancy of the three parameters is reached after 20,000 iterations while the model including the cavity require between 50 to 60% increased run time in order to reach a fair residual level of stability, compared to the shroudless model. (Flores and Seume 2015)

The complexity of cavity simulations arises from the interaction between high Mach number flows in the main channel and pressure driven low Mach flow regimes in the cavities. Therefore, as cavity geometries are added to the domain, the convergence monitors also include the monitors of mass flow, total pressure and total temperature at cavity outlet as depicted Figure D.1b. The mass flow and total pressure monitors oscillate, and gradually reach stability after 60,000 iterations. Total temperature monitor needs 65,000 iterations to reach constancy presumably because of the slow convergence of the temperature gradient in the cavity. The cavity model reaches a fair residual level of stability after 65,000 iterations in the main channel and at the cavity outlet monitors. However, the simulation runs 5,000 more iterations to assure complete constancy. In the case of unsteady simulations, strictly speaking, a solution never will depict monitors with a flat constancy when compared to a steady solution. In lieu of constant values, the monitors will depict instantaneous variations in time, and the convergence criteria are mostly considered as these instantaneous variations become temporarily periodic. In this work, the unsteady cases consider the monitoring of the global parameters in the main flow path of all four stages. As all monitors depict periodicity, the unsteady solution is considered as periodically stable and thus converged in time.

Figure D.2 shows the instantaneous and averaged monitors of mass flow $\dot{m}_{\text{red}}$, total pressure ratio π_{P} and isentropic efficiency η_{is} of the third stage at 90° with the tightest clearance near the design point. At this point, the unsteady periodic convergence is reached within one rotation. However, the convergence depends strongly on the operating point that is being simulated. As the load increases, the periodic convergence is achieved after 8∼10 rotations. Thus, increasing the run time. Once the variables reach the temporal periodicity the solution is temporarily evaluated.

(a) Third stage performance monitors
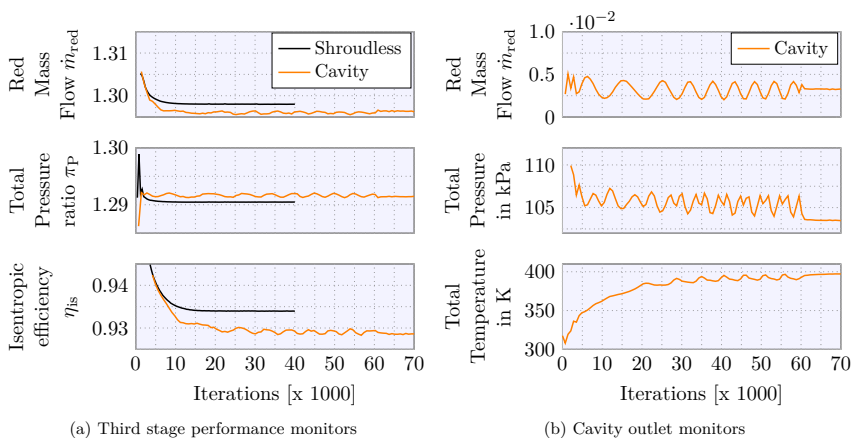
(b) Cavity outlet monitors

Figure D.1: Steady-state convergence monitors for the third stage with the shroudless model and the cavity model
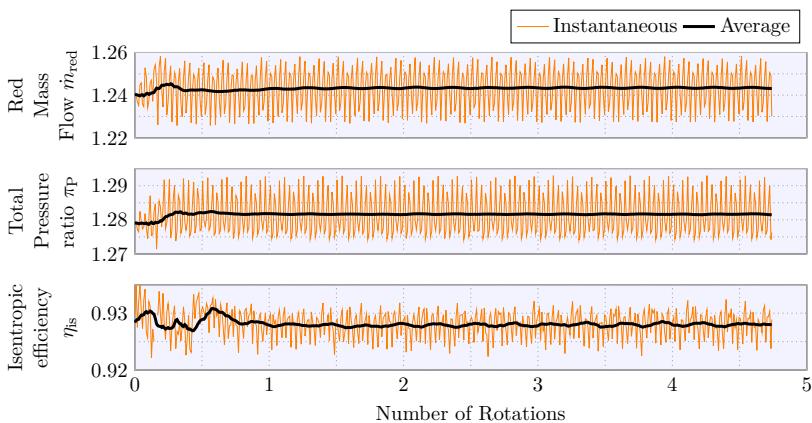

Figure D.2: Average and instantaneous convergence monitors at the third stage for an unsteady simulation with cavity

Bibliography

ACARE (2012): Strategic Research and Innovation Agenda. Advisory Council for Aviation Research and Innovation in Europe. URL www.acare4europe.com.

Adamczyk, J. (1996): Wake Mixing in Axial Flow Compressors. In: Proceedings of ASME Gas Turbine Conference. Birmingham, UK, 96-GT-29.

Ali, Z. and Tucker, P. G. (2014): Multiblock Structured Mesh Generation for Turbomachinery Flows. In: Sarrate, J. and Staten, M. (Ed.) Proceedings of the 22nd International Meshing Roundtable. Springer International Publishing, PP. 165–182. ISBN 978-3-319-02334-2. doi: 10.1007/978-3-319-02335-9_10. URL http://dx.doi.org/10.1007/978-3-319-02335-9_10.

Argüelles, P.; Bischoff, M.; Busquin, P.; B.A.C., D.; Evans, S. R.; Kröll, W.; Lagardére, J.-L.; Lina, A.; Lumsden, J.; Ranque, D.; Rasmussen, S.; Reutlinger, P.; Robins, S. R.; Terho, H. and Wittlöv, A. (2001): European Aeronautics: A Vision for 2020 - Meeting society's needs and winning global leadership. European Comission.

Ashby, G. J. (1957): Investigation of the Effect of Velocity Diagram on Inlet Total-Pressure Distortions through Single-Stage subsonic Axial-Flow Compressors. Technical Report NACA RM L57A03, NACA, Washington, USA.

ASME V & V 20 Committee (2009): Standard for Verification and Validation in Computational Fluid Dynamics and Heat Transfer. The American Society of Mechanicsl Engineers, New York, USA.

Aungier, R. H. (2000): Centrifugal Compressors - A Strategy for Aerodynamic Design and Analysis. ASME PRESS.

Bayley, F. J. and Childs, P. (1994): Air Temperature Tises in Compressor and Turbine Stator Wells. In: International Gas Turbine and Aeroengine Congress and Exposition. The Hague, Netherlands, ASME-94-GT-185.

Becker, B.; Kupijai, P. and Swoboda, M. (2009): High Fidelity CFD on a High-Speed 4.5-Stage Compressor by means of the Non-Linear Harmonics Approach and Transitional Model. In: Proceedings of European Turbomachinery Conference. Graz, Austria, ETC2009-081.

Braun, M. (2007): Experimentelle und Numerische Untersuchungen einer Vorwärtsgepfeilten Beschaufelung in einem Mehrstufigen Hochbelasteten Axialverdichter. Dissertation, Institut für Turbomaschinen und Fluid-Dynamik, Leibniz Universität Hannover, Hannover, Deutschland.

Braun, M. and Seume, J. R. (2006): Forward Sweep in a Four-Stage High-Speed Axial Compressor. In: Proceedings of ASME Turbo Expo. Barcelona, Spain, GT2006-90218.

Chupp, R. E.; Hendricks, R. C.; Lattime, S. B. and Steinetz, B. M. (2006): Sealing in Turbomachinery. In: Journal of Propulsion and Power, Volume 22:P. 313.

Dai, Y.; Tyacke, J. and Tucker, P. (2016): Effect of Labyrinth Seal Configurations on Leackage Performance using LES. In: AIAA SciTech. San Diego, California, USA, AIAA 2016-2127.

Demargne, A. A. J. and Longley, J. P. (2000): The Aerodynamic Interaction of Stator Shroud Leakage and mainstream Flows in Compressors. In: Proceedings of ASME TURBO EXPO 2000. Munich, Germany, 2000-GT-570.

Demargne, A. A. J. and Longley, J. P. (2001): Cavity and Protrusion Effects in a Single-Stage Compressor. In: Proceedings of ASME TURBO EXPO 2001. New Orleans, Louisiana, USA, 2001-GT-433.

Denton, J. (1993): Loss Mechanisms in Turbomachines. In: Journal of Turbomachinery, Volume 115:PP. 621–656.

Du, Y. (2010): Numerical Simulation of Mechanical and Thermal Fluid-Structure Interaction in Labyrinth Seals. Dissertation, Technischen Universität Darmstadt, Darmstadt, Deutschland.

E-BREAK Partners (2014): E-BREAK: Engine Breakthrough Components and Subsystems European FP7 Program. http://www.e-break.eu/. Last opening on 13.04.2015.

Egli, A. (1935): The Leakage of Steam Through Labyrinth Seals. In: ASME Transactions, 1935. PP. 115–122.

ENOVAL Consortium (2014): ENOVAL: Ultra-High Bypass Ratio Aeroengines. http://www.enoval.eu/. Last opening on 13.04.2015.

Erdos, J.; E., A. and W., M. (1977): Numerical Solution of Periodic Transonic Flow through a Fan Stage. In: AIAA Journal, Volume 15(11):PP. 1559–1568.

Eser, D. and Kazakia, J. (1995): Air Flow in Cavities of Labyrinth Seals. In: International Journal of Engineering Science, Volume 33:PP. 2309–2326.

European Commission (2005a): EEFAE: Efficient and environmentally friendly aircraft engine. http://cordis.europa.eu/project/rcn/52463_en.html. Last opening on 13.04.2015.

European Commission (2005b): EEFAE Report Summary. http://cordis.europa.eu/result/rcn/40042_en.html. Last opening on 13.04.2015.

European Commission (2010a): Aeronautics and Air Transport Research 7th Framework Programme 2007-2013 Project Synopses - Volume 1 Calls 2007 & 2008. European Commission, European Research Area, 7th Framework Programme. ISBN 978-92-79-14287-1. doi: 10.2777/83373.

European Commission (2010b): VITAL: EnVIronmenTALly Friendly Aero Engine. http://cordis.europa.eu/project/rcn/94198_en.html. Last opening on 13.04.2015.

European Commission (2012a): Aeronautics and Air Transport Research 7th Framework Programme 2007-2013 Project Synopses - Volume 2 Calls 2010 & 2011. European Commission, European Research Area, 7th Framework Programme. ISBN 978-92-79-22538-3. doi: 10.2777/87206.

European Commission (2012b): DREAM: valiDation of Radical Engine Architecture systeMs. http://cordis.europa.eu/project/rcn/93302_en.html. Last opening on 13.04.2015.

European Commission (2013): Aeronautics and Air Transport Research 7th Framework Programme 2007-2013 Project Synopses - Volume 3 Calls 2012 & 2013. European Commission, European Research Area, 7th Framework Programme. ISBN 978-92-79-29733-5. doi: 10.2777/14083.

Ferguson, J. D. (1988): Brushes as High Performance Gas Turbine Seals. In: Proceedings of Gas Turbine and Aeroengine Congress. Amsterdam, The Netherlands, 88-GT-182.

Fischer, A. (2004): Untersuchungen Hochbelasteter Bow-Statoren in einem mehrstufigen Axialverdichter. Dissertation, Institut für Turbomaschinen und Fluid-Dynamik, Leibniz Universität Hannover, Hannover, Deutschland.

Fischer, A.; Riess, W. and Seume, J. R. (2004): Performance of Strongly Bowed Stators in a Four-Stage High-Speed Compressor. In: Journal of Turbomachinery, Volume 126:P. 333.

Fischer, A. and Seume, J. R. (2003): Comparison of Multi-Stage CFD Calculations and Measurements in a High-Speed Compressor. In: Conference on Modelling Fluid Flow (CMFF'03), The 12th International Conference on Fluid Flow Technologies. Budapest, Hungary.

Flores, D. and Seume, J. (2014): Selecting Cavity Geometries for Improving the Aerodynamic Performance of an Axial Compressor. In: Proceedings of ASME Turbo Expo 2014. Düsseldorf, Germany, GT-2014-25328.

Flores, D. and Seume, J. (2015): The Influence of Labyrinth Flows on the Aerodynamic Performance of an Axial Compressor. In: Proceedings of European Turbomachinery Conference. Madrid, Spain, ETC2015-117.

Freeman, C. (1985): Effect of Tip Clearance Flow on Compressor Stability and Engine Performance. Tip Clearance Effects in Axial Turbomachines. von Karman Institute of Fluid Dynamics, Lecture Series 1985-05.

Freitas, R. B.; Fernandes, L. M. and Mendoca, M. T. (2012): Computational Evaluation of Labyrinth Seal Configurations. In: 50th AIAA Aerospace Sciences Meeting including the New Horizons Forum and Aerospace Exposition. Nashville, Tennessee, USA, AIAA 2012-0476.

Fröbel, T. (2012): Instationäre Strömungsvorgänge im Bereich von Randkavitäten mehrstufiger Hochdruckverdichter. Dissertation, Technischen Universität München, München, Deutschland.

Fröbel, T.; Kau, H. P.; Groth, C. and Gümmer, V. (2010): Numerical Investigation of Unsteady Flow Phenomena in an HP Axial Compressor Incorporating Stator Shroud Cavities. In: 46th AIAA/ASME/SAE/ASEE Joint Propulsion Conference & Exhibit. Nashville, Tennessee, AIAA 2010-6532.

Fuchs, R. (2008): The Visible Vortex-Interactive Analysis and Extraction of Vortices in Large Time-dependent Flow Data Sets. Dissertation, Technischen Universität Wien, Fakultät für Informatik, Wien, Österreich.

Gamal, A. (2007): Leakage and Rotordynamic Effects of Pocket Damper Seals and See-Through Labyrinth Seals. Dissertation, Texas AM University, Texas, USA.

Giles, M. B. (1988): Calculation of Unsteady Wake/rotor Interaction. In: Journal of Propulsion, Volume 4(4):PP. 356–362.

Giles, M. B. (1990): Nonreflecting Boundary Conditions for Euler Equation Calculations. In: AIAA Journal, Volume 28(12):PP. 2050–2058.

Giles, M. B. (1991): UNSFLO: A Numerical Method for the Calculation of Unsteady Flow in Turbomachinery. In: GTL Report #205.

Gourdain, N.; Sicot, F.; Duchaine, F. and Gicquel, L. (2014): Large eddy simulation of flows in industrial compressors: a path from 2015 to 2035. In: Philosophical Transactions of the Royal Society. 372.

Hah, C. (2015a): Effects of Unsteady Flow Interactions on the Performance of a Highly-Loaded Transonic Compressor Stage. In: Proceedings of ASME Turbo Expo 2015: Turbine Technical Conference and Exposition GT2015. Montreal, Canada, GT2015-43389.

Hah, C. (2015b): Unsteady Loss in the Stator due to Incoming Rotor Wake in a HIghly-Loaded Transonic Compressor. In: 22nd International Symposium on Air Breathing Engines 2015:IS-ABE 2015. Phoenix,Arizona, USA, ISABE-2015-20144.

He, K.; Li, J.; Yan, X. and Feng, Z. (2012): Investigations of the conjugate heat transfer and windage effect in stepped labyrinth seals. In: International Journal of Heat and Mass Transfer, Volume 55:PP. 4536–4547.

Heidegger, N. J.; Hall, E. J. and Delaney, R. A. (1996a): Aeropropulsion Technology (APT). Task 23 - Stator Seal Cavity Flow Investigation. Technical Report NASA-CR-198504, NASA Lewis Research Center, Cleveland, Ohio, USA.

Heidegger, N. J.; Hall, E. J. and Delaney, R. A. (1996b): Parameterized study of high-speed compressor seal cavity flow. In: AIAA, ASME, SAE, and ASEE, Joint Propulsion Conference and Exhibit, 32nd, Lake Buena Vista, FL, July 1-3, 1996. Florida, AIAA Paper-96-2807.

Henderson, A.; Walker, G. and Hughes, J. D. (2006): Unsteady Transition Phenomena at a Compressor Blade Leading Edge. In: Proceedings of GT2006 ASME Turbo Expo 2006: Power for Land, Sea and Air. Barcelona, Spain, GT2006-90641.

Hergt, A.; Dorfner, C.; Nicke, E. and Moening, R. (2011): Endwall Contouring for Axial Compressors by Generating an Aerodynamic Separator-Part 1: Principal Cascade Design and Compressor Application. In: Journal of Turbomachinery, Volume 133:P. 021026.

Hodkinson, B. (1939): Estimation of the Leakage through a Labyrinth Gland. In: Proceedings of the Institution of Mechanical Engineers, 141, 1939. PP. 283–288.

Holmén, V. (2012): Methods for Vortex Identification. Master's Theses in Mathematical Sciences, Lund University, Lund, Sweden.

Hunt, J.; Wray, A. and Moin, P. (1988): Eddies, stream, and convergence zones in turbulent flows. In: Center of Turbulence Research - Procdings of the Summer Program 1988.

Jefferson, J. L. and Turner, R. (1958): Some Shrouding and Tip Clearance Effects in Axial Flow Compressors. In: International Shipbuilding Progress, 1958, Volume 5:P. 78.

Kato, D.; Yamagani, M.; Tsuchiya, N. and Kodama, H. (2011): The Influence of Shrouded Stator Cavity Flows on the Aerodynamic Performance of a High-Speed Multistage Axial-Flow Compressor. In: Proceedings of ASME Turbo Expo 2011. Vancouver, British Columbia, Canada, GT-2011-46300.

Kato, M. and Launder, B. E. (1993): The Modeling of Turbulent Flow Around Stationary and Vibrating Square Cylinders. In: Proceedings 9th Symposium on Turbulent Shear Flows. Kyoto, Japan, PP. 10.4.1–10.4.6.

Kerrebrock, J. and Mikolajczak, A. A. (1970): Intra-Stator Transport of Rotor Wakes and its Effect on Compressor Performance. In: Journal of Engineering for Power, Volume 92:PP. 359–368.

Kim, T. S. and Cha, K. S. (2009): Comparative analysis of the influence of labyrinth seal configuration on leakage behavior. In: Journal of Mechanical Science and Technology, Volume 23:PP. 2830–2838.

Kim, T. S. and Kang, S. Y. (2010): Investigation of Leakage Characteristics of Straight and Stepped Labyrinth Seals. In: International Journal of Fluid Machinery and Systems, Volume 3:PP. 253–259.

Kolář, V. (2007): Vortex Identification: New requirements and limitations. In: International Journal of Heat and Fluid, Volume 28:PP. 638–652.

Korsia, J. J. (2009): VITAL - EUROPEAN R&D PROGRAMME FOR GREENER AERO-ENGINES. International Society of Air Breathing Engines.

Kožulović, D. (2007): Modellierung des Grenzschichtumschlags bei Turbomaschinenströmungen unter Berücksichtigung mehrerer Umschlagsarten. Forschungsbericht Deutsches Zentrum für Luft- und Raumfahrt. Deutsches Zentrum für Luft- und Raumfahrt. URL http://www-brs.ub.ruhr-uni-bochum.de/netahtml/HSS/Diss/KozulovicDragan/diss.pdf.

Kožulović, D.; Röber, T. and Nürnberger, D. (2007): Application of a Multimode Transition Model to Turbomachinery Flows. In: Proceedings 7th European Turbomachinery Conference. Athens, Greece.

Kügeler, E. (2004): Numerisches Verfahren zur genauen Analyse der Kühleffektivität filmgekühlter Turbinenschaufeln. Forschungsbericht Deutsches Zentrum für Luft- und Raumfahrt. Deutsches Zentrum für Luft- und Raumfahrt.

Kügeler, E.; Weber, A.; Nürnberger, D. and Engel, K. (2008): Influence of Blade Fillets on the Performance of a 15 stage Gas Turbine Compressor. In: Proceedings of ASME Turbo Expo. Berlin, Germany, GT2008-50748.

Kyprianidis, K. G. (2011): Future Aero Engine Designs: An Evolving Vision, Advances in Gas Turbine Technology. InTech. ISBN 978-953-307-611-9. URL http://www.intechopen.com/books/advances-in-gas-turbine-technology/future-aero-engine-designs-an-evolving-vision.

Lange, M.; Mailach, R. and Vogeler, K. (2010): An Experimental Investigation of Shrouded and Cantilevered Compressor Stators at Varying Clearance Sizes. In: Proceedings of ASME Turbo Expo 2010. Glasgow, United Kingdom, GT-2010-22106.

Langtry, R. (2006): A Correlation-Based Transition Model using Local Variables for Unstructured Parallelized CFD Codes. PhD Thesis, Universität Stuttgart, Stuttgart, Deutschland.

Langtry, R. and Menter, F. (2009): Correlation-Based Transition Modeling for Unstructured Parallelized Computational Fluid Dynamics Codes. In: AIAA Journal, Volume 47(12):PP. 2894–2906.

Langtry, R. B.; Menter, F. R.; Likki, S. R.; Suzen, Y. B.; Huang, P. G. and Völker, S. (2006): A Correlation-Based Transition Model Using Local Variables—Part II: Test Cases and Industrial Applications. In: Journal of Turbomachinery, Volume 128(3):PP. 423–434.

Lattime, S. B. and Steinetz, B. M. (2004): High-Pressure-Turbine Clearance Control Systems: Current Practices and Future Directions. In: Journal of Propulsion and Power, Volume 20:P. 302.

LeJambre, C. R.; Zacharias, R. M.; P., B. B.; J., G. A. and J., Y. C. (1998): Development and Application of a Multistage Navier-Stokes Flow Solver: Part II - Application to a High-Pressure Compressor Design. In: Journal of Turbomachinery, Volume 120:PP. 215–223.

LEMCOTEC partners (2012): LEMCOTEC: Low Emissions Core-Engine Technologies. http://www.lemcotec.eu/. Last opening on 13.04.2015.

Lewis, L. V. (2002): In-Engine Measurements of Temperature Rises in Axial Compressor Shrouded Stator Cavities. In: Proceedings of ASME TURBO EXPO 2002. Amsterdam, The Netherlands, 2002-GT-30245.

Lieblein, S. and Roudebush, W. H. (1956): Theoretical Loss Relations for Low-Speed Two-Dimensional-Cascade Flow. Technical Report NACA TN 3662, NACA, Washington, USA.

Ludwig, L. P. (1978): GAS PATH SEALING IN TURBINE ENGINES. In: AGARD CONFERENCE PROCEEDINGS No. 237 Seal Technology in Gas Turbine Engines. PP. 1.1–1.41.

Lurie, D. and Breeze-Stringfellow, A. (2015): Evaluation of Experimental Data from a Highly Loaded Transonic Compressor Stage to Determine Loss Sources. In: Proceedings of ASME Turbo Expo 2015: Turbine Technical Conference and Exposition GT2015. Montreal, Canada, GT2015-42526.

Mailach, R.; Lehmann, I. and Vogeler, K. (2007a): Periodical Unsteady Flow within a Rotor Blade Row on an Axial Compresor-Part I-Flow Field at Midspan. In: Proceedings of GT2007 ASME Turbo Expo 2007: Power for Land, Sea and Air. Montreal, Canada, GT2007-27210.

Mailach, R.; Lehmann, I. and Vogeler, K. (2007b): Periodical Unsteady Flow within a Rotor Blade Row on an Axial Compresor-Part II-Tip Clearance Vortex Interaction. In: Proceedings of GT2007 ASME Turbo Expo 2007: Power for Land, Sea and Air. Montreal, Canada, GT2007-27210.

Malan, P.; Suluksna, K. and Juntasaro, E. (2009): Calibrating the $\gamma - Re_\theta$ Transition Model for Commercial CFD. In: 47th AIAA Aerospace Sciences Meeting, June 2009.

Malcevic, I. (2011): Automated Blocking for Structured CFD Gridding with an Application to Turbomachinery Secondary Flows. In: 20th AIAA Computational Fluid Dynamics Conference. Honolulu, Hawaii, USA, AIAA 2011-3049.

Marciniak, V.; Kügeler, E. and Franke, M. (2010): Predicting Transition On Low-Pressure Turbine Profiles. In: V European Conference on Computational Fluid Dynamics ECCOMAS CFD 2010. Lissabon, Portugal.

Marty, J. and Aupoix, B. (2012): Interaction of shrouded stator flow and main flow and its influence on performances of a three-stage high pressure compressor. In: Proceedings of the Institution of Mechanical Engineers, Part A: Journal of Power and Energy, Volume 226:PP. 489–500.

Menter, F. R. (1993): Zonal two equation k-ω turbulence models for aerodynamic flows. In: AIAA Paper 93-2906.

Menter, F. R.; Kuntz, M. and Langtry, R. (2003): Ten Years of Industrial Experience with the SST Turbulence Model. In: Turbulence Heat and Mass Transfer 4, Volume 4.

Menter, F. R.; Langtry, R. B.; Likki, S. R.; Suzen, Y. B.; Huang, P. G. and Völker, S. (2006): A Correlation-Based Transition Model Using Local Variables—Part I: Model Formulation. In: Journal of Turbomachinery, Volume 128(3):PP. 413–422.

Montomoli, F.; Hodson, H. P. and Lapworth, L. (2011): RANS-URANS in axial compressor, a design methodology. In: Proceedings of the Institution of Mechanical Engineers, Part A: Journal of Power and Energy, Volume 225:PP. 363–374.

Montomoli, F.; Naylor, E.; Hodson, H. and Lapworth, L. (2009): Unsteady Effects in Cantilevered Axial Compressors: A Multistage Simulation. In: XIX International Symposium on Air Breathing Engines 2009:ISABE 2009. Montreal, Canada, ISABE-2009-1104.

Montomoli, F.; Naylor, E.; Hodson, H. and Lapworth, L. (2013): Unsteady Effects in Cantilevered Axial Compressors: A Multistage Simulation. In: Journal of Propulsion and Power, Volume 29:PP. 1001–1008.

Naylor, E.; Montomoli, F.; Hodson, H. and Lapworth, L. (2009): Numerical Modeling of Cavities in Multistage Axial Compressors. In: XIX International Symposium on Air Breathing Engines 2009 (ISABE 2009). Montreal, Canada, ISABE-2009-1186.

Neumann, K. (1964): Zur Frage der Verwendung von Durchblickdichtungen im Dampfturbinenbau. In: Maschinenbautechnik, Vol. 13, 1964. PP. 188–195.

NEWAC partners (2011): NEWAC: New Aeroengine Core Concepts. http://www.newac.eu/. Last opening on 13.04.2015.

Nürnberger, D. (2004): Implizite Zeitintegration für die Simulation von Turbomaschinenströmungen. Forschungsbericht Deutsches Zentrum für Luft- und Raumfahrt. Deutsches Zentrum für Luft- und Raumfahrt.

Oezturk, H. K.; Childs, P. R. N.; Turner, A. B.; Hannis, J. and Turner, J. (1998): A Three Dimensional Computational Study of Windage Heating within an Axial Compressor Stator Well. In: International Gas Turbine and Aeroengine Congress and Exhibition. Stockholm, Sweden, ASME-98-GT-119.

Oezturk, H. K.; Turner, A. B. and Childs, P. R. N. (2002): The Effect of Labyrinth Seal Clearance on Stator Clearance on Stator-Well Flow and Windage Heating. In: International Journal of Turbo and Jet Engines, Volume 19:PP. 219–231.

Oeztürk, H. K.; Turner, A. B.; Childs, P. R. N. and Bayley, F. (2000): Stator well flows in axial compressors. In: International Journal of Heat and Fluid Flow, Volume 21:PP. 710–716.

Riéra, W. (2014): Evaluation of the ZDES method on an axial compressor: analysis of the effects of upstream wake and trothle on the tip-leakage flow. Dissertation, Université de Lyon, Lyon, France.

Rigby, D. L. (2004): TopMaker: A Technique for Automatic Multi-Block Topology Generation Using the Medial Axis. Technical Report NASA/CR-2004-213044, NASA Glenn Research Centre, Clevelend, Ohio, USA.

Roache, P. (1994): Perspective: A Method for Uniform Reporting of Grid Refinement Studies. In: Journal of Fluids Engineering, Volume 116:PP. 405–413.

Roache, P. (1997): QUANTIFICATION OF UNCERTAINTY IN COMPUTATIONAL FLUID DYNAMICS. In: Annual Review of Fluid Mechanics, Volume 29:PP. 123–160.

Roth, M. (2000): Automatic Extraction of Vortex Core Lines and other Line-Type Features. Dissertation, Institute of Scientific Computing, Computer Graphics Group, ETH Zürich, Zürich, Switzerland.

Scharrer, J. K. (1988): Theory Versus Experiment for the Rotordynamic Coefficients of Labyrinth Gas Seals: Part 1 - A Two Control Volume. In: Journal of Vibration, Acoustics, Stress, and Reliability in Design, Volume 110:PP. 270–280.

Scott, R. M.; Childs, P. R. N.; Hills, N. and Millward, J. (2000): Radial Flow into Downstream Cavity of a Compressor Stator Well. In: Proceedings of ASME TURBO EXPO 2000. Munich, Germany, 2000-GT-0507.

Siemann, J.; Krenz, I. and Seume, J. (2016): Experimental Investigation of Aspiration in a Multi-Stage High-Speed Axial Compressor. In: Proceedings of ASME Turbo Expo 2016. Seoul,South Korea, GT2016-56440.

Silverstein, A.; S., K. and W., K. B. (1939): Downwash and Wake Behind Plain and Flapped Airfoils. Technical Report NACA Report No. 651, NACA, Washington, USA.

Smith, L. (1958): Recovery Ratio - A measure of the Loss Recovery Potential of Compressor Stages. In: Transactions of the ASME, Volume 80:PP. 517–524.

Smith, L. (1966): Wake Dispersion in Turbomachines. In: Journal of Basic Engineering, Volume 88:PP. 688–690.

Soemarwoto, B. I.; Kok, J. C.; de Cock K. M. J.; B., K. A.; A., K. G. and A., V. J. F. (2007): Performance evaluation of gas turbine labyrinth seals using computational fluid dynamics. Technical Report NLR-TP-2007-624, National Aerospace Laboratory NLR, Amsterdam, The Netherlands.

Sohn, D. W. and Song, S. J. (2006): Influence of the Leakage Flow tangential Velocity on the Loss generation and Leakage Flow kinematics in Shrouded Axial Compressor Cascades. In: Proceedings of ASME turbo Expo 2006: Power for Land, Sea and Air. Barcelona, Spain, GT2006-90979.

Speidel, L. (1954): Berechnung der Stromungsverluste von Ungestaffelten ebenen Schaufelgittern. In: Ing. Arch., Vol.22. PP. 295–322.

Sriti, M.; Agouzoul, M.; Ouazar, D. and Micheau, P. (1997): Simulation numérique d'écoulement compressible dans les joints labyrinthe. In: Journal de Physique, Volume 3:PP. 1025–1037.

Suresh, K. (2003): Automating the CAD-CAE Dimensional Reduction Process. In: 8th ACM Solid Modeling Conference. Seattle, USA.

Swoboda, M.; Ivey, P. C.; Wenger, U. and Gümmer, V. (1998): An Experimental Examination of Cantilevered and Shrouded Stators in a Multistage Axial Compressor. In: International Gas Turbine and Aeroengine Congress and Exhibition. Stockholm, Sweden, ASME-GT-98-282.

Trojanovskij, B. M. (1950): Dampfdurchsatz durch die Labyrinthdichtungen von Dampfturbinen (In Russian). In: Isvestija WTI 1950. No.1. 12-24. PP. 12–24.

Tyacke, J.; Jefferson-Loveday, R. and Tucker, P. (2012): On LES Methods applied to Seal Geometries. In: Proceedings of ASME Turbo Expo 2012. Copenhagen, Denmark, GT2012-68840.

Vakili, A. D.; Meganathan, A. J.; Michaud, M. and Radhakrishnan, S. (2005): An Experimental and Numerical Study of Labyrinth Seal Flow. In: Proceedings of ASME Turbo Expo 2005. Reno-Tahoe, Nevada, USA, GT-2005-68224.

Valkov, T. and Tan, C. (1998a): Effect of Upstream Rotor Vortical Disturbances on the Time-Average Performance of Axial Compressor Stators-Part 1-Framework of Technical Approach and Wake-Stator Blade Interactions. In: Proceedings of ASME Gas Turbine Conference. Stockholm, Sweden, 98-GT-312.

Valkov, T. and Tan, C. (1998b): Effect of Upstream Rotor Vortical Disturbances on the Time-Average Performance of Axial Compressor Stators-Part 2-Rotor Tip Vortex/Streamwise Vortex-Stator Blade Interactions. In: Proceedings of ASME Gas Turbine Conference. Stockholm, Sweden, 98-GT-313.

VanZante, D.; Admaczyk, J.; Strazisar, A. and Okiishi, T. H. (1997): Wake Recovery Performance Benefit in a High-Speed Axial Compressor. In: Proceedings of ASME Gas Turbine Conference. Orlando, Florida, USA, 97-GT-535.

Vermes, G. (1961): A Fluid Mechanics Approach to the Labyrinth Seal Leakage Problem. In: Journal of Engineering for Power, Volume 83:P. 161.

von der Bank, R.; Donnerhack, S.; Rae, A.; Poutriquet, F.; Lundbladh, A. and Schweinberger, A. (2015): Invited Lecture: Advanced Core Engine Technologies Assessment and Validation. In: European Turbomachinery Conference Proceedings.

Vorreiter, A.; Fischer, S.; Saathoff, H.; Radespiel, R. and Seume, J. R. (2012): Numerical Investigations of the Efficiency of Circulation Control in a Compressor Stator. In: Journal of Turbomachinery, Volume 134:P. 021012.

Walkenhorst, J. (2000): Axialverdichter mit wandkonturierten Leitschaufeln-Prüfstandentwicklung und Strömungsuntersuchung. Forschritt-Berichte VDI Reihe 7 Nr. 390, Düsseldorf. VDI-Verlag.

Weinberger, T. (2014): Einfluss geometrischer Labyrinth- und Honigwabenparameter auf das Durchfluss- und Wärmeübergangsverhalten von Labyrinthdichtungen. Dissertation, Karlsruher Institut für Technologie, Stutensee, Karlsruhe, Deutschland.

Wellborn, S. R. (2001): Details of Axial-Compressor Shrouded Stator Cavity Flows. In: Proceedings of ASME TURBO EXPO 2001. New Orleans, Louisiana, USA, 2001-GT-495.

Wellborn, S. R. and Okiishi, T. H. (1996): Effects of Shrouded Stator Cavity Flows on Multistage Axial Compressor Aerodynamic Performance. Technical Report NASA-CR-198536, NASA Lewis Research Center, Cleveland, Ohio, USA.

Wellborn, S. R. and Okiishi, T. H. (1999): The Influence of Shrouded Stator Cavity Flows on Multistage Compressor Performance. In: Journal of Turbomachinery, Volume 121:PP. 486–497.

Wellborn, S. R.; Okiishi, T. H. and I., T. (2000): Modeling Shrouded Stator Cavity Flows in Axial-Flow Compressors. In: Journal of Turbomachinery, Volume 122:PP. 55–61.

Wheeler, A.; Miller, R. and Hodson, H. P. (2007): The Effect of Wake Induced Structures on Compressor Boundary-Layers. In: Journal of Turbomachinery, Volume 129:PP. 705–712.

Wilcox, D. C. (1988): Reassessment of the scale-determining equation for advanced turbulence models. In: AIAA Journal, Volume 26(11):PP. 1299–1310.

Wiseman, M. and Guo, T. (2001): An Investigation of Life Extending Control Techniques for Gas Turbine Engines. In: Proceedings of the American Control Conference, Volume 5:P. 3706.

Wisterfeld, G. (1978): Seal Technology in Gas Turbine Engines. In: AGARD CONFERENCE PROCEEDINGS No. 237 Seal Technology in Gas Turbine Engines. London, U.K., AGARD CP-237.

Yamagani, M.; Kodama, H.; Kato, D.; Tsuchiya, N.; Horiguchi, Y. and Kazawa, J. (2011): CFD Modeling Effects on Unsteady Multistage Simulation for a Transonic Axial Compressor. In: Proceedings of ASME Turbo Expo 2011. Vancouver, British Columbia, Canada, GT-2011-46198.

Yan, X.; Li, J.; Song, L. and Feng, Z. (2009): Investigations on the Discharge and Total Temperature Increase Characteristics of the Labyrinth Seals with Honeycomb and Smooth Lands. In: Journal of Turbomachinery, Volume 131:PP. 041009–1–041009–8.

Yang, H.; Nuernberger, D.; Nicke, E. and Weber, A. (2003): Numerical Investigation of Casing Treatment Mechanisms With a Conservative Mixed-Cell Approach. In: Proceedings of ASME Turbo Expo. Atlanta, GT-2003-38483.

Yoon, S.; Selmeier, R.; Cargill, P. and Wood, P. (2015): Effect of the Stator Hub Configuration and Stage Design Parameters on Aerodynamic Loss in Axial Compressors. In: Journal of Turbomachinery, Volume 137:P. 091001.

Zimmerman, H. and Wolff, K. H. (1987): Comparison Between Empirical and Numerical Labyrinth Flow Correlations. In: Proceedings of ASME Gas Turbine Conference. Anaheim, California, USA, 87-GT-86.

Curriculum Vitae

Personal Data

Name	Diego Rodrigo Flores Galindo
Date of Birth	04 December 1982
Place of Birth	Mexico City
Family Status	Married

Education

1999 - 2003	Bachelor of Sciences in Aeronautical Engineering at National Polytechnic Institute, Mexico
2004 - 2006	Master of Sciences in Mechanical Engineering at National Polytechnic Institute, Mexico
2011 - 2017	PhD in Mechanical Engineering at Institute for Turbomachinery and Fluid Dynamics, Leibniz University Hanover, Germany

Work Experience

2007-2011	Project Engineer in Heating, Ventilation and Air Conditioning (HVAC) Department in General Motors Mexico
2011-2017	Research Assistant at Institute for Turbomachinery and Fluid Dynamics, Leibniz University Hanover, Germany

Hannover, December 2017

The leakage flow has affected the performance of turbomachinery since the manufacturing of first steam turbines due to the poor sealing between rotating and stationary parts. Therefore, this work investigates the interaction of labyrinth seal flows with the mainstream of an axial compressor in order to look deeper into and understand the physical mechanism behind this interaction. The most significant interaction between the cavity leakage flow and the main stream occurs in the discharge region between the hub and the upstream cavity-trench. Based on this, the modification of the cavity outlet angle could reduce the aforementioned interaction and consequently minimize the losses. The main aim of this work is to evaluate the influence of the cavity outlet discharge angle on the stage performance. To this end, three variants have been designed for the third stage of a four-stage high-speed axial compressor.

The overall performance of the third compressor's stage shows that the effect of the cavity outlet angle is more sensitive with respect to lower leakage rates. As the leakage rate progressively increases, the cavity outlet angle reduces its sensitivity. The case pointing against the main flow direction achieves the lowest total pressure ratio reduction but the highest total temperature ratio compared to remaining cases. Independently of the cavity outlet angle, the interaction of the upstream rotor wake and the leakage flow induces a wake-leakage vortex which provokes the formation of an adjacent induced leakage vortex. This mechanism repeats until the next adjacent rotor wake induces a new wake-leakage vortex. The cavity outlet angle modifies the number of induced-leakage vortices.

Leibniz
Universität
Hannover